Northumbria Research Link

3D Printing Assisted Development of Bio-inspired Structure and Device for Advanced Engineering

ANSU SUN

PhD

2022

3D Printing Assisted Development of Bio-inspired Structure and Device for Advanced Engineering

ANSU SUN

A thesis submitted in partial fulfilment of the requirements of the University of Northumbria at Newcastle for the degree of Doctor of Philosophy

Department of Mechanical and Construction Engineering

August 2022

Abstract

Smart materials with bio-inspired structure and stimuli-responsive features can sense the external and internal condition changes, such as temperature, light intensity, pH or ion concentration. Those unique functions have been widely utilized in cutting edge engineering applications, such as flexible sensors, soft robotics and tissue engineering. Meanwhile, conventional manufacturing methods such as moulding, and lithography-based microfabrication still represent the mainstream force in scale up manufacturing. Considerable limitations for these technologies, such as on demand rapid prototyping, the high cost and low-volume production, remain to be overcome. In this PhD project, I explored the advanced manufacturing in facilitating the complex structure, with higher controllability, lower prototyping cost and extended applications (flexible sensors, soft robots, bio-medical devices, etc.). The key practice is to utilize the high-resolution 3D printing technology to create dedicated bio-inspired structures based on functional materials. Combined with advanced micro/nano engineering, we have achieved a variety of techniques/prototypes for future applications, such as optical control, micro-fluidic and bio-medical systems, etc.

Acknowledgement

First, I would like sincerely to thank my PhD supervisors, Prof. Ben Bin Xu and Dr. Yifan Li. Ben is my principal supervisor, who have given a lot of guidance from the beginning of my research life until today. Moreover, when I was confused and stressed in the personal life, he enlightened me, helped me to solve my doubts and relieve my pressure. Dr. Yifan Li has been my supervisor when I was a master student. He has always been helpful to me to address the issues/challenges in my project.

Secondly, I would like to thank our group members, Dr. Ding Wang, Dr. Yingzhi Liu and Dr. Sreepathy Sridhar. Ding was my senior, I learned rigorous experimentation, data analysis and paper writing methods from him. In addition, Yingzhi and Sreepathy are my co-workers, we helped each other a lot during our co-operation work. The hardworking of Yingzhi and the scientific research ability of Sreepathy, have inspired me a lot.

Thirdly, I would like to thank our technical team: Adam Cosheril, Rebecca Payne and Pietro Maiello. Without their help, I could not successfully complete all my experiments.

Last but not least, I want to thank my family. In the past two years, the Covid-19 pandemic and grandmother's pass away have caused great destress for me. My family's support means a lot to me, they are the biggest motivation for me to move forward.

Declaration

I declare that the work contained in this thesis has not been submitted for any other award and that it is all my own work. I also confirm that this work fully acknowledges opinions, ideas and contributions from the work of others.

Any ethical clearance for the research presented in this thesis has been approved.

I declare that the word count of this thesis is currently 35,545 words

Name : Ansu Sun

Signature :

Date : 25/08/2022

Contents

Table of Contents

List of Figures

	gel structure. The observations of swelling-induced morphological developments at 8 mins for the axial edges with a) optical microscope, fluorescence microscope and reconstructed 3D image from LCSM based on the selected area in optical image, and for the circumferential out surface with b) optical microscope, LCSM and the cross-sections along the axial and circumferential direction from LSCM based on the selected area in optical image. The analytical plots of time dependent evolutions of structure deformation during swelling: c) wavelength (λ) and amplitude (A) of buckling, d) surface crease depths (μ_H and μ_V) and crease spacings (x_H and x_V); e) The experimental observation and finite element simulation of the post-buckling development; f) $\frac{G}{L}$ versus $\frac{H}{H_0}$. Green area: I-closing regime; pink area: II-holding regime; purple area: III-reopening regime.	
Figure 5.4	Buckling on circumferential edge, inner zone and swelling-induced mechanical instabilities of the hemispherical shell hydrogel; a) The schematic of the circumferential edge (green arrow) and the circumferential inner zone (red arrow); b) Optical micrograph of gel structure swelling at 2 mins, the dash lines highlight the inner edge with a label Din. The gel structure has initial D_{out} =L_o=10 mm, D_{in} =5 mm, θ=180°. The scale bar is 5 mm; c) The observations of morphologies at various time intervals of the hemispherical shell hydrogel under optical microscope. The analytical plots of time dependent evolutions of structure deformation during swelling: d) B/L, where B refers to the gap distance between edges,	127

List of Tables

Achievement

Journal Paper:

1. ***Ansu Sun***, Ding Wang, Honghao Zhou, Yifan Li, Chris Connor, Jie Kong, Jining Sun, Ben Bin Xu, Spatially Engraving Morphological Structure on Polymeric Surface by Ion Beam Milling, *Polymers* **2019**, 11 (7), 1229-1239. (Q1, Google Citation: 2)

2. Zhenghong Li, Yingzhi Liu, Ming Lei, ***Ansu Sun***, Sreepathy Sridhar, Yifan Li, Xuqing Liu, Haibao Lu, Richard Fu, Ben Bin Xu, A Stimuli-responsive Gel Impregnated Surface with Switchable Lipophilic/Oleophobic Properties, *Soft Matter* **2020**, 16 (6), 1636-1641. (Q1, Google Citation: 4)

3. Dongjie Liu, Yong Li, Fei Liu, Wenjing Zhou, ***Ansu Sun***, Xiaoteng Liu, Fei Chen, Ben Bin Xu, Jinjia Wei, Interfacial Interaction Enhanced Rheological Behavior in PAM/CTAC/Salt Aqueous Solution-A Coarse-Grained Molecular Dynamics Study, *Polymers* **2020**, 12 (2), 265-281. (Q1, Google Citation: 2)

4. Sreepathy Sridhar, Cong Wang, Jonathan G. Terry, Xue Chen, ***Ansu Sun***, Zhenghong Li, Haibao Lu, Ben Bin Xu and Yifan Li, Controlled Cooperative Wetting Enabled Heterogeneous Structured 3D Morphing Transducers, *Advanced Materials Interfaces* **2020**, 8 (2), 2001211. (Q1)

5. Ziyu Xing, Haibao Lu, ***Ansu Sun***, Yong Qing Fu, Muhammad Wakil Shahzad and Ben Bin Xu, Understanding Complex Dynamics of Interfacial Reconstruction in Polyampholyte Hydrogels Undergoing Mechano-chemo-electrotaxis Coupling, *Journal of Physics D: Applied Physics* **2020**, 54 (8), 085301. (Q1, Google Citation: 2)

6. Yingzhi Liu, ***Ansu Sun***, Sreepathy Sridhar, Zhenghong Li, Zhuofan Qin, Ji Liu, Xue Chen, Haibao Lu, Ben Zhong Tang and Ben Bin Xu, Spatially and Reversibly Actuating Soft Gel Structure by Harnessing Multimode Elastic

Instabilities, *ACS Applied Materials & Interfaces* **2021**, 13 (30), 36361-36369. (Q1, equal contribution as first author)

7. ***Ansu Sun***, Sreepathy Sridhar, Xue Chen, Yifan Li and Ben Bin Xu, A Tuneable Morphological Deformation Polyelectrolyte System for Smart Ocular Applications, in preparation.

Conference:

1. *UK Fluid Networks (UKFN) – Members of the Special Interest Group (SIG)*, 26 May 2017, Northumbria University, Newcastle upon Tyne, UK

2. *EE PGR Conference 2017 – Research Connects,* 15 June 2017, Northumbria University, Newcastle upon Tyne, UK (**Poster**)

3. *The 24ᵗʰ Joint Annual Conference of UKFN SIG and CSCST-SCI*, 23 – 24 June 2017, Newcastle upon Tyne, UK (**Poster**)

4. *Bruker SPM Conference & Users Meeting,* 10-11 October 2017, Leeds, UK

5. *UKFN SIG mini-symposium: Structural surfaces and liquid/surface interactions*, 20 April 2018, Heriot-Watt University, Edinburgh, UK (**Video Presentation**)

6. *EE PGR Conference 2018 – Research for a Better Tomorrow,* 21 June 2018, Northumbria University, Newcastle upon Tyne, UK (**Oral Presentation**)

7. *The 25ᵗʰ Joint Annual Conference of CSCST-SCI*, 6 - 7 September 2018, University of Manchester, UK (**Poster**)

8. *UK Fluid Networks (UKFN) – Multiscale Modelling of Wetting Phenomena*, 12 - 13 September 2018, Durham, UK (**Poster**)

9. Cong Wang, Sreepathy Sridhar, Jonathan G. Terry, ***Ansu Sun***, Zhenghong Li, Haibao Lv, Ben B. Xu, Yifan Li, Advanced 3D Morphing Transducers by Smart Hydrogel Patterning, 2019 20th IEEE TRANSDUCERS, Berlin, Germany, DOI: 10.1109/TRANSDUCERS.2019.8808453

10. *Droplet 2019*, 15 - 18 September 2019, Durham, UK (**Oral Presentation & Poster**)

11. *Reforming Multi-disciplinary Engineering Innovation for the New Normal*, 28 August 2020, Northumbria University, UK (**Oral Presentation**)

12. *The 27th Annual Conference of the Chinese Society of Chemical Science and Technology in the UK and Society of Chemical Industry's Chinese UK Regional Group (CSCST-SCI)*, 11 - 12 September 2020, Online, UK (**Oral Presentation**)

13. *RSC Materials Chemistry Division Poster Symposium*, 20 January 2021, Northumbria University, Online, UK (**Oral Presentation**)

14. ***Ansu Sun***, Sreepathy Sridhar, Sherry Chen, Yifan Li, Ben Bin Xu, A Tunable Morphing Polyelectrolyte System for Smart Ocular Applications, 2021 21st IEEE TRANSDUCERS, Online, DOI: 10.1109/ Transducers50396.2021.9495587

Seminar & Workshop:

1. *AM3PS 2017 workshop – Additive Manufactured Metallic Materials Properties & Structures*, IOM3, 24 May 2017, Coventry, UK

2. *Academical visiting*, 18 – 26 September 2018, Chongqing, China

Chapter 1

Introduction

This Chapter describes the general background for this project. This section will start by briefing on some natural existing structures, then introducing manufacturing techniques and recent developments (including additive manufacturing). The aim and objectives of this thesis will be stated.

1.1 3D Printing of Bio-inspired Structure and Device for Advanced Engineering

3D printing is an advanced method of manufacturing products by means of layer-by-layer construction, with the assistance of computer-aided design (CAD) [1, 2]. 3D printing has led to a revolution in the modern manufacturing technology. The existing printing technologies (fused deposition modelling, selective laser sintering, selective laser melting, etc.) have been able to print products regardless of the geometrical constraints [3] with good resolution [4]. In contrast to old method like casting, 3D printing can print any shape products and be brought into real use very quickly. Moreover, 3D printed objects can be more detailed and require much less post processing, which can decrease the costs by as much as 75% [5]. 3D printing has been used not only in engineering, but also in the medical field. Before 3d printing, doctors would replace the crushed skull part with metal mesh which

has two major disadvantages: it is weak and imprecise. 3D printing make the surgery safer and easier [6] by allowing doctors to precisely design parts of the skull to replace the broken parts. 3D printing technologies have been developed for multiple requirements, and the printable materials include ABS, PLA, metals, ink, photopolymer resins, etc. It is applied to the production of metal, biocompatible and composite parts with responsive functions. Some of the most credited challenges for 3D printing are to develop related bio-inspired structures and devices for biological and medical applications [7-11].

Through natural selection over millions of years, naturally occurring structures have been optimized. Mimicking the features that exist in natural materials is not a trivial undertaking. Researchers developed many epoch-making designs by imitating a wide variety of natural structural materials — ranging from wood, antler, bone and teeth, to silk, fish scales, bird beaks and shells. For example, based on the ultrasonic location ability of bats and porpoises, Sokolov produced the first optical image in 1939 [12]; the first volta battery was invented by generating organs of electric fishes [13]; those buildings with large-span and thin-shell, such as the Sydney Opera House, were created in imitation of the eggshell structure [14]. These bio-inspired properties enable new functions and thus lead to frontier applications, such as micro-fluidic [15], optical control [16, 17] and marine engineering [18]. The bioinspired materials/structure effectively combine the desirable properties of their components often perform significantly better than the sum of their parts. They offer a path to tackle the challenges through the development of a

confluence of mechanisms that interact at multiple length scales, from the molecular to the macroscopic. While there some underlying nano/micro-scale mechanisms need be clarified to address the critics, the bioinspired materials strategies have advanced the technical innovation in the frontier to engineering. I have implemented same principle here, to design an octopus enabled soft robotic griper in Chapter 5, and develop a human lens inspired intraocular lens in Chapter 6.

With the recent development of soft robotics structures, responsive materials fulfil the control with their stimulus responsive feature. For example, a hydrogel structure can be triggered by pH value [19], temperature [20], magnetic [21], electric potential [22], ion concentration [23] etc. Our project focuses on developing soft robotics with responsive materials. Once these materials receive external stimuli, the robotics can grip, swell/shrink, re-structure, etc. Stimuli-responsive materials were also developed to multiple stimuli. These stimuli-responsive materials can achieve colour changes, electronic performance changes (such as direction), etc. These properties have a wide range of further applications, especially in such areas as medical applications, various sensors as well as and information technology [24]. However, the challenge remains in the manufacturing, especially in the scale-up fabrication of products in a higher customized way, with more efficiency and lower costs.

1.2   Aims and Objectives

The main aim of project is to develop advanced structures and production methods which meet certain needs as inspired by the existing biological structures in nature i.e., the advanced bio-inspired structures and the advanced production methods.

The knowledge required for this project is:

1. Develop the structural designs for this project according to the existing natural structures using CAD and Solidworks software to design our own structures.

2. Develop manufacture Methods which can produce our own designed structures as mentioned above, such as 3D Printing.

3. Develop materials that can meet the design requirements. This project uses hydrogel, elastomers (i.e., PDMS).

The performance of our bio-inspired structures can be obtained from DSA, optical microscope, SEM, optical test and simulations. The optical microscope provides an initial rough assessment of the 3D printed moulds in the first instance. DSA provides swell and shrink, which influence the overall structure. SEM shows the deposition distribution of all chemical elements on the surface. Optical test verifies the practicability of the product from the perspective of application, and whether it achieves the expected effect.

The primary aim of the project is to develop a new type of advanced manufacturing technology to produce corresponding bio-inspired structures and develop further applications.

Objectives of this project are listed as below:

1. Explore the relationship between conductivity and fabrication accuracy on the surface of conductive polymers. Seeking find a way that FIB can manufacture on the polymer surface with high precision at low cost.

2. Based on existing soft materials (hydrogel), research and develop bio-inspired soft robotic structures.

3. Using advanced manufacture technology, such as 3D Printing, to produce our designed IOLs based on soft materials (hydrogel).

1.3   Thesis Structure

Chapter 1: Introduction. A general description of this project and its contribution to the bio-inspired structures design and manufacturing and soft robotics.

Chapter 2: Literature review. The current developments related to my project are introduced in this chapter. Typical soft robotics and their development history are introduced. Soft, responsive materials are presented. Advanced manufacturing methods are provided as part of this chapter.

Chapter 3 Experimental Methods. This chapter introduces surface characterization methods including Optical Microscopy (OM), Laser Scanning Confocal Microscopy (LSCM), Scanning Electron Microscopy (SEM), Drop Shape Analysis (DSA) etc. In addition, the simulation method which provides mathematic characterization.

Chapter 4 Spatially Engraving Morphological Structure on Polymeric Surface by Ion Beam Milling. This chapter reports a new and highly efficient fabricating method to achieve a controllable roughness polymer surface using focused ion beam (FIB) technology.

Chapter 5 Spatially and Reversibly Actuating Soft Gel Structure by Harnessing Multimode Elastic Instabilities. Autonomous shape transformation soft robotics are described in this chapter. It is achieved by swelling competition of hydrogel between the cylindrical surface area and the annulus surface area.

Chapter 6 Tuneable Morphological Deformation of Polyelectrolyte System as a Tool for Ocular Applications with Facile Fabrication Process. Controllable focal length of hydrogel IOLs can be changed using a different ion concentration.

Chapter 7 Theoretical Development.

Chapter 8 Conclusion and Future Work.

Chapter 2

Literature Review

The aim of this PhD project is to investigate the use of 3D printing to develop a novel Bio-inspired structure and device for advanced engineering. This chapter systematically reviews the developments of bio-inspired structures, the role of structure-property relationships and related manufacturing techniques, materials and applications. The review starts from naturally existing and bio-inspired structures and includes some related and developed examples. Then, the fundamental understanding of advanced manufacturing techniques is presented. Developments on responsive materials and applications are also briefly covered.

2.1 Bio-inspired Topography Structures and Their Enable Functions

It is well known that bio-inspired structures with unique features are essential for many engineering applications. Soft bio-tissues can generate the deformations or mechanical instabilities structure by growing under constraint. These deformations or mechanical instabilities (i.e., undulation and fold) have brought the unique properties to fulfil the physiological and pathological functions [25-31]. The shortening of smooth airway muscle can create the mucosa folds and obstruct the airways, and in asthma such

obstruction increases due to the thickening of the airway walls [30, 31]. Another example is fingerprint patterns which can result from the buckling of the layer of basal cells of the foetal epidermis [25]. Compared to those structures which are not inspired by biological structures, bio-inspired structures show significant improvements in properties (**Figure 2.1**). This chapter briefly details some of the latest developments on bio-inspired traditional structures and their engineering applications. The role of structure-property relationships and related manufacturing techniques will be explored to give an insight into the rise of 3D printing in the modern manufacturing.
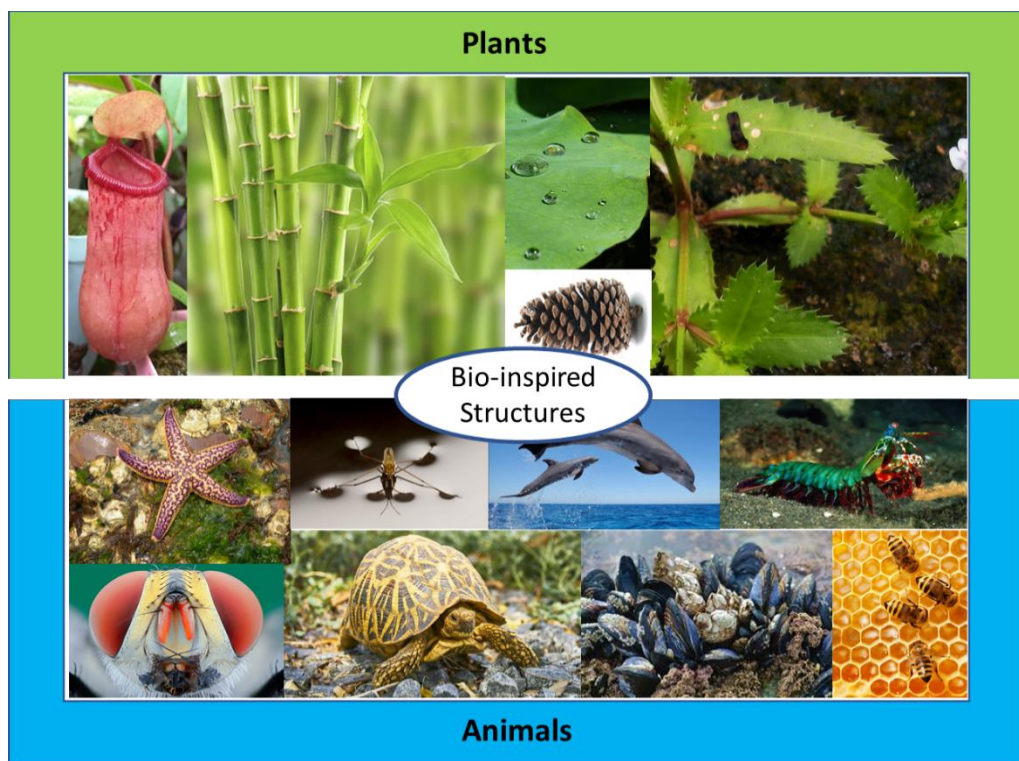
Figure 2.1: Biomaterials can provide inspiration for the design of novel bio-inspired structures.

2.1.1 Smart Surface with Switchable Wetting Feature

Wettability is the ability of a surface to be wet by a liquid and for a drop of a liquid to move across a solid interface seeking to reduce its own surface area, leading to the balance of the three forces. The physics behind a static contact angle is the balance of forces of the three interfaces [32, 33]. The Young's Equation (**Equation 2.1**) give a mathematical illustration of solid-vapor interface, the solid-liquid interface, and the liquid-vapor interface, as shown in **Figure 2.2**, where the biphasic interfaces as possessing "contractile forces" acting on the three-phase contact line of the liquid drop.

$$\gamma_{sv} - \gamma_{sl} = \gamma_{lv} \cos \theta \qquad\qquad \textbf{Equation 2.1}$$
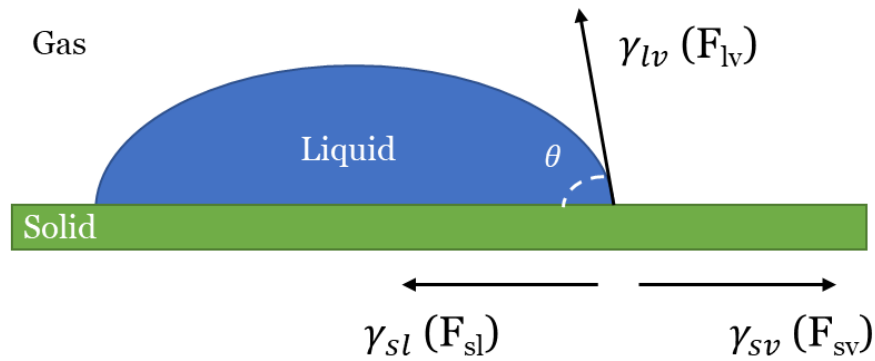
Figure 2.2: Interfacial tensions leading to the formation of a water drop.

The Wenzel (**Equation 2.2**) [34] and Cassie-Baxter (**Equation 2.3**) [35] equations describe the wettability theory in an advanced format by

considering the chemically heterogeneous surfaces and rough surfaces from the thermodynamic perspectives.

$$\cos \theta_r = r \cos \theta \qquad \textbf{Equation 2.2}$$

$$\cos \theta_c = f_1 \cos \theta_1 + f_2 \cos \theta_2 \qquad \textbf{Equation 2.3}$$

Where r is a roughness factor, equivalent to the ratio of the surface area of the rough surface with the surface area of the smooth surface. f_1 and f_2 are the surface area fractions of two surface chemistries, and θ_1 and θ_2 are the contact angles for the respective pure surfaces.

The above equations have brought enormous advantages to design and fabrication of the surface with desired wetting status, for a variety of engineering applications. Inspired by the surface of a lotus leaf in nature, Feng et al. proposed the use of super-hydrophobic/super-lipophilic ("oiling-remove") metal mesh for oil/water separation [36, 37], as shown in **Figure 2.3** [38]. Since then, superhydrophobic membrane materials have received widespread attention due to their potential to selectively absorb oil from water [39], their self-cleaning ability [40], anti-icing coating [41] and corrosion resistance. The part of the oil-water mixture made by the leakage of offshore crude oil and the discharge of oily wastewater from industrial production is in an immiscible form, which brings great challenges to the initial treatment, oil recovery and environmental protection [42-44]. Due to the selectivity for the relative density of oil and water, the single special wettability material generally used to achieve the separation process through intermittent

operation, limits the practical application. Therefore, it is of great significance to design a new material with inverse special wettability to separate oil/water mixtures [45, 46].
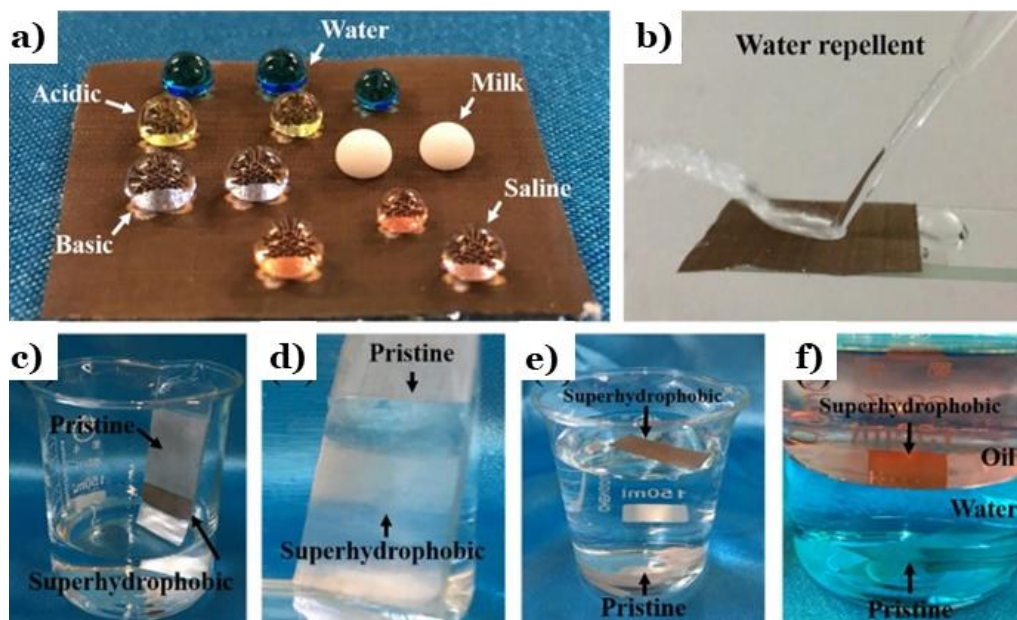
Figure 2.3: a) Different kinds of droplets on the surface of the SSM@NWs-PFDS; **b)** A jet of water was bounced off by the surface of the SSM@NWs-PFDS; **c) - d)** The pristine SSM and SSM@NWs-PFDS were immersed into the water; **e)** The SSM@NWs-PFDS floated on the surface of water while the pristine SSM sank to bottom; **f)** The as-prepared SSM@NWs-PFDS suspended at the interface of oil and water while the pristine SSM sank to bottom [38].

Generally, the surface properties of solids are strongly influenced by the surface geometry and chemical composition. In recent years, surface wrinkling has attracted great interest as a key technology for the dynamic control of surface morphology. The reversible wrinkling process has been extensively

developed and widely used in many applications, such as tuneable diffraction gratings [47], micro lens arrays [48, 49], dry adhesives [50, 51], flexible electronic devices [52], dynamic scaffold [53], and colloid transfer [54]. However, most studies on the reversible wrinkling process have tried to control the surface characteristics of the non-patterned plane, and the adjustable surface characteristics with wrinkles have not been extensively studied.

With the above perspectives, there is an interesting development of a multi-functional transparency adjustable smart window with a layered structure. Seung Goo Lee et al. demonstrated stretchable smart windows, whose surface morphology consists of an array of nanopillars on a corrugated Polydimethylsiloxane (PDMS) film (**Figure 2.4**) [55]. The surface can be reversibly switched between a transparent stretched state and an opaque released state. In addition to the controllable optical properties, the wetting performance can also be systematically adjusted between the water-pinned state and the superhydrophobic state by changing the surface topography (such as the aspect ratio of nanopillars or the amplitude of micro-wrinkles) [56]. **Figure 2.4 a** outlines the process of preparing a layered PDMS film [57]. After the strain is released, due to the different elastic moduli between the relatively hard silicate-like top layer and the soft and compliant PDMS substrate, periodic wave microstructures perpendicular to the pre-strain direction will be generated on the PDMS surface covered with nanopillars [58]. The wrinkled film is stretched back to the initial strain and the microscale structure is removed, leaving only the nanopillar array structure. The

mechanically sensitive reversible wrinkle patterns can control the micro-roughness. Since the optical and wetting properties can be simply switched and controlled by changing the external strain, the system can develop potential applications, such as multifunctional smart windows, microfluidic device and biological sensor.
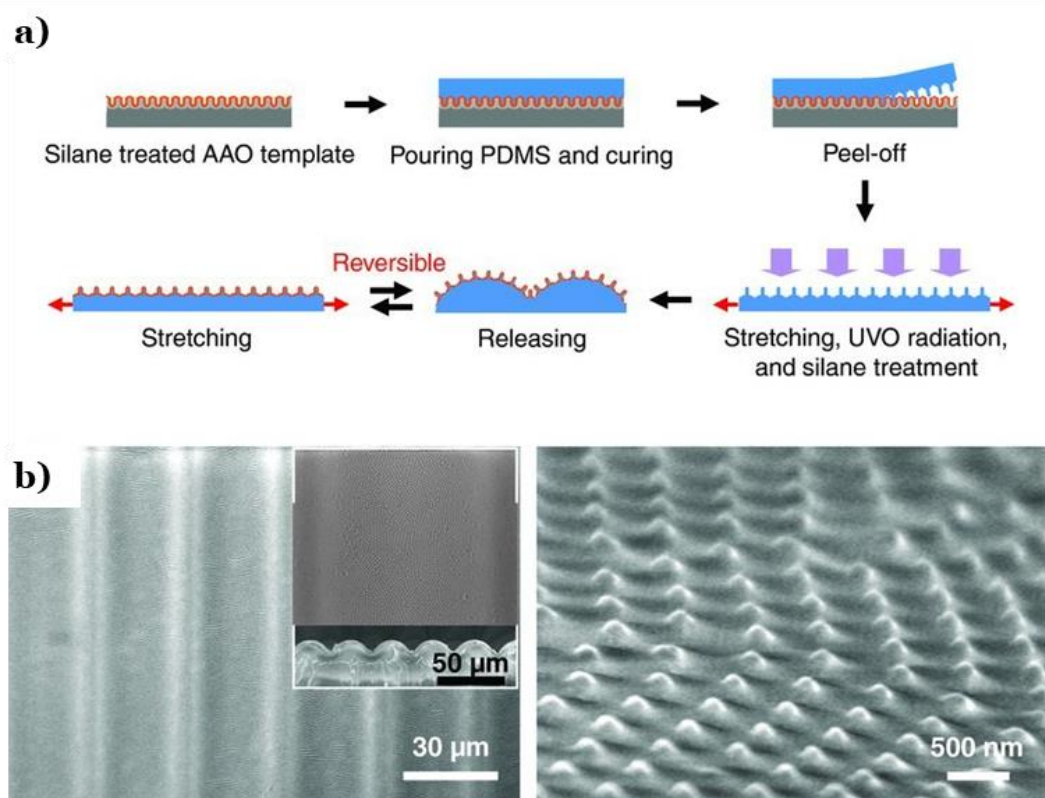
Figure 2.4: Fabrication of hierarchically structured PDMS films. **a)** Scheme describing the fabrication process comprising replica moulding, surface wrinkling, and treatment of the PDMS film; **b)** Low magnification scanning electron microscopy (SEM) image of the fabricated surface. The insets show a higher magnification image and a cross-sectional view [55].

2.1.2 Autonomous Structures for Soft Robotics

Robotics is especially important and provides a wide range of important functions (from positioning and motion control to visualization). Unlike traditional robots, which are made from rigid materials and components to fulfil the requirements of high precision, such as rapid movement, high force, and easy control, soft robots are primarily made of soft and pliable materials for the functions. Recently, there has been a rapid growth in the field of soft robotics which has been accelerated by the following technologies [59-61]:

- Rapid evolution of computing techniques and computer-based systems for complex design, precision manufacturing, control and hard robotics;

- Polydimethylsiloxane (PDMS) elastomers which are used widely as a structural material to facilitate manufacturing (to achieve rapid prototyping) with its unique properties (transparency, ease of disinfection, biocompatibility, etc.) [62];

- Soft lithography [63] and microfluidics [62] which have been developed into products/prototypes with suitable pneumatic and hydraulic chambers or channels;

- Digital manufacturing;

- The development of mechanics in soft composite material for controlling anisotropic motion when driving [64].

In short, the combination of all of the above technologies provides: elastic materials with excellent properties, suitable for prototyping and production; manufacturing methods derived from mature methodology, soft lithography which is suitable for prototyping and production; manufacturing methods are derived from mature methodology, soft lithography is suitable for prototyping and production; manufacturing methods are taken from mature methodology, soft lithography [63] and PDMS microfluidics [62]; a convenient and flexible method of manufacturing most of the moulds required for the design of pneumatic channel networks; direct methods to control strain anisotropy by forming flexible but non-expandable sheets (or other composite designs) and PDMS composites based on origami/paper-cutting structures [64]; computer-based design, control and vision tools.

Because of the practicability and ease of manufacturing of robotic grippers, they have been widely used, and various supporting structures have also been designed and manufactured. Tentacles [65] has been designed and displayed in large numbers, influenced by the admirable dexterity of the octopus. Simple Walker [66] proved easy to make and was developed with limited applications. However, they all provide a useful test platform for the development of autonomous, mobile systems. Exploring other possibilities has led to many interesting, even strange features. For example, the chameleon's tongue [60] demonstrates the surprisingly fast movement of the soft actuator (it takes less than 200 milliseconds to fully coil the tentacles [67], and combustion-driven jumper [68] demonstrates the possibility of generating

much pressure on-board (by using the methane-air mixture filled with PneuNet, and then it is ignited with a spark) [69, 70]. Other methods of internal pressure generation—for example, the decomposition of hydrogen peroxide into oxygen and water [71-75] have been created, but with limited practical use.

2.1.3 Adaptive Structures for Flexible and Variable Electronic

The adaptive multi-layer structure has been an important design for the microelectronics. For example, the layered array of posts composed of micron-sized polymer bristles covered with carbon nanotubes is designed for microelectronics applications to provide a spatulate, mimicking the fibrous bonding surface of a gecko. These bionic structures can better adhere to rough surfaces, providing a new platform for various applications [76]. Adaptive structures are structures that change their structures, form or characteristics in response to change in the environment. Bilinear systems with adaptive structures are common in nature and can be used for engineering design and control. In many cases, they provide higher performance and controllability than linear systems.

The flexible bionic electronics that combine electronics and bionics, it is expected to be used in biological systems, such as monitoring equipment. For example, electronic skin imitates natural skin and can sense ultra-low pressure (<1 Pa) [77-80]. The electronic nose mimics the human olfactory system's ability to distinguish smell and has been developed for food and

beverage detection, environmental monitoring, and disease diagnosis [81-84]. The electronic eye can achieve an equal biaxial tension of more than 50% and a total field of view of 180°, and it has a compressible and stretchable design [85]. In order to allow the electronic ear to "hear" the sound, the rigid diaphragm in the microphone has traditionally been used to detect the sound; however, the planar and rigid format limits its in-vivo application [86]. Recently, flexible mechanical sensors based on force-induced resistance changes [87-94], capacitance [95, 96], current [97], and piezoelectric voltage [98, 99] have shown potential for sound pressure detection. Previous studies have shown that the microstructure is beneficial to achieve high sensitivity and fast response in pressure detection. Gold plated cylindrical PDMS microstructures have been used to make connectable devices for throat voice monitoring [100]. A resistance pressure sensor composed of PEDOT: PSS-polyurethane coated on the pyramid structure has been used to detect the neck pulse by connecting it to the throat [101]. Flexible tactile sensors based on pyramidal microstructure graphene arrays have been proven suitable for information transmission applications [102]. However, it is very challenging to simulate a flexible eardrum that responds to sound/voice vibration in a suspended state which has similar flexible mechanical properties (with Young's modulus of 20–32 MPa), a wide frequency response range (approximately 20–22050 Hz) and responds to sound/voice vibration in a suspended state, high sensitivity (the lowest sound pressure detection limit is 20 μPa), and ultra-fast response time real-time detection and recording.

Yang Gu et al. designed and manufactured a new type of flexible electronic tympanic eardrum (EE, **Figure 2.5**) based on single-walled carbon nanotubes (SWNT) and flexible substrates, which can detect and record sounds in the 20-13000 Hz frequency domain with ultra-fast response time resolution (76.9 µs) and high signal-to-noise ratio (SNR, 55 dB) [103]. The performance of flexible EE paves the way for implantable acoustic bioelectronics in clinical prosthetics applications.
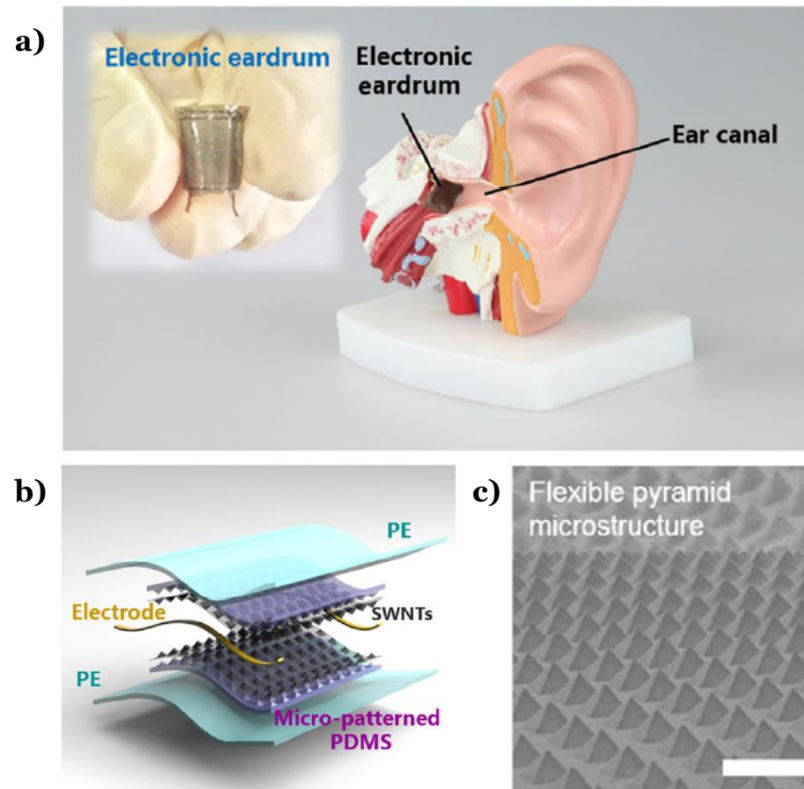
Figure 2.5: Configuration of the electronic eardrum (EE). **a)** Image of the flexible EE placed in an ear model. The inset figure shows the image of the bended EE; **b)** Schematic configuration of the EE device. It has double-layered structure. Each layer has one PE layer, micro-patterned PDMS film, SWNTs-network and copper wire electrode; **c)** Side-view SEM image of curved PDMS film with pyramid microstructures, scale bar is 30 µm.

Stretchable, conductive and flexible films (SCFFs) are ubiquitous in sensors [104-107], touch screens [108-110], supercapacitors [111], conductive electrodes [112-117], and flexible electronics [118-120]. High mechanical flexibility, electrical conductivity, and elongation are the basic characteristics that SCFFs should have to achieve high-performance flexible devices [121-123]. In addition, the components of such films need to include an elastic substrate and a conductive network to give the film flexibility and high conductivity, even during mechanical deformation [124-126]. Flexible electronic films are usually used under frequent tension, bending or pressing conditions. However, SCFF is limited by the properties of elastic materials, and is expected to have longer-term and stable electrical performance under certain deformation states in practical applications [127]. In this regard, SCFF can simultaneously achieve shape fixation and the deformation reversible continuous elongation range of electrical conductivity will be valuable.

Recently, there have been several alternative methods to develop a new type of SCFF by using various types of conductive shape memory polymers (SMP), and their composite materials have been sought [128-131]. SMP is a stimulus-responsive polymer material that can memorize and maintain a deformed shape and can return to its original shape in response to external stimuli (thermal, electrical, magnetic, optical, or chemical) [132-139]. Some examples of SCFFs with shape memory effect (SME) include shape memory self-powered mechanical sensory sensors [139], shape memory light-emitting diodes [140, 141], shape memory thin film transistors [142-145] and optical

devices [146, 147], which represent the future of flexible electronics devices. Although recent progress has been made in the realization of shape memory conductors in stretchable composites, many studies have focused on mixing conductive nanoparticles or nanowires into elastic polymers and electro spun polymer nanofibers [140, 148, 149]. This may hinder electron transmission, and the separated conductive components from the substrate can cause unstable conductivity when the plastic substrate deforms [124, 126]. Another approach relies on the use of shape memory conductive composites that are inherently stretchable, fixable, and reversible, so that they can achieve variable, stable, and programmable conductivity for flexible electronic devices.

Pandeng Tang et al. reported a SMP-based flexible electronic film (**Figure 2.6**) which involves a double-layer interpenetrating architecture to promote the responsiveness and programmable conductivity of variable flexible electronic devices [150]. One of the advantages of using silver nanowires (AgNW) in conductive composites is the excellent electrical, optical, and mechanical properties produced by the material itself, or the overall interconnect structure [151, 152]. Polycaprolactone (PCL)/polyethylene stretchable matrix ethylene glycol (PEG)/AgNWs films (PPAFs) are composed of covalently cross-linked PCL/PEG hybrids obtained by electrospinning technology. In addition, double-layer nanofiber composites benefit from the combined AgNW through spin coating technology to form interpenetrating fibre conductors. The double-layer nanofiber composite material is composed of a covalently cross-linked PCL/PEG hybrid obtained by electrospinning

technology. The hybrid is realized as a fibre matrix of a stretchable film, and spin coated silver nanowires to be a fibre conductor.
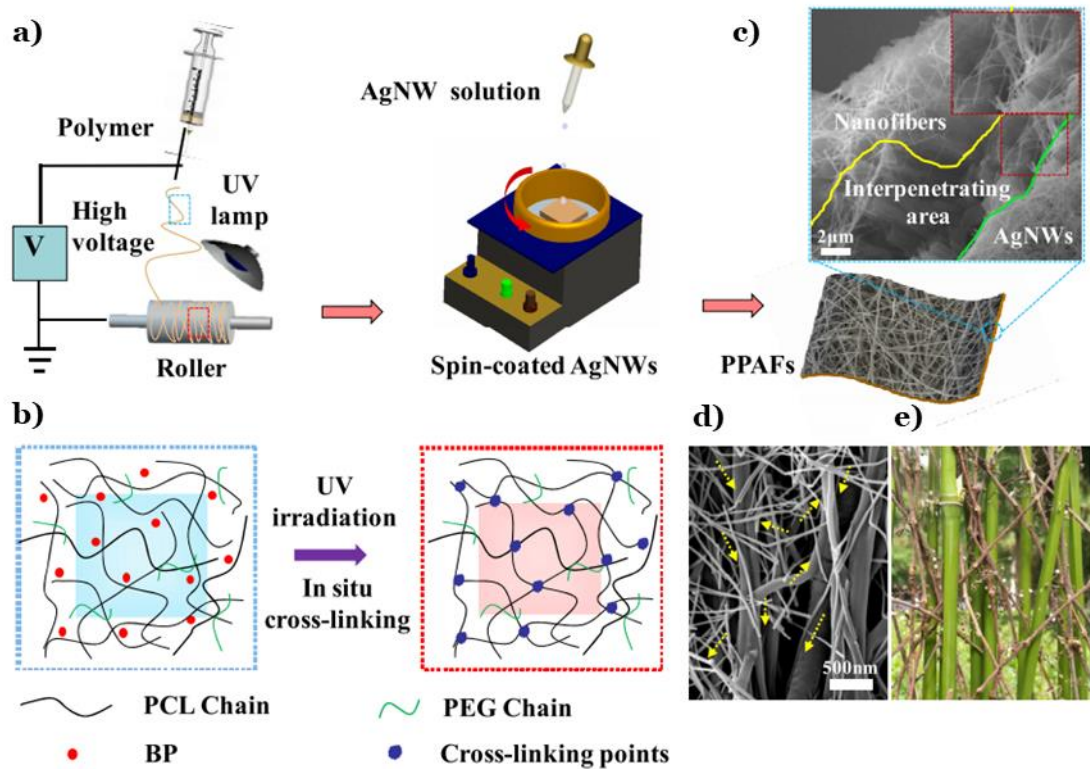
Figure 2.6: Fabrication and structure of dual-layer composite films with the shape memory property. **a)** Illustration of the fabrication of PPAFs via electrospinning nanofibers and spin-coating AgNWs; **b)** Molecular mechanism of preparing the matrix layer with a crosslinked network; **c)** Cross-sectional and **d)** interface SEM images of the interpenetrating area in PPAFs; **e)** Digital photograph depicting the persistent integration of the creeper twining the bamboo stem in nature. The AgNWs interpenetrating into the matrix network are marked by yellow arrows [150].

2.2 Advanced Manufacturing Techniques

Advanced manufacturing is a leading manufacturing technology that adopts the computer-aided design techniques to the real-time manufacturing process, which can improve the efficiency of product manufacturing significantly [153-155]. This manufacturing technique has been well established in the past few years, and it also has been expanded into varied downstream application fields with predicted business advantages [156, 157]. While 3D printing fabricates inanimate objects, the emerging 4D printing allows for animated structures that change their shape, function, or properties over time when exposed to specific external stimuli after fabrication. The shape-morphing in 4D printed structures is normally driven by a stress mismatch in the parts of the structure under a stimulus. This project mainly focuses on the development of a new advanced manufacturing route by printing bio-inspired structures [158] using novel materials [159] for future engineering applications. The general mainstream manufacturing techniques will be scoped with Photolithography for micro-fabrication, precision manufacturing (FIB) for nanofabrication and additive manufacturing. Within additive manufacturing, we will holistically review the 3D printing technologies and the applications. We will make an extension to the responsive materials and structures that are sensitive to stimuli, and mechanics enabled morphing structures.

2.2.1 Photolithography

In last few decades, we have witnessed exciting progress in transforming the technologies from lab to fabrication, however, there are more research outcomes yet to be transfer into products to enter the market. For scale up production and commercialization, industrial manufacturability of newly developed materials/fabrication techniques is a prerequisite. Lithography, a technique originated from the ancient Greek, has been proven as a very successful modern form of microfabrication as a key technology in producing integrated circuits, microsensors, photonic crystals, biomedical devices, ink jet printers, solar cells, and projection display systems [160]; Since the 1960s, lithography has played a leading role in the manufacture and mass production of integrated circuits. Continuous progress in micro technologies has led to the need to manufacture much smaller features than a micron for increased device performance, lower power consumption, and faster response time [161]. Moore's Law reflects the market need for ever-decreasing transistor sizes, usually requiring photolithographic exposure at the shortest possible wavelength [162]. At the same time, emerging nanotechnology requires miniaturization of the mechanical, chemical or medical systems of the lab-on-a-chip in the fields of photonics, biophysics, and photo fluidics.

As a current mainstream and representative manufacturing method that linked to multiple processes in my thesis, Lithography offers high-precision fabrication. It can potentially open new avenues for the manufacture of 3D engineered materials exhibiting optimized properties and multifunctionality, by integrating the nano-materials processing method.

Therefore, it is very important to review the development of this fabrication so that it can shed the lights on the related design and manufacturing of the product in my thesis. A typical lithography technology (**Figure 2.7**) includes the following steps: (1) coating a substrate with a UV-sensitive polymer thin layer(photoresist); (2) selectively exposing the UV light/electron/ ion beams; (3) subsequently removing the selected areas of the film through dissolution in an appropriate solvent and developing the resist image (a.k.a. Lift-off) [163]. Conventional lithographic techniques can be broadly divided into two groups based on the type of mask used. In methods where a physical mask is used, patterns are generated by exposing the resist to photoirradiation through a mask that is in contact or in close proximity with the resist surface [164]. In methods where a software mask is employed, a scanning beam irradiates the resist surface sequentially through a software-controlled program where the patterning mask is defined. The most used form of mask less (or software mask) lithography today is electron beam (e-beam) lithography.
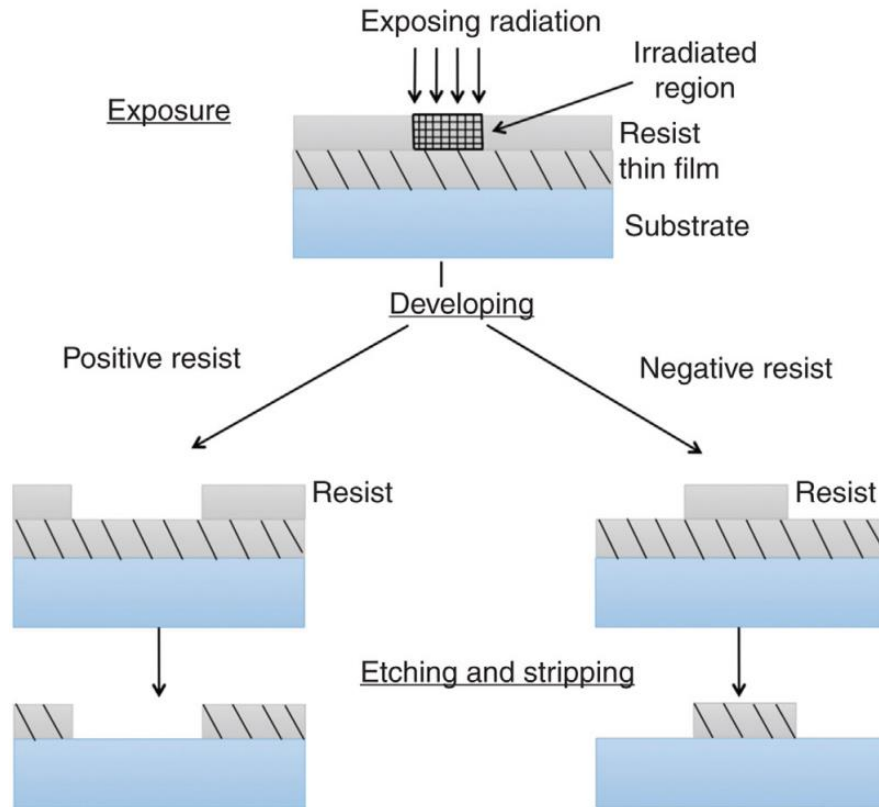
Figure 2.7: Schematic illustration of lithography process [165].

The optical projection lithography at 193 nm wavelength is one of the widely applied techniques in the scale-up manufacturing due to the ability to extend its service life and achieve an astonishing 10 nm state-of-the-art resolution. For further miniaturization, alternative methods need to reach industrial production [166]. Ultraviolet-assisted NIL can break through the current resolution limit of DUV technology and EUV lithography technology. Its light intensity is 13.5 nm, and its position, which can guide the transistor to expand to smaller nodes, is very good. However, shorter wavelengths are

required to produce ICs with smaller features therefore pushing the physical limits and leading to the development of alternative techniques.

The next-generation lithography (NGL) techniques including extreme ultraviolet (EUV) lithography, X-ray lithography, e-beam lithography and focused ion beam (FIB) lithography have been studied [167]. The current target resolution is 7 nm, and the feature size of semiconductor devices is rapidly approaching the size of molecules and polymers in these photosensitive materials. The inherently disordered polymer resist has inhomogeneities on a length scale of less than 10 nm, which leads to defects and structural collapse and is therefore not ideal for this extreme lithography technique. Therefore, it is necessary to develop alternative systems that exhibit a well-controlled morphology at these dimensions. Highly ordered molecular systems such as calixarene or metal oxide-based resists are promising systems for this technology. Including photo-responsive units, such as azobenzene, nanoparticles in self-assembled resist materials also show great potential for molecular alignment, and feature resolution and orientation can be better controlled. By combining top-down and bottom-up patterning strategies, these optically addressable systems have achieved sub-5 nm capabilities.

Since the 1990s, non-conventional patterning methods have attracted considerable interest as simpler and cheaper choice to fabricate micro/nano structures. Two representative methods are nanoimprint lithography and soft lithography where the patterning is facilitated by pressing a mould against a softened thermoplastic polymer or a liquid polymer precursor and trapping the

pattern in the solid state either by cooling the mould material (thermal NIL) or by UV-curing the polymer precursor (UV-NIL). Nanoimprint lithography is a competitive method of patterning sub-10 nm features [168]. The imprint process is fast and repeatable and commercial nanoimprint tools are already available for academic and industrial purposes [164]. Therefore, NIL has been attracting more and more attention in both research and commercial applications. However, there are still certain drawbacks. NIL, based on a hard, stiff mould, requires very high pressure (4.1-13.1 MPa) [169] and an extremely flat surface for patterning [170]. Soft lithography based on an elastomeric stamp has emerged as an attractive alternative to thermal NIL and will be explained in detail in the next section.

Soft lithography in which the elastomeric mould with patterned structures on its surface is used to generate features from nanometre to micrometre is a promising alternative to thermal NIL. The key element of soft lithography is the soft elastomeric mould which is typically prepared by pouring an elastomer prepolymer over the master whose surface has been patterned with complimentary structures as described above. The mould is then cured and peeled off from the master. In principle, any elastomer can be used to cast the mould, but the most common mould material used in soft lithography is polydimethylsiloxane (PDMS). Sylgard® 184, containing a liquid silicone rubber base (i.e. a vinyl-terminated PDMS) and a catalyst or curing agent, is a commercial two-part PDMS kit that is widely used for fabrication of stamps with feature sizes of 500 nm and larger [171].

2.2.2 Precision Manufacturing Technique - Focused Ion Beam (FIB)

Focused ion beam (FIB) systems use a finely focused ion beam (usually gallium ions), which can be used to locally sputter or grind the sample surface exposed to the ion beam under high beam current conditions during operation. FIB systems have been commercially produced for many years and are mainly used in the semiconductor industry, so they are mature and can be widely used. **Figure 2.8 a** shows the process scheme using FIB [172] milling structure. In FIB milling, usually a gallium (Ga) primary ion beam hits the sample surface and sputters off a small amount of material which leaves the surface in the form of secondary ions or neutral atoms [172, 173]. Therefore, under a high primary current, material can be effectively removed from the sample surface, so that samples with feature sizes less than 1 micron can be accurately milled. The material removal rate by sputtering, also called sputtering yield, depends on the substrate materials and many other processing parameters, including ion energy, incident angle of the ion beam, and grinding conditions.

At the same time, the sample can be imaged with very high accuracy during the milling process (for example, using the attached scanning electron microscope (SEM) in a dual-beam tool). As a result, FIB milling has become a popular tool for processing high-quality 3D micro-devices and high-precision microstructures made of high-performance bulk materials [173, 174]. **Figure 2.8 b** shows the SEM image of the cutter head structure processed by FIB milling. FIB milling has also been used as a post-processing tool, for example,

to fine-tune the quality of the resonator by ablating a small amount of material [175].
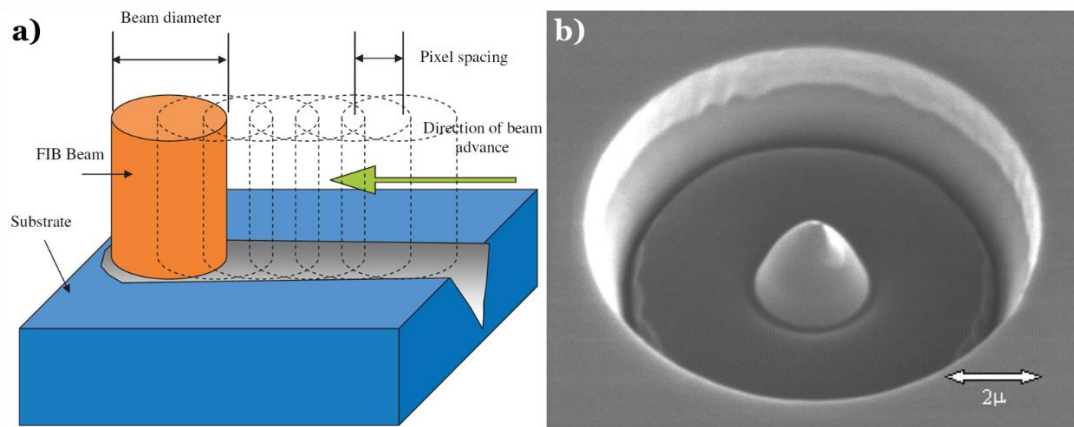
Figure 2.8: a) Schematic diagram of FIB milling; **b)** Tip structure milled using a Ga focused ion beam [173].

The potential disadvantage of FIB milling is its slower processing speed. To improve the material removal rate in FIB milling, FIB assisted etching (FIBAE), also known as chemical or gas assisted ion etching, can be used. In FIBAE, the ion beam is used to initiate a chemical reaction between the surface of the sample and the gas molecules adsorbed on the surface of the sample, thereby increasing the material removal rate. In addition, by injecting reactive gas precursors into the grinding process, the material removal mechanism can be changed locally, and the related grinding shape can be changed [173]. Commercial FIB tools for FIB milling are widely available from various suppliers.

There is an urgent demand for the further miniaturization of devices from the micro scale to the nanoscale for practical applications. FIB irradiation is a robust technique for surface engineering of polymers and can be used in an array of multi-disciplinary fields from medicine to engineering. Examples are designing bio interfaces for tissue engineering and regenerative medicine, microfluidics, biosensors and optics [47, 48, 176, 177]. The area exposed to the ion beam can be selected by controlling the relative movement of the ion beam and polymeric substrate, or for applications that need very precise control over the exposed area by maskless patterning method. In 2015, Lobo et al. used focused ion beam (FIB) technology to fabricate MSC devices with an interelectrode spacing of 1 μm, which demonstrated a large capacitance, low time response and a low equivalent series resistance [178]. Until recently, only one work using FIB to prepare the rudiments of NSCs with nanoscale slits has been reported. The prepared NSCs showed apparent enhanced capacitive performances [179] which triggered the development of NSCs. However, the research remains lacking without further study of fine structure and unique charge storage mechanisms. Transition metal dichalcogenides (TMDs), an emerging kind of 2D material, have shown extraordinary potential in pseudo capacitance.

The ion bombardment induced manufacturing has been previously investigated for different surfaces such as glassy metals [180], amorphous [181-184] and crystalline materials [185, 186]. In these experiments, the ion effect is characterized by the mean penetration depth and longitudinal and

lateral straggling widths [183, 187]. The FIB irradiation is a robust technique for surface engineering of polymers and can be used in an array of multidisciplinary fields from medicine to engineering. Examples are designing bio interfaces for tissue engineering, microfluidics, biosensors and optics [47, 48, 188]. The surface pattern can be designed by the ion beam by controlling the relative movement of the ion beam and polymeric substrate, which can have promising applications over the exposed area by maskless patterning method.

2.2.3   Additive Manufacturing Techniques

The key feature of additive manufacturing is to produce or assemble a proportional model of physical components by means of layer-by-layer construction with the assistance of CAD data. Additive manufacturing techniques include three-dimensional (3D) printing technology and four-dimensional (4D) printing technology.

Although 3D printing technologies may vary in detail, nearly all 3D printing use a layer-by-layer approach to build up a 3D object, by stacking 2D "slice" layers to form an 3D object. The method used to create each layer determines many of the final material properties of the object. The existing 3D printing technology has been able to print products regardless of the geometrical constraints, with good resolution. It applied to the production of metal, biocompatible, and composite parts with responsive functions. Some of the most credited attempts for 3D printing are to develop related bio-inspired structures and devices for biological and medical applications. Compared with

conventional methods, 3D printing allows rapid prototyping and mass customization and is ideal for processing soft polymer materials. 4D printing is a term that was recently coined [189] by introducing the fourth dimension "time" into 3D printing, to realize printed components that can change their shapes, properties, or functions under external stimulations (heat, light, magnetic field, etc.) [190, 191]. Due to the nature of stimuli-triggered response, 4D printing has attracted tremendous interest as the obtained object will undergo certain changes, such as assembly, disassembly, 1D, 2D and 3D transformations. The active materials (i.e., hydrogel, shape memory materials, etc) feature the advantages of large deformation, light weight, strong recovery stress, and fast response rates, plays a vital role in the 4D printing for various applications.

In the following section, we will introduce the development of 3D printing techniques, as per the main streams in the market. The additive manufacturing has been developed to a few different methods to meet the demand of complicated structures and higher resolution. The major method of 3D printing is fused deposition modelling, also known as FDM. It normally uses polymer filaments, such as ABS. Stereolithography (SLA) is a typical method of printing-out photosensitive resin objects. For powder/liquid or high melting point materials, laser is introduced into 3D printing. Selective laser sintering (SLS) and selective laser melting (SLM) are both able to print metals. However, SLS is also used to print polymer and powder. Based on the 3D

printing concept, 4D printing has been introduced as well. In the following sections, we will describe each of them in detail.

2.2.3.1   Fused deposition modelling (FDM)

In the late 1980s, S. Scott Crump invented the Fused Deposition Modelling (FDM) technology (**Figure 2.9**) which was applied to production by Stratasys, Ltd. in 1990. After this, a large open source was formed to use this technology for 3D printers. As this result, the price of FDM technology has been reduced since its invention.
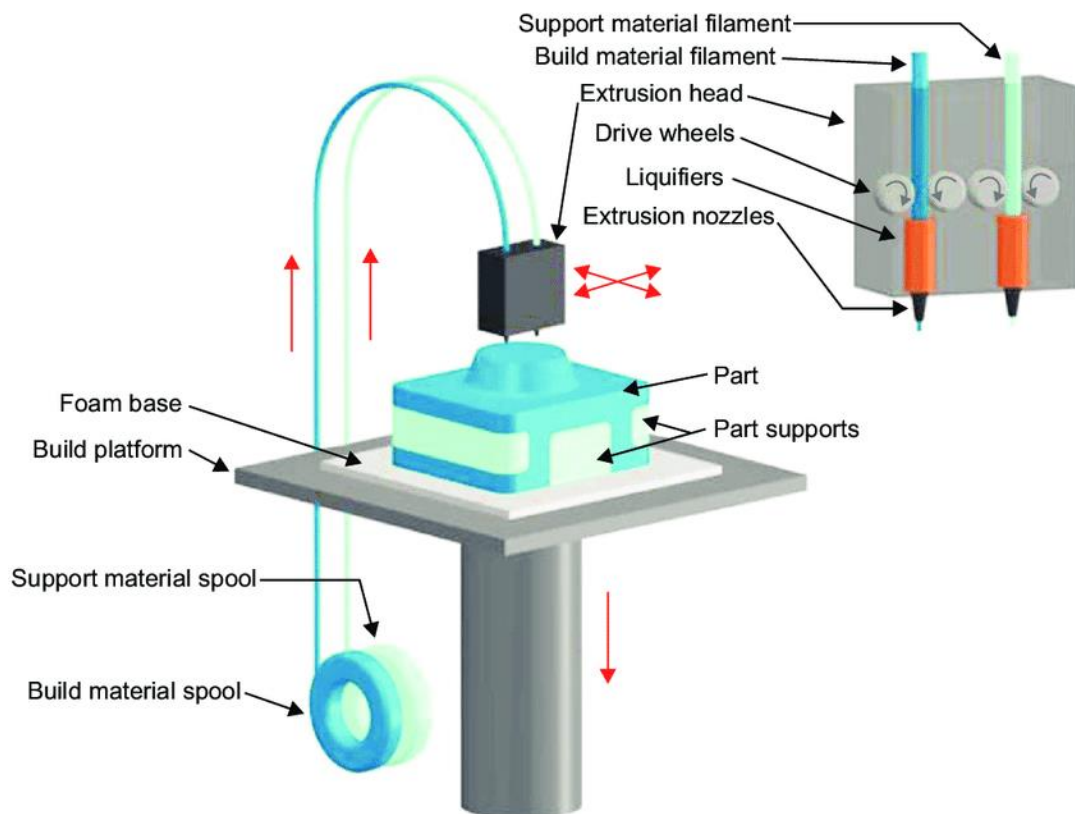
Figure 2.9: Fused deposition modelling setup [192].

The method of FDM technology to print models is to use a type of filament which can be instantly hardened to form layers. The thermoplastic or metal filament is rolled on the reel, gradually unrolled and delivered to the extrusion nozzle. The nozzle is heated to squeeze melted filaments output. Normally, stepping motors or servo motors are used to control the extrusion nozzle and regulate the output of filaments. The print head (normally includes heating part and nozzle) can be moved horizontally and vertically, and the computer-aided manufacturing (CAM) software package is usually used to monitor the output process of the print head.

Acrylonitrile butadiene styrene (ABS) resin, polycarbonate (PC), polylactic acid (PLA), high density polyethylene (HDPE), polystyrene (PPSU) and other high molecular polymers can be used with this method. In general, these polymers are filamentous and rolled. During actual processing, failed printing and too many support parts can cause wasting. So, a further issue is how to convert waste plastic to usable filaments has become a further issue. Right now, these wastes can be smashed to pieces and remelted to filaments as in the original manufacturing process by a 3D printer filament recycler.

Models produced by FDM technology will have some limitations. For example, hollow structures are difficult to produce because there is no support for the printed object during the printing process. Therefore, FDM must design a support which is not too thick and can be peeled off once the process has finished.

2.2.3.2   Stereolithography (SLA) and PolyJet

In 1986 Chuck Hull obtained a patent for stereolithography (SLA,

Figure 2.10). SLA mainly uses photopolymerization technology which was

invented by Mitsubishi's Matsubara to separate solid products from liquids.

When using photopolymerization technology, a bucket of liquid polymer needs

to be irradiated by the controllable light. The surface layer of the liquid

polymer exposed to the light is gradually solidified. At this time, the solidified

object moves downward, and the liquid polymer is exposed to light and

solidifies again. This is repeated until the entire model is finished. The

remaining liquid polymer is cleaned out, and the rest is the solid model.
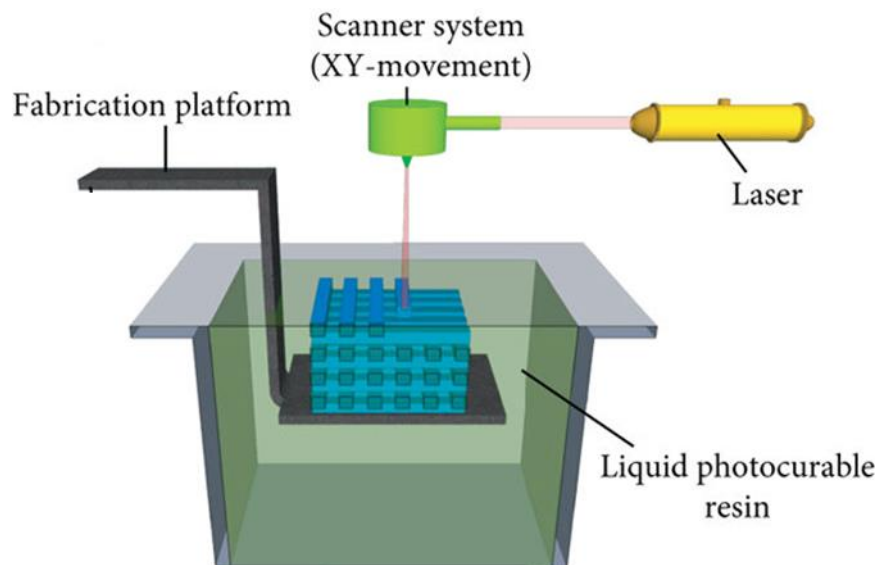
Figure 2.10: Stereolithography setup [193].

PolyJet 3D printing (such as Objet series printers of Stratasys, Ltd.) use

the same technology but another method which sprays a very thin layer of

photopolymers on the trays (between 16 and 30 microns). Each layer of photopolymer needs ultraviolet light to cure after being sprayed so that the final cured model can be put into use immediately without post-curing which is different from the SLA process. The support material used to support the complex shape model can be removed manually or by spraying water. This technology is also applicable to elastomer materials.

2.2.3.3 Selective laser sintering (SLS) and selective laser melting (SLM)

Casting is the traditional manufacturing technique for metal products. It is also known as a forming process and requires expensive moulds or mould tools to form the desired shape. And secondary processing can give the material its final shape and characteristics. The entire manufacturing cycle is called a subtractive process because the material is removed to make the final product. However, in additive manufacturing, materials are added layer by layer in the form of liquid, powder or solid to give the final product a desired shape.

From the 1980s, the additive manufacturing (AM) technology developed to use stereolithography (SLA) method. Slowly, Selective Laser Melting (SLM, **Figure 2.11**) and Selective Laser Sintering (SLS) appeared on the market, which started the additive manufacturing technology of metal products. Most SLM and SLS technologies use a heat source (laser beam or electron beam), which is focused on a bed of raw material (plastic, metal or

ceramic) to melt it from its initial state (mostly powder) to the final shape. Another method called Electronic Beam Melting (EBM) also used for metal production. It is a similar method to SLM but uses an electron beam to replace high-powered laser. Due to its wide range of applications, this process is currently used in automobiles [194], aerospace [194], biomedicine [195], consumer electronics [196] and the jewellery industry [197]. Functional parts made of metals and alloys, such as aluminium [198], steel [199], martensitic stainless steel [200], stainless steel [201], maraging steel [194], titanium [202], Inconel [203, 204], and cobalt-chromium-based superalloys [196] are being manufactured by this technology.
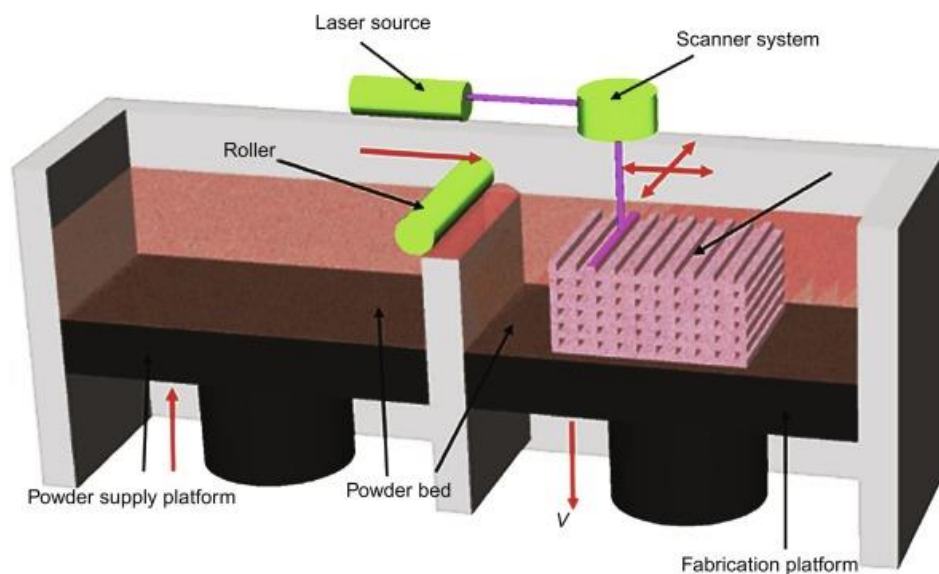
Figure 2.11: Selective laser sintering setup [205].

2.2.3.4   4D Printing

MIT successfully designed a set of 4d printing cases in 2014 [206]. They designed a strip structure (**Figure 2.12**), which is a joint printed with material and several pieces of material b connected. These two materials have different swelling rates in water, so when the strip structure, which is composed of two materials is placed in water, the joints will be bent in a designed direction due to the fast swelling rate. The material b is driven by the joints, forming designed patterns (2d) or structures (3d). And because of the swelling in water, this 1d to 2d/3d process is reversible, so this design can achieve a closed loop of 1d - 2d/3d - 1d.
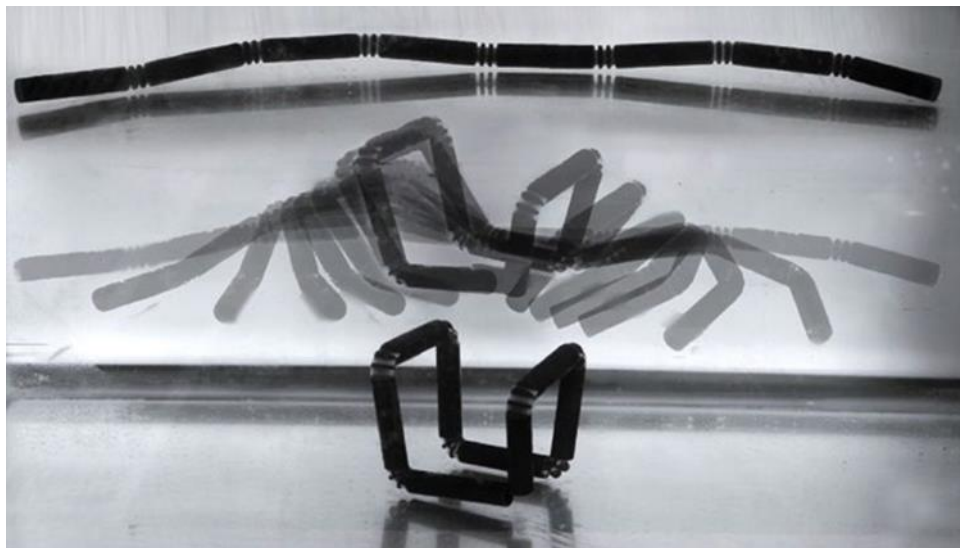
Figure 2.12: A series of photographs showing the self-folding of a 4D printed multi-material single strand into a Hilbert cube [206].

Jenifer's group reported similar 4D printing in 2016 [190], but they did not use the swelling competition between two materials, they only used one

kind of material. In their paper, a high-resolution 3D printer was used to print the pre-designed petal (**Figure 2.13**), and the distribution of the initial layout is the key to determining the deformation of the structure after swelling. Therefore, the design used different 1d layouts to generate different stresses (during swelling) in 2d structure, which made the structure deform (2d to 3d). Using the same petals, the same external environment, and a changing the 1d lay out, can create a different deformation structure.
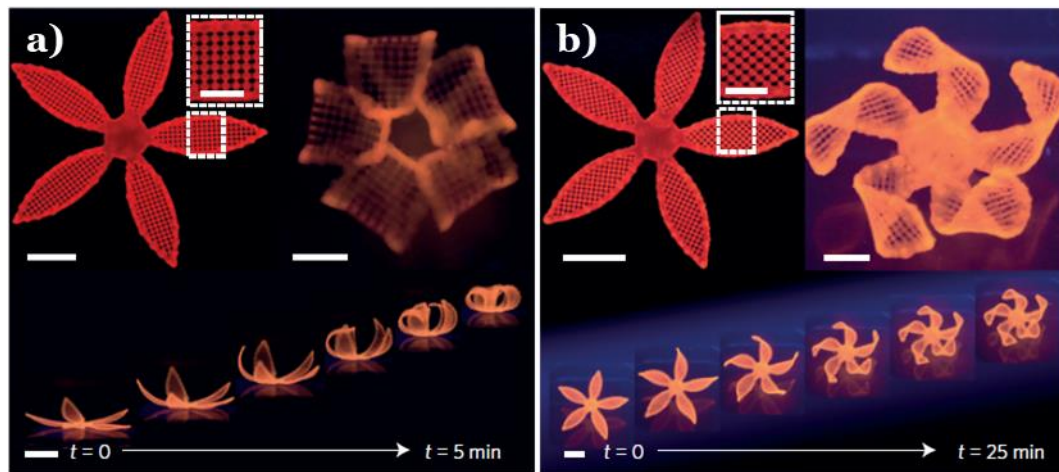
Figure 2.13: Complex flower morphologies generated by biomimetic 4D printing. **a)** Simple flowers composed of 90°/0° and **b)** -45° /45° bilayers oriented with respect to the long axis of each petal, with time-lapse sequences of the flowers during the swelling process (bottom panel) (scale bars, 5 mm, inset D 2.5 mm) [190].

To date, hydrogels [71, 207-210] and shape memory polymers (SMPs) [135, 211-216] are the two main active polymers used in 4D printing. In hydrogel-based 4D printing, hydrogels are integrated with a non-swelling

polymer or filament. When the printed structure is immersed in a solvent, the hydrogel swells, creating mismatch strains between the two materials that lead to overall shape change [190, 217, 218]. The advantage of this approach is that it does not require programming after printing; however, there are a few drawbacks. First, the stiffness of the printed structure is relatively low due to the softness of hydrogels. This can be overcome by a composite strategy, where the soft gel is combined with a stiff SMP [190, 218]. Second, the swelling mechanism is based on species transport (diffusion), and thus, the responsive speed is relatively slow, especially for large structures. For example, although the active element (a hinge) in Tibbits' work is small (~0.8 mm), it takes about 7 min to achieve a bending angle of 36° [217]. Third, the actuated shape by swelling is unstable, because it will change with the subsequent loss of solvent in the hydrogel.

Photocured SMPs have been used in 4D printing with both commercial and research printing technologies based on photopolymer inkjet [219-221] and projection micro stereolithography [191, 222]. 4D printing with SMPs generally requires a series of steps: (1) synthesis/ processing by 3D printing; thermomechanical programming, including (2) heating, (3) mechanical loading, (4) cooling, and (5) removal of load; and (6) deployment/actuation. Thermomechanical programming often requires special jigs and fixtures to apply mechanical loads and a well-controlled thermal environment [213]. However, 4D printing with SMPs offers the advantages of a stiffer structure

and higher actuation speed; both are orders of magnitude higher than those obtained with printed hydrogels.

2.2.3.5   Additive Manufacturing in Engineering Applications

Nowadays, 3D printing is developing rapidly and has been used in manufacturing, industrial, and medical fields, etc. These applications also promote 3D printing to be a better commercial technology. 3D printing is used as open-source designs in these application fields, especially during the prototyping stage, and it can print an object directly from a computer aided design (CAD) model. In this way, while the research and development process are accelerated, the cost is also greatly reduced.

Soft sensors and actuators - Inspired by the concept of 4D printing, 3D printing occupies a place in the manufacture of soft sensors and actuators. Most traditional soft sensors and actuators are manufactured using a multi-step low-yield process requiring manual manufacturing, post-processing/assembly and lengthy iterations, and the final product has low flexibility in customization and reproducibility. 3D printing has changed the rules of the game in these areas by introducing custom geometry, functions and control attributes to avoid the cumbersome and time-consuming aspects of the early manufacturing process.

Space - The Zero-G printer is the first 3D printer designed specifically for zero gravity, and it is located at NASA's Marshall Space Flight Centre

(MSFC) and Made In Space, Inc. It was built under the cooperation of the People's Republic of China. In September 2014, SpaceX launched a zero-gravity 3D printer to the International Space Station (ISS). On December 19, 2014, NASA sent CAD drawings for socket wrenches to astronauts on the International Space Station via email, and they used its 3D printer to print the tool (**Figure 2.14**). Space applications provide the ability to print parts or tools on-site, instead of using rockets to bring pre-manufactured items to human colonies on the moon, Mars, or elsewhere. The second 3D printer in space, the European Space Agency's Portable Car 3D Printer (POP3D) was scheduled to be delivered to the International Space Station before June 2015. In 2016, Digital Trends reported that BeeHex was manufacturing a 3D food printer for a manned missions to Mars.
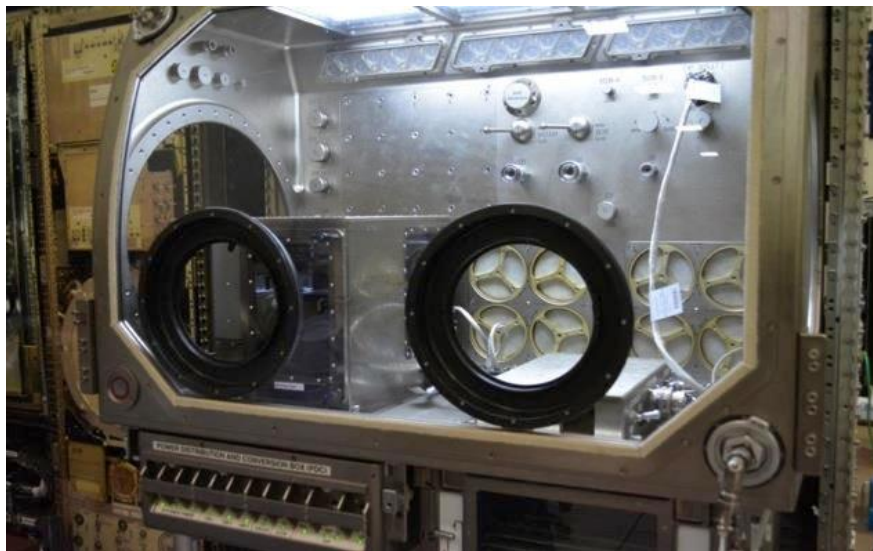
Figure 2.14: 3D print was tested in the MSG Engineering Unit at NASA MSFC prior to payload integration [223].

Most buildings planned on asteroids or planets will use the materials available on these objects to bootstrap in some way. 3D printing is usually one of the steps. The Sinterhab project is studying the use of lunar weathered fossils as a basic material to build a lunar base through 3D printing. Researchers are experimenting with microwave sintering to produce solid blocks from raw materials instead of adding a binder to the weathered layer.

Medical - In 2014, a five-year-old girl became the first child in the UK to avail of 3D printing technology when it was used to make a prosthesis for the incompletely formed fingers her left hand. Her hand was designed by e-NABLE in the United States, an open-source design organization that uses a network of volunteers to design and make prostheses for children. The artificial hand was based on a plaster model made by her parents. For a boy named Alex who was born with an arm missing just above the elbow, the team was able to use 3D printing to upload the e-NABLE Myoelectric arm, which is composed of electric muscle-driven servo batteries and batteries. So far, e-NABLE has distributed thousands of plastic hands to children using 3D printers.

Printed prostheses have also been used to repair mutilated animals. In 2013, a 3D printed foot allowed a crippled duckling to walk again. In 2014, a Chihuahua born without front legs was equipped with a harness and wheels with a 3D printer. The 3D printed hermit crab shell allows hermit crabs to live in a new style home. The prosthetic beak is another tool developed using 3D printing technology to help a bald eagle named Beauty whose beak was

severely mutilated due to a severe face injury. Since 2014, commercially available 3D printer-made titanium knee implants for dogs have been used to restore animal mobility. Only one year later, more than 10,000 dogs in Europe and the United States were treated.

In February 2015, the FDA approved the sale of surgical bolts, which facilitate minimally invasive foot surgery without the need to drill through bones. The 3D printed titanium device "Fast-forward Bone Tether Plate" is approved for corrective surgery to treat bunions. In October 2015, Professor Andreas Herrmann of the University of Groningen developed the first 3D printable resin with antibacterial properties. Using stereolithography, the quaternary ammonium group is incorporated into the dental appliance and kills bacteria upon contact. This type of material can be further used in medical devices and implants.

Customized 3D printed spectacles can also be created (**Figure 2.15**) and applied to patients with facial deformities [172]. Because many children with facial deformities (such as Goldenhar syndrome) need corrective glasses, it is necessary to provide appropriate frames for this group of patients. Fitting the spectacle frame to the face of a child with a severely deformed face is particularly challenging. The contact points of the glasses with the nose, ears and cheeks play an important role in the stability and weight distribution of the facial glasses [224]. Special consideration should be given to the frame size, panoramic lens inclination, and temple design during the selection of nose pad glasses to maximize the optical alignment, beauty and comfort of patients with

facial deformities [224]. For these children with conventional commercially available glasses, there are few other options. It is also feasible to use this technology to produce customized glasses to maximize optical alignment and comfort under special conditions.
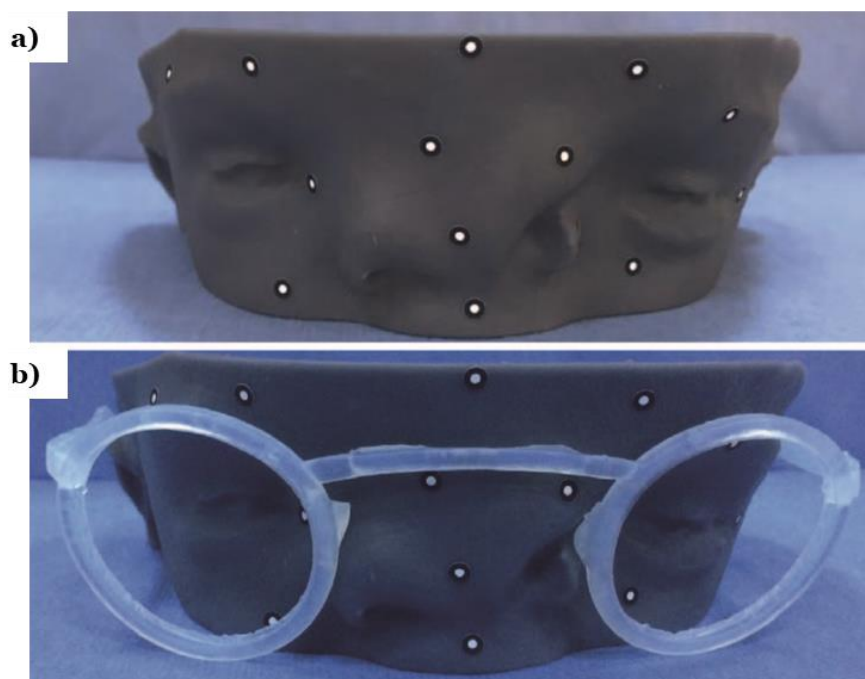
Figure 2.15: 3D printed phantom model of the mid face. **a)** Phantom model of the mid face 3D printed from hard acrylic resin material and **b)** try on process of spectacles after printing, before trying on the patient [172].

Researchers have also developed a 3D printing technique to fabricate a gel based multimode tactical sensing structure [225]. The sensor array (**Figure 2.16**) can be fabricated by the facile and large-scalable additive manufacturing method, opening a new window for the future scale-up manufacturing. Furthermore, the 3D printed hydrogel electronics are capable

of accurate deformation and temperature sensitivities. The physical crosslinking gel network enables an ultra-stretchability as high as 975%. The multimode tactical sensing has been demonstrated with potential to be used in motion capture, physiological and psychological health assessment, and human-machine interface, etc.
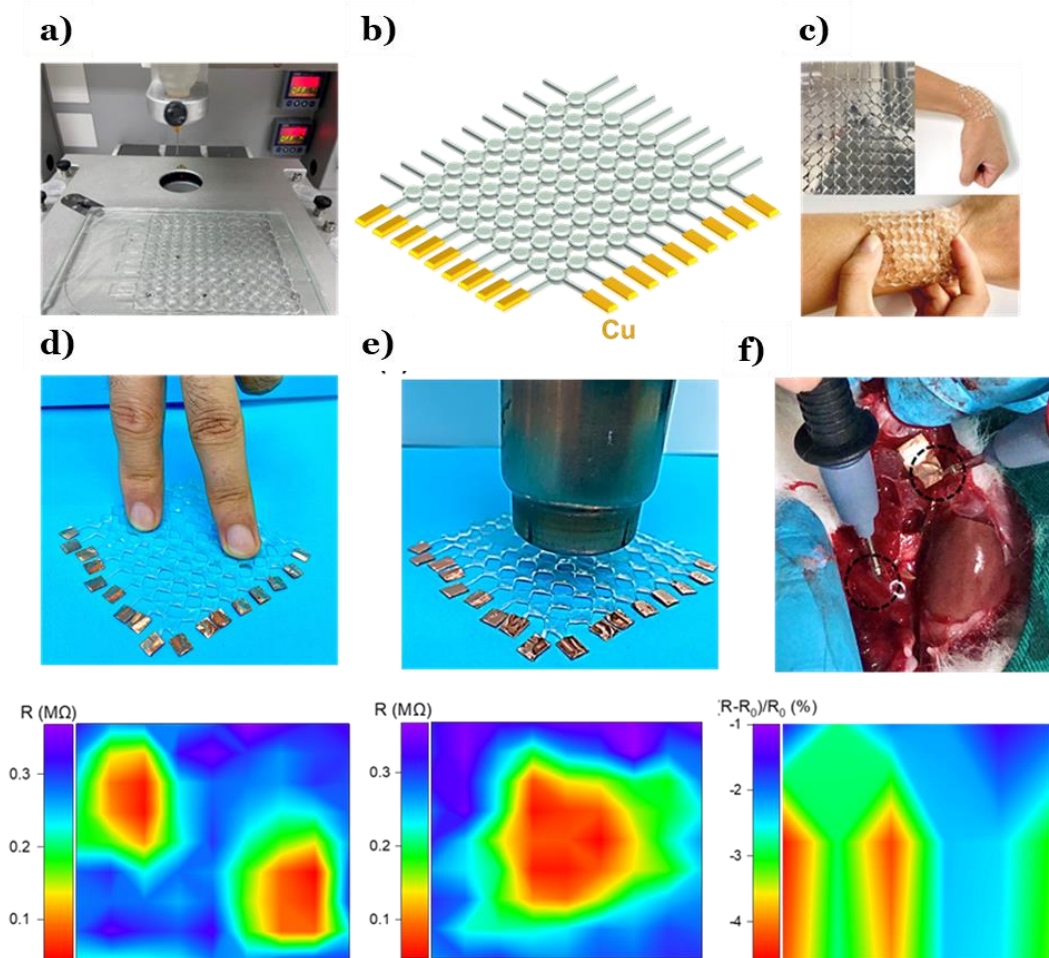
Figure 2.16: a) 3D printing setting and **b)** 3D printed hydrogel sensor array with 9×9 pixel (8×8 cm²); **c)** Pictures of the sensor array on wrist to show its conformality with skin; **d)** Pictures of two-finger pressing on the sensor array; **e)** heating above the sensor array with a real-time 2D mapping of resistance change; **f)** the demonstration of the printed gel sensor for monitoring the

rabbit's heart beating motion. The corresponding mapping profiles of pixel signals are shown on the right [225].

2.3   Responsive Soft Materials

Stimuli-responsive soft materials (**Figure 2.17**) can sense both external and internal condition changes, such as temperature, light intensity, pH or ion concentration. Additionally, these materials can fold 1D structures to 2D/3D. This has proven popular in bio-inspired engineering applications, such as flexible sensors, soft robotics and tissue engineering. For example, Kim's group manufactured temperature-responsive gel sheets which can transform between a flat state and a three-dimensional shape. Conventional hydrogel structure manufacturing methods such as moulding and lithography-based microfabrication are still popular, but there are some limitations for these methods such as high prototyping and low-volume production costs. Hence a new method with 3D printing has been reported. It has the advantages of complex structure, lower prototyping cost and facilitation of many new applications (flexible sensors, soft robots, bio-medical devices etc.).
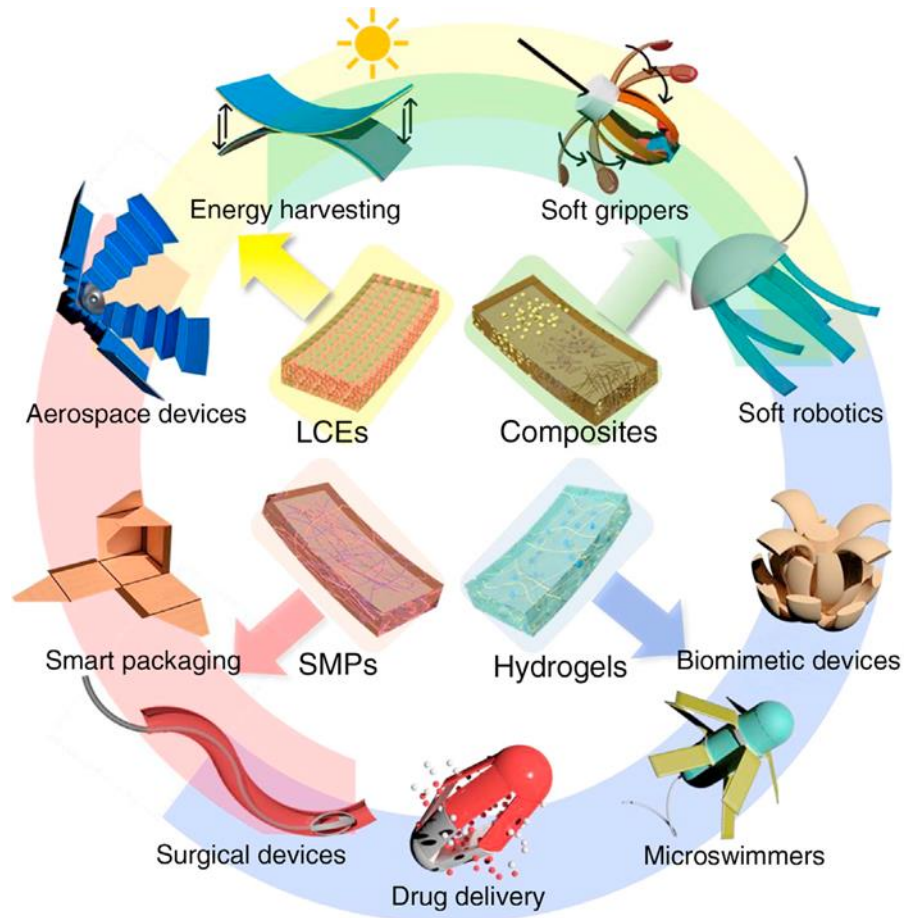
Figure 2.17: Abbreviations: LCE, liquid crystal elastomers; SMP, shape memory polymer [226].

3D-printed architectures of programmed materials will not only mimic highly organized, biological constructs, but also provide new functions as responsive materials and devices [227, 228]. However, the benefits of harnessing programmed materials as active components in 3D printing have not been well explored. This is due to the challenges of integrating programmed elements into macroscopic structures with high precision while maintaining their viability and responsiveness. The design of 3D printed

structures is guided by quantitative models that account for the responses of programmed materials/structures in printed microstructures.

2.3.1 Moisture-responsive

Because of the ubiquitous stimulation and wide application of water or moisture-sensitive materials, these have aroused great interests. Hydrogels are extraordinary moisture-responsive materials because of their hydrophilicity which allows them to swell to 200% of their original volume. In addition, hydrogels, as a class of polymer materials, exhibit high printability. The advantages of using hydrogels are their biocompatibility and ease of printing by direct ink writing [229, 230]. However, their slow reverse reaction means that researchers must wait hours until the hydrogel dries and shrinks. To program the behaviour of the hydrogel, swelling must be anisotropy. Gladman et al. combined hydrogel ink and cellulose fibrils which can be uniformed by the sheer force generated by the contact between the ink and the printing bed [190]. This alignment causes the lateral expansion strain to be four times the pre-strain; thus, a structure can be 4D printed where the hydrogel is confined in one direction by the hard material, so that the swelling achieves anisotropy [218]. Zhang et al. also reported a rapid response. He designed a hydrophobic film made of cellulose streamside ester (CSE), which can be rotated and reacts more precisely [218].

The hydrogel is usually immersed in an aqueous environment, causing it to absorb water to its water saturation point, which limits the intermediate

controllability of the hydrogel. However, the swelling of the hydrogel can be controlled by the temperature of the aqueous environment. Breger et al. achieved a micro-gripper joint made of gradient cross-linked PNIPAM-AAc soft hydrogel [231]. By heating or cooling the water in which the fixture is immersed, reversible driving can be achieved by adjusting the saturation point. A special hinge design is also applied to avoid excessive swelling. Tibbits et al. demonstrated a self-folding double-layer structure made by a PolyJet printer [232]. The rigid board is printed at the seam so that the folding stops at a pre-programmed angle. When this angle is reached, the tips of the plates touch each other to prevent excessive bending.

2.3.2   Thermo-responsive

The deformation of thermo-responsive materials is mainly driven by one of two mechanisms: shape memory effect (SME) [233] or cosmic change effect (SCE) [234]. SME-based materials known as shape memory materials (SMM), can further be shape memory alloys (SMA), shape memory composites (SMP), shape memory traces (SMH), shape memory ceramics (SMC) and shape memory alloys (SMG) [235]. SMP is favoured as it is easy to print. SMP usually have a glass transition temperature (Tg) higher than their operating temperature. They are programmed under specific heat and mechanical treatments above their glass transition temperature, and then cooled to fix on a temporary shape without external load. Then after the temperature rises above its Tg, the sample returns to its original permanent shape [233]. In order to take advantage of their special properties, the researchers modified and

made available various SMP materials. The SMP ball was manufactured using SLA, the liquid resin was polymerized under ultraviolet irradiation to fix the permanent shape. The ball can extend into a plane and retract back with high durability [236]. Ge et al. printed an SMP flower that can bloom when heated [222]. This flower is a gripper used to make smart assembly or electromechanical equipment. The latest discovery by Bodaghi et al., is the SMP structure which is pre-programmed by making full use of the heating process in the FDM printer [237, 238].

SMP follows the SME mechanism and usually has two or three different states in which an intermediate stable shape cannot be maintained. In contrast, SCE is directly proportional to the applied simulation, that is, it changes continuously between its states [234]. As they are thermally responsive materials, SCE often appears in the coefficient of thermal expansion (CTE). Since the interface area between the layers must remain constant, the heating field structure may bend. Hu et al. demonstrated this with a graphene-based twin crystal structure that can expand into a flat plate when heated and roll back into a moving body when cooled. To achieve severe deformation through SCE, you need your own temperature change or a combination of special materials. As shown, there are two orders of magnitude difference between the CTE of different layers in the film [239].

2.3.3 Photo-responsive

Unlike moisture and thermo, light is a selective absorption; the exposed area of the photosensitive material absorbs light as a transfer. Liu et al. show the self-folding structure of sequential control [240]. The absorption rate is determined by the colour of the connector and the light source. Kuksenok et al. use light to trigger deformations in very different ways. A certain number of light-responsive chromophores penetrate into certain positions of the polymer gel, so these parts will only swell when exposed to light [241]. Therefore, there is versatility in injecting light use to print patterns as a stimulus. By projecting weak ultraviolet onto the liquid resin, deep gradient crosslinking can be achieved, most of which helps to bend the 4D printed structure [242].

2.3.4 Electro-responsive

Like light, electric current can be used as an indirect stimulus in 4D printing. Miriyev et al. demonstrated a printed soft artificial muscle made of a mixture of silicone elastomer and ethanol. When an electric current is applied, heat is generated by resistance heating, causing the ethanol to evaporate. This phase shift from liquid to gas greatly increases the volume of ethanol, thereby enlarging the entire matrix [243]. Electric current is also applied to the polypyrrole (PPy) film to control water absorption or desorption. Okuzaki et al. applied PPy film to an origami micro-robot which has a special geometric shape for its feet, so it encounters less resistance when moving forward. When placed in a humid environment, the voltage drives the head forward due to the absorption of moisture, and the tail follows when the desorption is caused by the lack of voltage [244].

2.3.5 Magneto-responsive

3D/4D printed structures that respond to magnetic fields are called magnetically responsive materials. Breger et al. combined magnetic nanoparticles into a microgripper printed by hydrogels and realized remote control by applying a magnetic field [231]. Embedding is performed in pre-treatment, where iron oxide powder is mixed with the material solution. This technology also has potential in polymer printing and metal printing. One disadvantage is the limitation of the size of the printed matter, which must be light enough to be affected by the magnetic field.

2.4 Soft Mechanics Theory

Surface morphologies may have a variety of elastic instabilities, including wrinkling and creasing of surfaces, fold and ridge. Traditionally, these deformations are generally avoided because they usually represent a type of mechanical failure. However, a new trend called buckling mechanics has emerged in recent years and this can be used to give materials beneficial functions. For many such applications, it is desirable that such deformations occur reversibly and respond to well-defined signals or changes in the environment [245].

2.4.1 Wrinkles

When in-plane compressive stress is applied to a thin rigid plate, elastic instability will occur when the critical stress is exceeded, causing the plate to

buckle out of plane. The length of the buckle is commensurate with the size of the plate, as Euler first described it in detail in the 18th century [246]. However, if a rigid plate is connected to a soft elastic foundation instead of forming a single buckle, the plate will form a periodic buckle pattern, often called folds (**Figure 2.18**). Following the mechanics similar to the Euler stability problem, ε_w found that the critical strain of this wrinkle instability depends on the comparison of the mechanical properties of the double layer:

$$\varepsilon_w = \frac{1}{4}\left(\frac{3\bar{E}_s}{\bar{E}_f}\right)^{\frac{2}{3}}$$
                         Equation 2.4

where, $\bar{E}_s$ and $\bar{E}_f$ are the plane strain modulus of the soft substrate and the hard film respectively [176]. Wrinkling was first researched in detail by Allen, et al. [247] from the 1960s in the context of buckling of sandwich plate. It was later developed by Bowden, et al. as microscopic wrinkles in the thermally deposited metal film of the elastomeric substrate [248, 249]. A detailed description of wrinkles can be found in the literature [249-252]. The appearance of wrinkles can be understood by considering the total energy of the system, which is the sum of the tensile energy of the soft foundation and the bending energy of the rigid plate. Qualitatively speaking, the short-wavelength buckling minimizes the stretching of the soft foundation, while the long-wavelength deformation minimizes the bending of the rigid board. Therefore, the system selects the optimal wrinkle wavelength λ, thereby minimizing the total energy of the system. The optimal wavelength is

determined by the film thickness t and the contrast of the material characteristics, and is given by the following formula:

$$\lambda = 2\pi h \left(\frac{\bar{E}_f}{3\bar{E}_s}\right)^{\frac{1}{3}}$$
Equation 2.5

The amplitude A of the wrinkles is a function of the applied compressive strain ε, which for small strain is

$$A = t \left(\frac{\varepsilon}{\varepsilon_w} - 1\right)^{\frac{1}{2}}$$
Equation 2.6
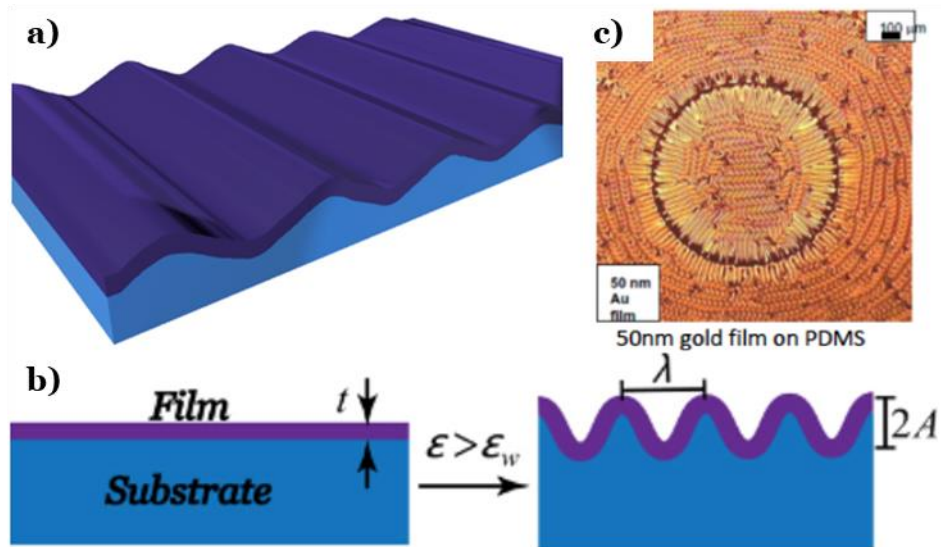
Figure 2.18: a) A schematic illustration of wrinkles developing in a bilayer of a stiff skin attached to a soft substrate above a critical compression; **b)** Cross section of the wrinkles with detailed geometrical definitions; **c)** The experimental observation of wrinkle formation on the gold film over a liquid surface [249].

Within the above general framework, wrinkling has been achieved in various material systems and possible applications, including stretchable electronic devices [52, 253, 254], microfluidics [255, 256], tuneable optical devices [47, 257], control wetting [258], and metrology [259].

2.4.2 Crease

Although the almost inextensibility of the hard skin layer will be produced during compression, if there is no hard skin, the soft elasticity will remain stable and change rapidly under small materials. Using the elastic stability analysis of the semi-infinite new Hooke material in compression, Biot first predicted that, except for simple surface compression, the free surface of the elastic half space will not recover [260]. In order to differentiate from the wrinkling of the skin film, we use the term "Biot instability" to refer to this forecast.

Although there are some reports of Biot's instability [261, 262], these usually have been ignored. One example of this is **Figure 2.19** when a soft elastic material (such as hydrogel or elastomer) is compressed, the material will be crease unstable where the free surface suddenly forms sharp self-contact features [263, 264]. Creases, also called "brain grooves" because they are similar to folds in the human brain [264], can be seen in everyday situations, such as on a baby's arm [264] or on the surface of a bread dough raised in a bowl [265]. Our group have described a topo-optical sensing strategy by targeted generating creases on a micropatterned surface [266]. An

inherited automatic optimization on optical contrast is also introduced by oxygen quenching the Ir-III based optical indicator layer, which leads to an ultra-high contrast by significantly reducing the background noise. This high-contrast topo-optical sensing strategy will open new windows for future applications such as flexible/wearable electronics and bio-devices [267, 268].
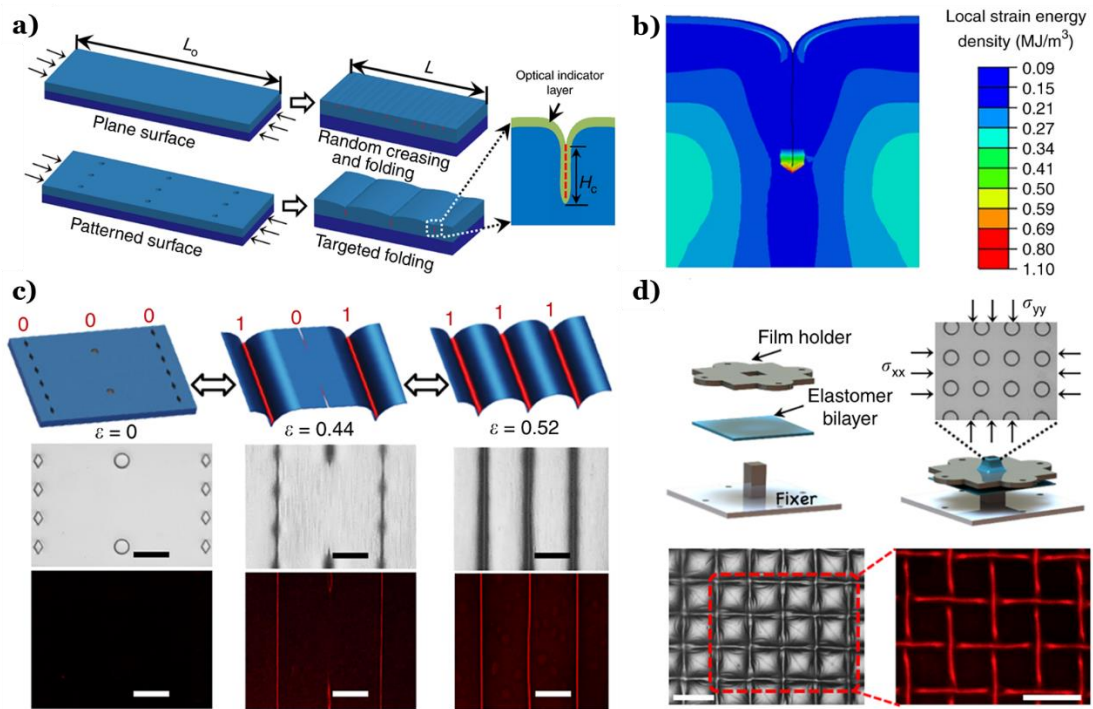
Figure 2.19: a) Schematic illustration of the formation of crease with and without surface pattern; **b)** Simulation of the self-folding for the crease pattern; **c)** Develop 2D creasing pattern to facilitate logical sensing function through surface micro-patterns; **d)** The realization of 2D creasing grid [266].

2.4.3   Buckling, Fold and Ridge

While wrinkling and creasing represent two important modes of surface instability, polymer films can also experience global buckling instabilities, where the middle of the buckled section undergoes large displacement. Many different types of global buckling can occur depending on the geometry and stress state of the film. For example, delamination blisters will form when the compressive stress within a surface attached thin polymer film becomes sufficiently large to overcome adhesion to the substrate [269-273]. This can provide an alternative pathway to relax stress instead of creasing or wrinkling. Buckling induced folding and delamination may represent an interesting route for surface patterning.

The threshold state with a small σ_{zz} to initialize the release of equiaxial compression energy, $\varepsilon_{yy} = \varepsilon_{yy}$ is illustrated in **Figure 2.20 a**. Two stages of buckling induced delamination are often discussed: an irregular blister (**Figure 2.20 b**) and a Euler blister with larger out of plane deformation (**Figure 2.20 e**). By confining a responsive gel layer on a micro-engineered substrate with a designed electrode pattern (**Figure 2.20 c**), a spatially defined and electrically controlled release of the hydrogel can be expected. Irregular blisters or Euler blisters can be electrically induced along the surface areas defined by the electrodes (**Figure 2.20 d-e**). For gel thin films, the topography of the buckling and post-buckling behaviour is expected to be similar to those of inorganic films. The theoretical profile is normally approximated by a cosine form known as the Euler mode [274, 275], and the profile is theoretically given by

$$A = \left(\frac{A_i}{2}\right)\left(1 + \cos\frac{2\pi x}{w}\right) \qquad \textbf{Equation 2.7}$$

where A_i is the max out of plane displacement and w is the electrode width.

For irregular buckling, some theoretical understanding has been provided by approximations for determining the critical stress, buckling amplitude and relevant energy release rates [245, 276].
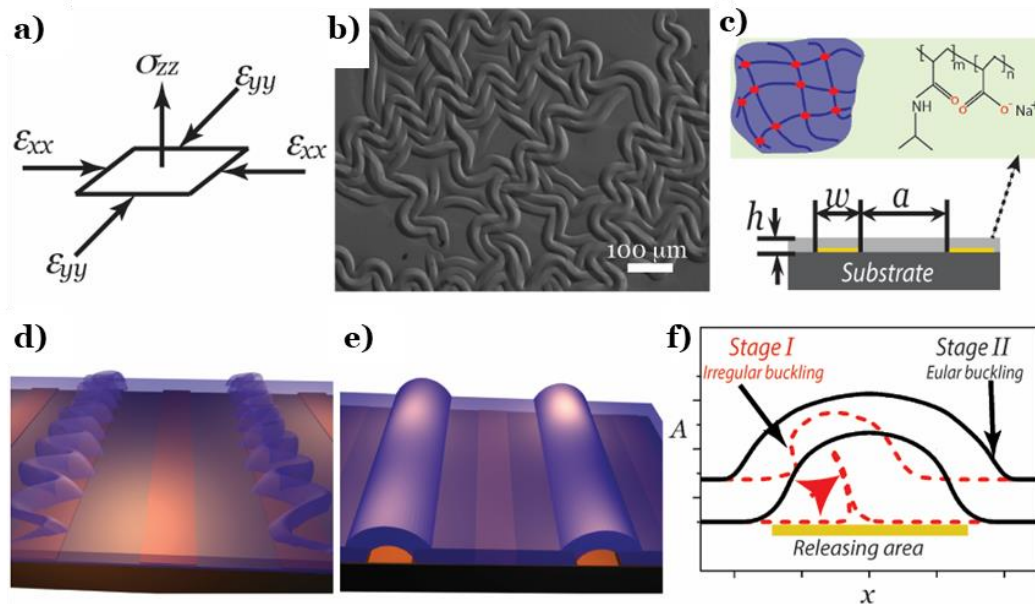
Figure 2.20: **a)** Stress state before buckling; **b)** Buckling induced delamination stripes patterns; **c)** Structure design and PNIPAM gel; **d)** Electro-actuated irregular buckling blisters and **e)** Euler buckling blisters; **f)** Cross-sections of irregular buckling blister and Euler buckling [228].

2.5 Applications of Structures and Devices by Bio-structures

2.5.1 Intraocular Lens

The human lens is the main refractive structure of the human eye, and it is also the only refractive structure that has the ability to adjust the focal length of eye; it has a biconvex oblate body covered with a transparent capsule. The anterior convex curvature radius of the lens is 10mm, the kyphotic curvature radius is 6 mm, the axial anteroposterior size (depth) averages 22.0–24.8 mm. The reason for near-sightedness or hyperopia is that part of the lens disfunctions. If the lens is partially or completely opaque, it will cause visual impairment. Cataracts which are caused by protein deposition in the lens, are the most typical example. More than half of blindness is caused by cataracts. This does not include those who are not completely blind but have 30% of visual impairment.

Because of the high blindness rate mentioned above, IOL was invented to replace the diseased human lens. IOL, an artificial lens implanted in the eye, replaces the role of the natural lens. The first intraocular lens was designed by John Pike, John Holt and Harold Ridley. In 1949, Dr. Ridley implanted the first intraocular lens for a patient at St. Thomas's Hospital in London. The development of intraocular lenses is inseparable from the discovery of qualified materials. In World War II, scientists observed that some injured pilots had glass fragments in their eyes, but the glass did not cause obvious and

sustained inflammatory reactions. This led them to believe that glass or some polymer organic materials could remain stable in the eyes, and thus the intraocular lens was invented [277].

The shape of the intraocular lens is usually composed of a circular optical part and peripheral supporting loops. **Figure 2.21** shows three typical designs which have a similar diameter to the optical part which is generally about 5.5-6mm and the overall diameter is generally about 12-14mm. This is because at night or under dark light, the pupil of a person will be enlarged and the diameter can extend to about 6mm. Additionally intraocular lenses which are too large pose certain difficulties in manufacturing or surgery, so major manufacturers use 5.5-6mm optical part diameter. The function of the support loop is to fix the intraocular lens, and although there are many forms, it can basically be two C-shaped wire-mounted support loops (**Figure 2.21 c**). All three designs in **Figure 2.21** have been 3D printed and tested as **Figure 3.2**.
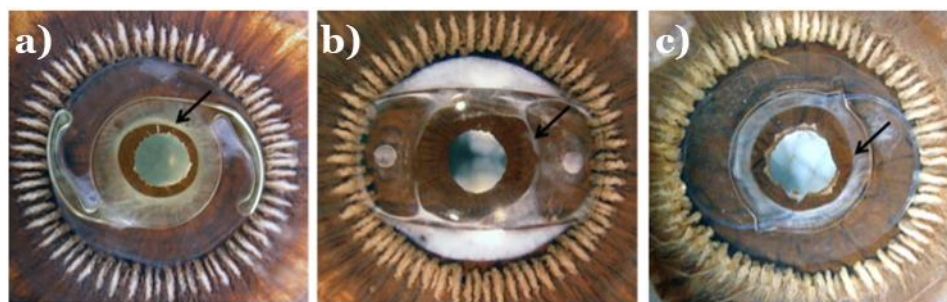
Figure 2.21: Three typical IOL designs which have already been implanted in the human eyes. **a)** Single-piece hydrophobic acrylic IOL; **b)** Plate haptic silicone IOL; **c)** Multi-piece IOL [277].

The materials that have been used in IOLs are: polymethylmethacrylate (PMMA), silicone resin, hydrophobic/hydrophilic acrylate and collamer, etc. Polymethyl methacrylate (PMMA) is a rigid material and cannot be folded. Therefore, in order to put an IOL made of this material into the patient's eye, the incision must be equal to the size of the IOL. This increases the difficulty and risks of surgery. Therefore, the material development trend of IOL began to shift to soft and foldable type [277].

IOLs made of silicone materials are designed to solve the above-mentioned problem of non-foldable rigid materials. IOLs of this kind of material can be implanted through surgical incisions smaller than their size. Silicone intraocular lenses are suspected to facilitate bacterial adhesion, leading to a higher risk of postoperative infection. In addition, in some specific cases, it can cause retinal detachment, so nowadays, silicone IOL is no longer used [278, 279].

Acrylic hydrophobic IOL is the most widely used modern foldable IOL today. They are designed from copolymers of acrylate and methacrylate derived from PMMA. The purpose of the new design is to make the IOL foldable. They can be manipulated during surgery and always return to their original shape in a short time. The first IOL implantation was in 1993. The hydrophobic foldable acrylic material can be divided into three-piece and one-piece designs, with an optical diameter of 5.5-7 mm and a total length of 12-13 mm, transparent or coloured yellow. The refractive index can be 1.44−1.55 [278].

Hydrophilic foldable acrylic is a combination of hydroxyethyl methacrylate (polyHEMA) and hydrophilic acrylic monomers. The refractive index of this material is 1.43, and the water content is 18 to 34%. They are soft, compressible, and their hydrophilic surfaces have excellent biocompatibility. They can be implanted through a small incision less than 2 mm, so they are very suitable for MICS. The folding of the poly-HEMA chain depends on the degree of hydration, so the physical and optical properties of the polymer vary with the water content. When the lenses are hydrated, they absorb moisture and become soft and transparent.

2.5.2 Drug Delivery

The traditional 'one-size-fits-all' treatment approaches have become a thing of the past as the healthcare industry experiences rapid changes. According to a report by the National Health Service (NHS) in the United Kingdom, this conventional treatment involving mass-produced drugs is ineffective for more than 70% of patients, so there is an urgent need for personalized new treatments for individuals. Traditional manufacturing processes are completely unsuitable for producing customized drug delivery therapies, and involve inherently labour-intensive, non-fixed dosage and time-consuming processes. This is the demand that the healthcare industry has created to adapt and accept new platforms to tailor treatment products.

Three-dimensional (3D) printing will become the main destructive technology in the field of healthcare by producing customized objects of almost

any shape and size layer by layer. Computer-aided design (CAD) software or imaging techniques (such as magnetic resonance imaging (MRI) or computer tomography (CT) scans) can be used to create structures from digital 3D files to easily create personalized objects for each patient. The 3D printing process has different shapes according to the properties of the materials used (such as plastics, ceramics, metals, resins), deposition techniques, layer formation mechanisms, or the characteristics of the products obtained (such as surface finish, texture, geometric shapes), Mechanical behaviour. These materials are divided into seven types of machines. That is, material extrusion, material injection, powder bed melting, binder injection, vat photopolymerization, sheet lamination and directed energy deposition.

In fact, 3D printing will become a revolutionary technology in the field of healthcare because of its ability to produce customized and personalized objects, personalized medical prostheses, implants and equipment that can be customized according to the individual needs of each patient. In the field of drug delivery, various implants have been prepared using 3D printing (**Figure 2.22**), including drug implants, medical devices, and personalized solid oral dosage forms. Therefore, this technology has been regarded as a viable method for personalizing medicines during use and is expected to be extended to 3D printed biological tissues to quickly screen new drug alternatives to identify treatment responses in individuals. 3D printing has a competitive advantage for small-scale production of medical equipment and medicines that require customization and replacement of adjusted doses, and products that require

complex geometric shapes. This customization cannot be achieved using conventional mass production methods and has shown advantages in patient compliance and achieving customized drug release profiles. The description will give a comprehensive overview of the latest progress in 3D printing in the healthcare sector, covering modern and future applications of drug delivery and drugs, as well as new innovations and concepts, such as the impact of 4D printing on drug delivery.
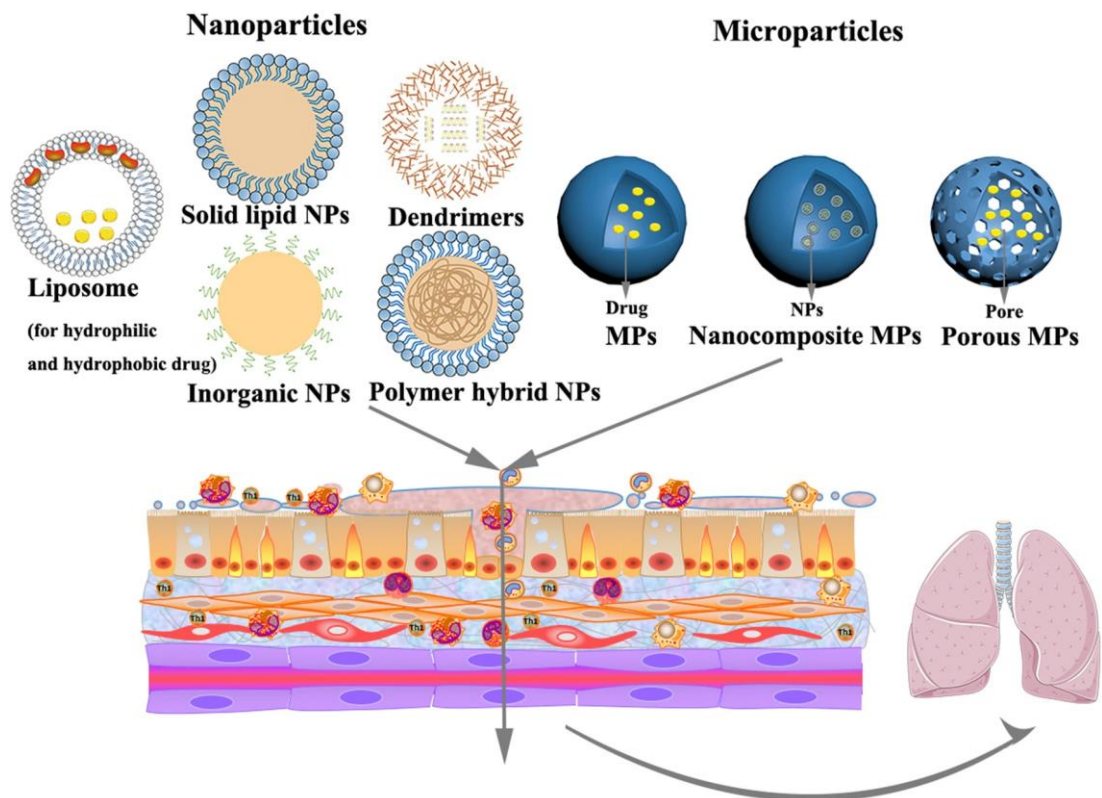
Figure 2.22: Representative nanoparticles and microparticles used for delivering antioxidants in COPD [280].

2.5.3   Physiological Medical Phantoms

Medical phantoms that are specific to patients and imitate tissues contain individual information and have great potential in many biomedical applications and clinical diagnosis (such as computational model verification, customized medical device [281-283], surgical planning [284], medical education [285], and doctor-patient interaction). As mentioned earlier, 3D printing technology has proven to be an effective manufacturing method for this kind of phantom. However, the existing technology is still insufficient to completely imitate human organs and tissues. For example, due to the oriented tissue structure, many human organ structures (such as the heart) cannot be precisely imitated. However, conventional 3D printed phantoms do not have the same special size and mechanical properties. Therefore, most 3D printed medical phantoms, even those with patient-specific characteristics and the phantom of the characteristics that the tissue imitates, are only close to the structure of human organs in anatomically rather than physiologically.

2.5.4 Micro-fluidics

The integration of smart stimuli-responsive polymers as functional elements within microfluidic devices can greatly improve the performance capabilities of controlled fluid delivery. One of the most common experiments is to apply controlled strains on a flexible substrate such as polydimethylsiloxane (PDMS) or within a hydrogel matrix, yielding a flexible membrane with centimetre scale lateral dimensions that can be macroscopically deformed [286]. Stimuli-responsive PDMS is of particular interest to researchers in terms of controllability and functionality. Examples

of stimuli include electric potentials [287], pH [288], temperature [289] and photonic [290]. However, PDMS has several drawbacks, mainly in terms of solvent compatibility, limited deformation (except from mechanical inputs) and surface wettability [291]. Recent approaches focus on designing reconfigurable surfaces/structures to produce fluidic control with higher deformation in forms which are easier to integrate into devices. A potential technique proposed is to regulate flows in a microfluidic device **(Figure 2.23)** by structurally coordinating the operation of each sub actuator in a designed soft machine system [292].
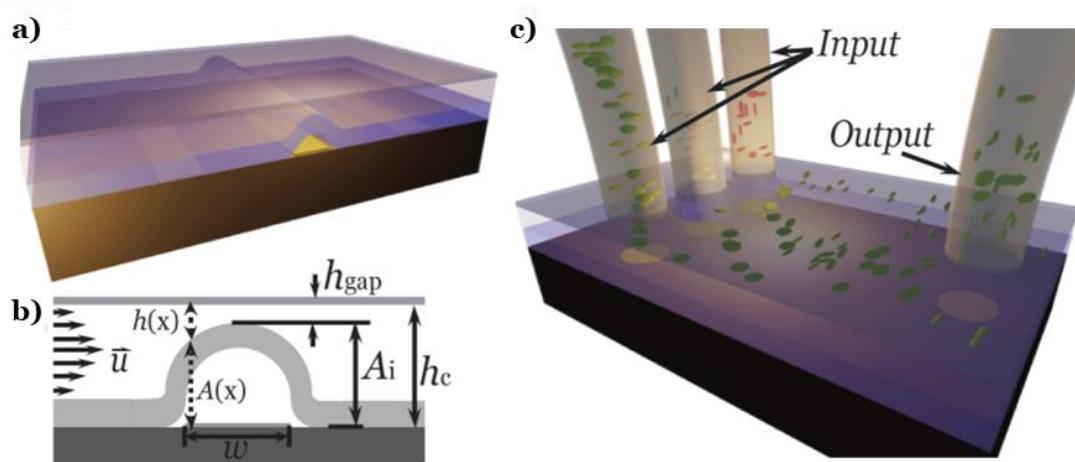
Figure 2.23: The schematic illustration of using bucking to regulate flow in **a)** micro channel with **b)** geometrical definition; **c)** The concept of integrating the buckle switch into the micro-fluidic device.

A recent approach by Holmes *et al* utilized elastic deformations *via* mechanical actuation to control and direct fluid flow within a flexible

microfluidic device [293]. The device consists of a microchannel with a flexible arch prepared by the buckling of a thin elastic film. The fluid flow rate is regulated by coupling the elastic deformation of the arch to the gap within the micro-channel. However, 'on-demand' switching has not been validated and the prospects for integrating the proposed structures/devices into a commercial chip are relatively low. This is because the driving stimulus for the surface deformation is mainly mechanical, and thus requires a large moving part(s) to achieve the global compression. Based on recent developments in electro-actuated instabilities, this proposal suggests an alternative strategy to design and fabricate a novel electrically controlled gel valve with high compatibility with existing microfluidic devices.

2.5.5   Soft Robotics

Unlike traditional rigid robots, soft machines made of flexible or elastic materials may show broad application potential in unstructured environments (such as human interaction, interaction with soft objects, and other natural environments). There are various materials used to make soft robots. In contrast to rigid robots, soft robots are made of inherently soft and malleable materials, such as silicone elastomers or alginate hydrogels, and their Young's modulus is generally lower than conventional rigid materials for example [294]. In addition, flexible pneumatic actuators have been widely used to manufacture soft robots and biomedical devices, such as soft multigait robots [66, 295] and soft gloves for rehabilitation (**Figure 2.24 a**) [296]. So far, the most commonly used materials for the manufacture of pneumatic actuators

are silicone elastomers, such as polydimethylsiloxane (PDMS) and Eco flex [297-302]. These silicone elastomers have mechanical properties similar to those of the organism, which allows them to design soft robotic fish that have been designed to swim forward, rotate degrees of freedom, and adjust their depth (**Figure 2.24 b**) [303]. In addition, some functional materials have been tried to drive soft robots based on electric or magnetic fields, and even chemical reactions. For example, electroactive polymers (EAP) have been widely used to design flexible actuators and soft robots (**Figure 2.24 c**) [304-309].
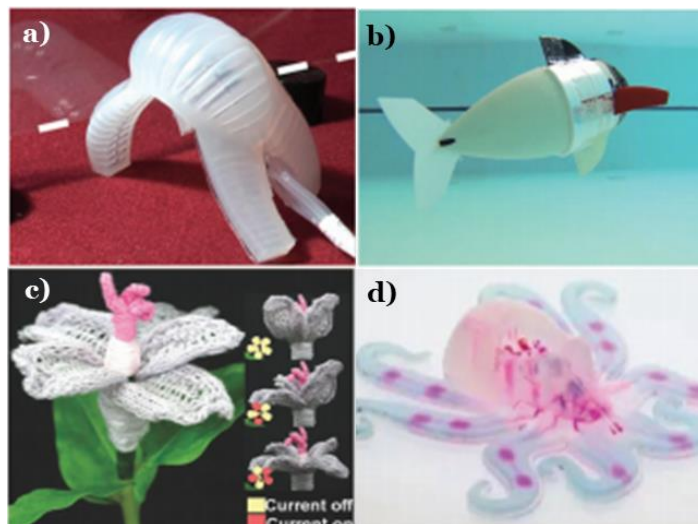
Figure 2.24: a) The multigait soft robot based on flexible pneumatic actuators [296]; **b)** The soft robotic fish with a large number of degrees of freedom [303]; **c)** SMA for driving soft robots [310]; **d)** A soft robot powered by chemical energy [71].

So far, researchers have developed many kinds of electroactive polymers (EAP), including dielectric elastomers, thermally stimulated liquid crystal elastomers [311], electrolytically active polymers [312], polyelectrolyte gels [313], and gel-metal composite materials [314]. For example, Hu et al. demonstrated a magneto-elastic soft millimetre-level robot that can navigate in the gastric phantom by jumping, rolling, climbing and landing to achieve targeted drug delivery and minimally invasive surgery [315]. Zhao et al. developed magnetically driven fast-transforming soft materials which have important application prospects in soft robotics [316]. Shape memory alloy (SMA) is another important material for manufacturing soft robots. Recently, fuel-powered artificial muscles have aroused great interest in the soft robotics community. In these studies, some materials were introduced to convert the chemical energy of the fuel into mechanical energy [70, 71, 317]. Nitinol is often used to design specific structures that drive soft robots and there are other soft materials that are more significant. Researchers have also designed semi-biological robots in combination with biological tissues, such as tissue engineering soft robot Ray [318] and tissue engineering jellyfish [319].

Our group developed a novel robotic surface consisting of 3D printed miniature groove structure and injected a stimuli-responsive hydrogel pattern (**Figure 2.25**), which is capable of switching between lipophilicity and oleophobic under certain stimuli [320]. Under swelling, the geometrical change of hydrogel will buckle the surface due to the structural confinement and create a continuous transition of surface topology. Thus, it will yield a

change on surface wetting property from oleophilic to super-oleophobic with a contact angle of oil of 85° to 165°. This morphing surface also holds its potential to be developed into an autonomous system for future sub-sea/offshore engineering applications to separate oil and water.
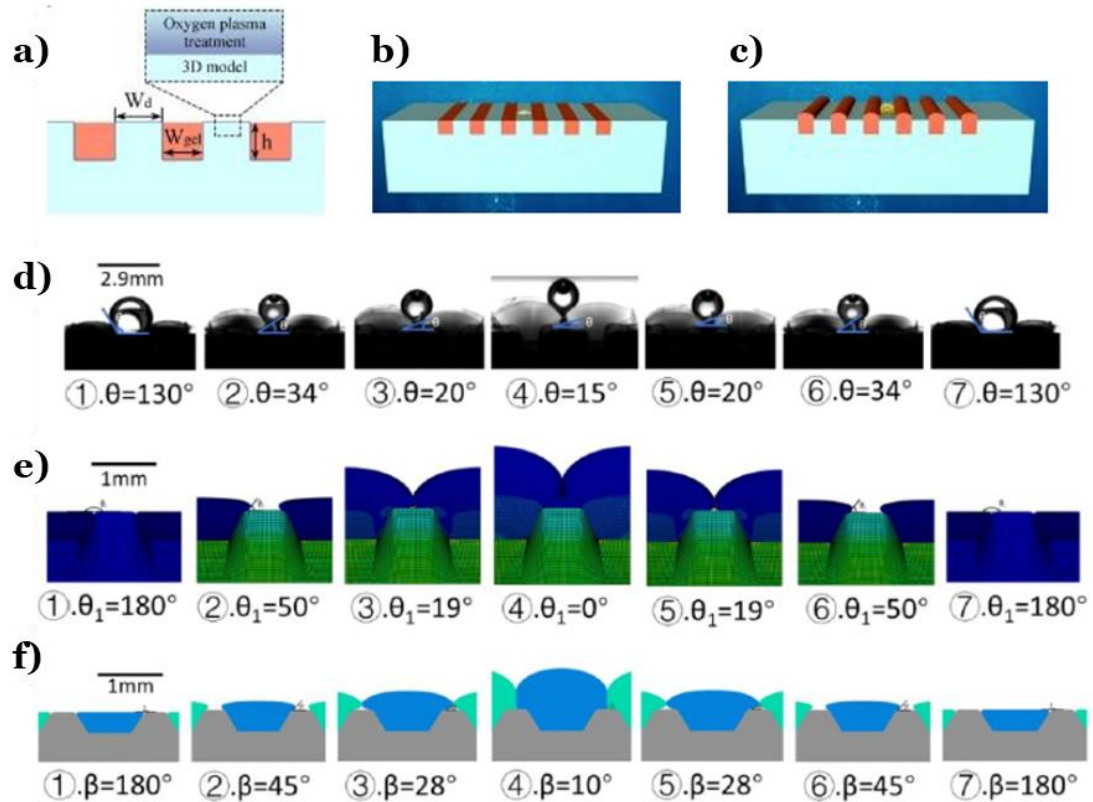
Figure 2.25: a) Geometrical definitions on the responsive gel/3D printed smart hybrid surface; **b)** Oil droplet on the hybrid surface and swelling induced surface transformation to **c)**; **d)** The experimental observation of reversible morphological change during hydrogel swelling/deswelling, θ is three phase contact angle (3D model, hydrogel and water), scale bar is 2.9mm; **e)** The simulation of the morphology change in hydrogel swelling, θ1 is three phase contact angle (3D model, hydrogel and water), scale bar is 1mm; **f)** The simulation of the morphology change in individual hydrogel swelling, β is three phase contact angle (3D model, hydrogel and water), scale bar is 1 mm [320].

2.6   Economic Impact and Research Statement

The world market size for Metal based additive manufacturing was over USD 345 Million in 2021 and is estimated to grow at over 21% CAGR between 2022 and 2030 [321], to the technological advancements in the medical industry which well spread in the developed and developing countries including the U.S., Canada, Germany, France, Italy, China, and India. Similar trend can be observed in automotive and aerospace industries, which was around USD 298 Million in 2021 and is projected to grow at a CAGR of 21.5% over the forecast period.

Why the global additive manufacturing market for bio-inspired structures have not been summarized yet, some figures can be collected from the global healthcare additive manufacturing market, which was estimated at US$ 1.35 billion in 2020 and is expected to hit around US$9.87 billion by 2030, poised to grow at a noteworthy CAGR of 22% from 2021 to 2030. The global soft robotics market size was also valued at $573.8 million in 2019, and is projected to reach $3.41 billion by 2027, registering a CAGR of 30.7% from 2020 to 2027.

Soft robotics is a specifically designed subfield of robots that offers reprogrammable, multi-functional, and versatile systems intelligently linking to the sensing action. The additive manufacturing can be more beneficial to the healthcare and soft robotic industrials by providing customized design and manufacturing, in a close relation to the material preparation and application

conditions. The economic impact will also include the save on the logistical cost of the manufacturing and deployment, and the life cycle cost of products.

In this research, we explore the 3D Printing Assisted Development of Bio-inspired Structure and Device for Advanced Engineering. The project was carried step-wisely to understand the micro-/nanofabrication of the materials and the optimization of the materials properties. The Polymer surface patterning and modification at the micro/nano scale has been firstly investigated. I propose a highly efficient fabricating strategy, to achieve a functional polymer surface, which has control over the surface roughness. The key development in this fabrication method is the polymer positive diffusion effect (PDE) for an ion-bombarded polymeric hybrid surface through focused ion beam (FIB) technology. The PDE is theoretically explored by introducing a positive diffusion term into the classic theory. The conductivity induced PDE constant is discussed as functions of substrates conductivity, ion energy and flux. The theoretical results agree well with the experiential results on the conductivity induced PDE, and thus yield good control over roughness and patterning milling depth on the fabricated surface. Moreover, we demonstrate a controllable surface wettability in hydrophobic and superhydrophobic surfaces (contact angles (CA) range from 108.3° to 150.8°) with different CA hysteresis values ranging from 31.4° to 8.3°. This study will effectively enrich our scope on the precision manufacturing on polymer substrates.

We next study the autonomous shape transformation with the expectation to develop high-performance soft robotics technology; the search

for pronounced actuation mechanisms is an ongoing mission. Here, I present the programmable shape morphing of a three-dimensional (3D) curved gel structure by harnessing multimode mechanical instabilities during free swelling. First of all, the coupling of buckling and creasing occurs at the dedicated region of the gel structure, which is attributed to the edge and surface instabilities resulted from structure-defined spatial nonuniformity of swelling. The subsequent developments of post-buckling morphologies and crease patterns collaboratively drive the structural transformation of the gel part from the "open" state to the "closed" state, thus realizing the function of gripping. By utilizing the multi-stimuli-responsive nature of the hydrogel, we recover the swollen gel structure to its initial state, enabling reproducible and cyclic shape evolution. The described soft gel structure capable of shape transformation brings a variety of advantages, such as easy to fabricate, large strain transformation, efficient actuation, and high strength-to-weight ratio, and is anticipated to provide guidance for future applications in soft robotics, flexible electronics, offshore engineering, and healthcare products.

I then design and develop a focal-length tunable intra-ocular lens (IOL) device via a standard-shaped, homogeneous "one material" system. Different to existing technologies, this poly(N-isopropylacrylamide) gel (PNIPAM) based polyelectrolyte system doesn't require any additional materials (e.g., metal electrodes, movable mechanical structures) to achieve a controllable lens shape transformation for the focal-length shifting actuation. The designed morphological deformation mechanism employs ionic-strength responsive

mechanical buckling via controlled swelling of PNIPAM in phosphate buffered saline (PBS) with similar concentration to human eye liquid. This unique approach will unlock great potential in a wide range of smart ocular applications.

To extend the theoretical understandings on the mechanics to form surface morphology, I carried a finite element study on the material's dynamic behaviour at different levels of conditions by a dynamic model. Analytical expressions of the material's behaviour (i.e., stable strain amplitude) as a function of in-plane compressive conditions is further derived. It is also found that the material's stable morphology can be guided by the surface micro-structure. The theoretical understanding will bridge the gap on understanding the guided formation of elastic instability on soft surface, thus will fulfil another dimension of control to generate ordered structure.

Chapter 3

Experimental Methods

This chapter summarises the general experimental methodologies used throughout the project, including the fabrication process for structures and the characterization method used for investigation.

3.1 Fabrication of Morphological Structure on a Polymeric Surface by FIB

This section is preparation of polymer and FIB processing that were used in **Chapter 4**.

Conductive polymer nanocomposites such as polystyrene–carbon nanoparticles (CNPs) were used to create the conductive polymer surfaces [149, 322-324]. The styrene-based precursor (PS, Veriflex®, CRG Co. Ltd., Miamisburg, OH, US) [322, 323] and the carbon NPs (VULCAN® XC72R, CABOT, Boston, MA, US), were ultrasonically agitated in a three-neck flask for 2 h at 1000 rpm [325]. Then the curing agent (Luperox ATC50, Sigma-Aldrich, St. Louis, MI, US) was added, and the mixture stirred for 45 min. Polystyrene–carbon nano-particles composite (CNP/PS) films with a thickness of 200 μm were made by casting the mixture into a PTFE mould and baking in a vacuum oven at 75 °C for 36 h.

Electrical conductivity is the inverse of resistivity. It represents the ability of a material to conduct electrical current. It can be divided into two types: bulk and surface. The dedicated conductivity testing needs four probe station so that the conductivity could be measured in a precision manner. Here, we simplified test structure as surface and measure the electrical conductivity by using an I-V testing set-up and thermo-electrical testing was performed through a Schlumberger Solartron 1250 Frequency Response Analyser from 20 to 100 °C in an isolated chamber with an ambiance of air [326].

A dual-beam FIB instrument shown in **Figure 3.1** (FEI Quanta3D FEG, Thermo Fisher Scientific, Waltham, MA, US) equipped with liquid gallium ion source (Ga+, 30 KeV) and Scanning electron microscopy (SEM) was used. The topographic surface was assessed with an atom force microscopy (AFM, Triboscope, Bruker, Coventry, UK). Sputter yield was calculated through Monte Carlo simulation (TRIDYN, binary collision approximation ion irradiation simulation) [196, 327], which simulates the ion irradiation of amorphous targets in the binary collision approximation. It allows for a dynamic rearrangement of the local composition of the target material [328].

Therefore, effects in high-fluence implantation, ion mixing, and preferential sputtering caused by atomic collision processes can be concluded [329]. Considering the current macromolecular-based hybrid system, an enthalpy of sublimation value (6.2 eV) was set in the simulation by consulting the chemically covalent bond energies and atom composition.
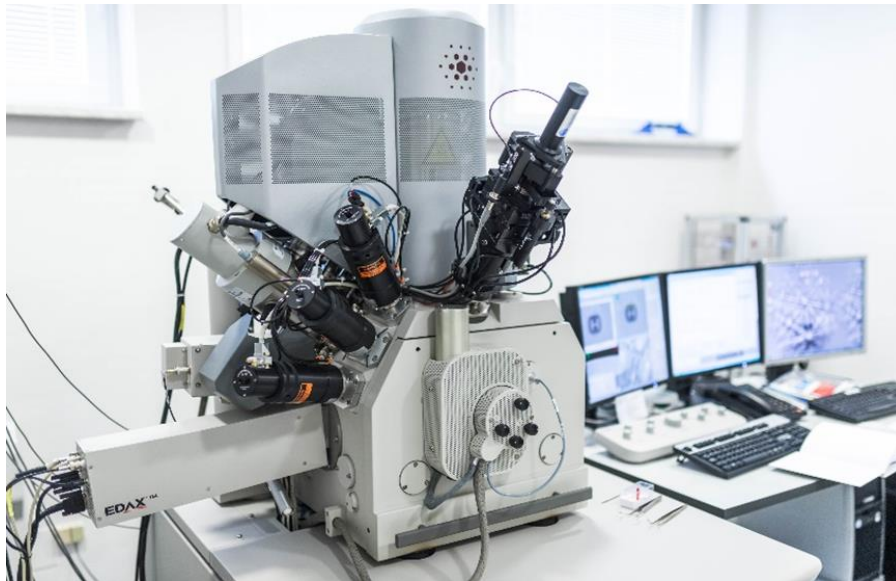
Figure 3.1: FEI Quanta 3D FEG FIB System, Thermo Fisher Scientific.

3.2 Design and Fabrication of 3D Printed Moulds and Hydrogel Structures

This section is 3D design and printing moulds, and hydrogel synthesis that were used in **Chapter 5 & 6**.

3.2.1 3D Printing Mould

Following the representative 3D printing process, I firstly design the IOL moulds via CAD software (Solidworks®, Dassault Systems). A set of hydrogels IOL moulds (**Figure 3.2**) were designed based on existing

commercial designs (**Figure 2.21**, Henan - Universe IOL Ltd.). All designs have the same parameters for the optical part: diameter 6 mm, central thickness 2.41 mm, R1 3.6 mm and R2 6 mm (**Figure 6.1 a**), which is 1:1 size of the commercial products. Design moulds show as **Figure 3.2 g-h** have been chosen for later optical test in **Chapter 6**.
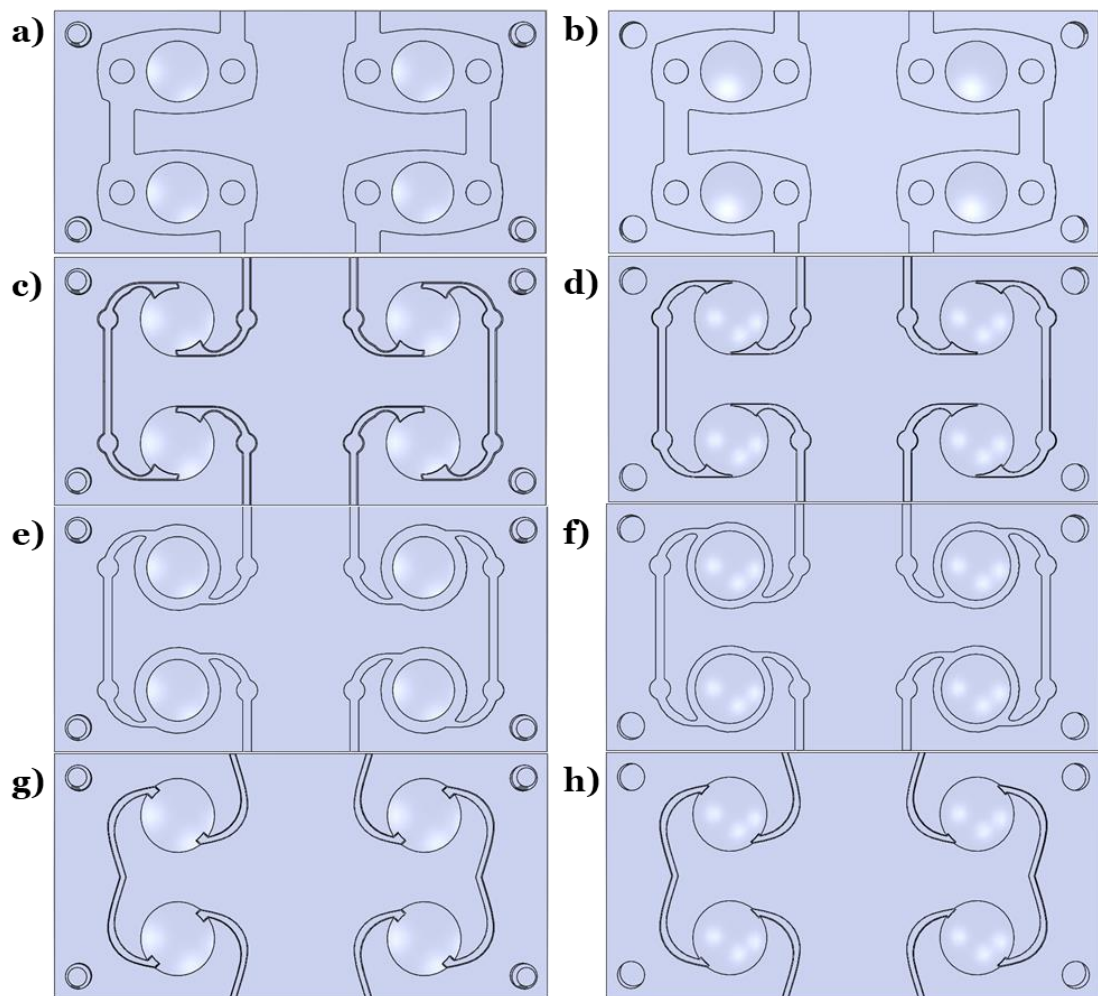
Figure 3.2: Schematics of IOL moulds designs based on commercial products (**Figure 2.21**): **a)** Design 1 cover part; **b)** Design 1 bottom part; **c)** Design 2 cover part; **d)** Design 2 bottom part; **e)** Design 3 cover part; **f)** Design 3 bottom part; **g)** Design 4 cover part; **h)** Design 4 bottom part.

The second part is to build the moulds by Solidworks and print them with Objet 30 (Stratasys, Ltd.) (**Figure 3.3 a**), with vender provided acrylate-based photopolymer (VerowhitePlus (VW), Stratasys). The illustration of PolyJet 3D printing is shown in **Figure 3.3 b**. Objet can print at 28 microns per layer but due to limitations of the printer the accuracy of the Objet is about 0.1 mm and hence the theoretical design change. The printed parts were cleaned and rinsed with isopropanol (IPA). The assembly of the gelation chamber was constructed by the printed parts and wax based sealants to prevent any possible leaking. The printed moulds were examined by Nikon LV100 optical microscopy system (**Figure 3.10 b**), in addition to surface roughness characterization using a stylus surface profiler (Bruker Dektek®, see **Chapter 3.3.6**). PAM gels were injected inside the 3D printed moulds and polymerized as **Chapter 3.2.2** [245, 254]. To test the full potential of the printer's precision I will design a 1mm thick slide with a range of different sized bars in width and in height to determine the best aspect ratios for the final design. Our printing jobs were manufactured by Objet 30, other than specially noted.
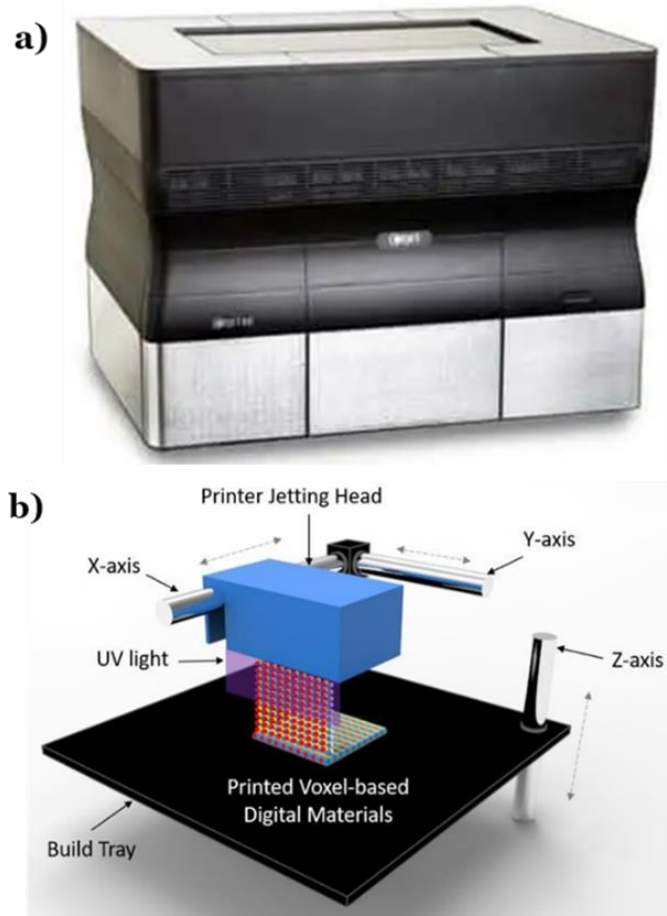
Figure 3.3: a) Objet 30 3D Printer (Stratasys, Ltd.); **b)** Illustration of PolyJet 3D printing. The printer jetting head moves along the x- and y-axis while printing a digital material on the build tray. The build tray moves up and down along the z-axis during printing. The printed each layer is cured by the UV ramps mounted on the printer head [330].

3.2.2 Hydrogels Synthesis

3. The gel solution procedure: the pre-gel solution from step 2 is mixed with 0.3 μL of N,N,N′,N′-tetramethylethylenediamine (TEMED) and 1 μL of ammonium persulfate solution (prepared solution in step 1). These two

solutions are added one by one and as soon as possible. After they are added, mix them in the container for 10 seconds.

4. gelation procedure: the ready solution from step 3 was rapidly injected into the 3D printing moulds. The moulds had been cleared by Isopropyl alcohol and Acetone before injecting. After 30 mins gelation process, the structures are ready to be released from moulds.

The procedures of hydrogels synthesis for IOLs are summarized in detail as following:

Step 1: The pre-solution is made by dissolving acrylamide (6g) in DI water, using a vortex mixer (Vortex-Genie SI-0146) to ensure complete dissolution (ensure solution reaches 20 ml by adjusting DI water volume). The solution is filtered by filters (Fisherbrand™ Sterile PES Syringe Filter), loaded into silanized glass vials and sealed for further use. (other chemicals have the same procedure but different gram: sodium acrylate (sodium) 4g in 20 ml solution; N,N'-Methylenebisacrylamide (BisAA) 0.4g in 20 ml solution; Ammonium persulfate (APS) 2g in 20 ml solution)

Step 2: gelation procedure: The pre-solutions will be mixed by following the receipt in Table 3.1, and then dilute the solution to 197.7 μL with DI water. Vortex mixer used to ensure complete mixture as well. Then mix the solution with 0.3 μL of N,N,N′,N′-tetramethylethylenediamine (TEMED) and 1 μL of ammonium persulfate solution (prepared solution in step 1). These two

solutions are added one by one and as soon as possible. After they are added, mix them in the container for 10 seconds. Then the ready solution was rapidly injected into the 3D printing moulds. The moulds had been cleared by Isopropyl alcohol and Acetone before injecting. After 30 mins gelation process, structures are ready to be released from moulds.

Table 3.1: Hydrogel Formulations.

Chemicals names (short name) & Concentrations	Volume in 200 μl mix solution (μl)		
	Hydrogel 1	Hydrogel 2	Hydrogel 3
Acrylamide pre-solution (0.3 g/mL)	55.61	55.61	55.61
Sodium acrylate (Sodium) pre-solution (0.2 g/mL)	0	15.856	0
N,N'-Methylenebisacrylamide (BisAA) pre-solution (0.02 g/mL)	41.6	41.6	83.2
DI water	100.49	84.6	58.89
N,N,N',N'-Tetramethylethylenediamine (TEMED)	0.3	0.3	0.3
Ammonium persulfate (APS) pre-solution (0.1 g/mL)	2	2	2

There are three types of hydrogels (**Table 3.1**) which have been tested for swelling ration (**Figure 3.4**) and hydrogel 1 chosen for the later experiments.
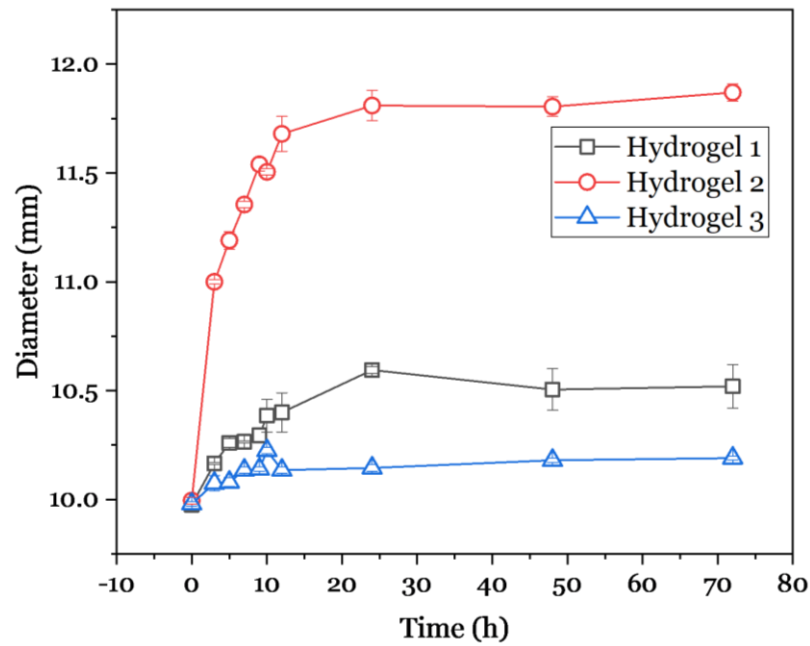
Figure 3.4: Swelling ration in DI water of three types of hydrogels.

We also designed a soft gel gripper (please see design route in **Chapter 3.2.3**). The polyacrylamide hydrogel was synthesized by free-radical polymerization using ammonium persulfate as an initiator. 1 mL aqueous pre-gel solution containing 1173.3 mM acrylamide (monomer), 168.6 mM sodium acrylate (NaAc, charged monomer) and 6.8 mM N,N′-methylenebisacrylamide (BisAA, crosslinker) was prepared, and degassed under 1 mTorr for 10 min after mixing and dissolving sufficiently. After that, this pre-gel solution was mixed with 1.5 μL of N,N,N′,N′-tetramethylethylenediamine (TEMED, accelerator) and 5 μL of a 10 g/ml aqueous ammonium persulfate solution (APS) and then it was rapidly loaded into the 3D printing mould. The mould had been treated by 1H,1H,2H,2H-perfluorooctyltrichlorosilane from the

vapour-phase at room temperature (23 °C) for 2 hours to facilitate the release of the hydrogel structure after 30 min gelation process. All chemicals were used as received from (Sigma Aldrich).

3.2.3 3D Design of 3D Printing Mould for IOL and Soft Gel Gripper

IOL moulds (used in **Chapter 6**)

At beginning, the contact lens is imitated to design the mould as in **Figure 3.5 a**, but due to the fact that the material is hydrogel and the lens designed thickness is 0.04 – 0.2 mm, the lens is hard to take out. Consider the IOL design. The side struts are added to the contact lens design as in **Figure 3.5 b**. The connection between optical lens part and side struts is weak, easy to be broken. Then the final design has been devised as in **Figure 3.5 c**. The imitate human lens with the optical part design as a convex lens with double curve surface is imitated and the side struts can hold the position in the eye.
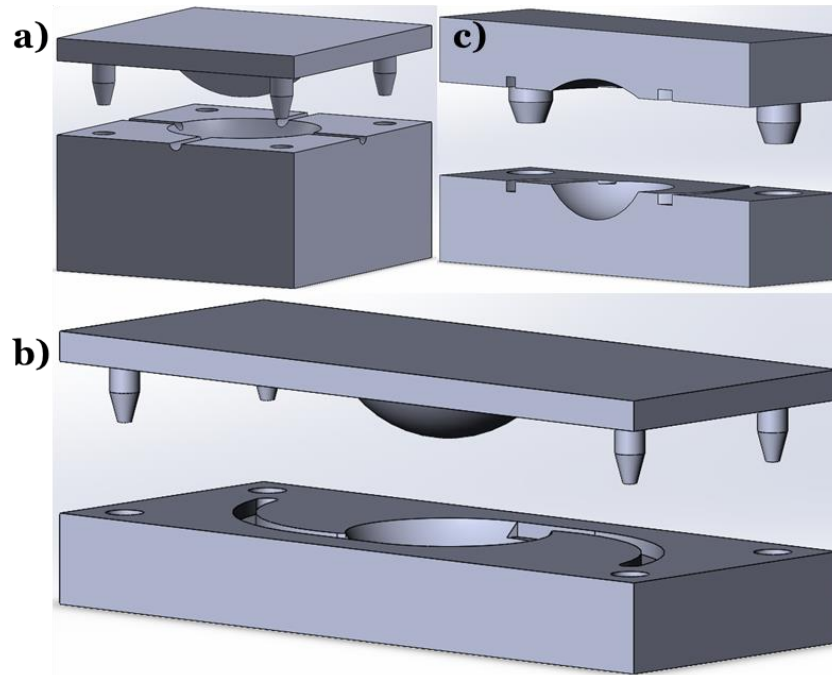
Figure 3.5: IOL 3D design mould: **a)** Imitate contact lens design; **b)** Imitate contact lens design with side struts; **c)** Imitate human lens design with side struts.

Gel gripper moulds (used in **Chapter 5**)

To develop a soft gripper, a few designs have been developed as in **Figure 3.6**. After the test with **Figure 3.6 b**, it is much harder to manufacture as high quality as in **Figure 3.6 a**, so **Figure 3.6 c** has been designed as a flower which can work like a gripper, and it comes from the basic design shown in **Figure 3.6 a.** Also, like **Figure 3.6 d**, the cylinder is designed to compare the results with sphere designs.
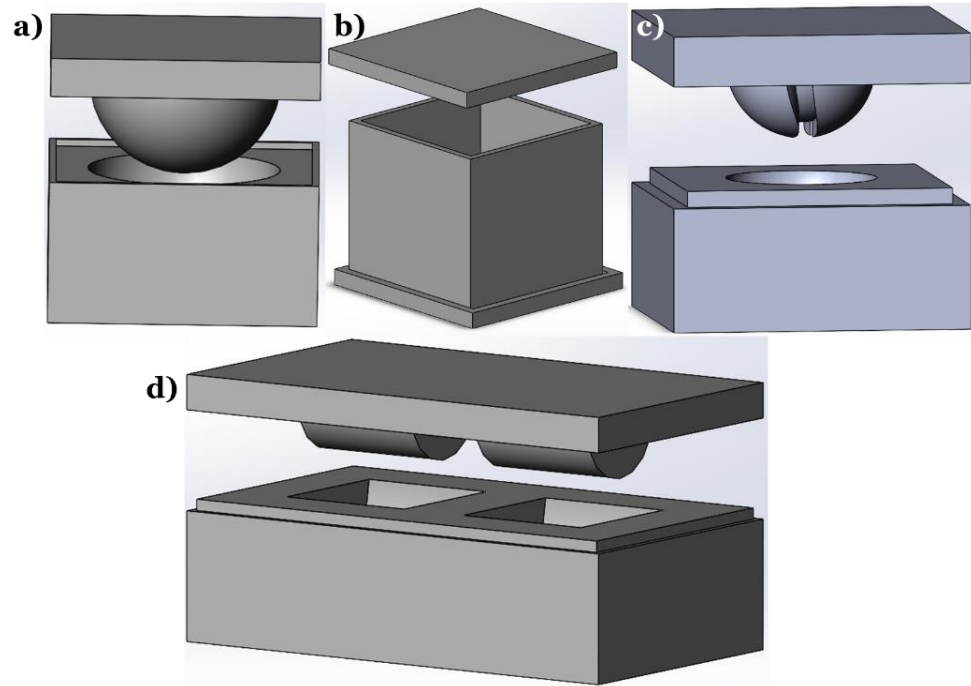
Figure 3.6: 3D designs of soft gel gripper: **a)** Hemi-spherical shell structure mould; **b)** Cube shell structure mould; **c)** Flat finger structure mould; **d)** Hemi-cylinder shell structure mould.

3.3   Characterization Method

This section is characterization methods that were used in **Chapter 6**.

3.3.1   Droplet Shaping Analysis (DSA)

The change of the focal length of the IOL is related to the values of R1, R2, x, and d. According to formula 123, the focal length can be calculated by all these four values. DSA (**Figure 3.7**) is used to measure the deformation of the IOL samples during the swelling. Based on the size of the reference needle,

ImageJ can be used to measure the above four values. Use these values to verify the change of IOL focal length.

Figure 3.7: Drop Shape Analyzer, DSA30S, Kruss.

3.3.2 Sample Preparation and Characterization with Scanning Electron Microscopy (SEM)

The sample preparation is very important to acquire ideal Scanning Electron Microscopy (SEM) results. First, moulds were printed, and intensive cleaned, to be used to synthesize IOLs. After manufacturing, all IOLs are placed in PBS (Sigma-Aldrich) solution (0.01M) to simulate the storage of

products before use. Then eight kinds of calcium solutions (0.05mM, 0.1mM, 0.5mM, 0.8mM, 1mM, 1.5mM, 2,5mM) are prepared and the actual concentration of normal human body is about 0.5mM [331]. Place IOLs that have been simulated and store them in these calcium solutions. There will then be two groups of calcium solutions (both groups contain all 8 concentrations), one is placed at room temperature, and the other is placed in an Incubator (Heratherm Incubator IMC 18, Thermo Fisher Scientific, USA). The temperature is set to 37°C to imitate the temperature of the human body.

The sample placed in the calcium solution will not be returned to the solution after being taken out for observation. The samples soaked in the calcium solution will last for 3 days, 7 days, 10 days. 15 days, 20 days, and 30 days. They will then be taken out the samples for follow-up observation. One group of IOLs will be characterized without the calcium solution process, as a reference group. The IOLs will be taken out to observe their calcium deposition. Before observation, samples will be frozen dry for 24 hours. During the freeze dry process, the samples are immersed in liquid nitrogen and placed in the Freeze Dryer (Freeze Dryer Alpha 2-4 LDplus, Martin Christ Gefriertrocknungsanlagen GmbH, **Figure 3.8 a**) for 24 hours. After the freeze dry is completed, SEM (TESCAN MIRA3, **Figure 3.8 b**) is used to observe the calcium deposition on the surface and cross-section of the samples. The EDS module (Oxford X-Max detector 51-XMX1028, **Figure 3.8 b**) marks carbon (red, hydrogel) and calcium (green, calcium deposits) on SEM Figures. From the colour distribution, the calcium deposition can be drawn.
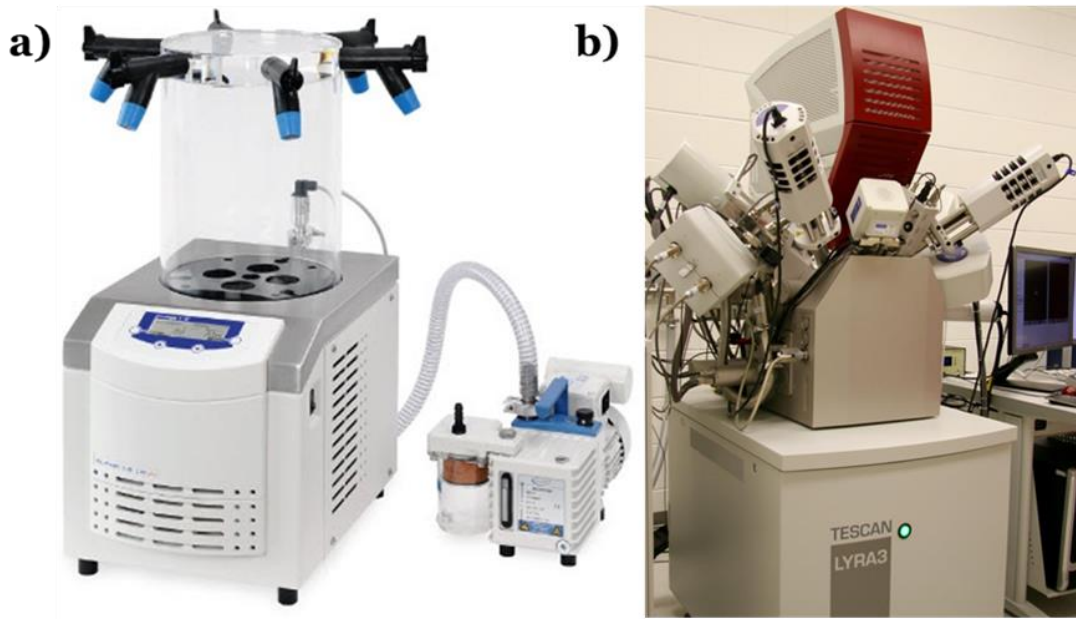
Figure 3.8: The photos for **a)** Freeze Dryer Alpha 2-4 LD plus; **b)** SEM, MIRA3.

3.3.3 Optical Test

The change of IOL focal length can be calculated based on the data from DSA measurement. This chapter introduces the focal length obtained after optical testing, which is mutually confirmed with the calculated focal length to verify the change of IOL focal length.

According to the lens imaging principle, when the image distance is between one- and two-times focal length, the object distance is greater than twice the focal length. Based on the pre-test, the image distance is fixed to 10.9mm. A clear image is obtained by adjusting the object distance. CMOS

sensor camera (DCC1645C, Thorlabs, USA, **Figure 3.9 a**) is used to take

figures (**Figure 6.3 a**). Above the camera is a 3D printed holder to hold the

position of the IOL samples. The camera and holder are placed on a jack table.

Above the camera and holder is an optical test target (Negative 1951 USAF Test

Target, **Figure 3.9 b**). The target is fixed, the object distance adjusted by

adjusting the jack table and object distance is marked with a ruler.
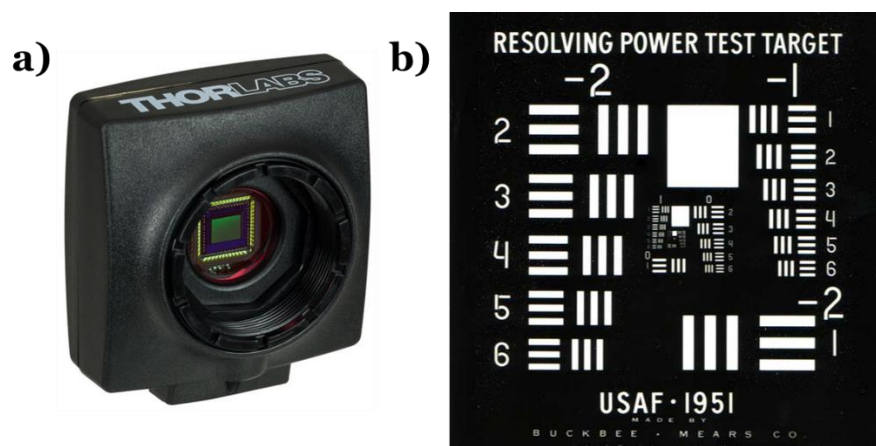
Figure 3.9: a) Optical Test Camera DCC1645C, Thorlabs, USA; **b)** Negative 1951 USAF Test Target.

3.3.4   Atom Force Microscopy (AFM)

Atom force microscopy (D3100, Veeco, **Figure 3.10**) was used to

characterize the surface of materials and 3D printed parts in this project. The

sample surface was cleaned using the IPA and dried in the open air. The

scanning speed was varied depending on the samples, but normally it would

be in tapping mode.
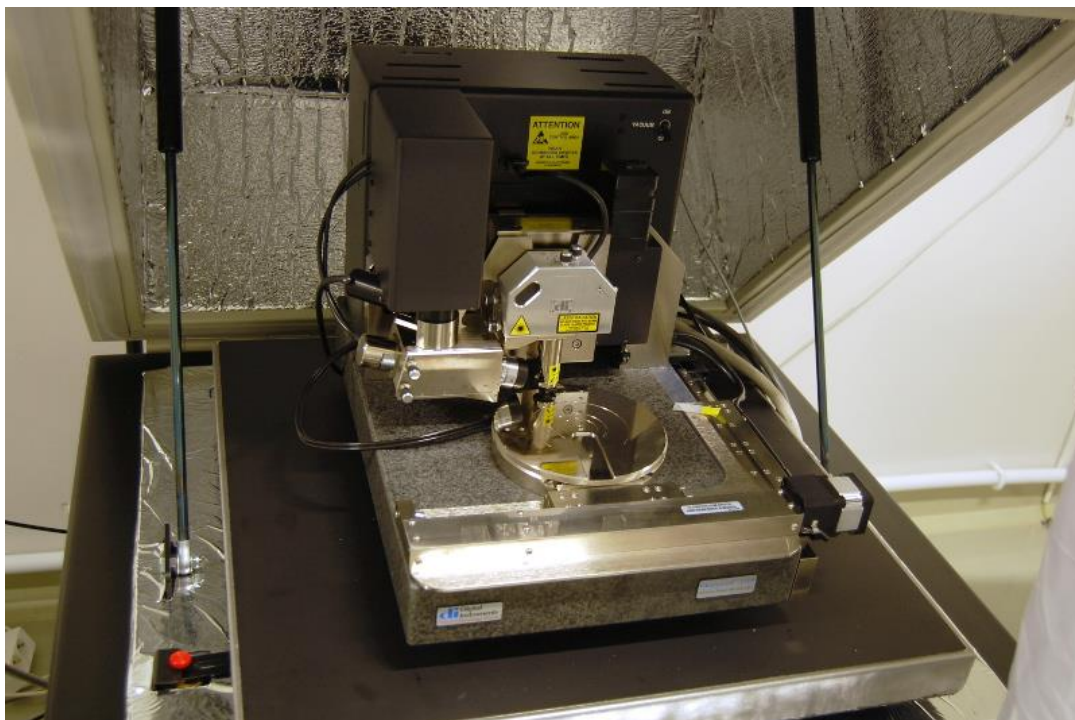
Figure 3.10: Atom force microscopy (D3100, Veeco).

3.3.5 Optical Microscope & Laser Scanning Confocal Fluorescence Microscope (LSCM)

To monitor the formation and evolution of surface/structure morphologies, a trace amount of Rhodamine-B monomer (**Figure 3.11 a**) was added into the pre-gel solution to enhance the visual contrast and allow the high-resolution imaging with a camera. The as-fabricated hydrogel was submerged into DI water to swell. During the swelling process, the hydrogel was gently taken out from DI water to be observed under an optical microscope (Nikon LV100, **Figure 3.11 b**) at regular time intervals. A small amount of fluorescein isothiocyanate-dextran (~1 mg) was added into the pre-gel mixture

to label the gel part and facilitate imaging under a laser scanning confocal fluorescence microscope (LSCM, Nikon A1R, **Figure 3.11 c**).
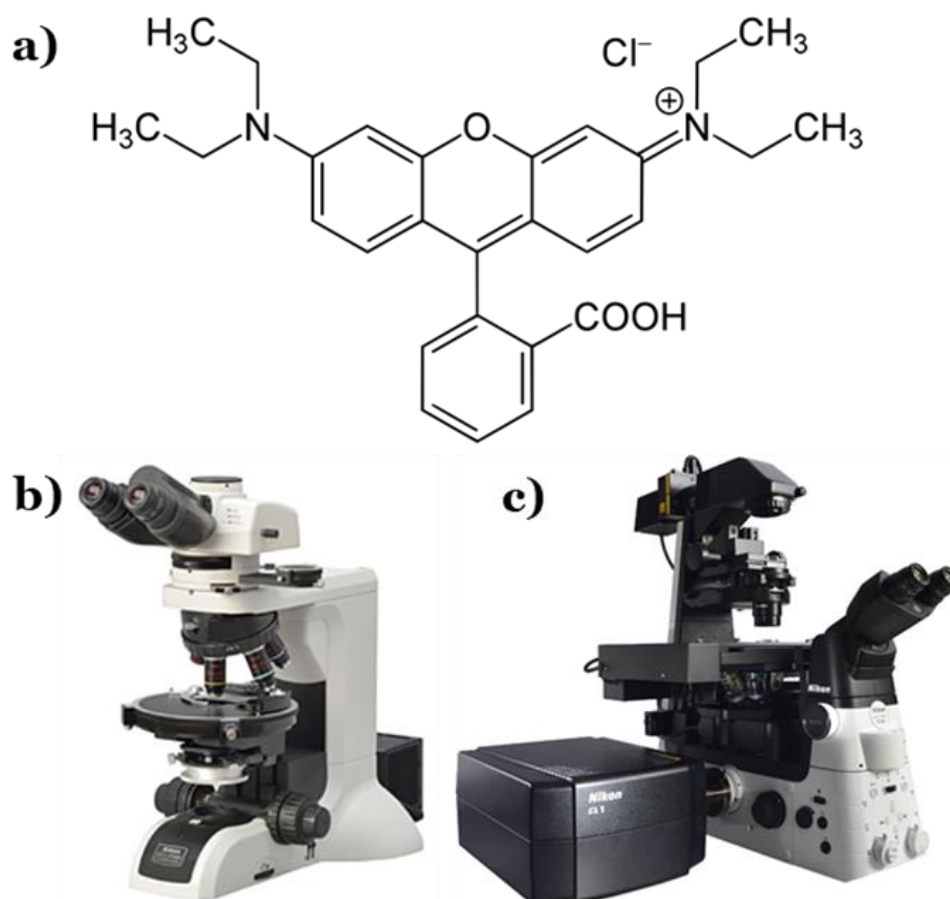
Figure 3.11: a) Rhodamine-B Chemical Formula; **b)** Nikon Upright Microscopes Eclipse LV100ND; **c)** Nikon Confocal Microscopes A1R.

3.3.6   Optical Profile Observation

The Bruker ContourGT (**Figure 3.12 a**) and Alicona Infinite Focus (**Figure 3.12 b**) machines are very similar as they both send a light source down upon a part where the light gets reflected back and thus allows it to

analyse the surfaces at high level of detail and plot the data as a 3D drawing on a screen. However, the Bruker is a better-quality machine and allows a closer look at small parts in a lot more detail in a single spot. The Alicona is similar and can still provide sufficient amount of detail at nanoscale and can also set the light source to move along a surface instead of a single point, so it is good for analysing large objects. From both machines you can collect all data points and make graphs and 3D images for further analysing.
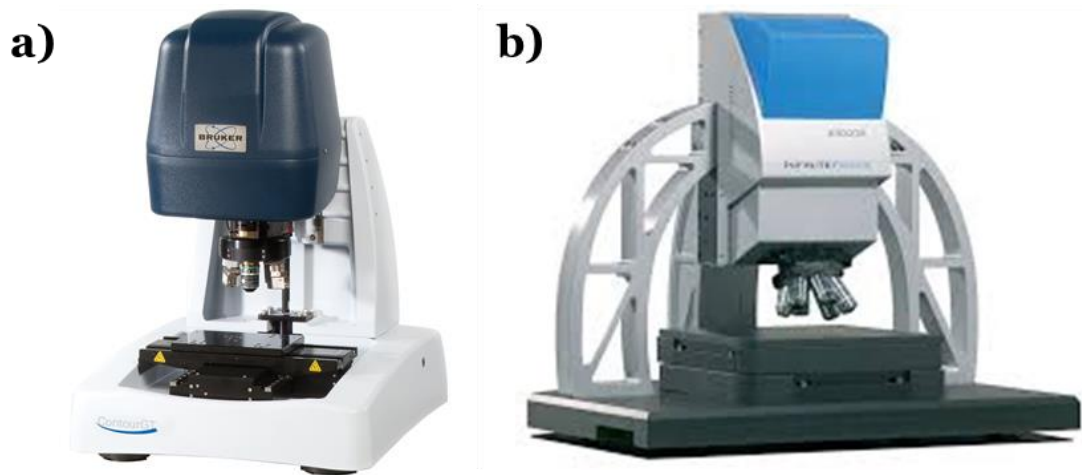
Figure 3.12: a) Bruker Contorti and **b)** Alicona Infinite focus.

Chapter 4

Spatially Engraving Morphological Structure on Polymeric Surface by Ion Beam Milling

The surface engineering techniques for polymers has yielded various methods from lithography and plasma and UVO to thin film deposition on polymers. While the above approaches have been proven effective to some extent to create variety of patterns, such as dots, network structures, complex hierarchically assembled patterns, honeycomb-like structures and ring-like patterns on the surface of polymers, there are bottleneck to be overcome such as the manufacturing precision and efficiency. By far, Focused ion beam (FIB) can only be applied to manufacture on conductive surface, due to insufficient conductivity of the polymer surface, this high precision method is hard to be used on polymer surface. To extend the capabilities of this technique, we have to develop the advanced understanding on the relationship between conductivity and surface pattern accuracy on the surface of conductive polymers. The area exposed to the ion beam can be selected by controlling the relative movement of the ion beam and polymeric substrate, or for applications that need very precise control over the exposed area by maskless patterning method. This approach will benchmark my exploration of advanced manufacturing technology and support the following study on choosing the proper techniques to fabricate the bio-inspired structure.

4.1   Introduction

Surface patterning and modification at micro-/nano-scales have been of great importance in creating functional surfaces for a wide range of applications, such as water repelling and self-cleaning [332-335], antifouling [336], anti-icing [337], adhesion control, and drag reduction technologies [338, 339]. To create surfaces with desired roughness and topography, some techniques have been commonly used. These include lithography-based plasma etching and deposition, coating on top of patterned substrates, and/or soft-lithography pattern transferring, and, more recently, creating stimuli-responsive surface cracking, wrinkling [252, 340-343] and other deformations on smart material surfaces [344-346].

The focused ion beam (FIB) technique, with its unique capability for rapid prototyping and high precision [347, 348], has proven its efficiency in manufacturing semiconductors, metals and metal oxides. The fundamental mechanism of FIB is that highly energetic ions driven by an electrical field knock atoms off the material surface by electro-collision and the recoil action between the ion and target material surface (**Figure 4.1**). For ion-milled surfaces, the morphological evolution can cause kinetic roughness, which has attracted increasing research interest in recent decades [349-351].
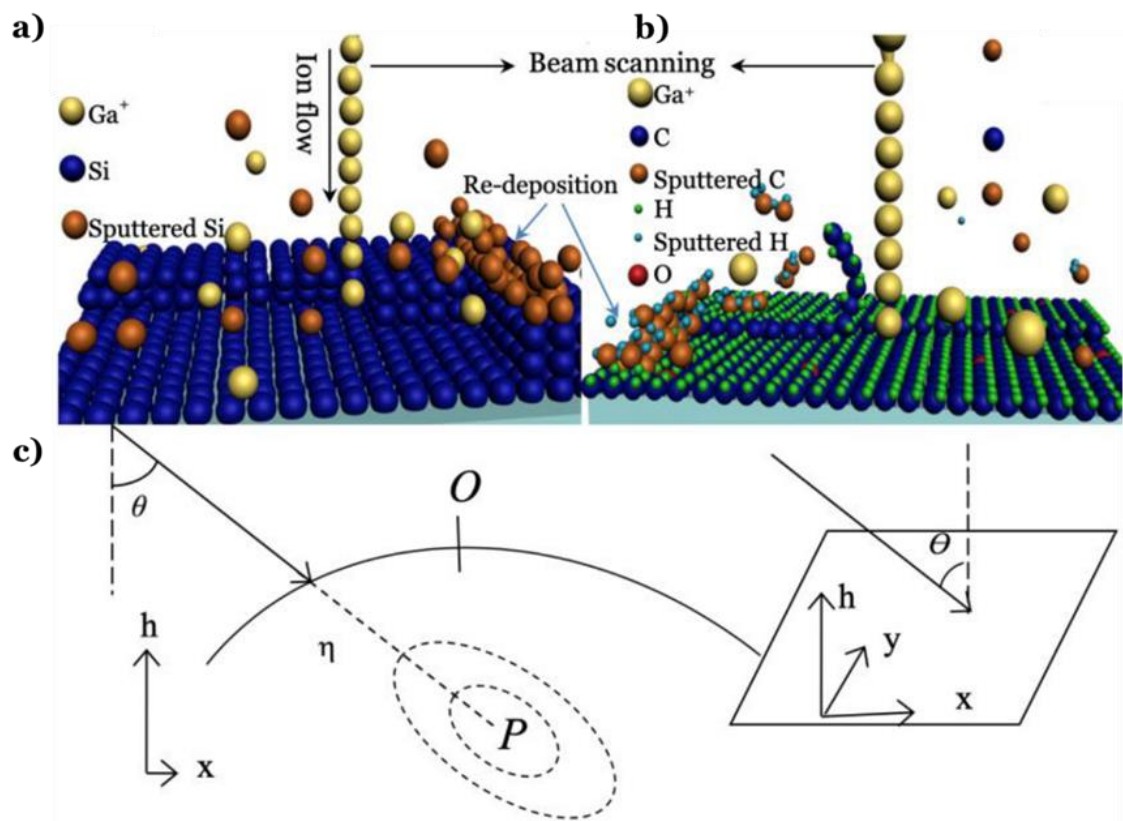
Figure 4.1: Schematics of focused ion beam (FIB) milling on **a)** silicon and **b)** conductive polymeric hybrid surface; **c)** Following a straight trajectory (solid line), the ion penetrates an average distance α inside the solid (dashed line) and completely releases its kinetic energy at P. The dotted equal energy contours indicate the energy decreasing area around point P. The energy released at point P contributes to erosion at O. The inset shows the laboratory coordinate frame: the ion beam forms an angle θ with the normal to the average surface orientation, z, and the in-plane direction x is chosen along the projection of the ion beam.

However, limited attempts have been reported on the topic of FIB processing on polymeric substrates since the charging effect from the insulated polymer matrix significantly reduces manufacturing precision, and the

understanding of the morphological evolution for an ion-milled polymer surface remains yet to be fully explored [352-355]. Compared to other surface morphology modification techniques, the FIB method has great potential for scalable patterning with both roughness level and geometry size ranging from a few nanometres to 10 μm.

4.2   Theoretical Background

As shown in **Figure 4.1**, ion bombardment is commonly considered as an atomic process taking place inside the bombarded material within a finite penetration depth. The electrically manipulated ions pass through a distance *a* before they completely release their kinetic energy with a spatial distribution inside the target substrates. An ion releasing its energy at point P in the solid contributes energy to the surface point *O* that may induce the atoms in *O* to break their bonds and leave the surface or diffuse along it. The pattern formation by ion beam sputtering has been previously understood as the interplay between the unstable dependence of the sputtering yield on surface curvature and stabilizing surface relaxation mechanisms [356, 357]. The most successful model to predict surface evolution under ion sputtering was the Bradley and Harper (BH) equation [358]. BH theory describes the ripple formation by discussing the surface topography *h (x, y, t)*, measured from an initial smooth configuration in the *(x, y)* plane. However, it does not explain the surface roughening well [359-361]. Therefore, Makeev, Barabási and Cuerno [362] refined the noisy Kuramoto-Sivashinsky (KS) equation [363, 364]

based on the Sigmund theory of sputter erosion [183], where surface material was bombarded by ions, and included the Kardar-Parisi-Zhang (KPZ) nonlinear term to the BH equation. Cuerno et al. [356, 365, 366] further developed the equation as:

$$\frac{\partial h}{\partial t} = -v\nabla^2 h + \lambda_1(\nabla h)^2 - \lambda_2\nabla^2(\nabla h)^2 - K\nabla^4 h, \qquad \textbf{Equation 4.1}$$

where v, λ_1 and λ_2 are the average coefficients determined by the experimental parameters such as ion flux, ion energy, etc. For an amorphous solid in equilibrium with its vapor, the $K\nabla^4 h$ (known as MBE equation) [367] has been studied and obtained [368, 369]. **Equation 4.1** was originally used to describe the dynamic scaling on the surface under the thermal surface diffusion. Here, the conditional surface diffusion factor, K, can be decomposed with conductive induced PDE constant, D^c [368, 370]:

$$K = \frac{D^c \beta \Omega^2 M_{con}}{k_b T} \exp\left(\frac{-\Delta E}{k_b T}\right), \qquad \textbf{Equation 4.2}$$

Where β is the surface free energy per unit, Ω represents the atomic volume, M_{con} denotes the number density of conductive particles, k_b is the Boltzmann constant, and T is the absolute temperature, ΔE is the activation energy for surface diffusion. The value of D^c could be determined by the evolved Nernst–Einstein equation [371, 372]:

$$D^c \equiv \frac{\sigma_{dc} k_b T}{e^2 M_{con}} \qquad \textbf{Equation 4.3}$$

Here σ_{dc} represents the DC conductivity of sample, e is the elementary charge. To simplify the discussion, the symmetric case ($\delta = u$, which are the distribution distances in directions parallel and perpendicular along beam) was applied to the current model, and the incident angle θ is zero. The linear wavelength instability could be calculated as [364]:

$$l_i = 2\pi\left(\frac{2K}{v}\right)^{1/2} \qquad \textbf{Equation 4.4}$$

Which correlated to ion flux and matrix conductivity, and i refers to the direction (x or y). With small incidence angle $= \frac{-(Fa)}{2\delta}$, which is negative, and $F \equiv (\frac{\epsilon Jp}{\sqrt{2\pi}})\exp\left(-\frac{a^2}{2\delta^2}\right)$ [200, 373], where J means the average ion flux, ϵ denote the total energy carried by the ion and p is a proportionality constant between power deposition and rate of erosion. By considering the conductivity induced ion diffusion by **Equation 4.2** and **4.3**, **Equation 4.1** the surface roughening caused by PDE could be described.

The surface roughness evolution could be predicted from the following equation [356]:

$$\tau = v\lambda_2/(K\lambda_1) \qquad \textbf{Equation 4.5}$$

Equation 4.5 has been applied at different experimental conditions [374, 375].

We have recently demonstrated carbon-based polymer composites with exciting properties induced by the enhanced electrical conductivity [130, 376]. In this project, polymer composites with tuneable electrical conductivities will be selected for comparative study of FIB induced polymer surface evolution. We describe an advanced FIB polymer surface patterning technology at micro/nano scale enabled by overcoming the challenge from the dielectric surface charging effect. A new concept of conductivity induced PDE is proposed to understand ion impacting on a conductive polymer surface and predict the surface evolution during FIB. The ion bombarded surface topographic features with conductivity induced PDE are theoretically predicted using Monte Carlo simulation, and also experimentally assessed. The emerging application of fabricated surface is explored with surface wetting control. We expect that the findings in this work will advance the current understanding on the FIB fabrication on a polymer surface.

4.3   Results and Discussion

Figure 4.2 a illustrates the conductive hybrids, based on the SEM fracture surface morphologies for 2 vol.% CNP/PS. The background SEM showed that the CNPs were distributed uniformly throughout the textured polymer matrix. **Figure 4.2 b** presents the DC conductivity results with little variations as a function of CNP concentrations at room temperature. When CNP concentrations (φ_{CNP}) increased from 0.5 to 2 vol.%, the conductivity dramatically increased from 1×10^{-8} to 100 s/m, and this increment slowed

down when the CNP concentration exceeded 2 vol.%. The conductivity for φ_{CNP} > 2 vol.% was sufficient to enter the general semiconductor region. The preparation process of the polymer is detailed in **Chapter 3.1**.

Most polymers are electrically insulating, the addition of conductive fillers has been proved as an effective means to improve their conductivity [377, 378]. While the conductive particles are usually randomly distributed in the insulating matrix, the initiation of conductive pathway will allow the entire composite to reach the conducting state [378]. This kind conductive polymer composites have a feature that its electrical conductivity increases nonlinearly with the increase of the volume fraction of conductive filler particles. When the volume fraction of conductive particles increases to a critical value, the electrical conductivity increases suddenly; then, the volume fraction of conductive particles keeps increasing, the conductivity decreases slowly. This phenomenon is defined as electrical percolation phenomenon, where the corresponding critical value of conductive particles volume fraction is defined as a percolation threshold [379]. A critical parameter of percolation model is to determine the sharp transition of the system upon the formation of conductive pathway/network structure. Percolation theory has been widely applied to describe/predict the electrical behaviour of polymer-based composite.
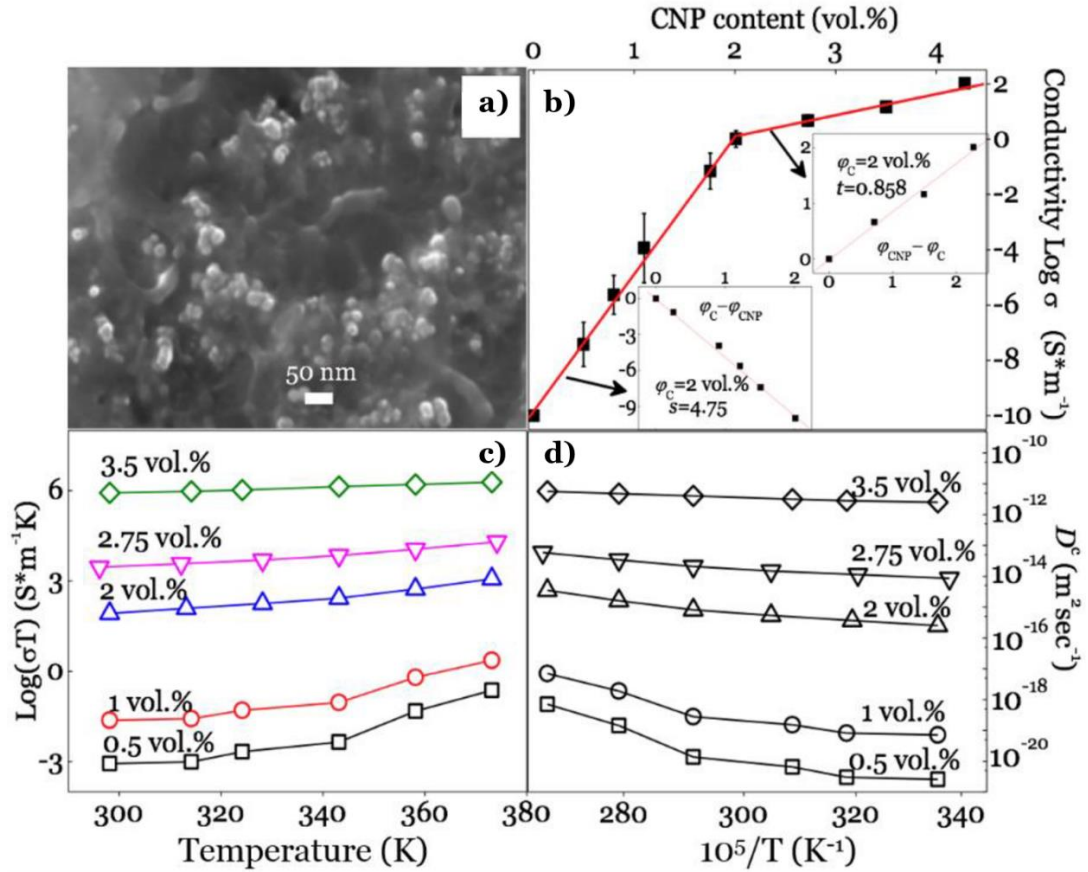
Figure 4.2: a) Scanning electron microscopy (SEM) observation of the conductive surface for 2 vol.% CNP/PS; **b)** DC conductivity results as a function of CNP content and the inset linear fitting curves needed for determining the threshold value; **c)** DC conductivity for composites with dependency on temperature and CNP concentration; **d)** calculated conductivity diffusion coefficients as a function of temperature.

Such a percolation network has been well understood as a polymer-based inorganic (σ_1)–organic (σ_2, $\sigma_2 << \sigma_1$) conducting system, or resistors and capacitors [199, 380, 381]. At a lower CNP concentration, conduction is mainly dominated by conduction among the nanofillers, thus appearing closer

to the insulator [380, 381]. They became conductors when the filler concentration increased to a critical value, i.e., the percolation threshold (φ_C), which formed the electron bridge within the substrate by the filler state [382]. To determine φ_C, the conductivity σ was fitted based on the power laws [380, 383]:

$$\sigma(\varphi_{\text{CNP}}) \propto (\varphi_C - \varphi_{\text{CNP}})^{-s} \text{ when } \varphi_{CNP} < \varphi_C \qquad \textbf{Equation 4.6}$$

$$\sigma(\varphi_{\text{CNP}}) \propto (\varphi_{\text{CNP}} - \varphi_C)^{t} \text{ when } \varphi_{CNP} > \varphi_C \qquad \textbf{Equation 4.7}$$

where t and s are the critical exponents in the conducting and insulating regions. The linear-fitting results clearly defined the threshold network with φ_C = 2 vol.%, t = 0.858, and s = 4.75 (the inset in **Figure 4.2 b**). Previous reports [197, 384] noted that a higher critical value (t > 2) in a polymer/CNP system will reduce the conductive efficiency , whereas, a good conductive efficiency (t = 0.858) was achieved due to the uniform nanofiller distribution by the adopted techniques.

The conductivity–temperature relationship is shown in **Figure 4.2 c**, where the measured conductivity gradually increased with the rising temperature, which enhanced the conductivity in composites [194]. The sample conductivity for 2 vol.% CNP/PS approached the percolation limit of an insulator-dominating state, and further rises in temperature significantly increased the conductivity. When the CNP content was above φ_C, the CNP particles/clusters were more likely to link with each other, forming a

continuously distributed CNP network in the matrix. **Figure 4.2 d** summarizes the calculated conductivity diffusion coefficients with dependency on temperature. For the composites that hadn't formed the threshold network, the diffusion coefficients were low, and the value was located in the ion diffusion range inside of the insulated solid ($<10^{-18}$ m²/sec) [385]. With the CNP content increased, the PDE constant significantly increased from 10^{-21} to 10^{-11}. It should be noted that the diffusion constant for an ion-liquid system is $10^{-11} - 10^{-9}$ m²/sec [385]. This conductive network, which was generated by adding CNP, enhanced the overall ion diffusion capability dramatically. It can be seen from the information in **Figure 4.2 c**, **d**, that the thermal effect on sample conductivity, or D^C, which caused a changing factor of $10-100$, is negligible when comparing with the large improvement caused by increasing conductivity.

Since all coefficients in **Equation 4.1** are determined by ion flux and K, the coefficient K can be calculated with D^C (in **Figure 4.2 d**) by **Equation 4.2** and **4.3**. We next investigate the influence from material with a fixed ion flux $\emptyset = 1.2 \times 10^9$ ions/(µm²/sec). With the Monte Carlo algorithm it could be obtained that $v = 187$ nm²/min, $\lambda_1 = 78.4$ nm/min, $\lambda_2 = 4373.2$ nm³/min. The simulated roughness τ is displayed in **Figure 4.3 a−c**, compared with the experimental AFM plots. The quantitative agreement in the order of magnitude between the experimental and the theoretical results was found for predicting the surface evolution trend, and the surface roughness decreased constantly with the CNP content increases. The experimental values were only

half of the theoretical values for 1 vol.% and 2 vol.% CNP/PS composites. For 3.5 vol.% CNP/PS, the magnitude of the experimental result agreed well with theory. This could be attributed to the metallic type of surface morphological evolution occurring during ion milling on the samples with high conductivity. Furthermore, the asymptotic morphologies revealed the increasing l_i values as well as the reduction of τ with the target conductivity increases. This implies that a higher self-smoothing effect and a thermal relaxation mechanism led to a less defined pattern order for the hybrids. The discrepancy between the experimental data and theoretical prediction can be explained by ignoring the rapid temperature rises during ion sputter, which induces a thermal diffusion.
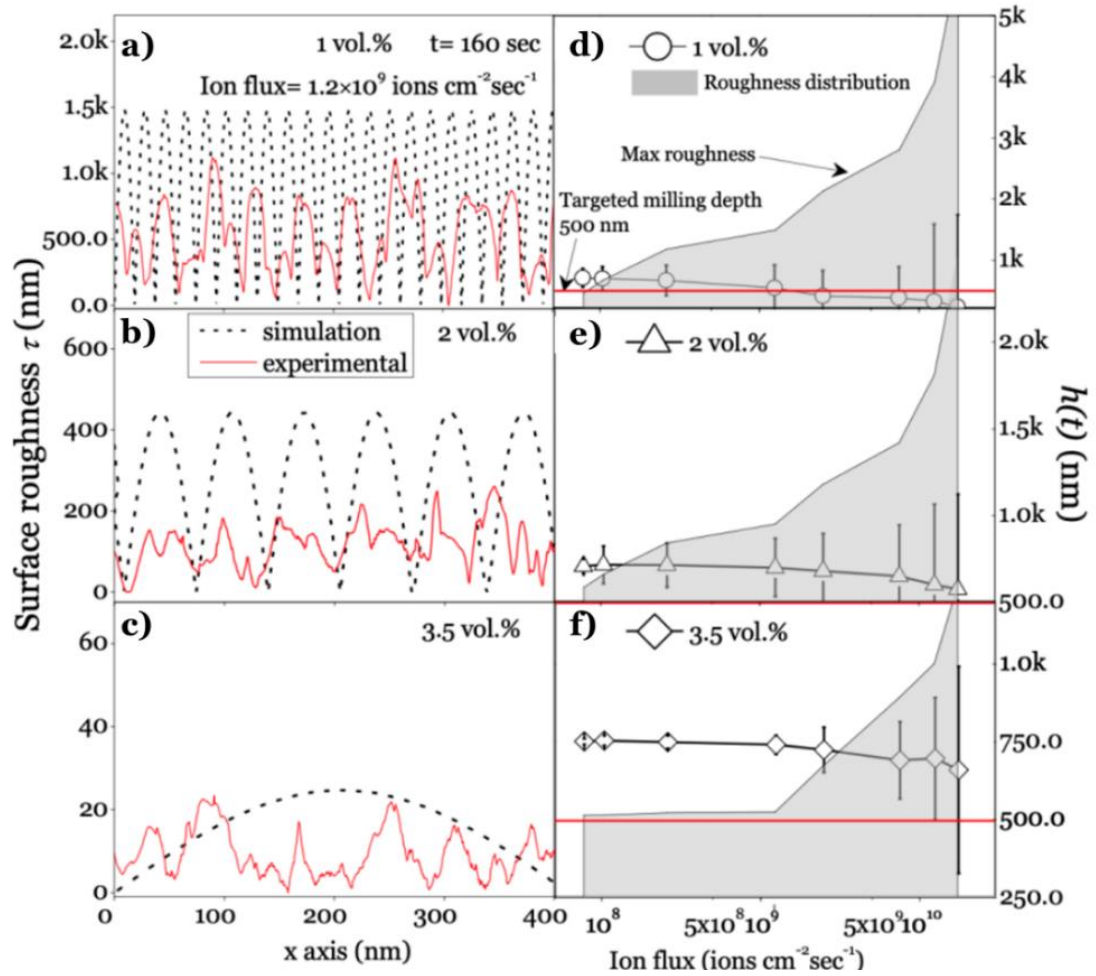
Figure 4.3: a–c) Experimental atom force microscopy (AFM) profiles on a milled surface and numerical longitudinal plots for different composites (milling time = 160 sec); **d–f)** Time evolving milling efficiency (removal depth, h(t)) with surface roughness; the grey area represents the roughness with targeted removal depth of 500 nm.

The milling depth values are plotted as a function of ion flux in **Figure 4.3 d–f**; the grey areas represent the overall removal depth, including the targeted milling depth (500 nm), and the calculated roughness, while the up-edge indicates the accumulating value of roughness and targeted removal

depth. As predicted, the self-smoothing conductive-induced PDE was found as shown in each figure. Both the experimental and numerical morphologies presented a low surface roughness associated with low ion flux values, contrary to the much higher roughness values under higher ion flux. This could be derived from the flux related parameters in **Equation 4.5**, v, λ_1 and λ_2, which change significantly with the application of higher ion flux. Moreover, the experimental average removal depth was reduced at high ion flux for all samples; this could be due to the inaccurate numerical calculation at high roughness. **Figure 4.3 d−f** shows the roughness reduced with increased conductivity both in experimental and numerical results, proving that the pattern characteristics are dominated by the sample conductivity. **Figure 4.3 a−c** also reflects that the roughness peak at high conductivity values is broader when the sample was bombarded at the same flux values. It should be noted that the ion flux employed in this work is 10−1000 times higher than those which have been reported [356, 365, 386]; the thermally activated surface diffusion effect cannot be ignored when the target's temperature increases, which causes the self-smoothing effect on the milled surface as well as conductivity-induced PDE does.

The experimental topographic information is summarized in **Figure 4.4** with SEM images, AFM profiles and statistical analysis for AFM data. The deteriorating trends are presented with dependencies on the ion flux and sample conductivity; the SEM observation illustrates that higher ion flux creates more surface roughness, probably combined with the re-deposition

[387]. The milling precision was improved with sample conductivity increases which could be identified from the evolving morphology in the SEM images under different ion flux. Simultaneously, the AFM contour plots agree with this improvement well showing concentrated milled depth. The contour plots also reflect that the highest roughness appears for 1 vol.% CNP/PS, which indicates milling accuracy was lowered with low conductivity. The statistical analysis from AFM suggests wide distributed milling depths for the 1 vol.% sample especially under the high ion flux (1.25×10^{10} and 1.75×10^{10} ions/(μm^2/sec)). Meanwhile, a concentrated distribution for 3.5 vol.% CNP/PS was observed under the low ion flux which represented high uniformity for the milling depth. **Figure 4.4** also reveals that the actual average milling depths were around 700 nm for most conditions with considerable errors, which is some distance from the target removal depth of 500 nm. The possible reason could be the thermal induced polymer chain which was broken during the high energy ion sputter process, and which could be understood as the thermal induced positive effect. Although improved milling precision was achieved for 2 vol.% and 3.5 vol.% CNP/PS, the actual milling depth decreased for 1 vol.% CNP/PS when the ion flux increased. This could be attributed to the calculation uncertainty caused by the ultimate roughness, as previously mentioned, the residual surface charge and the re-deposition caused by molecular chain breaking [388]. Additionally, the Monte Carlo codes in this work considered the effects in high-fluence implantation, ion mixing, and preferential sputtering caused by atomic collision processes, and proved a positive correspondence between ion milling efficiency and sample conductivity.

However, it did not take account of the thermal induce surface diffusion which has been previously proved with the stabilization effect on a milled surface [200, 356, 389]. Some other materials also have been tried to testify the conductivity enhanced precision manufacturing by FIB, such as epoxy and shape memory PU. However, because of the alignment of materials in the whole project and polystyrene does have a better performance, it has been chosen.
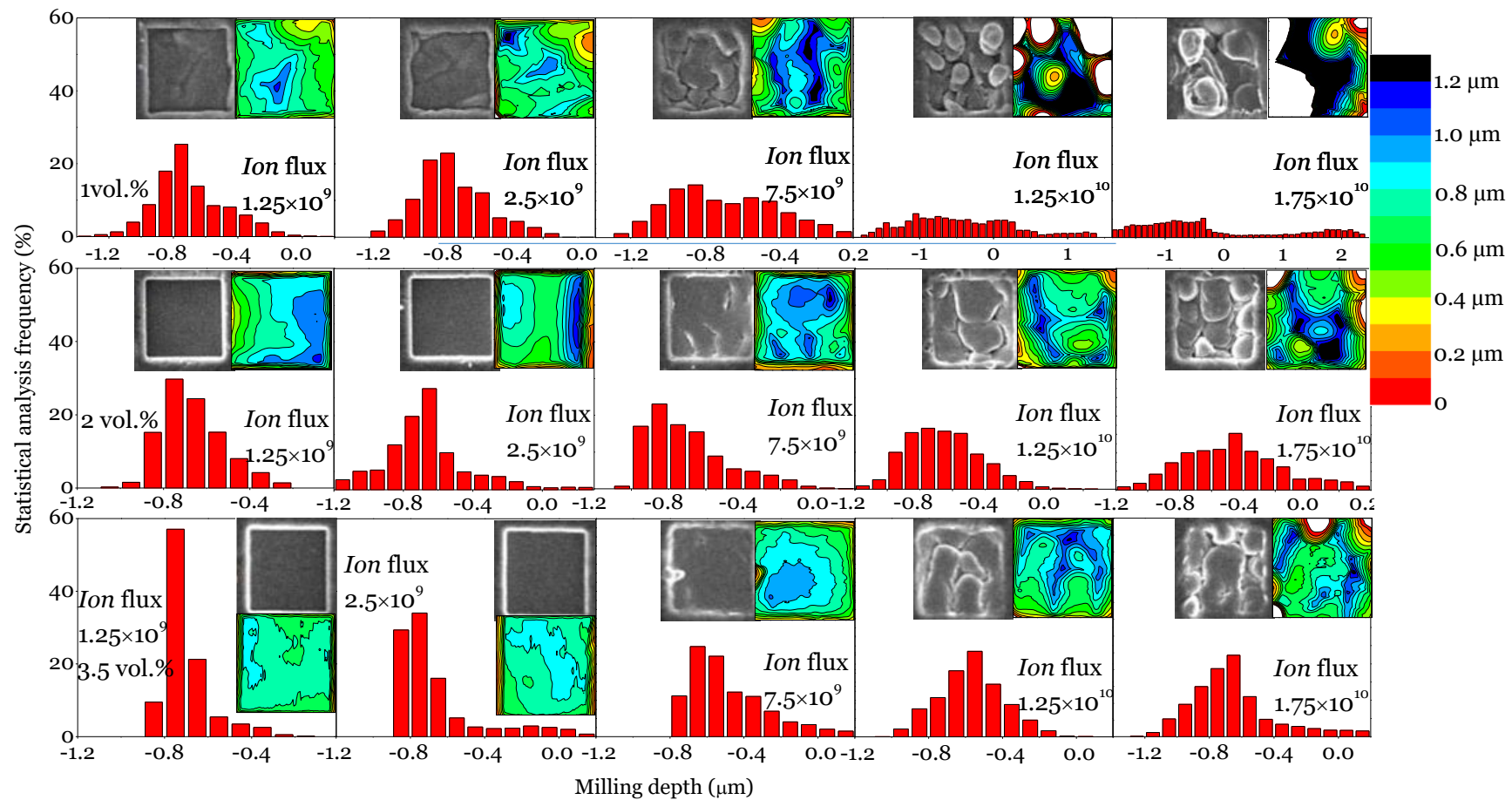
Figure 4.4: Statistical depth analysis for the milled patterns (5×5 μm², milling time = 160 s) based on AFM results (inset, contour plots) under different ion flux, combined with the SEM images (inset).

4.4   Application Demonstration

The CNP/PS polymer matrix surfaces were FIB ion milled into different micro-roughness regions (2 × 2 mm² areas pre-patterned with 20 × 20 μm² square pattern arrays) with milling depths ranging from 0.5 to 1.2 μm, and R_a (arithmetic mean roughness) values ranging from 700 to 4800 nm (0.7 to 4.8 μm). Different patterns are demonstrated in **Figure 4.5 a**, from line array to dedicated probe shape. The processing efficiency and the precision are significantly increased. We next selected the dot array pattern (**Figure 4.6**) for the surface wetting testing. A self-assembly monolayer (SAM) of Trichloro(1H,1H,2H,2H-perfluorooctyl)silane (FOTS, Sigma-Aldrich, St. Louis, MI, US), was applied from the vapor phase at room temperature (~20 °C) for 30 min to facilitate a conformal hydrophobic layer over the CNP/PS topologies.
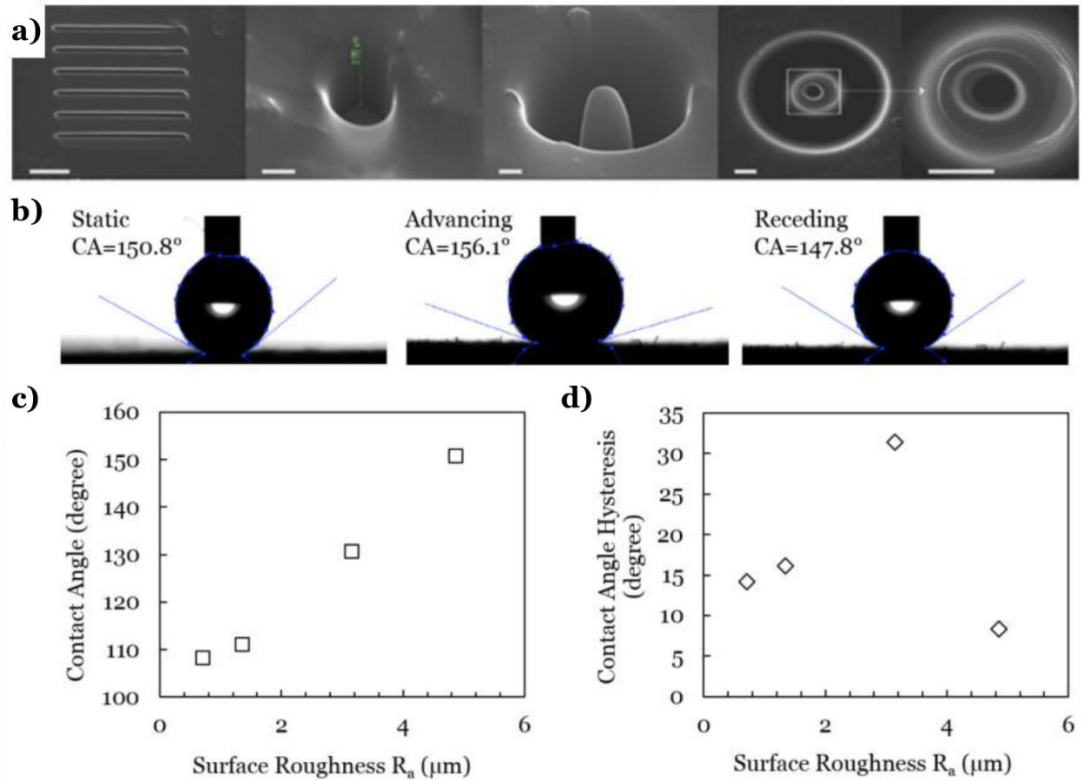
Figure 4.5: a) FIB engineered nanostructures, from left to right, lines pattern, nano-hole, nano-probe, nano-tunnel; the scale bar is 500 nm. Static contact angle (CA) and contact angle hysteresis (CAH = advancing CA - receding CA) characterization on patterned CNP/PS polymer with FOTS layer; **b)** CA and CAH values of a DI water droplet on superhydrophobic surface (Ra = 4.8 μm). Relationships between **c)** CA and surface roughness, and **d)** CAH and surface roughness.

We next selected the dot array pattern (**Figure 4.6**) for the surface wetting testing. A self-assembly monolayer (SAM) of Trichloro(1H,1H,2H,2H-perfluorooctyl)silane (FOTS, Sigma-Aldrich, St. Louis, MI, US), was applied from the vapor phase at room temperature (~20 °C) for 30 min to facilitate a conformal hydrophobic layer over the CNP/PS topologies. To set a benchmark,

the static contact angle measured as 107° when a 2 µL deionized (DI) water drop on a smooth FOTS surface. To set a benchmark, the static contact angle measured as 107° when a 2 µL deionized (DI) water drop on a smooth FOTS surface. As **Figure 4.5 b** shows, the contact angles on the modified CNP/PS surface have been measured as well. From them, the contact angle ranges confirmed as ranging from 108.3° to 150.8° (**Figure 4.5 c**). Dynamic contact angle measurements (advancing and receding) were also taken **(Figure 4.5 b)** with different contact angle hysteresis (**Figure 4.5 d**) values ranging from 31.4° to 8.3°. Values of **Figure 4.5 c**, **d** show two different states on different roughness surfaces. They were close to Wenzel state prediction (with contact angle = 150.8°) at lower roughness (<3.5 µm), and closer to the Cassie–Baxter state (contact angle hysteresis = 8.3°) at higher roughness [343]. It follows the superhydrophobic surfaces (SHS) criteria and obtains a contact angle > 150° and a contact angle hysteresis < 10°.
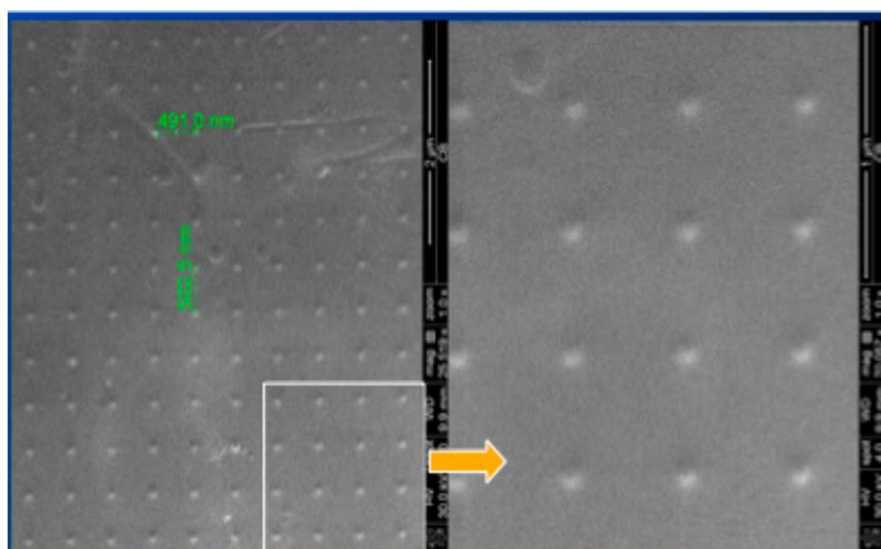
Figure 4.6: FIB milled nano hole array for surface wetting control.

4.5   Summary

Good structure property relationships were revealed with the homogeneous dispersing state of CNPs in a PS matrix from SEM observation, measured conductivity and the stable electrical–temperature performance. The assessment of ion milled surfaces indicated that milling accuracy and surface roughness are highly dependent on the sample's conductivity. A good agreement between experimental results and the theoretical prediction was achieved in describing the surface's evolving trend, including the general analytical conditions for the coarsening process to occur and the roughness of the surface with different ion flux and material conductivity. Resulting micro-roughness patterns were coated with hydrophobic monolayer FOTS and demonstrated surface wettability control, resulting in hydrophobic and superhydrophobic surfaces (CA ranging from 108.3° to 150.8°) with different CA hysteresis values ranging from 31.4° to 8.3°.

It must be noted that the ion bombardment on a macromolecular surface is far more complicated than a silicon surface. In future work it would thus be interesting to investigate ion sputtering on conductive polymer (composites) surfaces with conductivity and thermal-induced PDEs, and more substrate-related factors, such as molecular chain movements and polymer degradation. In the actual application of FIB processing to fabricate micro-nano structures on soft materials that can be deformed thermally at low temperatures, the effects of FIB process have even greater impacts. This beam

impact may occur by several mechanisms, including beam-induced localized heating, knock-on damage and radiolysis.

As the soft materials typically have low thermal conductivities compared to metals or semiconductors (0.5 W/mK - 1 W/mK for polymers and 100 W/mK for Si) and making them more susceptible to beam-induced heating and even melting. For the knock-on damage, soft materials are typically amorphous and also undergo beam damage during evaluation in the TEM, so the surface damage is harder to assess. Radiolysis damage involves irreversible changes in the electronic structure of a material due to incoming ionizing radiation, which can include the destruction of chemical bonds and changes in chemical coordination. Radiolysis damage in soft materials may result in a change in appearance and the preferential destruction or creation of organic functional groups. All above impacts in our system have been particularly investigated in the current research and I will add them in the plan for future work.

Chapter 5

An Emerging Robotic Griper Technique by Autonomously Snapping Gel Structure

5.1   Introduction

Soft matter-based bio systems widely exist in nature to support creatures such as octopus, starfish, caterpillars, etc., by fulfilling adaptive shape changes and responsive motions to allow them to survive in the complex environments [71, 390-393]. Inspired by those features, a number of soft actuator concepts [394-399] have been developed to mimic dedicated actuations/motions, e.g., soft grippers actuated by inflation of a pneumatic network to manipulate fragile and irregular objects [400]; a humidity and light driven liquid-crystal-network actuator [401] to mimic self-shape-morphing of flowers; bellows-like actuators [402] with origami structure enabled various motions. The discovery of superior bio-inspired robotic structure/mechanism with desired working capacity, efficient actuation, high strength-to-weight ratio, on demand shape programmability and low cost, is highly desired for frontier engineering applications.

Responsive hydrogel based configurable structures can undergo shape transformation and perform complicated pattern generation spontaneously

and reversibly in the presence of external stimulus, such as temperature, ionic strength, pH, light, solvent, and electric field [201, 245, 403-405]. Together with its soft, biodegradable and biocompatible properties, hydrogel has been seen as an ideal candidate to build soft robotics [406], soft actuators [198, 407] and soft electronics [408, 409]. Notably, Palleau et al. [410] created soft hydrogel tweezers through electrically assisted ion printing, and demonstrated the gripping/releasing of small objects. By using 3D printing technique, Xu and co-workers [411] fabricated an airplane-like swimming gel robot that could remotely control the different motions under near-infrared light. Yuk et al. [406] exploited hydraulic actuation of hydrogels to develop soft robotics which are capable of optical and sonic camouflage in water. While the above attempts provide advancements in exploring novel actuating mechanism, the overall fabrication, assembly and actuation of those devices relies heavily on the support of instrument and infrastructure, which will considerably limit the application/commercialisation of hydrogel actuators at scale-up level.

Mechanical instabilities including wrinkling [412-418], creasing [263, 419-421], folding [273, 422, 423], ridging [424-427], buckling [428, 429] and bending [430] have engendered an unique approach to realise programmable shape transformations of soft tissue. When the structural soft hydrogel is under confined swelling/compression, it cannot only cause instability to induce structural deformation, but induce an increase in volume (**Figure 5.1 a**). Those instabilities can be actuated upon the mechanical compression (or equivalent energy inputs) under certain geometrical confinements, and the soft structure can fully resume to original state when the stimulus is withdrawn.

Therefore, substantial efforts have been devoted in developing a planar structure with multi-layer [431, 432], different responsiveness [433] or density gradient [434, 435] to improve the controllability and efficiency of instability-induced 3D shape transformations, or preparing hydrogel structures upon constrained swelling [436] (**Figure 5.1 a-b**). Specifically, Gong et al. studied the formation of surface creasing and bulk bending of a piece of hydrogel with a cuboid shape or disc-shape induced by free swelling [437, 438]. Recently, researchers explored the generation of instabilities on the curved structures [436, 439] where the structural anisotropy guided formation of non-uniform stresses could create instabilities in a designable and efficient fashion to induce the shape transformations, as discussed by non-Euclidean shell theory [440, 441]. However, the actuation of shape transformation by modulating and coordinating multimode instabilities induced by free swelling in a 3D curved gel structure has been rarely exploited.

In this work, we propose a novel actuation technology by introducing locally confined development of mechanical instabilities on a 3D curved gel structure with the shape of 'semi-cylinder shell'. Under freestanding swelling, instabilities are firstly initialised at dedicated areas with the buckling occurring on the axial edges and the creasing on the circumferential outer surface. Subsequently, the developments of post-buckling geometries and crease patterns enable a directional releasing of strain energy, and thus drive the shape transformation of gel structure from 'open' state to the 'close' state and realise the function of gripping. By optimising the inputs from the gel composition and geometrical design, we achieve swelling-driven

programmable shape morphing and demonstrate the potential application as an autonomous gripper.
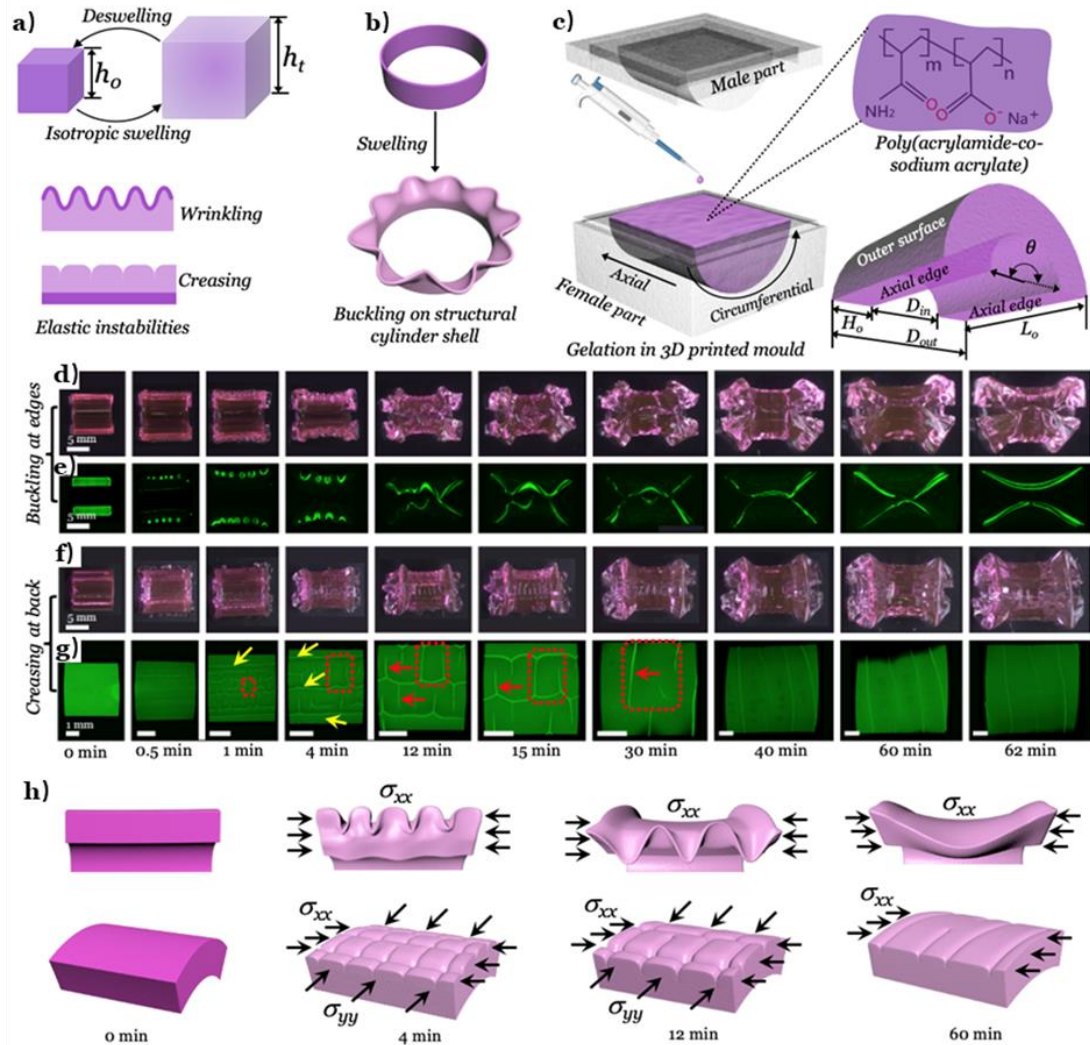
Figure 5.1: Swelling-induced multimode elastic instabilities. **a)** Illustration of the isotropic swelling of a homogeneous gel unit and the swelling induced instabilities in a multi-layer gel structure; **b)** The schematic of buckling on the edge of a gel cylinder shell; **c)** Schematic illustration of fabricating gel structure by injecting the pre-solution into a 3D printed 'semi-cylinder shell' mould, the molecular structure of hydrogel, and the definitions of geometrical factors. The observations of morphologies at various time intervals on the axial edges of the gel structure under **d)** optical microscope and **e)** Laser Scanning Confocal

Fluorescence Microscope (LSCM); and on circumferential outer surface with **f)** optical microscope and **g)** LSCM on the selective zone in optical image (scale bar = 1 mm); **h)** the illustration of stress states for the edge and back areas at designated time. Scale bar is 5 mm in **d-f)**.

5.2 Results and Discussion

5.2.1 Gel Gripper Enabled by Harnessing Multimode Elastic Instabilities

The 3D curved gel structure with the shape of a 'semi-cylinder shell' is designed and fabricated by synthesising the poly (acrylamide-co-sodium acrylate) hydrogel (PAAm-*co*-NaAc) in a 3D printed mould, as shown in **Figure 5.1 c** (more details in **Section 3.2.3**). The original rationale to take the curved shell design is to utilize the stain growth on circumferential direction to achieve a 'close' state (see **Figure 5.2 a**). The obtained hydrogel structure is subsequently immersed into deionized (DI) water to introduce freestanding swelling. An exemplified design is selected to show the swelling-induced morphological developments, with outer diameter D_{out}=10 mm, inner diameter D_{in} =5 mm, initial thickness $H_o = \frac{D_{out}-D_{in}}{2} = 2.5$ mm, initial axial length L_o=10 mm and open angle θ=180°. After swelling, morphological developments are observed on the specific locations: buckling (**Figure 5.1 d-e**) occurring at the axial edges and reticulated creases (**Figure 5.1 f-g**) appearing on the circumferential outer surface. The geometrical characteristic

of this designed structure enabled co-existence of buckling and creasing with clear preferences on location and unveils an interesting energy distribution throughout the designed gel structure which has not been reported elsewhere.

The buckling at the axial edges is early onset (< 30 seconds, **Figure 5.1 d**), then a post-buckling development is observed with a reduction in buckling numbers, but an increase in wavelength (λ, **Figure 5.1 e**). Another interesting event taking place at the circumferential outer surface is the initiation of axial creasing lines whose length aligns with the axial direction at round 30 seconds (**Figure 5.1 g**), which means that the region undergoes circumferential compression. The overall stress evolutions as per location are illustrated in **Figure 5.1 h** with uniaxial stress localizing (σ_{xx}) on the edge section. However, a translational biaxial stress state (σ_{xx} and σ_{yy}, σ_{yy} represent the stress in circumferential direction) is presented for the back area where an equiaxial stress state ($\sigma_{xx}=\sigma_{yy}$) appears to occur as soon as the hydrogel swells, by generating a biaxial 'grid' type creasing at around 1 min. This biaxial creasing explicitly grows till 12 mins with the aspect ratio of a single unit of 'grid' (see red dash box in **Figure 5.1 g**) being reasonably maintained. When the gel structure swells from 12 mins to 30 mins, the neighbouring axial creasing separate from each other faster than the circumferential creases, leading to the disappearance of axial creasing lines at 30 mins (see red and yellow arrows in **Figure 5.1 g**). The circumferential creases rule the place thereafter until they reach the global isotropic swelling state (see **Figure 5.2 b**) after 4 hours. The trans-directional development of the creasing pattern from the axial creasing lines to the biaxial 'grid', then to circumferential creases, represents a self-

regulation of strain energy and then a release of the strain energy in circumferential direction.
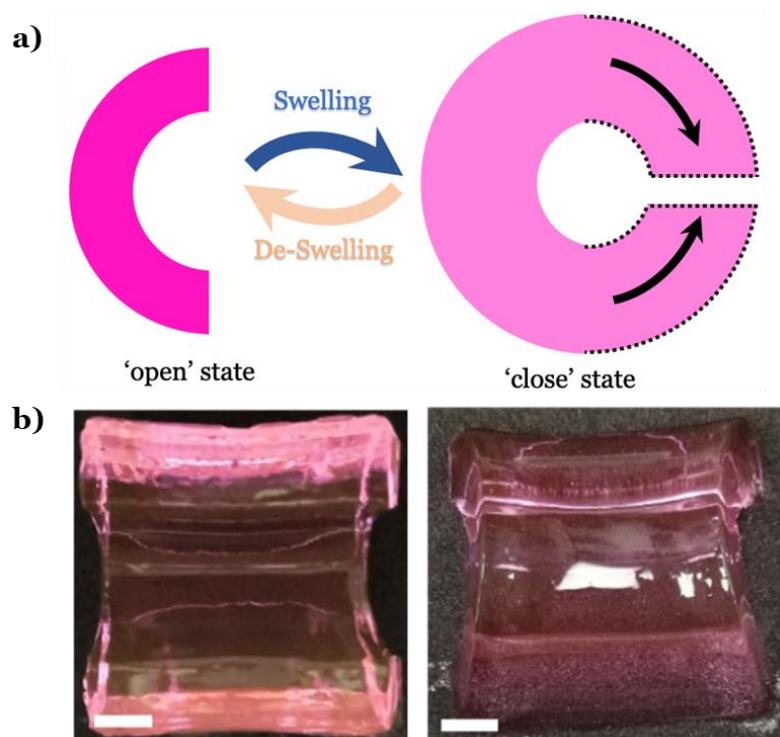
Figure 5.2: a) Schematic of reversible morphing of 'semi-cylinder shell' shaped gel part under swelling/de-swelling; **b)** Final equilibrium state of gel structure at an immersion time of 240 mins. Observations from the axial edges (left) and circumferential.

Macroscopically, we observe a global transformation of the gel structure from 'open' to 'close', then a return to the 'open' state (**Figure 5.1 d-e**). The post-buckling development and evolution of the creasing pattern collaboratively drive the gel structure to close from 4 mins to 15 mins. The geometrical developments at the axial edges make a direct effort to allow the edges to make physical contact with each other. On the other hand, the release

of energy in a circumferential direction regulated by the creasing pattern supports these buckling developments to accelerate structure closing. Beyond that, an adaptive structural harmonization starts from 30 mins, by developing a single buckling pattern at each axial edge towards $\lambda > L$ (L refers to the axial length after gel structure swollen). The gel structure stays at the 'close' configuration until 60 mins, then gradually reopens. Once the end of the morphing process is reached, all surfaces of the gel structure resume to a smooth state and the instabilities patterns completely disappear (**Figure 5.2 b**). An isotropic swollen 'semi-cylindrical shell' shaped gel structure is presented (D_{out}=29.2 mm, H=7.2 mm and L=28 mm).

5.2.2   Localised Multimode Instabilities

Once the gel structure swells, water molecules diffuse onto the surface to create a thin gradient layer with swelling induced strain. This leads to a multi-layer configuration in a finite depth generating a spatially non-uniform stress in the thin gradient layer. Wavy buckling patterns are found on both of the axial edges (**Figure 5.3 a**) and the circumferential edges (**Figure 5.4 a**). However, the post-buckling phenomenon on the axial edges with strong out of plane morphological development directly contribute to the 'closing' of gel structure. The crease patterns are observed both on the circumferential inner (**Figure 5.4 b**) and outer (**Figure 5.3 b**) surfaces initially, but the full sequence transition (from axial creasing lines to biaxial creasing 'grid', then to circumferential creasing lines) only occurs at the circumferential outer surface where the trans-directional regulation on strain energy leads to a releasing of

strain energy along the circumferential direction and effectively drives the shape morphing. It is worth noting that hydrogel parts in a 'hemi-spherical shell' shape are also fabricated, and the observations of morphologies at various time intervals of the hydrogel part are summarised in **Figure 5.4 c-e** where a similar shape transformation from 'open' to 'close' is found by swelling the part. However, the underlying mechanics seems more complicated as the strain development on the hemi-spherical shell is arbitrary. Therefore, we defer this research to future work.
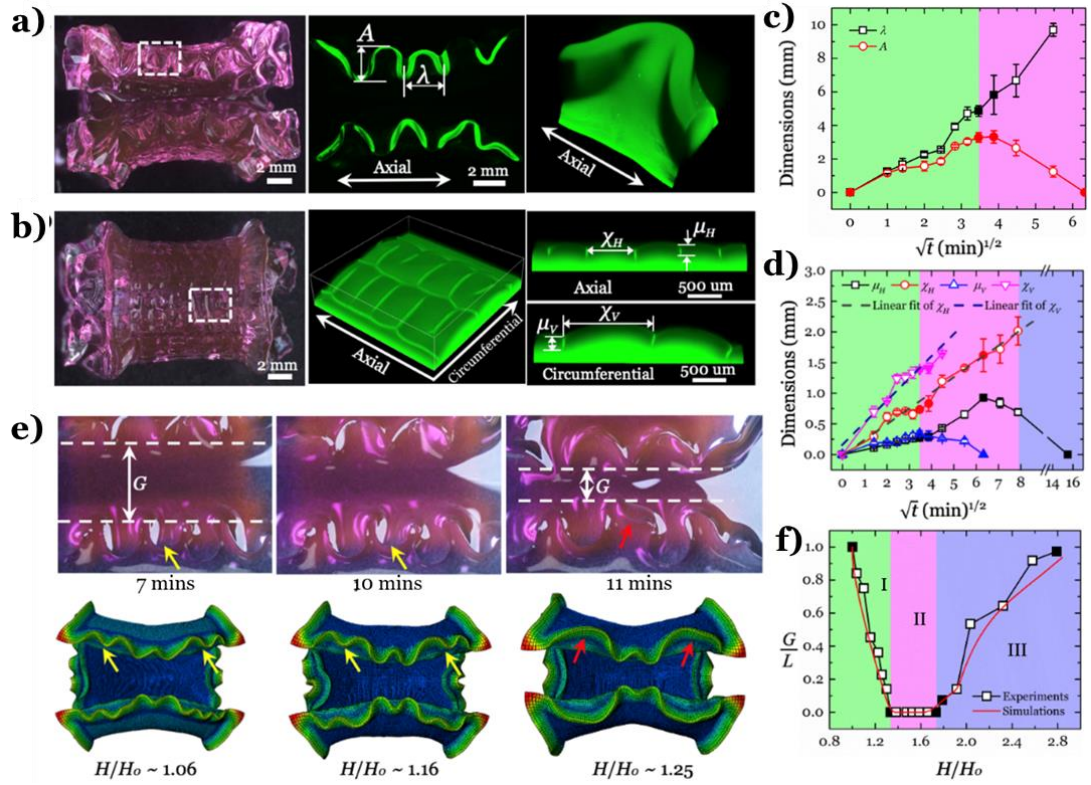
Figure 5.3: Geometrical analysis on the multimode instabilities and their collaborative effect on the transformation of gel structure. The observations of swelling-induced morphological developments at 8 mins for the axial edges with **a)** optical microscope, fluorescence microscope and reconstructed 3D image from LCSM based on the selected area in optical image, and for the

circumferential out surface with **b)** optical microscope, LCSM and the cross-sections along the axial and circumferential direction from LSCM based on the selected area in optical image. The analytical plots of time dependent evolutions of structure deformation during swelling: **c)** wavelength (λ) and amplitude (A) of buckling, **d)** surface crease depths (μ_H and μ_V) and crease spacings (x_H and x_V); **e)** The experimental observation and finite element simulation of the post-buckling development; **f)** $\frac{G}{L}$ versus $\frac{H}{H_0}$. Green area: I-closing regime; pink area: II-holding regime; purple area: III-reopening regime.

5.2.3 Geometrical Analysis on the Localised Multimode Instabilities

To trace the morphological evolutions, we plot the wavelength (λ) and amplitude (A) of the buckling in **Figure 5.3 c**, and creases spacing and depth (χ, μ) in **Figure 5.3 d** as the function of swelling time (t). When swelling progresses, the coalescence of adjacent buckling is observed. When the gel structure transforms from 'open' state (green area) into 'close' state (pink area), the wavelength keeps growing, while the amplitude increases to the peak value at the closure and then decreases to 0 (**Figure 5.3 c**). In **Figure 5.3 d**, the creases depths (μ_H and μ_V) first achieve maximum and then start to fade. The evolution trend of average crease spacing (x_H and x_V) follows a linear relationship with the square root of swelling time, which agrees well with the theory [442, 443].
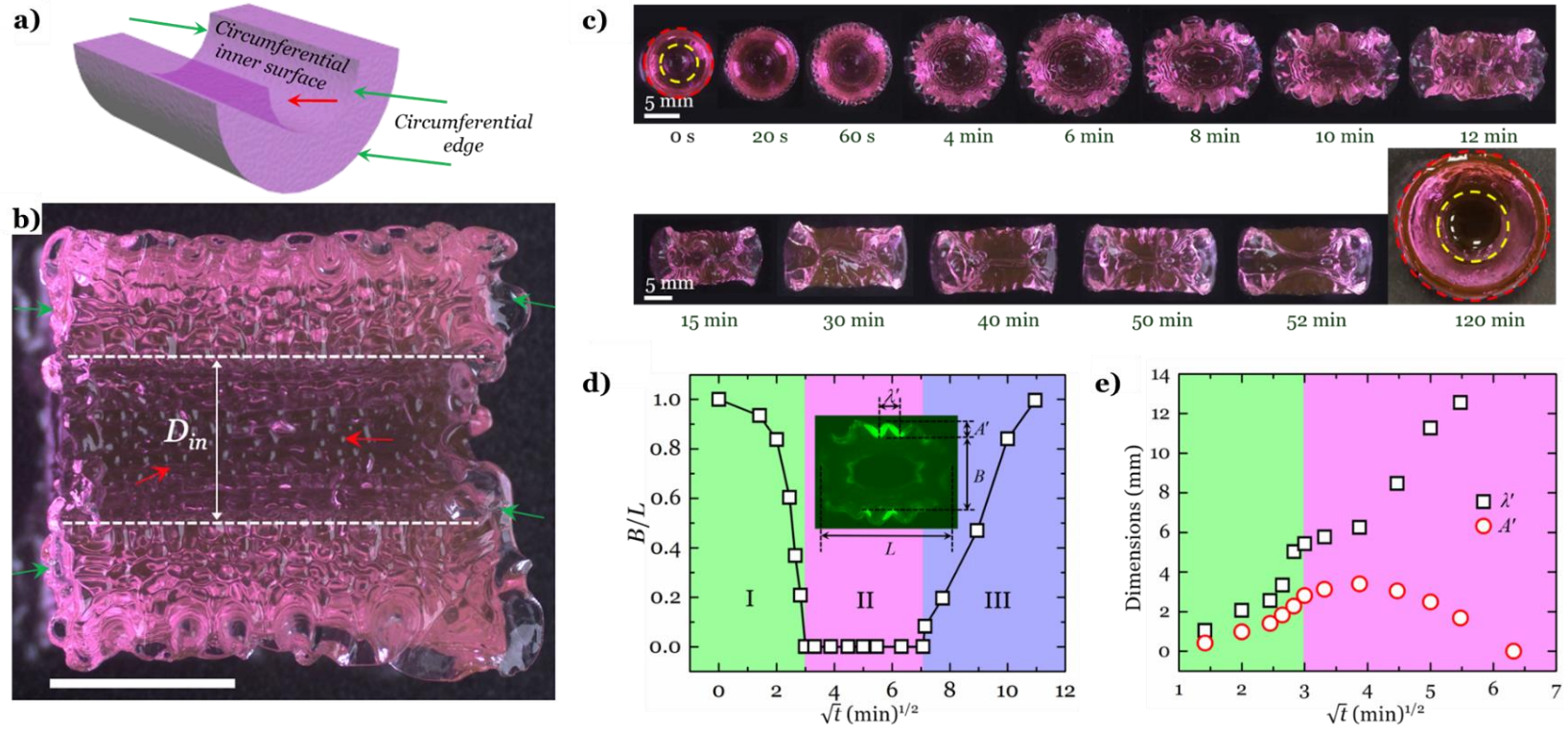
Figure 5.4: Buckling on circumferential edge, inner zone and swelling-induced mechanical instabilities of the hemispherical shell hydrogel; **a)** The schematic of the circumferential edge (green arrow) and the circumferential inner zone (red arrow); **b)** Optical micrograph of gel structure swelling at 2 mins, the dash lines highlight the inner edge with a label Din. The gel structure has initial $D_{out}=L_o=10$ mm, $D_{in}=5$ mm, $\theta=180°$. The scale bar is 5 mm; **c)** The observations of morphologies at various time intervals of the hemispherical shell hydrogel under optical microscope. The analytical plots of time dependent evolutions of structure deformation during swelling: **d)** B/L, where B refers to the gap distance between edges, L is defined as the structure length of swollen hydrogel, green area: I-closing regime, pink area: II-holding regime, purple area: III-reopening regime; **e)** wavelength (λ) and amplitude (A) of buckling.

We next investigate how buckling contributes to the global 'closure' of soft structure. The degree of swelling is defined as $\frac{H}{H_0}$, where H is the thickness of the swollen structure at certain swelling time. The development of the wavy buckling profile on the axial edges can be evidenced with neighbouring waves merging into a big one (see the yellow and red arrows in **Figure 5.3 e** and **Movie 5.1**). A diagram (**Figure 5.3 f**) is created by plotting the normalized closing factor of $\frac{G}{L}$, where G refers to the gap distance between edges (see **Figure 5.3 e**). **Figure 5.3 f** presents three regimes for the morphing of gel structure: I-closing regime with $\frac{G}{L}$ decreasing from 1 to 0 and close at $\frac{G}{L}$=0 (green area), the swelling time when $\frac{G}{L}$=0 is defined as the close time; II-holding regime with $\frac{G}{L}$ remaining at 0 (pink area); III-reopening regime with $\frac{G}{L}$ gradually increasing from 0 to ~1 (purple area), the open time is the time when $\frac{G}{L}$ starts increasing from 0, and the recovery time is the time when $\frac{G}{L}$ returns to ~1. The results of finite element analysis (full simulation in **Movie 5.2**, **Figure 5.3 e-f**) show a good agreement with the experiment results.

We also fabricated the gel structure with the shape of a hemispherical shell. The observations on morphologies at various time intervals under optical microscope are shown below in **Figure 5.5 a-b**. The swelling of the hemispherical shell hydrogel produces a similar deformation. However, the mechanism for the hemispherical shell is more complicated, thus we will focus on the research of this structure in our future work.

5.2.4 Time Dependent Shape Morphing Analysis by Varying Geometrical Factors

We then explore the efficiency of shape transformation by tuning the geometrical variables with different initial thicknesses (H_o) in **Figure 5.5 a**, initial axial lengths (L_o) in **Figure 5.5 b** and open angles (θ) in **Figure 5.5 c**. In **Figure 5.5 a**, we fix the values of the outer diameter (D_{out}=10 mm), angle (θ=180°) and length (L_o=10 mm), thus, the area of the circumferential outer surface ($S_{cy} = \frac{\pi D_{out} L_0 \theta}{360°}$) remains unchanged, while the area of the annulus surface area ($S_{an} = \frac{0.25\pi(D_{out}^2 - D_{in}^2)\theta}{360°}$) increases with the increases of thickness. It is found that the gel structure with a smaller H_o reaches the full closure earlier. The gel structure with H_o= 5 mm (D_{in} = 0) cannot close completely, because the bending stiffness resists the closing. In **Figure 5.5 b**, S_{an} remains unchanged while S_{cy} decreases as L_o decreases when the values of the outer diameter (D_{out}=10 mm), angle (θ=180°) and thickness (H_o=2.5 mm) keep constant. We discover that the gel structure with a longer axial length is likely to hold the 'closing' stage for an extended period. The gel structure with L_o of 3 mm does not close completely, and the reason could be the insufficient axial length which does not allow the buckling profile to evolve. In **Figure 5.5 c**, without changing D_{out}, L_o and H_o (D_{out}= L_o=10 mm, H_o=2.5 mm), both S_{an} and S_{cy} increase as θ increases. The gel structure with bigger θ need less time to close, and those with smaller θ (e.g., 120° and 150°) are unable to reach a full closure. With the decrease of θ, extra circumferential distance is needed

for the gel structure to reach the 'close' state, which brings more challenges to be overcome in order to fulfil this configuration change.
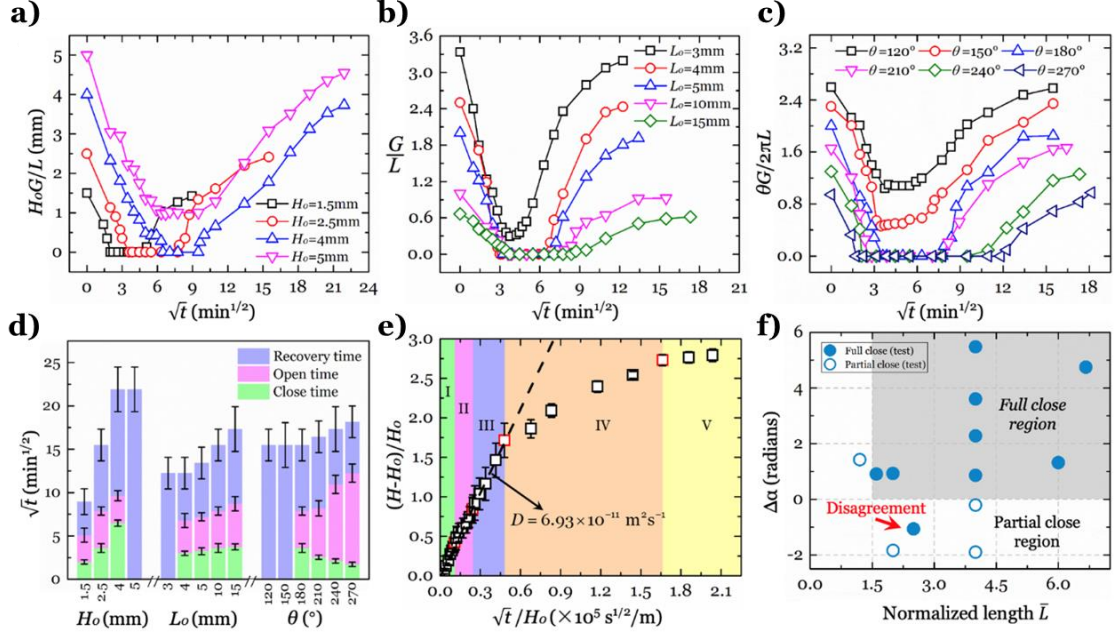
Figure 5.5: Time dependent shape morphing analysis by varying geometrical factors. **a)** Different initial thicknesses (H_o), $D_{out} = L_o = 10$ mm, $\theta = 180°$; **b)** Different initial Lengths (L_o), $D_{out} = 10$ mm, $H_o = 2.5$ mm, $\theta = 180°$; **c)** Different initial angles (θ), $D_{out} = L_o = 10$ mm, $H_o = 2.5$ mm; **d)** The effects of geometry factors on shape transformation times; **e)** The normalized thickness follows an apparently diffusive scaling at short times (slope of the dashed line); **f)** Phase diagram by plotting the bending angle difference $\Delta\alpha$ and normalized length $\bar{L}$, shaded area represents the full close region (i.e. $\frac{G}{L} = 0$) and un-shaded part is the partial close region (i.e. $\frac{G}{L} > 0$).

Apparently, the 'close' state is easier to achieve for the gel structure with a larger S_{cy} and a smaller S_{an}, where the geometrical landscape is energetically favoured by the post-buckling development. Longer open time and recovery time are needed once the volume of the gel structure increases,

i.e., increased thickness/length/angle (see **Figure 5.5 d**), providing a better control for the morph structure. In **Figure 5.5 e**, we map the swelling kinetics by plotting the change in thickness of the gel structure normalized by its initial thickness, $\frac{H-H_0}{H_0}$ as a function of $\frac{\sqrt{t}}{H_0}$. After transforming from 'open' state into 'close' state (regime I, green area), and then 'holding' stage (regime II, pink area), the gel structure recovers (regime III, purple area) to the 'semi-cylindrical shell' shape and regains the homogeneity. Even at this time, the gel structure is not fully swollen, and it continues swelling isotopically (regime IV, orange area) to the final state (regime V, yellow area) in which the hydrogel can no longer absorb the water. By linear fitting of the initial slope of data in **Figure 5.5 e**, a diffusion coefficient constant of D=6.93×10^{-11} m^{2}s^{-1} is estimated from the 'open' state to the end of 'holding' stage, which is in the similar magnitude to that for polyacrylamide hydrogel in previous reports [203, 404, 444].

5.2.5   Numerical Analysis of Fully-closed State

We next numerically scale the 'close' state by utilising Euler-Bernoulli curved-beam theory and considering the swelling competition between the circumferential outer surface and annulus surfaces (see *experimental section* for the details). We define $\Delta\alpha > 0$ and $\bar{L} > \bar{L}_c$ with the bending angle difference $\Delta\alpha = ac\left(\frac{H}{H_0-1}\right)\theta' - (2\pi - \theta')$ and the normalized length $\bar{L} = \frac{L_0}{H_0}$, where a is the parameter associated with the geometric parameters of the sample and $a =$

$D_{out} \dfrac{\ln\frac{D_{out}}{D_{in}}}{D_{out}\ln\frac{D_{out}}{D_{in}} - 2H_0}$, $\theta' = \dfrac{\pi\theta}{360°}$, and $\dfrac{H}{H_0}$ is the swelling ratio after regime III, at

which the gel structure starts to swell isotropically. The two parameters c and

$\bar{L}_c$ generally depend on the diffusion kinetics and the mechanical behaviour of

the hydrogel. Currently, there is no explicit mathematical expression to

calculate their exact values. Here we estimate the two parameter values of our

experiments, i.e., choosing the values which can satisfy the most experimental

data. Therefore, $c = 0.19$ and $\bar{L}_c = 1.5$ are taken as the best fit for the current

experiments. A phase diagram (in terms of $\Delta\alpha$ and $\bar{L}$, **Figure 5.5 f**) can be

therefore created to show the threshold of closure by applying the above

definitions and experimental inputs.

The critical length $\bar{L}_c$ characterizes the swelling competition between the

circumferential outer surface and the annulus surfaces, and it depends on the

diffusion kinetics and mechanical properties of the hydrogel. Currently, there

is no explicit mathematical expression to calculate the exact value of $\bar{L}_c$. The

theoretical work to expand this part could be substantial, which is outside of

the focus of this paper. Instead, we estimate the value of $\bar{L}_c$ from our

experiments in the paper, i.e., choosing a value of $\bar{L}_c$ that satisfies the most

experimental data. So, the value $\bar{L}_c = 1.5$ is chosen here because it can satisfy

all data except one.

Overall, a good quantitative agreement has been reached between

theoretical predictions and experimental results, with one exceptional data

(pointed out by red arrow in **Figure 5.5 f**) from a gel structure with a bigger

thickness (H_o= 4 mm). Since Euler-Bernoulli theory is only applicable to thin beams, its estimation on the shift of the bending angle for a thick gel structure might be less accurate. This led to a decision to extend the research on modelling the shape morphing in the thick structure in the future work.

5.2.6 The Spontaneous Shape Transformation of Gel Gripper Controlled by Swelling Ratio

The swelling behaviour of the gel structure (D_{out}= L_o=10 mm, D_{in}=5 mm, θ=180°) is assessed with different BisAA contents in **Figure 5.6 a**. For the gel structures with higher BisAA concentrations (e.g., 37.4 mM and 44.2 mM in **Figure 5.6 a**), they hardly reach a full closure. For those gel structures with lower BisAA concentrations (e.g., between 3.4 mM and 13.6 mM in **Figure 5.6 c**), their close time are almost identical, while the automatic open time and the full recovery time decrease as BisAA content increases. The swelling behaviour of the gel structure is also studied for swelling at various concentrations of phosphate buffer saline solution (PBS). Our hydrogel has an ionic strength of 168 mM, which is similar to the ionic strength in 0.01 M PBS (156.6 mM). Thus, the gel structure achieves limited swelling when it is immersed into 0.01 M PBS (**Figure 5.6 d**). As shown in **Figure 5.6 b**, with the lower concentration of PBS, the gel structure closes more rapidly. While these results show some interesting phenomena, we unfortunately have not got any systematic clue from these results. We will keep exploring this part of the research in our future work plan to create complicated swelling gradients in the soft gel structure.
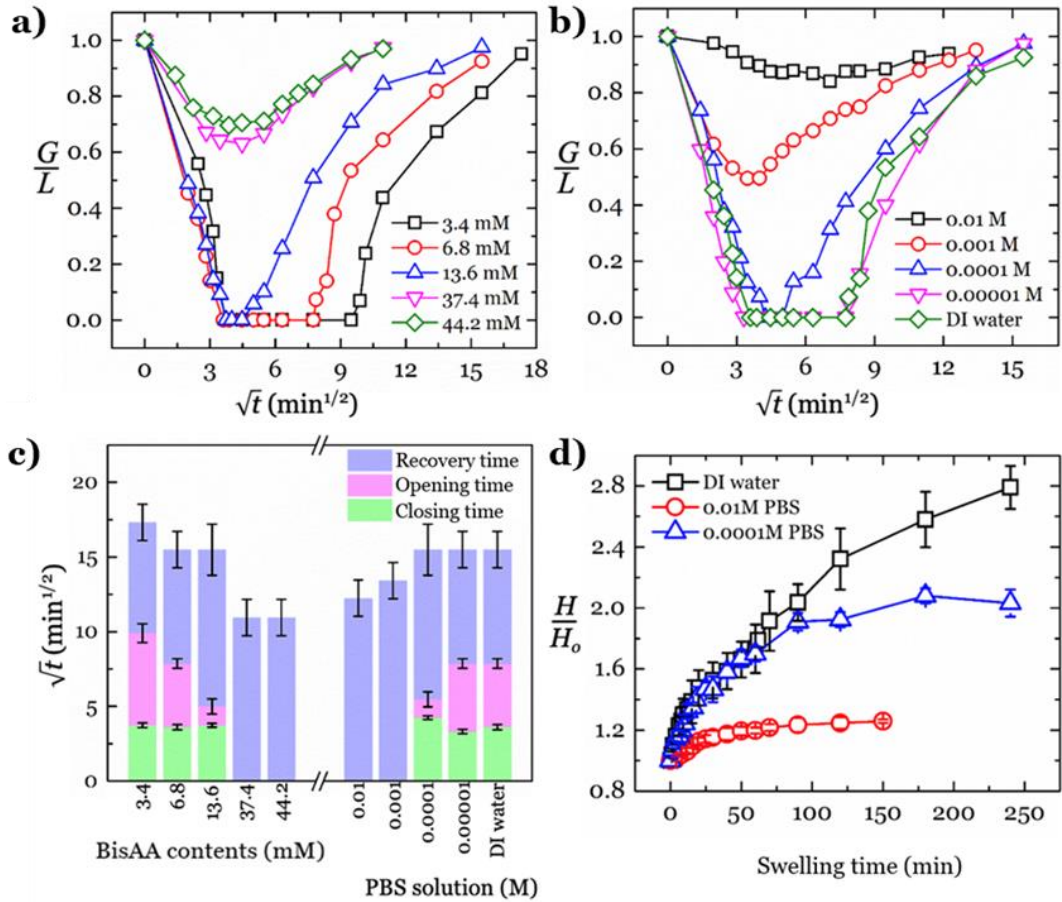
Figure 5.6: Spontaneous shape transformation of the gel structure controlled by the swelling ratio. Time evolution of the shape deformation of gel structure with initial $D_{out}=L_0=10$ mm, $D_{in}=5$ mm, $\theta=180°$: **a)** with different BisAA contents swelling in DI water, **b)** swelling in PBS with different concentrations; **c)** The influence of crosslinking and solution on shape deformation times of gel structure; **d)** The swelling ratio as function of time in different PBS.

5.2.7   The Reproducibility of Gel Gripper

We perform the cyclic actuation (**Figure 5.7 a**) by de-swelling the 're-opened' gel structure through a conventional air-drying process, then

saturating in 0.01 M PBS for 10 mins until it reaches to the original shape, from which a new swelling cycle starts (**Figure 5.7 f-g**). Afterwards, we assess the reproducibility of shape morphing of gel structure with $D_{out}=L_o=10$ mm, $D_{in}=5$ mm, $\theta=180°$. The gel structure presents a good reproducibility for 30 cycles (**Figure 5.7 b**). After 30 cycles, the sample cannot recover completely, which could be attributed to trivial structure degeneration (fatigue) during the experiments. We further design gel grippers with four fingers to demonstrate their efficiencies of autonomous gripping.

We develop two types of flower-like gel grippers with four finger designs (sharp and flat fingers, **Figure 5.7 c-d**). The initial purpose is to show the designability to fit different purposes. Both hydrogel grippers undergo self-actuating in DI water within 3 min to reach full closure and 20 min to fully reopen in DI water. These four finger designs optimise the shape morphing by dramatically reducing the closing time. Since there are no significant differences on actuation performance for the devices between sharp finger and flat finger designs. The intention is not to show which design is superior. Both designs have the ability to realize an autonomous actuating performance upon free swelling, which would further broaden the potential applications of hydrogel in soft robotics. A demonstration of weightlifting is conducted for the gripper (with about 0.14 g weight) by using it to pick up a small magnetic stirrer (weight is about 2 g) from the water (**Figure 5.7 e** and **Movie 5.3**), which is 15 folds of the weight of gripper. In **Figure 5.7 a-b**, the demonstration of cyclic morphing can be repeated up to 40 times, where the morphing of flower-like gel gripper and weightlifting demonstration follows the same principle

(**Figure 5.7 c-d**). This gripping strength could be potentially applied in the soft robotics for offshore/marine engineering.
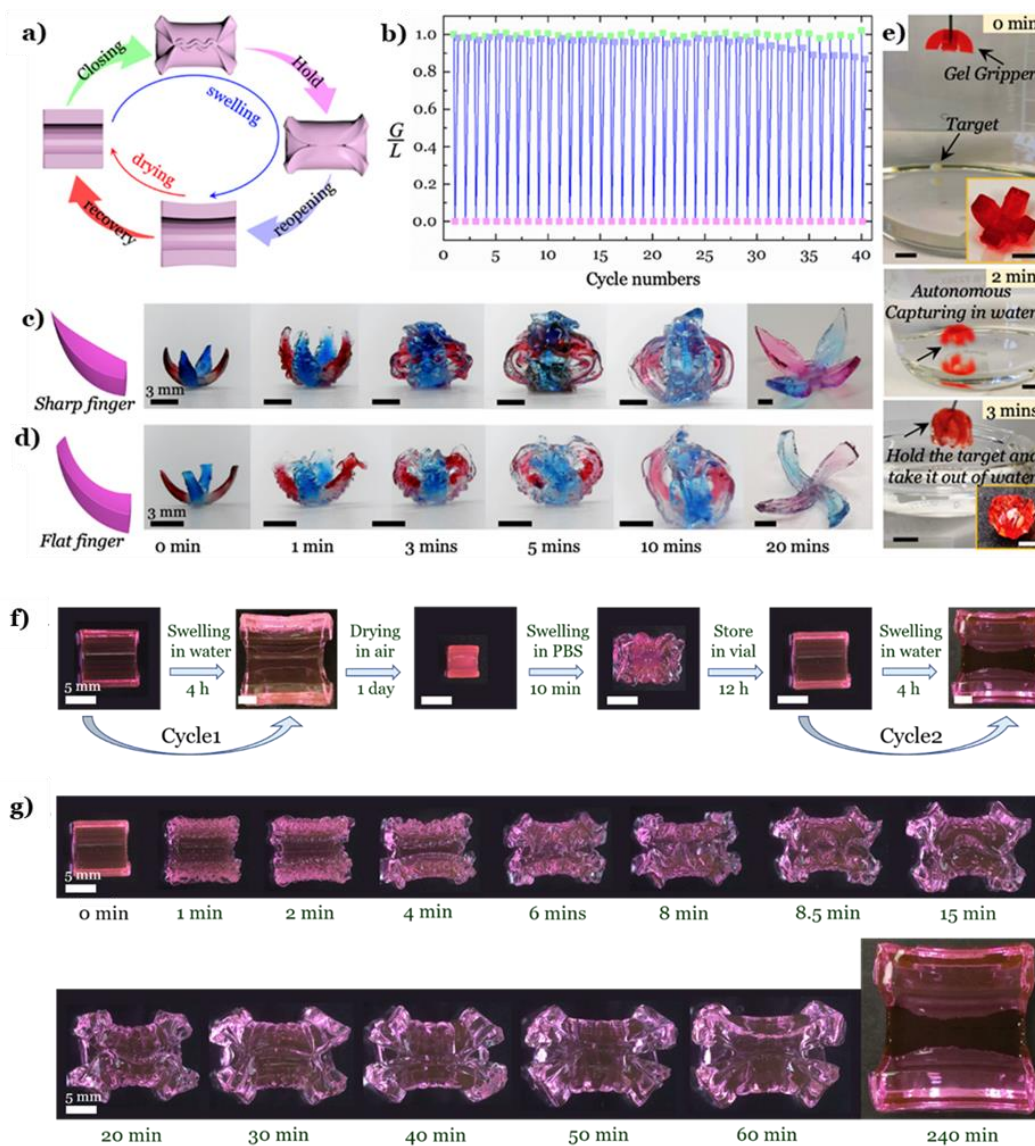
Figure 5.7: The demonstration of the hydrogel structure and reproducibility of the actuating gel structure. **a)** Schematic illustration of a loop of open-close-recovery cycle, and **b)** cyclic testing with open-close for the gel structure. Time lapsed gripping motion captures for the hydrogel gripper with **c)** sharp finger design and **d)** flat finger design; **e)** A demonstration of gripping strength by using the designed hydrogel gripper (4 fingers, D_{out}=10 mm, D_{in}=5 mm, L_0=3 mm, θ=180°) to pick up a magnetic stirrer from the water, the scale bar is 5

mm; **f)** The experiment design; **g)** Time evolution of shape deformation of gel structure with initial D_{out}= L_0=10 mm, D_{in}=5 mm, θ=180° during cycle 2.

We also studied the deswelling process in PBS, trying to optimise the control of this reversible morphing. However, its length recovered from 28 mm to 13 mm, rather than the initial size 10 mm. The exploratory study suggests that the hydrogel could not revert to its initial shape when deswelling in PBS purely. On the other hand, we have been able to sustain a good recovery with a combination of the drying and swelling process as shown in **Figure 5.7 f**.

In this study, we didn't extend the discussion on the de-swelling process for the following reasons:

1. There is no morphological development in de-swelling.

2. we use the de-swelling process as a controlling method to repeatedly trigger the shape transformation of the gel part, which is supposed to be more interesting for the design of a hydrogel actuator.

5.3   Summary

We describe an autonomous shape transformation of a 3D curved gel structure by harnessing swelling-induced multimode mechanical instabilities. The initiation and programmable developments of multimode instabilities, including buckling at axial edges and creasing at circumferential outer surface, have been realised in the dedicated regions. The co-existence and the regional

developments of buckling and creases collaboratively drive the global shape morphing of the gel structure from the 'open' state to the 'close' state. Numerical analysis creates a phase diagram to understand the effects of the geometries and swelling ratio on the 'gripping' efficiency. We successfully demonstrate the actuations of several conceptual designs with good reproducibility by tailoring the structure and tuning the swelling. This mechanics enabled shape transformation of 3D curved gel structure introduces a valuable approach to the design and development soft robotics with desired efficiency and integrability. This can be applied to future healthcare devices, human-machine interfaces, and wearable electronics, etc.

Although we covered many aspects in the study of the morphological transitions to the global morphing of the soft part, there are a number of limitations which we haven't got time to address in this work. For instance, the timescale if the entire actuation-recovery loop, the details of directional strain energy transition and the viscosity effect on the gel parts needs more study quantitatively. For the application, the gel gripper design could be optimized to achieve higher efficiency.

Supplementary Movie 5.1: The development of wavy buckling profile on the axial edges by optical microscope.

Supplementary Movie 5.2: The finite element analysis results.

Supplementary Movie 5.3: A demonstration of gripping strength by using a designed hydrogel gripper to pick up a magnetic stirrer from the water.

Chapter 6

Tuneable Morphological Deformation of Polyelectrolyte System as a Tool for Ocular Applications with Facile Fabrication Process

6.1   Introduction

Smart soft material with active shape-morphing has enabled a range of bio-inspired applications. An increasing recent interest in reconfigurable and scalable biomechanical mimicking native tissues and function of the human eye system at both cellular and tissue level has promised to unlock a set of new tools to empower the in-vitro eye disease modelling for ophthalmology research [445, 446]. Such technology can closely simulate in vivo/in situ conditions, significantly increase research efficiency while fulfilling the 3Rs principle (Replacement, Reduction and Refinement of animal tests), acknowledged by recent papers [447, 448].

In the human eye structure, the crystalline lens (CL) is the main functional part for the focusing control mechanism, directing the light coming through the cornea towards the retina. Cataracts are a common eye disease that affects the human eye via CL opacification. This disease accounts for

around half of the world's cases of blindness, and the number of patients will continue to increase with the aging population [449-451]. Since the invention of Intra Ocular Lenses (IOLs) in the 1940s, modern cataract surgery, which replaces the problematic CL with artificial IOLs, has been developed significantly into an effective way to cure this problem [452-454]. Challenges remain when choosing an IOL design and application scheme. These include adjustable geometry and optical function, material selection and posterior capsule opacification (PCO) related sight loss [455-457]. A typical example is child patients who underwent the IOL implantation, who have a higher risk of developing visual axis opacities when refractive errors appear at a later stage - still subject to further research [458].

IOLs usually consist of a small plastic lens and plastic side struts. Side struts are also known as haptics, are used to fix the lens inside the eye [459]. At beginning, IOLs are "single vision", and have a uniform refractive index. However, perceiving different distances requires different visual acuity. So recent science and engineering developments tend to address such challenges from the perspective of IOLs geometry and optical function, with the most popular design being multifocal IOLs, which can direct light to two or more focal points with improved patient satisfaction [456, 460]. While the multifocal IOLs provide a benefit for near and intermediate vision for some cases, the IOLs do not allow for a dynamic change of focus length in a continuous fashion as they have been manufactured with fixed visions. Furthermore, the IOL power calculation formulas are still being developed to

improve accuracy by countering the optical property errors [456, 461-463]. Technical innovations towards a new generation of eye implants are therefore highly desired in terms of improving patient experiences as well as driving efficiencies in public healthcare expenditure.

The mode for the latest IOL products is mostly acrylic copolymers which have the potential to bring additional features by introducing extra functional groups. Both hydrophobic acrylics (e.g., Acrysof Alcon), and hydrophilic ones (e.g., Hydroxyethylmethacrylate - HEMA) are frequently used in current cataract surgery due to their flexibility and capsular biocompatibility [464, 465]. Compared with hydrophobic acrylic IOLs, the hydrophilic acrylic (gel) shows lower post-surgery optical distortions, but a higher PCO, which can be corrected by adjusting the chemical composition (co-polymerization) and IOL structure. An early conceptual ionic responsive Polyacrylamide copolymer (PAM) gel-based lens structure was reported [466]. This switchable focal change is desirable, for example, when IOL is used in the eyes of children where adaptive vision correction is needed as a child grows.

Meanwhile, latest manufacturing technologies have enabled advanced materials for smart ocular system applications, such as 3D printed artificial cornea [467], customized ocular prosthesis [468], 3D printed iris [469], and smart contact lenses with ocular pressure sensing [468, 470]. Developing material and manufacturing technologies for such applications would provide both desired healthcare benefits e.g. surgical treatment [467, 468, 470], rehabilitation [468] and doctor training [471]. In 2019, Nicolas Famery and

his team have developed a new wet lab model of Descemet membrane endothelial keratoplasty (DMEK) for surgical teaching by 3D printing. This model offers "a close to reality, feasible, resource-sparing and valid teaching technique that permits to perform all DMEK surgical steps [471]". Looking beyond the ocular system, tuneable bio-optical configurations in other advanced devices have been achieved in recent developments, and these no longer require complicated mechanical units [472-474]. Some of the recently developed smart polymer devices achieve tuneable optical focal length, responding to and controlled by external stimulation such as pH-responsive [475], electric field [476], and ion concentration [466] with mechanical confinement structures or electrical interconnects. However, limited efforts have been found concerning the development of easy-to-implant artificial ocular devices with responsive focal shifting. This is due to the fact that the above required liquid/solid interactions and stimuli for actuation are hard to fulfil in-vivo, as in the human eye.

Given all of this, in this paper we proposed and demonstrated a new polyelectrolyte system based on polyacrylamide gel (PAM), to advance the robust optical implant technology with focal shifting. Compared with currently used IOL materials, the PAM, a responsive shape transformation material with superior elasticity and designability [477, 478] and bio-compatibility [479, 480] draw greater attention in biomedical applications [409, 481-486]. It is believed to hold great promise in the search to achieve switchable IOL focal length due to its elasticity and designable responsive features, and is compatible with the

human ocular system [487]. The tuneable morphological deformation and Rapid-Prototyping (RP) based manufacturing delivers a novel configurable optical technology with switchable focal length, adaptability to deployment conditions, anti-biofouling properties and resistance to calcification. This multi-functional break-through enabled by novel smart materials offers significant potential for use in future ocular implants, such as IOL and bionic eye devices.

For the first time, tuneable morphological deformation has been realized by a homogeneous PAM polyelectrolyte system with a freestanding, standard-shaped, dual-curved, mono-focal IOL structure created by a "one-step-moulding" facile fabrication process (**Figure 6.1 a**). The designed morphological deformation mechanism is to be achieved by responsive mechanical buckling, which is a common phenomenon in thin, soft structures that may yield rapid out-of-plane deformation (**Figure 6.1 b**). Such out-of-plane deformation results in dynamic changes in designed IOL morphology parameters (**Figure 6.1 c**) therefore achieving the desired tuneable optical properties – e.g., shifting in focal length f (reciprocal of the lens dioptre $D = \frac{1}{f}$). Through 3D printing based rapid prototyping (RP) and cast-moulding composition of PAM polyelectrolyte hydrogels (**Figure 6.1 a**) bespoke optical property shifting designs can be achieved, stimulated by a small ion-concentration change under constant temperature, verified by geometry and optical characterization processes. It should be noted that the targeted focal length shifting is around 10% of the original value, as required for the ocular

application we are interested in. IOL calcification tests were also conducted to demonstrate the suitability for potential human eye implantation.
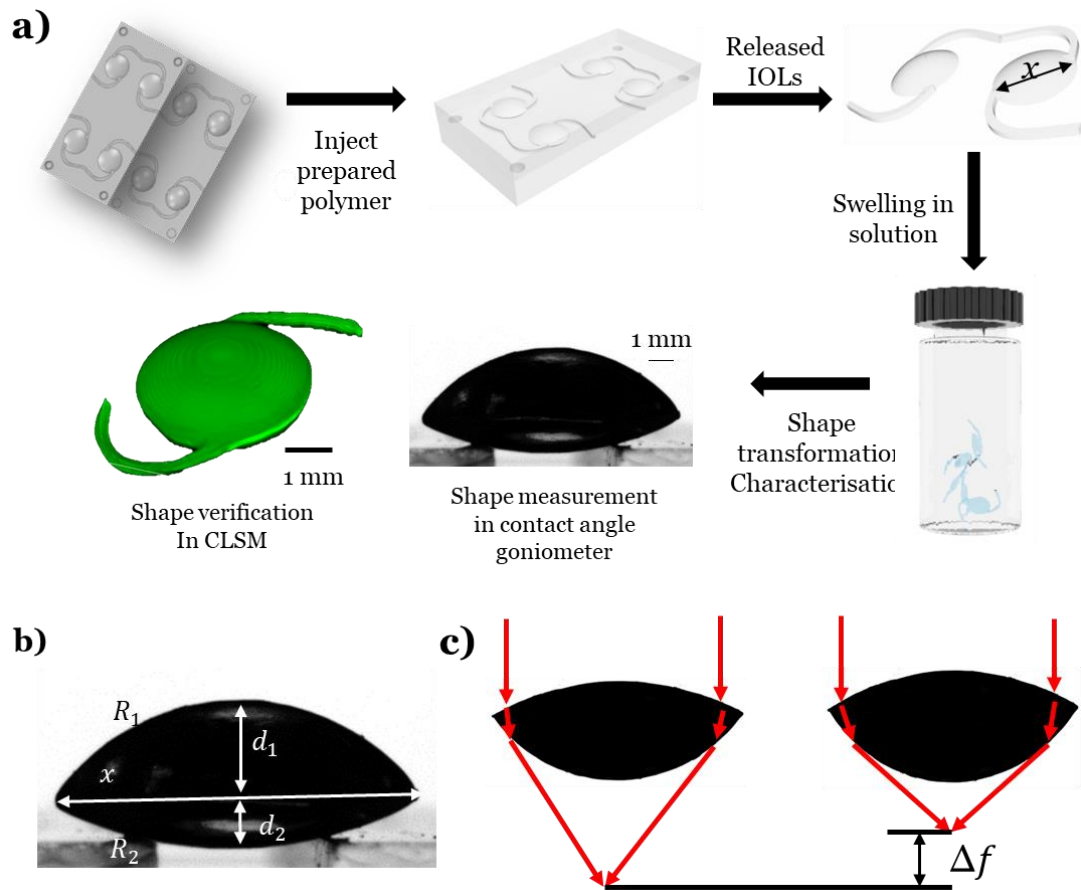
Figure 6.1: a) an innovative fabrication process enabling bespoke IOL designing and adaptive optical property tuning by combining Rapid prototyping, post processing and responsive hydrogel; **b)** IOL morphology profile related to optical characterizations; **c)** Optical model and concept of using responsive hydrogel to fine-tune the focal length: After swelling, shape change cause the focal length change.

6.2 Results and Discussion

6.2.1 Polyelectrolyte System Synthesize and Mechanical Property Characterization

PAM-based hydrogels have largely been used as thermal and pH responsive [488, 489] functional materials. However, such external stimulation is undesirable in human ocular applications. Therefore, we firstly characterized its ionic-strength responsive swelling behaviour in phosphate buffered solutions (PBS) together with the mechanical properties. **Figure 6.1 a** shows synthesizing of the proposed biocompatible PAM-based responsive IOL hydrogel structure. During cast moulding, the IOL device was formed through a polymerization in which a set volume of PAM gel is cured. The polymerization process, with different composites, is explained in the experimental **Section 3.2.2**.

6.2.2 Standalone, Dual-curved IOL Morphological Deformation Analysis

Next, we analysed the tuneable morphological deformation mechanism of the designed IOL structures via numerical simulation and experiments. The dual-curve IOL structures (**Figure 6.1 b**) were shaped by injecting pre-polymer solution to a cavity that is created when two halves of a mould (**Figure 6.1 a**) are brought together and fixed in a precise position relative to each other. After being released from the mould, IOLs were analysed as standalone structures, without any external mechanical confinement applied.

To understand the ionic strength effect on morphological deformation, IOLs with the same design (d = 2.41 mm, x= 6 mm, R_1=3.6 mm, R_2=6 mm) and composition (Hydrogel 1 in **Table 3.1**) were immersed in PBS solutions with different concentrations (0.001, 0.01, 0.1 M), 24 h. During the first hour, when the IOL swells rapidly, it was observed that the IOL expanded more along the *x*-direction (**Figure 6.2 b**), resulting a reduction in both curvatures (reciprocal of the radius, $\frac{1}{R_1}$ and $\frac{1}{R_2}$). After the first hour, swelling was slowed down with noticeably less curvature changes. **Figure 6.2 a** and **b** show the lens thickness d and lens diameter x increment over time, respectively. Both data plots show rapid increment in the first hour, with a noticeably greater *x* change, and reduced increment ratio between 1 and 24 hours. The data in this section collected by DSA as **Chapter 3.3.1**.
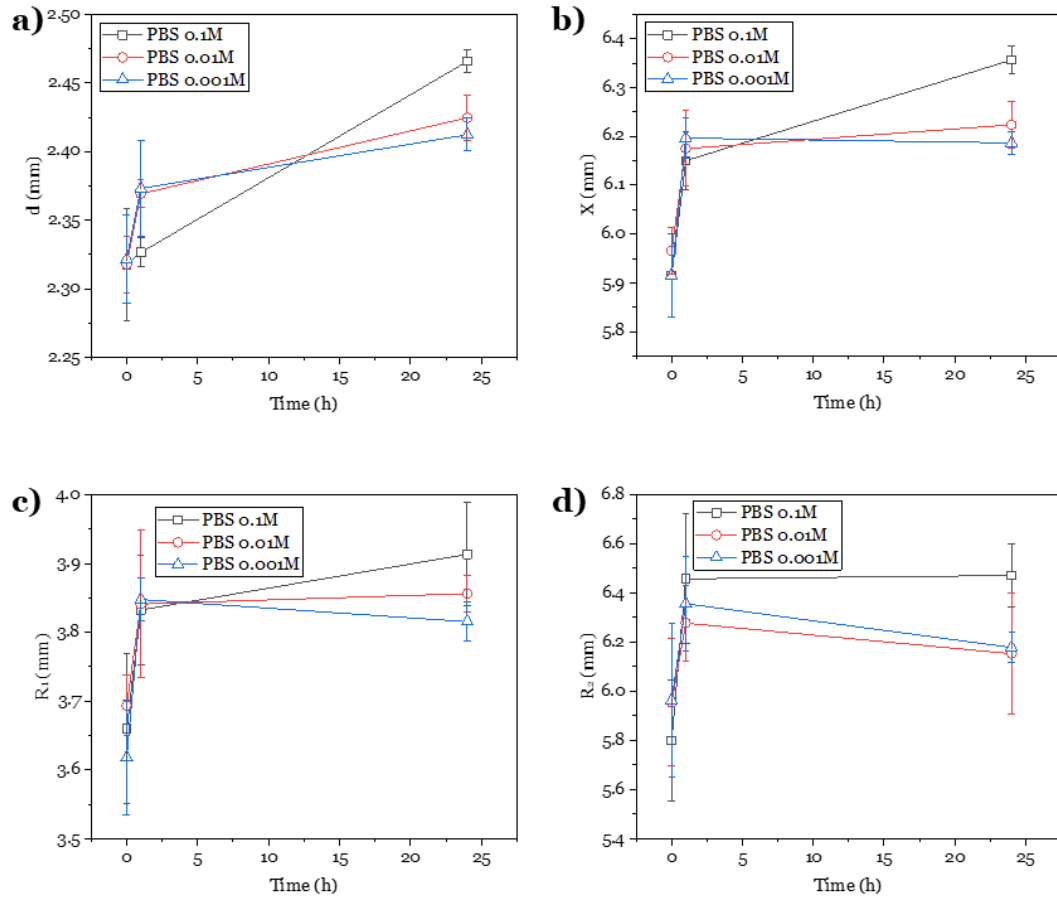
Figure 6.2: IOL (Hydrogel 1 in **Table 3.1**, Design g & h in **Figure 3.2**) swelling **a)** measured d; **b)** measured x; **c)** measured R_1; **d)** measured R_2.

6.2.3 Optical Model of the PAM IOL System

Once these morphology deformation parameters were obtained, the IOL's optical properties (e.g., focal length f) can be calculated. The focal length of human ocular systems mainly relates to key parameters such as the axial length, anterior chamber depth, geometries of the cornea and crystalline lens (or IOL), and refractive index of these materials and aqueous mediums. Calculation and prediction of the IOL focal length (reciprocal to power/dioptre)

for patients and surgical operations have continued to progress since the 1960s, with the latest developments including ray tracing based on vergence formula, and artificial intelligence [463, 490, 491]. The optical quality of an IOL is typically analysed in an optical bench on its own, or alternatively, in a system which simulates the conditions of a real human eye with artificial cornea etc. [492]. In this work, the main focus is on the optical design flexibility and the focal length shifting of the bio-optical devices. Hence the IOL characterization work has been performed on its own.

The relationship between optical properties and dual-curved IOL lens designs can be described by the following equation:

$$\varphi = \frac{1}{f} = (n-1)(\frac{1}{R_1} - \frac{1}{R_2} + \frac{(n-1)d}{nR_1R_2}) \qquad \textbf{Equation 6.1}$$

where φ is the dioptre of the optical power, f is the focal length, d is the lens thickness in the air, R_1 and R_2 are the surfaces with radii of curvature, and n is the refractive index according to [493]. And the refractive index of PAM gels is reported to be n=1.349 by Byron et al. [493]

Both the lens diameter x and thickness d in **Equation 6.2** were used as major morphology parameters and monitored during the hydrogel swelling process. During the morphology study, the radii R_1 and R_2 can be calculated following **Equations 6.3 and 6.4**:

$$d = d_1 + d_2 \qquad \textbf{Equation 6.2}$$

$$R_1 = \sqrt{\left(\frac{x}{2}\right)^2 + (R_1 - d_1)^2} \qquad\qquad \textbf{Equation 6.3}$$

$$R_2 = \sqrt{\left(\frac{x}{2}\right)^2 + (R_2 - d_2)^2} \qquad\qquad \textbf{Equation 6.4}$$

where θ and γ are the contact angle measurement values for the upper and lower surface from a DSA (Droplet Shape Analyser) based goniometer, respectively. The changes in R_1 and R_2 are translated into desired optical power and focal length shifting, reflected by **Equation 6.1**.

As shown in **Figure 6.2 c** and **d**, the calculated R_1 and R_2 were plotted against the swelling time. **Figure 6.2 e** shows the change in the calculated focal length f. For the designed IOL lens geometry and PAM composition, the length f for both 0.01 and 0.001M PBS immersion processes have shifted.
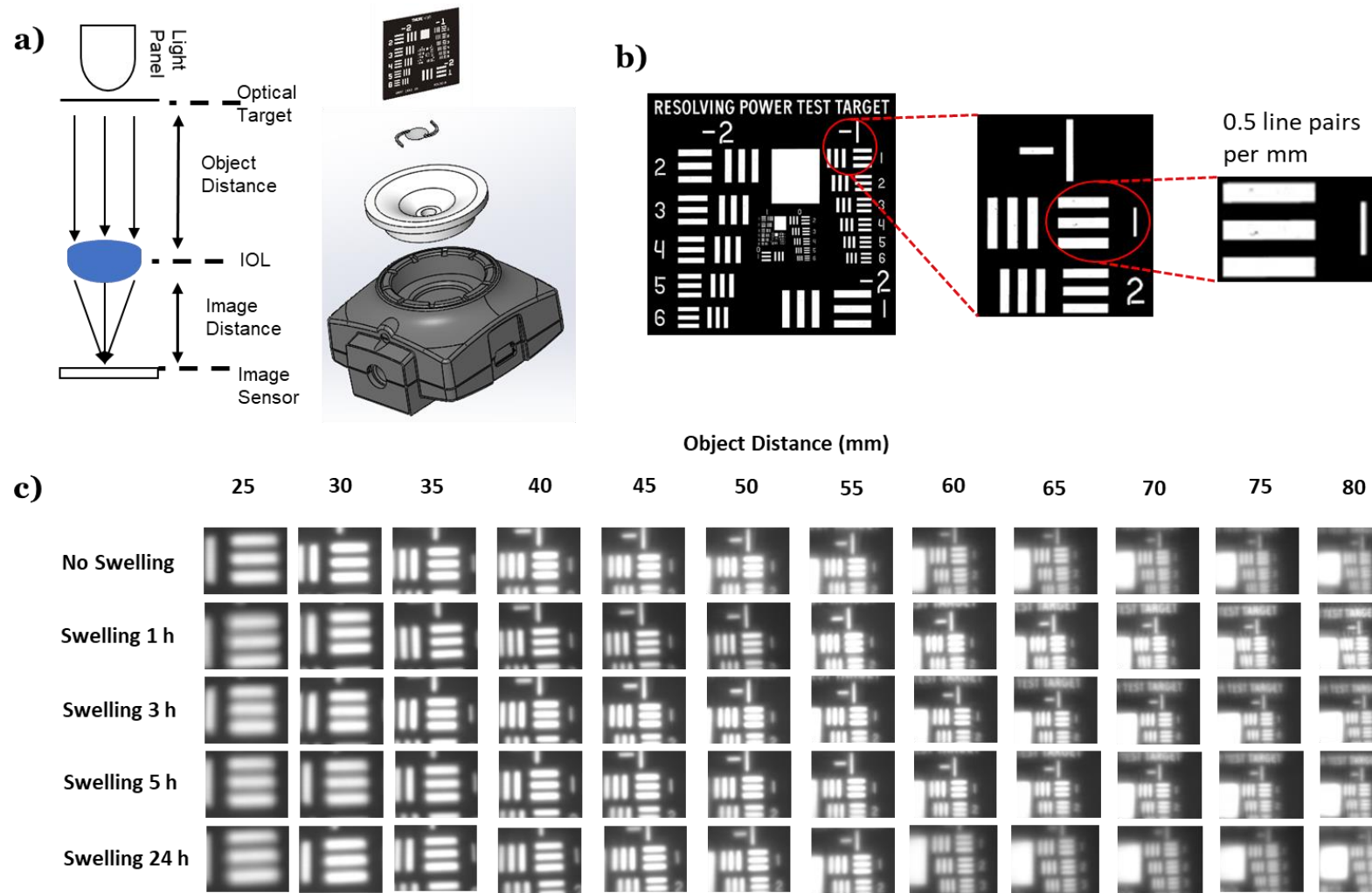
Figure 6.3: a) Optical testing bench schematic; **b)** 1951 USAF resolution test targets; **c)** Image processing with a fixed image distance 10.9 mm.

To validate the calculated R_1 and R_2 from x and d, image-processing software has been employed to directly measure the R_1 and R_2 values, as shown in **Figure 6.2 c** and **d** which largely agree with the data in **Figure 6.2 e** and **f**.

6.2.4 Demonstration - Controllable Focal-length Shifting Verification

An optical bench system has been designed for focal length shifting demonstration and verification have been designed and constructed with an IOL unit holder, digital image sensor and other accessories. This is where we will assess the responsive buckling of gel optical structure and the controllable focal length change (experiment set up show as **Figure 6.3 a**). The IOL design used design g & h in **Figure 3.2** and all samples stored in 0.01M PBS solution under room temperature.

With the image distance set to v = 10.9 mm, and object distances u were calculated based on focal length values as shown in **Figure 6.2 h**, following **Equation 6.5**:

$$\frac{1}{u} + \frac{1}{v} = \frac{1}{f} \qquad\qquad \textbf{Equation 6.5}$$

These calculated object distances and resulting images (**Figure 6.3 c**) were then evaluated by the optical bench system to characterize the configurable focal length shifting for the fabricated gel structure.

6.2.5 Calcification Assessment

Calcium deposition on the surface of the optical implant has been a major problem that frequently occurs after surgery and is related to the material surface and

interfaces properties [494-496]. While we used PAM, which is a biocompatible material, the resistance to calcification on the gel surface and inside of the gel has yet not been well exploited. In this section, accelerated calcification experiments were performed by immersing the PAM gels in a solution of 0.05 - 5 mM of calcium nitrate solutions for 1, 10, 30, and up to 60 days similar to that reported by Yokoi et al [497]. At these time points, the gel parts went through a "Cryo-SEM" process where the soft material structures were frozen in the liquid nitrogen before being sliced and the extent of calcification was examined by a Field Emission Scanning Electron Microscope (SEM, Tescan Mira 3) with EDS module (Energy-dispersive X-ray spectroscopy). All processing details have been written in **Chapter 3.3.2**.

To offer a clear understanding on the calcification status on the IOL, both the surface and cross-section of PAM IOLs were examined. Since the PAM gel contains carbon rather than calcium, the calcium deposits that may be produced on IOLs needs be carefully justification. In **Figure 6.4** calcium solution concentrations were set at an extreme value: 5 mM, which is ten folds of its concentration in the human eye (around 0.5mM) [498]. In this way, **Figure 6.4** clearly shows how to distinguish carbon and calcium by colours i.e., red marks carbon as hydrogel, and green marks calcium ions as calcium deposition. Therefore, **Figure 6.5 and 6.6** show the EDS surface view, where carbon and calcium elements were represented by red and green colours respectively. It can be seen that for concentrations of less than 2mM, the gel surface remains "calcium-free" even after 30 days' immersion. As the normal range of calcium in the human tear is around 0.5mM [499], and the majority of groups studied in a previous work were below 1.5mM [498], we can confirm this PAM gel has a low calcification risk in ocular applications.

20 µm
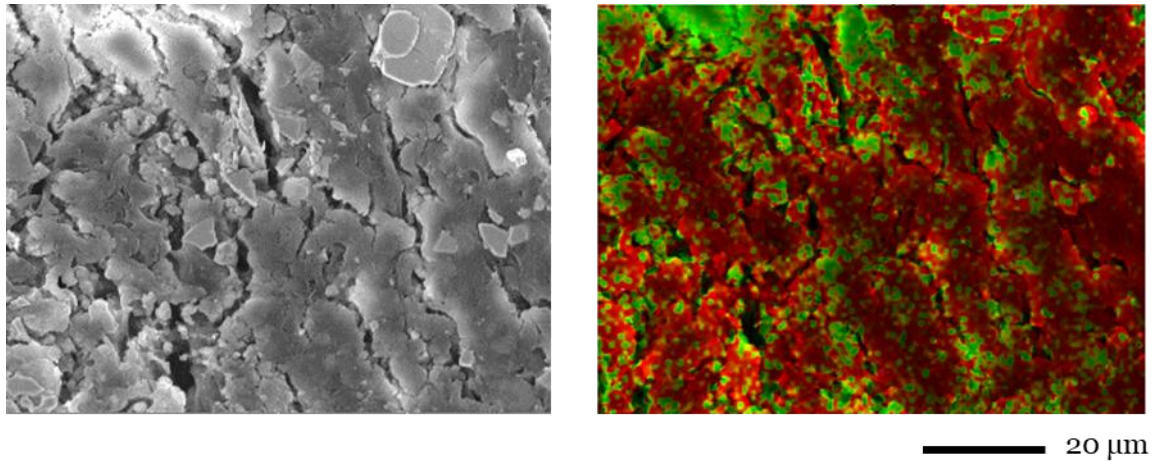
Figure 6.4: Calcium deposition characterization, SEM (left) and EDS (right) profile (cross view) of IOL samples preincubated in 0.01M PBS and immersed in 5 mM calcium concentrations at room temperature 30 days (red marks carbon as hydrogel, green marks calcium ions as calcium deposition).

So, **Figure 6.5** and **6.6** shows the EDS surface view, where carbon and calcium elements were represented by red and green colours respectively. It can be seen that for concentrations of less than 2mM, the gel surface remains "calcium-free" even after 30 days' immersion. As the normal range of calcium in human tear is around 0.5mM [498], and majority groups studied in a previous work were below 1.5mM [497], we can confirm this PAM gel has a low calcification risk in ocular applications.
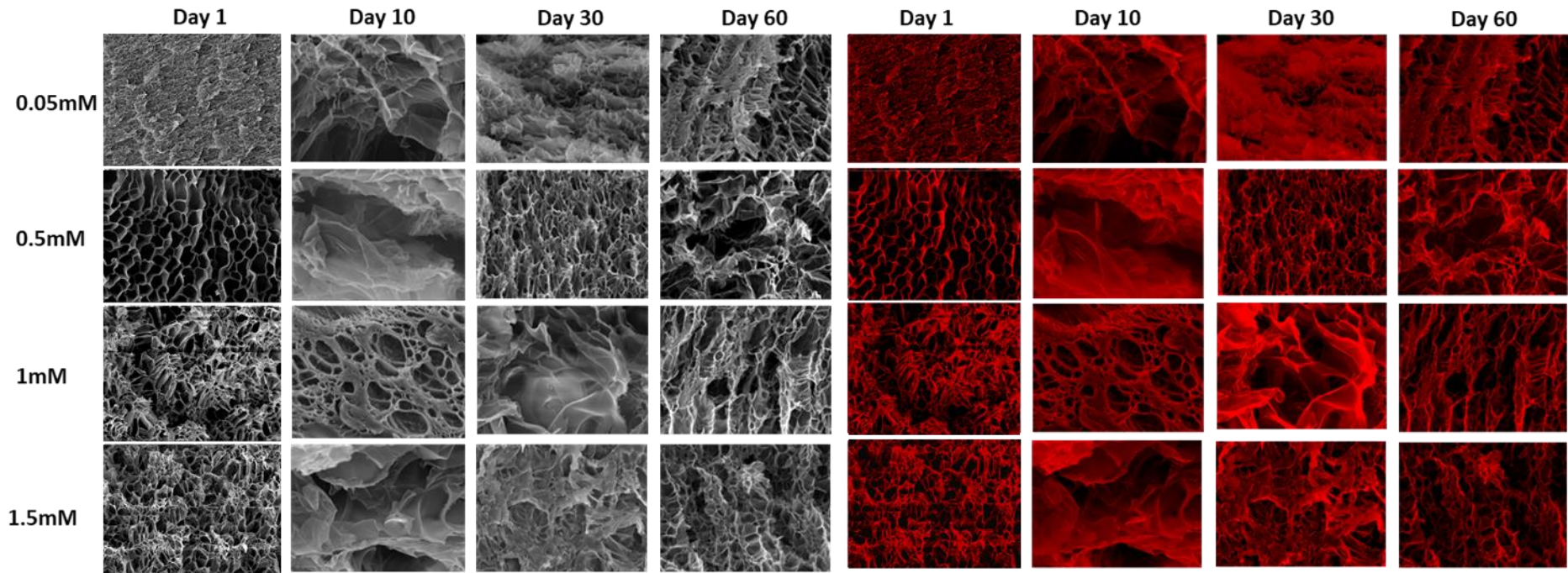
Figure 6.5: Calcium deposition characterization, SEM (left) and EDS (right) profile (cross view) of IOL samples preincubated in 0.01M PBS and immersed in different calcium concentrations at 37°C (red marks carbon as hydrogel, green marks calcium ions as calcium deposition).
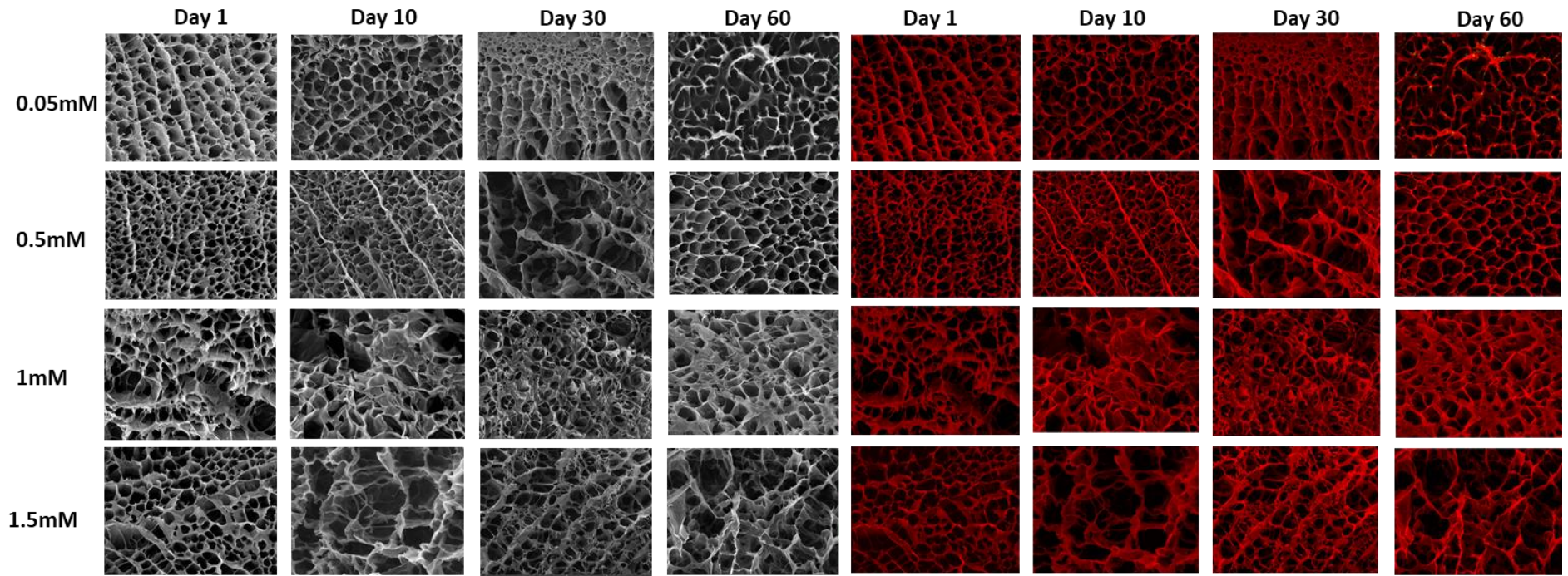
Figure 6.6: Calcium deposition characterization, SEM (left) and EDS (right) profile (surface view) of IOL samples preincubated in 0.01M PBS and immersed in different calcium concentrations at 37°C (red marks carbon as hydrogel, green marks calcium ions as calcium deposition).

6.2.6 The Bio-safety of the PAM Based IOL on LECs and ARPE19 Cells In Vitro

The bio-assessment of obtained IOL is critical which will be linked to the end application as an implant in the human eye. In this section, the cell culture experiment is performed to verify whether the PAM-based hydrogel meets the actual medical requirements [500]. And the experimental results showed below that confirmed the PAM-based hydrogel is a suitable material. The biosafety of PAH was first evaluated in vitro using human lens epithelial cells (LECs), and we cocultured the PAM with LECs and ARPE19 cells. The cultured cells positively expressed LEC markers, such as PAX6 and SOX2, and synthesized the specific α-A crystallin and negatively expressed the fibroblast cell marker α-SMA, which identified the LECs (**Figure 6.7 a-f**). When LECs were cocultured with the PAM, cell apoptosis emerged only at the adjacent area around the hydrogel (**Figure 6.7 g, h**). A similar result can be obtained when it is cocultured with ARPE19 cells [501].
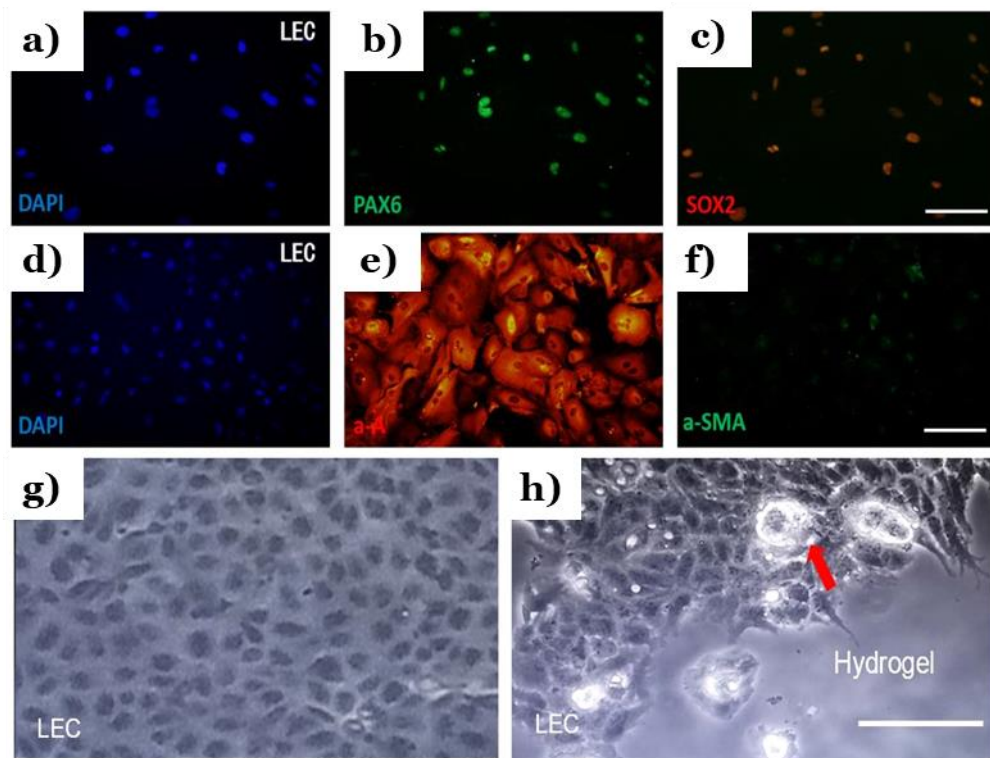
Figure 6.7: Coculture of PAM thin films with LECs or ARPE19 cells **a-f)**: Immunostaining of LECs showed that LECs were positively stained for the LEC markers PAX6 **a, b)**, SOX2 **c)**, and α-A crystallin **d, e)** and negatively stained for the fibroblast cell marker α-SMA **f)**; **g-h)**: Bright field images of LECs co-cultured with **h)** or without **g)** the PAM. Cells adjacent to the hydrogel were unable to attach to the matrix and ultimately underwent apoptosis (red arrow). Scale bar: 50 μm **a-f)**, 100 μm **g-h)**.

6.3   Summary

Combining 3D printing technology and the biocompatible hydrogel as the printing material, as well as a potential material for stimuli-responsive hydrogel fabrication, we propose the possibility of loading antibiotics, corticosteroids, and non-steroidal anti-inflammatory drugs into the IOL,

which integrates cataract surgery and postoperative treatments as a one-step procedure [502]. Moreover, IOLs can also be fused with telescopic lenses, presbyopia-correcting lenses, or accommodative polyfocal bio analogical lenses [503, 504]. These advanced designs could become more effective and personalized when combined with 3D printing and biocompatible hydrogels. However, all these IOLs inevitably require rigid biosafety assessments and more clinical studies to ascertain their safety and effectiveness.

The development of this responsive buckling induced configurable optical technology is a primary step in the translation of fundamental scientific knowledge into modern manufacturing technologies for future ocular implant product developments. Tunable focal length shifting has been characterized and demonstrated by the proposed PAM-based responsive morphing polyelectrolyte IOL devices. This concept benefits from a homogeneous "one material" approach, with great potential for adaptation to scalable, low cost, facile manufacturing process. Our research provides insight into the biosafety of PAMs in ocular tissue and demonstrates that PAM which hold great potential for future clinical applications, are a safe material for 3D printing of personal IOLs. The development of this responsive buckling induced configurable optical technology is also a primary step to translate fundamental scientific knowledge into modern manufacturing technologies for future ocular implant product developments.

Despite of the above achievements, some limitations do need our attention and therefore to be addressed in the future. The first one is the

timescale of buckling enabled optical tunning, which needs further validation for the practical application. The second one is optical focus which remain a big issue to meet the individual's needs as the natural IOLs are all in a 'customized' manner to fit in the human eye. The third one is the full bio-assessment, which will need significant work to complete in a long-term assessment with a biological environment.

Chapter 7

Theoretical Development

7.1   Theoretical Development

In my thesis, a number of analytical methods have been employed to cope with different scenarios, such as:

- A new theoretical concept of conductivity induced PDE was proposed to understand ion impacting on a conductive polymer surface and predict the surface evolution during FIB (**Chapter 4**). The ion bombarded surface topographic features with conductivity induced PDE are theoretically predicted using Monte Carlo simulation.

- The numerical analysis of the co-existence and the regional developments of buckling and creases collaboratively drive the global shape morphing of the gel structure from the 'open' state to the 'close' state (**Chapter 5**). Numerical analysis (**Chapter 6**) creates a phase diagram to understand the effects of the geometries and swelling ratio on the deformation induced actuation/sensing effect.

- Finite element simulations were conducted using the commercial software (ABAQUS) to model the gel as an incompressible Neo-Hookean material. Based on the analogy between heat transfer and solvent diffusion, thermal expansion was used here to simulate swelling, and the

corresponding coupled temperature-displacement analysis was conducted (**Chapter 5**).

In this section, we focus on a thin film with bilayer structure, where the top layer is an elastic surface after plasma treatment, and the bottom layer is an original elastic substrate. Such bilayers contain both non-linear properties of the material and non-linear geometry due to large deformation in thin film structure. In addition, there are also linear relations and linear transformations in the thin film. The phenomenon of buckling occurs when the structure is subject to tensile or compression which is illustrated by strain due to certain stress. With particular load applications and boundary conditions on the thin film, specific deformation can be observed in visualization.

7.1.1 Benchmarking the Simulation of Wrinkling

We utilize the PDMS for a specific subject of research, a type of hyper elastic material which is able to demonstrate non-linear properties of elasticity. There is also viscoelasticity which is the other mechanical property of PDMS. However, the study only involves in an analysis of statics, not a dynamic analysis. There is no consideration of temperature, hence, thermal dynamic properties and other properties which are a function of time are not taken into account during the study. We adopt the mechanical properties of Sylgard 184, which is a silicon base of PDMS elastomer from Dow Corning. The detailed properties are shown in **Figure 7.1**.
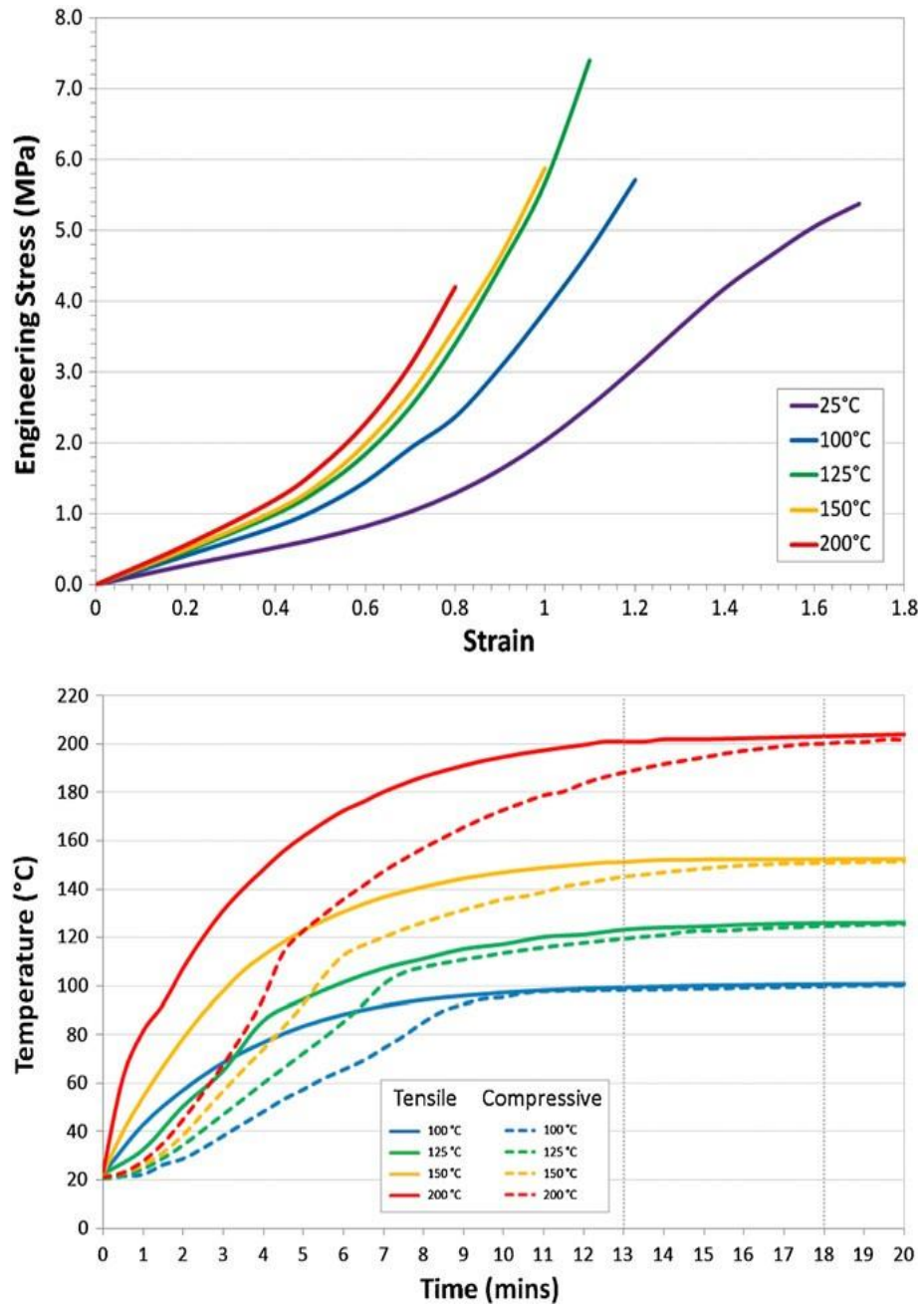
Figure 7.1: The top plot illustrates tensile stress-strain curves for the curing process at 25 °C, 50 °C, 125 °C, 150 °C, 200 °C. The bottom plot demonstrates the propagation of proposed temperature by heating during different tests [505].

Using the Finite Element Analysis (FEA) and Computer Aided Design (CAD), we design and simulate the surface morphologies under different conditions at the top layer of thin film. The analysis only contains elastic properties, such as density, in the mechanical property and general property sections. As a hyper elastic material, the stress-strain diagram of PDMS is nonlinear. Therefore, mechanical elastic properties of PDMS do not obey Hooke's Law, which is written as follow:

$$U = \frac{1}{2}E\varepsilon_1^2 \qquad \textbf{Equation 7.1}$$

$$\varepsilon_1 = \frac{F}{EA} \qquad \textbf{Equation 7.2}$$

U is strain energy density of linear elastic materials; E is Young's Modulus; ε_1 is principal strain with applied stress; F is compressive or tensile force; A is cross-sectional area.

Hence, a particular method for calculating the potential strain energy should be applied. In addition, for non-linear property of material, experiment data cannot be utilized directly in ABAQUS until it is converted into recognized parameters with a particular algorithm. There are many potential strain energy algorithm models for hyper elastic material, because PDMS is a rubber-like material. 3 energy models are most often utilized for rubber-like materials, which are Neo-Hookean, Mooney-Rivlin and Ogden. The Neo-Hookean Model is appropriate for PDMS, and the density of potential strain energy is as follow:

$$U = C_1(\bar{I}_1 - 3) + \frac{1}{D_1}(J^{el} - 1)^2 \qquad \textbf{Equation 7.3}$$

U is strain energy density, the strain energy per unit of reference volume; C_1 and D_1 are relative parameters of elastic modulus as defined below:

$$\mu_0 = 2C_1 \qquad \qquad \textbf{Equation 7.4}$$

$$K_0 = \frac{2}{D_1} \qquad \qquad \textbf{Equation 7.5}$$

μ_0 is the tangent modulus which is equal to $\frac{E}{2(1+v)}$; K_0 is the bulk modulus which is equal to $\frac{E}{3(1-2v)}$; E is the elastic modulus and v is the Poisson's Ratio.

$\bar{I}_1$ is first deviatoric strain invariant of the left Cauchy-Green deformation tensor defined as:

$$\bar{I}_1 = \bar{\lambda}_1^2 + \bar{\lambda}_2^2 + \bar{\lambda}_3^2 \qquad \qquad \textbf{Equation 7.6}$$

Where the deviatoric stretches $\bar{\lambda}_i = J^{-\frac{1}{3}}\lambda_i$; J is the total volume ratio and λ_i are principal stretches; J^{el} is the elastic volume ratio with "Thermal expansion" [506].

However, due to property of incompressible material (PDMS), which means that Poisson's Ratio is 0.5 in ideal circumstances, following $\frac{E}{3(1-2v)}$, magnitude of bulk modulus will be close to 0.

As shown in the literature review, there is a specific wrinkling model that is marked for significant parameters of wrinkle, with wrinkling which contains constant uniaxial compression and appropriate substrate. Assuming no delamination for the model, the pattern on the surface of the entire buckling mode is an almost sinusoidal curve and indicates the wavelength λ, amplitude

A of the curve, within a small range of deformation. Furthermore, the significant parameters are critical strain ε_C, elastic modulus of substrate $\bar{E}_f$ and top layer $\bar{E}_s$. With an incompressible specimen, which means that Poisson ratio ν is equal to 0.5, the relation between $\bar{E}_f$ and elastic modulus of material *E* can be obtained [507].

Wavelength: $\lambda = 2\pi h(\frac{\bar{E}_f}{3\bar{E}_s})^{\frac{1}{3}}$ **Equation 7.7**

Amplitude: $A = h(\frac{\varepsilon}{\varepsilon_c} - 1)^{\frac{1}{2}}$ **Equation 7.8**

Critical strain: $\varepsilon_c = \frac{1}{4}(\frac{3\bar{E}_s}{\bar{E}_f})^{\frac{2}{3}}$ **Equation 7.9**

Relation with tow modulus: $\bar{E}_s = \frac{E}{(1-\nu^2)}$ **Equation 7.10**

In our simulation based on ABAQUS, which is a numerical method for simulating the wrinkling, appropriate and specific data should be inputted in the software which contains material properties, features of the particular model, constraint for demand, etc. The first aim is to analyse wrinkling of a bilayer thin film without any pattern. The top surface, which is PDMS is plasma treated and bottom is substrate which is only comprised of PDMS without any treatment. There are two different material properties in the entire model.

In the module of part design, **Figure 7.2** illustrates the side view of the bilayer structure without pattern on the surface. With plasma treatment, the stiffness of the top surface is converted into an extremely high level, but the stiffness gradually decreases as depth increases. Stiffness follows the gradient distribution in depth direction, and it is difficult to draw a fixed dividing line

between the thin film and substrate. In simulation, the homogeneous part should be used, and a fixed dividing line must be used. Thus, the average thickness of a surface layer which has the maximum stiffness will be applied. Thickness T_f of thin film which is treated by plasma is between 20nm (0.02 μm) and 100nm (0.1 μm). In general, thickness T_s of substrate is about 50 to 200 times greater than thin film. In addition, it is conditional upon the theoretical amplitude and applied strain, which means that the thickness of substrate must be larger than the theoretical amplitude. Moreover, when the applied strain is increased, the wrinkling will be turned into a different type of phenomenon. In simulation, for holistic mesh quality and quantity, the recommended thickness T_s is 100 times greater than thin film.
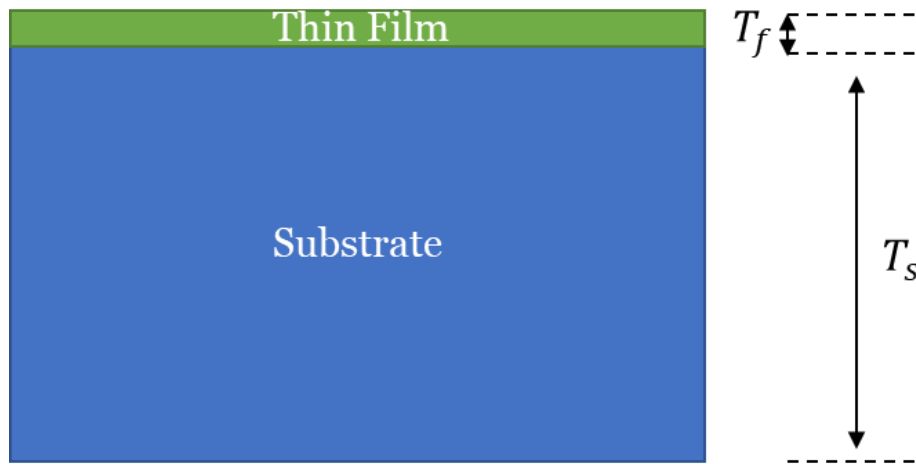
Figure 7.2: The side view of the bi-layer design with geometrical definition.

The 3D deformation model in Abaqus is utilized for obtaining concretely visual phenomenon. However, with consideration of precision and computational efficiency, the type of model will be converted into another equivalent model and will depend on the practical results in the simulation

process. In simulation, for material properties of substrate, the experiment data, which is obtained through uniaxial tensile test, is used for the Neo-Hookean Model. In addition, the significant parameters of material property, the tangent modulus, bulk modulus, etc., will be extracted from the method. For material properties of the top thin film with plasma treatment, the elastic property is defined as linear and elastic modulus is much greater than substrate. In addition, owing to mineralization, the range of Poisson's Ratio of thin film is between 0.3 and 0.35 in general.

The boundary conditions include the constraint between thin film and substrate, displacement load condition, which is symmetric compressive load, and constraint for degree of freedom at the bottom of substrate. The displacement load is able to show the precise applied strain directly. For both no pattern thin film and pattern thin film, the range of applied strain ε is 1% to 60%, moreover, some typical strain is applied, such as 5%, 10%, 15%, 20%, 30%, 40%, 50% and 60%. Nevertheless, restricted to computational efficiency and limitation of software for mesh quality and quantity, the analysis might be interrupted. Forasmuch as the excessive distortions of element are caused by large deformation, the applied strain might be decreased depending on actual analysis process.

According to the actual process, the core segment, specific analysers for simulation, contain two descriptions in ABAQUS, the standard/implicit analyser and the explicit analyser. The implicit analyser is based on the Newmark-beta method which is a method used for static analysis. Therefore, the non-linear analysis in implicit analyser will not be included in the section

about timescale. Moreover, the solution is worked out by the stiffness matrix of non-linear static equilibrium equations. Nevertheless, owing to iterations and convergence in the stiffness matrix, the convergence result may not be founded in the implicit analyser, especially for large deformation in which the compressive strain is more than approximately 5% in PDMS analysis. Consequently, the explicit analyser is based on time-scale dynamic analysis and there is no stiffness matrix in the calculation process. The process contains more varieties of parameters, for instance, a time period for each load step, a relationship between time and amplitude of specific load defined as demand, etc. The time period will be increased on account of precision. If a load in a step is defined in a time period which has insufficient numbers of increments, the magnitude of each increment would be very large so that would cause the distortion problem. In general, time for the similarly precise result which is worked out by the explicit analyser is greater than that worked out by the implicit analyser. However, the explicit analyser without iteration and convergence is specialized in large deformation problems which cannot be calculated by the implicit analyser.

For the mesh module in simulation, a hybrid formulation of element type is applied on substrate, which is comprised of the hyper elastic material, PDMS. The elements of the top layer treated by plasma do not need to use the hybrid formulation. Because of the accuracy of wrinkling analysis, the element shape must be hex or hex- dominated. The holistic mesh control technique for no pattern thin film and substrate should be defined as structure strategy. Moreover, for pattern on a surface, it should be swept with a medial axis

algorithm. The density of seeds for meshing the model requires the data to be calculated from an analytical method. The length on the aspect of compression direction for each element must be less than the theoretical value which is obtained by calculation. In addition, for patterns on surface, the number of seeds in the edge of patterns should be appropriate throughout the attempts in order to ensure the quality of most of the elements and regular alignment for holistic array. This is because the shape of patterns and aspect ratio of each pattern will make the model complicated in structure and cause excessive distortion of elements.

In the post-processing of analysis, the output field should contain a contour of deformation and distribution of stress, and the stress contour needs to be distinguished by different colours. The number of frames in the output field should be set to 50 to 100, these frames illustrate the morphological feature due to applied strain in the process of increasing the displacement load.

Figure 7.3 illustrates the simulation results for wrinkling. The parameters of the model contain length L=100 μm, width W=100 μm, thickness T_f =0.1 μm and T_s =5 μm. The contour profile of the surface is shown as approximately a sinusoidal curve. Stress on the two edges which were under the loads is highest. Then, the trough of the sinusoidal curve is the second highest area for stress. The theoretical result is that the wavelength λ is equal to 6 μm and amplitude A is equal to 0.4151 μm. Utilizing the numerical method, and observing the contour of simulation with measurement, the actual result

λ_0 is equal to 5.7145 μm and amplitude A_0 is equal to 0.4653 μm. In addition, all results and basic parameters are summarized in the **Table 7.1** as below.
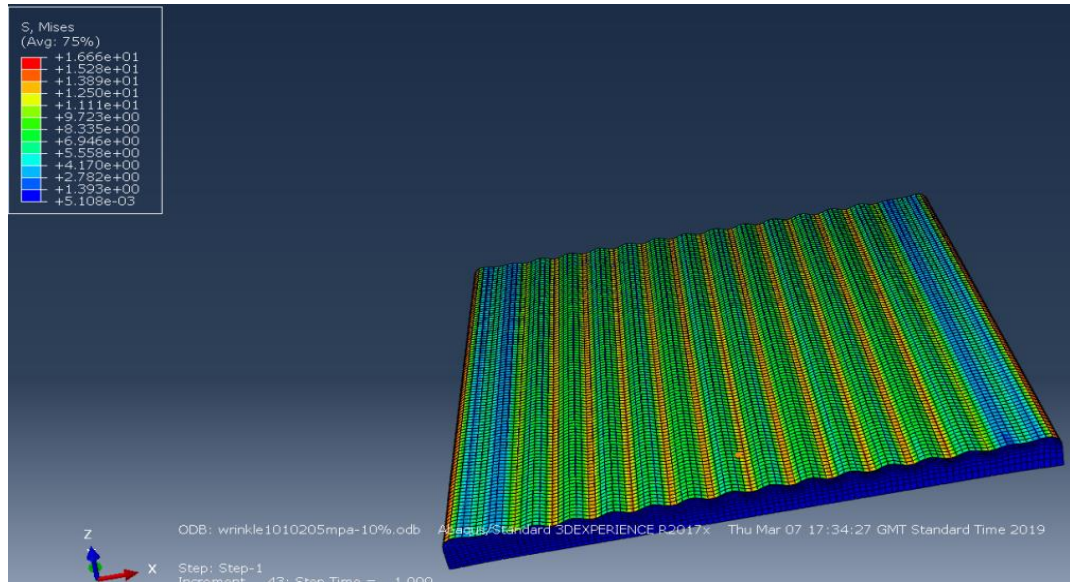
Figure 7.3: The simulation result for wrinkling on the bilayer.

As illustrated by **Figure 7.4**, the wrinkling is presented in 2D model. The initial 2D model is extracted from the 3D model, generated from the cross section of front view of the 3D model. The morphological feature of the thin film is clear, and the profile approximately follows the sinusoidal curve. The elastic modulus of the thin film with plasma treatment is E_f =1225 Mpa.
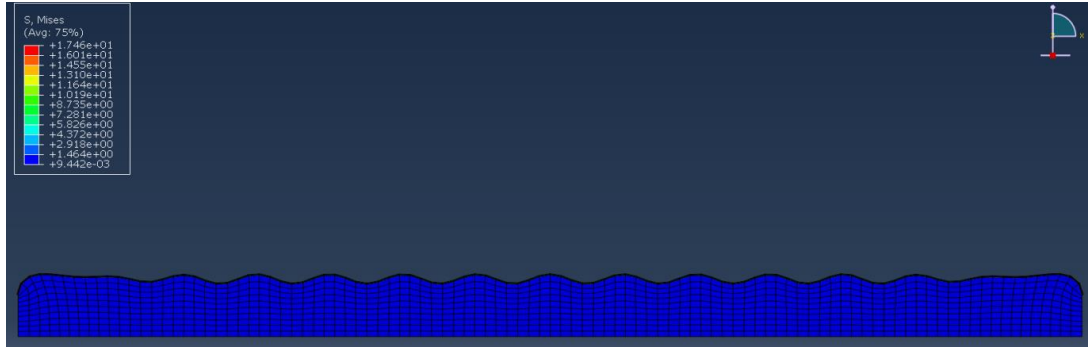
Figure 7.4: The cross-section view of the simulated wrinkle with the implicit analyser.

Moreover, the sinusoidal curve is gradually generated, and the distribution gradually becomes homogeneous from two sides to the centre of the model. There is no Width in 2D analysis. The theoretical result wavelength λ is equal to 6 µm and the amplitude A is equal to 0.4151 µm. Utilizing the numerical method, in the visual post-processing of the simulation, the actual result λ_0 is equal to 5.71898 µm and amplitude A_0 is equal to 0.4715 µm. All results and parameters are summarized in the **Table 7.1**.

Table 7.1: Data collection for simulated wrinkle with the implicit analyser.

Applied strain (ε)	Basic parameters of model			Analytical method		Numerical method	
	Thickness (T_f)	Thickness (T_s)	Length (L)	Wavelength (λ)	Amplitude (A)	Wavelength (λ_0)	Amplitude (A_0)
5 %	0.1 µm	5 µm	100 µm	6 µm	0.4151 µm	5.7189 µm	0.4715 µm

We next applied a higher density of elements (Elastic modulus of thin film with plasma treatment E_f =22466Mpa) as utilized in other 2D simulations. **Figure 7.5** illustrates the wrinkling at higher compression in 2D view.
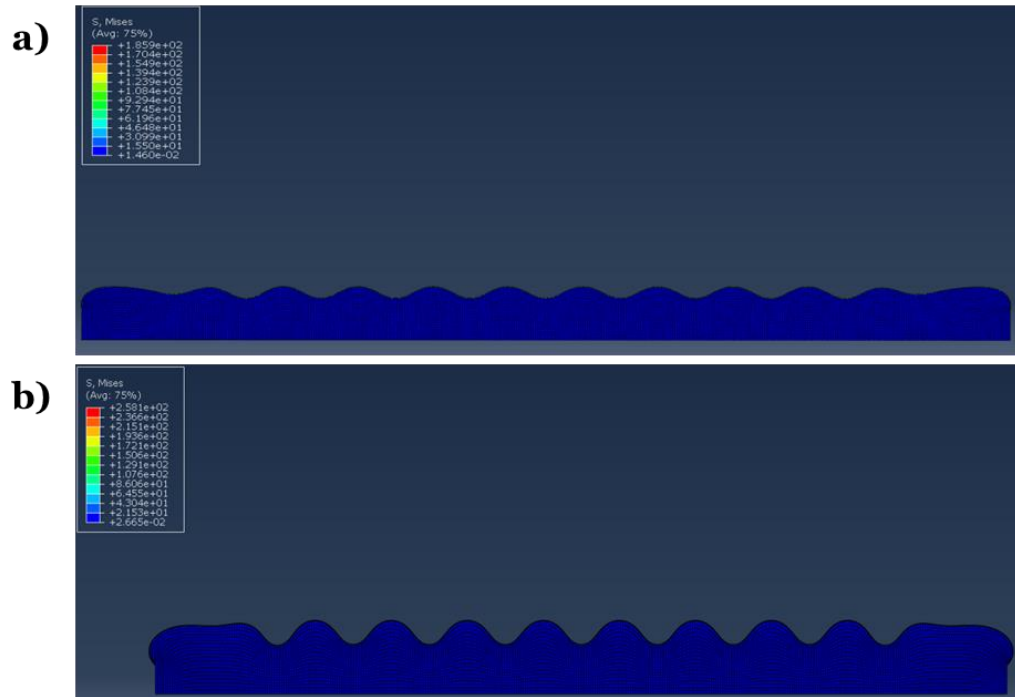
Figure 7.5: Illustrates the deformation of the model at an applied strain a) 8%, b) 20% with implicit analyser.

The theoretical result wavelength λ is equal to 15.8196 µm and the amplitude A is equal to 1.4208 µm. Utilizing the numerical method, in the visual post-processing of the simulation, the actual result λ_0 is equal to 14.9778 µm and amplitude A_0 is equal to 1.3032 µm. Moreover, maintaining the basic parameters of the model, **Figure 7.5 b** illustrates the deformation of the model when the applied strain was increased to 20%.

Table 7.2: Data collection for simulated wrinkle at higher elements with the implicit analyser.

Applied strain (ε)	Basic parameters of model			Analytical method		Numerical method	
	Thickness (T_f)	Thickness (T_s)	Length (L)	Wavelength (λ)	Amplitude (A)	Wavelength (λ_0)	Amplitude (A_0)
8 %	0.1 µm	10 µm	200 µm	15.8196 µm	1.4208 µm	14.9778 µm	1.3032 µm
20 %	0.1 µm	10 µm	200 µm	15.8196 µm	2.3998 µm	14.4130 µm	2.2345 µm

By reducing the length, **Figure 7.6** illustrates the deformation of the model when the applied strain was increased to 40%. The curve on surface is converted to another complicated shape from the sinusoidal curve. The amplitude of the outboard waves decreases and those of central wave increase gradually, and then the position of the outboard waves move slowly to the centre with the increments of applied strain. The previous perpendicular lines of the crest of the outboard waves incline to the centre of the model and the profiles of the outboard waves tend to touch each other and are closed at the position of the trough of the central wave.
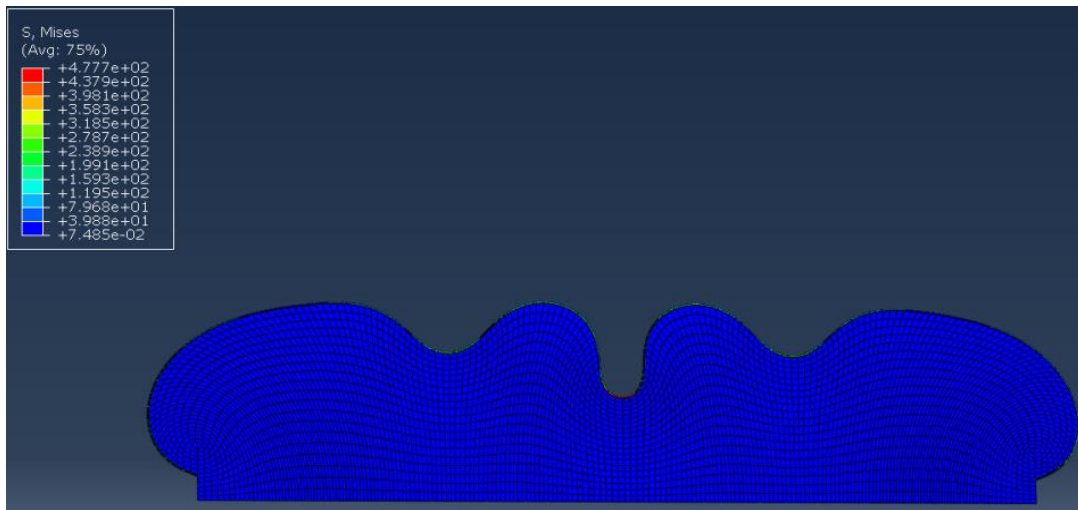
Figure 7.6: The illustration of the model at an applied strain 40% with implicit analyser.

We then perform the two-dimensional simulation of the explicit analyser with the elastic modulus of thin film with plasma treatment E_s =1225Mpa. The thickness of the thin film T_f was reduced to 0.02 μm and the explicit analyser was applied for the simulation. The time period was defined

as 15000. As illustrated in **Figure 7.7**, the distribution of the sinusoidal curve is similar to **Figure 7.4**.

Figure 7.7: The cross-section view of simulated wrinkle with the explicit analyser.

The wavelength λ and amplitude A are reduced to 1.1998 μm and 0.1465 μm with decreasing thickness T_f. Through observing the contour, the wavelength λ_0 and amplitude A_0 are 0.9951 μm and 0.1557 μm. All results are summarized in **Table 7.3** as below.

Table 7.3: Data collection for simulated wrinkle with explicit analyser.

Applied strain (ε)	Basic parameters of model			Analytical method		Numerical method	
	Thickness (T_f)	Thickness (T_s)	Length (L)	Wavelength (λ)	Amplitude (A)	Wavelength (λ_0)	Amplitude (A_0)
15 %	0.02 μm	4 μm	100 μm	1.1998 μm	0.1465 μm	0.9951 μm	0.1557 μm

With the further increase of applied strain, **Figure 7.8** illustrates the other type of buckling modes which are different from the wrinkling phenomenon on the thin film. The sinusoidal curve in wrinkling is converted into homogeneous doubling which has a particular profile. There are obvious gaps between each doubling. The profile of doubling is comprised of two

oblique and closed sinusoidal curves when they are in the wrinkling. In addition, the profile of each doubling is similar to the shape of the outboard wave in **Figure 7.6** but show much more homogeneity on the overall distribution. As the applied strain increases to 30%, doubling is converted into a new buckling mode, which is defined as crease. The curved edges of doubling coalesce into a line. There are closed boundaries at specific intervals in the crease. It worth noting that the simulation through the explicit analyser will be more time consuming (300% time longer), therefore, we will apply the implicit analyser to carry on the following work.
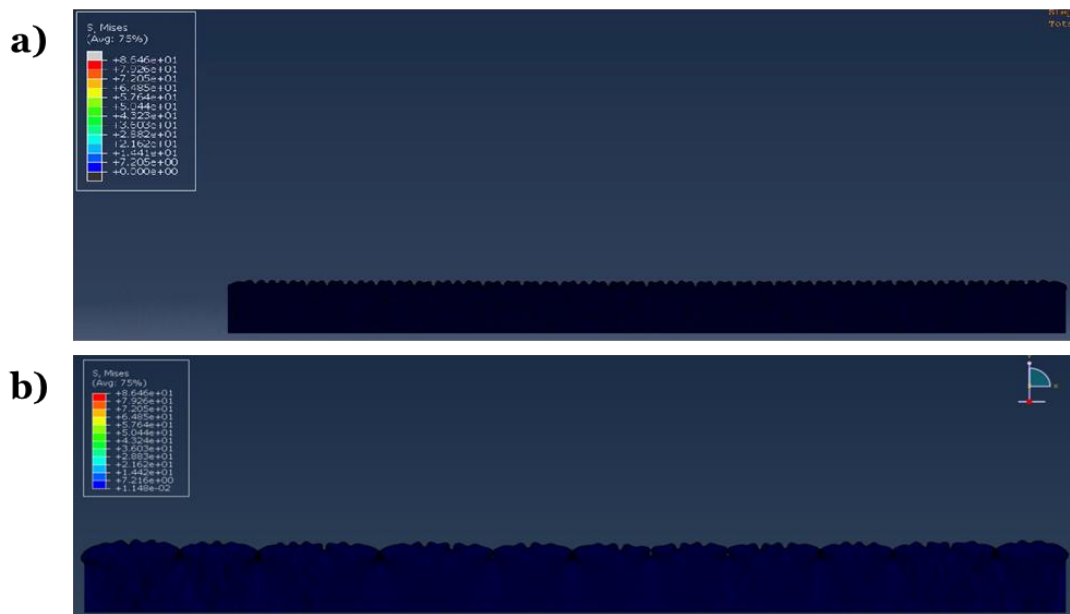
Figure 7.8: Illustrates the deformation of model at an applied strain a) 20%, b) 30% with explicit analyser.

7.1.2 The Simulation of Wrinkling on Patterned Surface

We also analysis the wrinkling on the surface with a micro-pattern. Through the analysis, the contour in post-processing can demonstrate the

effect of in-plane stress and stress-induced which appear owing to the pattern array on wrinkling. As shown in the **Figure 7.9**, the basic pattern is a circle. The proportion of diameter d_0 of each circle to the distance of each centre of circle d is defined as aspect ratio α, shown as $\alpha = d_0 : d$.
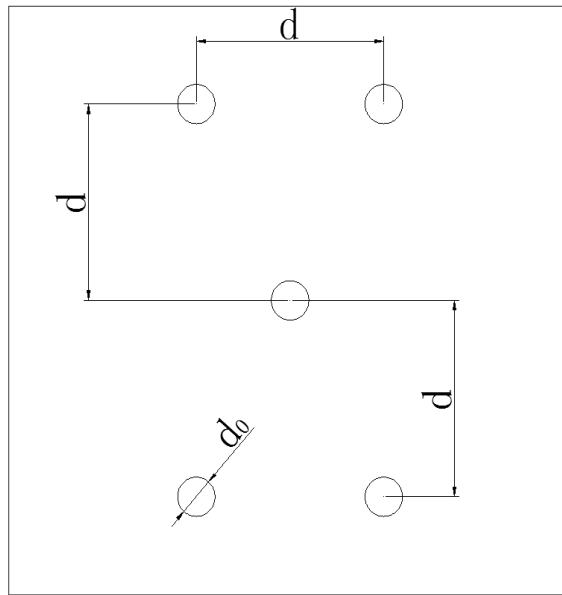
Figure 7.9: The design and geometrical definition for a patterned surface.

In addition, the circular blind hole will occur throughout the entire thin film and penetrate into the substrate. Adequate depth of the blind hole is essential to observe obvious features of wrinkling with in-plane stress. In simulation, with consideration of mesh quantity and quality, appropriate depth is approximately half the diameter of circle. The Aspect Ratio and applied strain are independent variables in analysis. Different values of these variables can affect the nature of in-plane stress in wrinkling. The morphological features of specimens have already been observed from experiments with SEM, and this will be illustrated as distribution of in-plane

stress by post-processing. Moreover, for adaption of the particular size of the pattern, the width, length and thickness of substrate might be changed, which means the magnitude is different from the no pattern model. However, the thickness of thin film will not

be changed.

We first simulate the wrinkle formation on a patterned surface with a single hole (data set shown in **Table 7.4**). **Figure 7.10** illustrates that the strain energy localized area 10 of the highest stress is located in the two troughs of wave.

Table 7.4: Data setting for simulating wrinkle on a patterned surface with a single hole through the explicit analyser.

Applied strain (ε)	Basic parameters of model							
	Thickness (T_f)	Thickness (T_s)	Length (L)	Width (W)	Depth of pattern (h)	Diameter (d_0)	Elastic modulus (E_f)	Aspect ratio (α)
6.26%	0.1 μm	10 μm	200 μm	200 μm	5 μm	40 μm	4136 Mpa	1:5

Figure 7.10: The simulation result for a patterned surface with a single hole with the implicit analyser.

The white arrow symbolizes the highest strain energy localization at two sides of the circle pattern at the original state and the red arrows represent the strain transporting areas around the hole. With the applied strain gradually increasing, the energy localization is symmetrically distributed in the annular regions located in a direction which is perpendicular to compressive direction.

We perform the simulation on the wrinkle formation on a patterned surface (**Figure 7.11**) with four holes (data set shown in **Table 7.5**). **Figure 7.11** illustrates that the distribution of in-plane stress and the profile of wrinkling are similar to the no pattern thin film in **Figure 7.3**. The waves of wrinkling cross over the circle and circle patterns are compressed into ellipse. The area of Highest stress is located in the trough of the central wave and the

crest of the wave on the circle patterns. There are also small areas around four

patterns subject to the second highest stress.

Table 7.5: Data setting for simulating wrinkle on a patterned surface with the explicit analyser.

Applied strain (ε)	Basic parameters of model							
	Thickness (T_f)	Thickness (T_s)	Length (L)	Width (W)	Depth of pattern (h)	Diameter (d_0)	Elastic modulus (E_f)	Aspect ratio (α)
20%	0.1 µm	10 µm	100 µm	100 µm	5 µm	10 µm	22466 Mpa	1:5

Figure 7.11: The simulation result for a patterned surface with four holes with the implicit analyser.

In **Figure 7.12**, four figures demonstrate four typical states which follow the applied strain sequence in the compressive process. The in-plane stress increases from area 2 of the cross shape where the cross shape is based on the centre of thin film and the four centre of circle pattern (**Figure 7.12 a**). The lower stress area is symmetrically arranged at both sides which is shown as elliptical area 1 of the centre line of the circle pattern in a compressive direction. In addition, the three relative magnitude of stress areas are represented as the sequence of green, pale blue and dark blue; green is the highest and pale blue is lowest. With an increasing load, the holistic in-plane stress increase. However, the relative in-plane stress follows the distribution in **Figure 7.12 b**. The stress in area 3 and area 4, which is located on the central ellipse area of two circle pattern is lower than other areas. The area 4 has the tendency of vertical elongation and is converted into a similar shape as in **Figure 7.12 a**. With an increasing load, the shape is similar to that shown as Figure 7.12 c. However, in **Figure 7.12 d**, the distribution of relative in-plane stress is different from the previous figures. The area of higher stress is located on the area 5 where the cross areas based on the circle patterns are combined with strip areas on two sides and turn into a complicated shape.
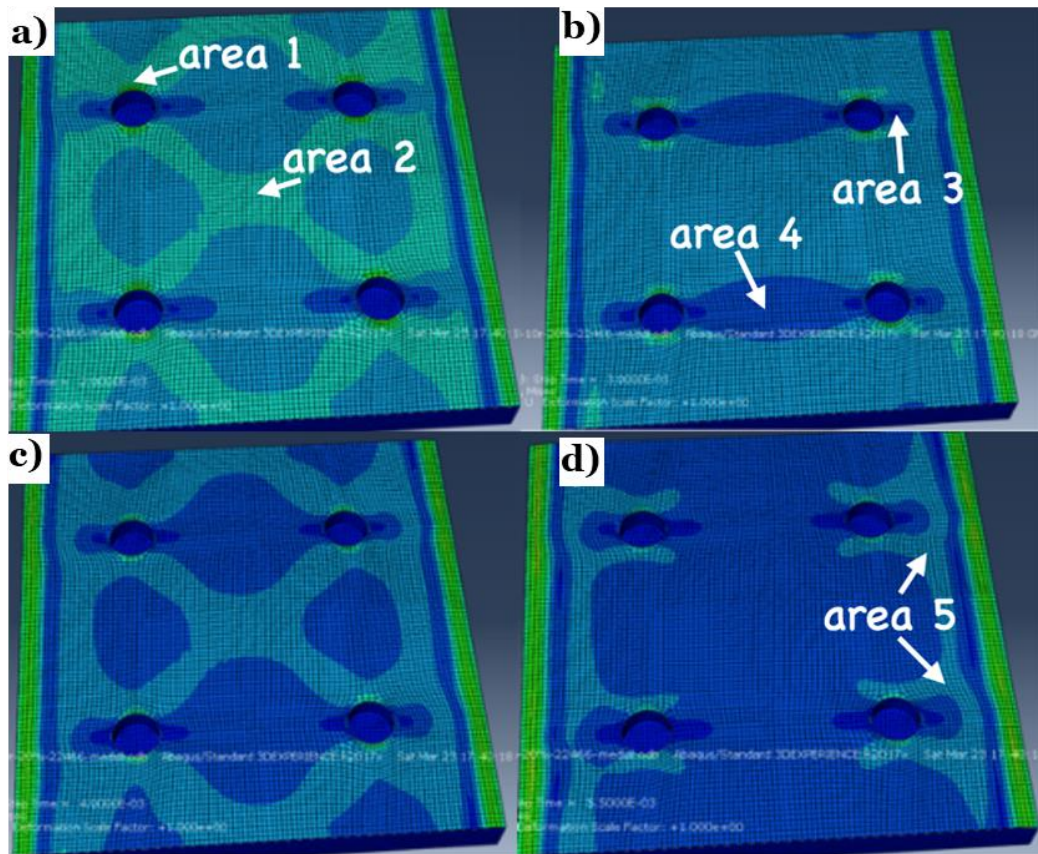
Figure 7.12: The simulation result for a patterned surface with the implicit analyser to show four typical states which follow the applied strain sequence in the compressive process, a) 2 %; b) 4%; c) 6%; d) 8%.

7.2   Summary

From **Section 7.1.1**, there are substantial differences between the implicit analyser and the explicit analyser. In the applications of the implicit analyser shown previously, the highest applied strain is 40%. However, there is only wrinkling with no buckling phenomenon. In order to simulate other modes of buckling, utilizing the analytical method of wrinkling, three effective ways to simulate another phenomenon can be used. These are reducing the

thickness of thin film, decreasing the value of elastic modulus and increasing applied strain correspondingly.

Nevertheless, in the simulation of the implicit analyser the convergence problem causes excessive distortions of elements which means the result of the further applied stain cannot be obtained. Therefore, the explicit analyser is utilized which means the time of calculation only depends on the time period and amount of elements. The results of the explicit analyser are demonstrated in **Section 7.1.1**. The elastic modulus of thin film is redefined as 1225 Mpa; the thickness of thin film is 0.02 μm; the applied strain is 15 %. The difference of wavelength and amplitude between the analytical results and the numerical results are

$$\frac{|\lambda - \lambda_0|}{\lambda_0} * 100\% = \frac{|1.1998\ \mu m - 0.9951\ \mu m|}{1.1998\ \mu m} * 100\% = 17.1\%$$

and

$$\frac{|A - A_0|}{A_0} * 100\% = \frac{|0.1465\ \mu m - 0.1557\ \mu m|}{0.1465\ \mu m} * 100\% = 6.28\%.$$

Through the difference of Amplitude, the result of the explicit analyser has sufficient accuracy, with limitations. However, the difference in wavelength is unusual because the simulation is probably the period of transition between wrinkling and doubling. However, the explicit analyser normally takes 300% time of that with the implicit analyser. Considering our focus on wrinkling (normally under 40 % strain), we apply the implicit analyser to the simulate patterned surface.

For the patterned surface with a single hole, we aimed to look into the feasibility, improve the precision and save the capacity of the computer. The model can be optimized through local pattern simulation, such as a one-hole pattern. From **Figure 7.10**, the distributions of in-plane stress for load process and final result are clear and symmetric. When the applied strain increases, waves of wrinkling firstly occur at two sides of the pattern and maintain a certain slope in the direction that is perpendicular to the compressive direction. The above simulation agrees well with our previous reported phenomenon [252]. The simulation on wrinkle formation on the surface with multiple holes (hole array) clearly shows the progression of strain energy concentration. **Figure 7.11** illustrates that the highest stress is distributed in the position where the wave and pattern overlap. Since localization of strain energy is subjected to the influence of pattern array and wrinkling, it is turned into the waviness at two sides of each pattern. However, the stress distribution on troughs and crests of waves is not homogeneous in the direction which is perpendicular to the compressive direction.

Chapter 8

Conclusion and Future Work

8.1 Conclusion

Additive manufacturing (AM) has been considered as an important steering technology that can realize this vision of future manufacturing in the engineering sectors, including automotive, energy, aerospace, civil, healthcare and biomedical. AM re-innovate the manufacturing concept by offering more freedom of design, higher level customization, more capacity with multimaterial fabrication, good flexibility to facilitate complex geometry, and mass customization at reasonable cost. While the paradigm of AM assisted manufacturing technique was poised to transformative bio-medical and healthcare areas at the very beginning, this transition from lab to fab is highly dependent on the advances in the materials and advancement of AM technologies as well as improved methods for digital design. There is a tremendous potential for applying AM technologies in the design of personalized and precise healthcare/medical devices to improve the experience of patient during treatment, to perform/deliver therapeutics more efficiently. Combination of AM with bio-inspired digital design is a critical enabling approach for the rapid and versatile fabrication of customized structure/device, to achieve unique structure-property relationship.

This PhD project aimed to explore and understand the manufacturing engineering of bio-inspired structure, especially through an additive manufacturing route. I investigated the manufacturing of soft material system first (Chapter 4) by studying how to achieve a functional polymer surface via a highly efficient FIB based fabricating strategy, which has control over the surface roughness. I extended the precision manufacturing approach and the nanofabrication on dedicated structure. The combined materials study included how to fabricate the composites and how to prepare the conductive materials and surface. Various factors influenced in the FIB process on soft surface, such as milling voltage, temperature, beam overlap, and mechanical stability of soft samples. I focus on studying the impact from the conductivity, based on the polystyrene-based material system. Minor chemical changes were induced in the coal samples during FIB-SEM preparation, and little effect was observed by changing ion-beam parameters. The key development was the polymer positive diffusion effect (PDE) for an ion-bombarded polymeric hybrid surface through FIB technology. The conductivity induced PDE constant was discussed as functions of substrates conductivity, ion energy and flux. The theoretical results agreed well with the experiential results on the conductivity induced PDE, and thus yield good control over roughness and patterning milling depth on the fabricated surface. A demonstration was made with a controllable surface wettability in hydrophobic and superhydrophobic surfaces (contact angles (CA) range from 108.3° to 150.8°) with different CA hysteresis values ranging from 31.4° to 8.3°.

Hierarchical instabilities are expected to have many applications such adhesion enhancement, wetting control with super hydrophobic/hydrophilic surfaces including anti-biofouling. The post-buckling evolution and the directional transformation among them have been considered as useful means to offer a transition of energy. Regarding to different hierarchical morphologies, it is essential to guide formation of surface pattern, to lead a higher control of structure morphing. Throughout this research work, the responsive soft material system such as stimuli-responsive gel, play a critical role to realize the bio-inspired structure/device. I developed programmable shape morphing of a three-dimensional (3D) curved gel structure (**Chapter 5**) by harnessing multimode mechanical instabilities during free swelling. The 3D printing mould was used to achieve the gel structure in the desired shape. First of all, the coupling of buckling and creasing occurred at the dedicated region of the gel structure. The subsequent developments of post-buckling morphologies and crease patterns collaboratively driven the structural transformation of the gel part from the "open" state to the "closed" state, thus realizing the function of gripping. By utilizing the multi-stimuli-responsive nature of the hydrogel, the swollen gel structure can recover to its initial state, enabling reproducible and cyclic shape evolution. The described soft gel structure capable of shape transformation brings a variety of advantages, such as easy to fabricate, large strain transformation, efficient actuation, and high strength-to-weight ratio, and is anticipated to provide guidance for future applications in soft robotics, flexible electronics, offshore engineering, and healthcare products.

From the application perspective, the research scope has also been extended to create a focal-length tuneable intra-ocular lens (IOL) device has been realized by a standard-shaped, homogeneous "one material" system. Different to existing technologies, this poly(N-isopropylacrylamide) gel (PAM) based polyelectrolyte system doesn't require any additional materials (e.g., metal electrodes, movable mechanical structures) to achieve a controllable lens shape transformation for the focal-length shifting actuation. We utilize buckled hydrogel as a dynamic platform to shift the focal length and demonstrated that using temperature as a stimulus to tune the different strain states and amplitudes, and cultured cells to test the bio-compatibility. The designed morphological deformation mechanism employed ionic-strength responsive mechanical buckling via controlled swelling of PAM in phosphate buffered saline (PBS) with similar concentration to human eye liquid. The biosafety of PAM was first evaluated in vitro using human lens epithelial cells (LECs) and the ARPE19 cell line, this unique approach will unlock great potential in a wide range of smart ocular applications. Compared to the current commercially available IOL devices, our design enables the in-situ control of bio focal length while programmable mechanical deformations are applied, thus introduces a versatile tool.

From the theoretical aspect, the simulation and analyse of deformation of soft elastic bilayer, by considering Neo-Hookean model and the hyper elastic behaviour of material. I have scoped literatures to obtain the specific parameters of the analysis, such as the hyper elastic material properties. Moreover, the essential theories will be obtained from literatures and to be

guided by the prospects or conjectures of literatures. I designed thin film models with suitable size and physical attributes. Different models were simulated on the FEA software separately. I combined finite element method and hybrid computational techniques for multi-scale analysis. Different analysis results of different patterns on the top layer have been indicated and compared through the visualization plot. The comparison of analysis illustrated a conclusion of the wrinkling model on elastic surface with and without patterns. However, more efforts are still needed to develop reliable numerical methods to resolve 2D or 3D calculations depending on the specific design, which require large element number and calculate time, of detecting bifurcation of equilibrium configuration of potential with multiple quasi-convexities, of simulating dynamics formation of elastic instabilities and the associated global shape transformation/motion.

Throughout my 3D printing practice with many designs, I have managed to create numerous designs even at micro scale level to realise the advanced properties. A systematic solution for a digitally driven 3D printing and direct write technologies will allow complexity and versatile control on the manufacturing, which need be facilitated. When applying the 3D printed mould with responsive materials, such as hydrogels, we can facilitate the desired prototyping with extra rooms to adjust the design. I envision a strategy where these technologies and processes are integrated into the numerical workflow to realize the unique product, where our multidisciplinary team members who collaborate from the point of diagnosis and therapeutic to testify the application. Despite the encouraging future for AM assisted fabrication of

bio-inspired structure, many future challenges and research opportunities remain prior to broad implementation of this paradigm.

8.2   Future Work

A major challenge in the scale up manufacturing and implementation of bio-inspired personalized products is the balance between unique structure-property relationship with customization and broad utility. The development of precision bio-inspired structure with AM assisted manufacturing route for ultimate customization, can introduce additional steps and cost in the design and processing. While the innovation on producing a specific material to fit the application are advancing rapidly, the cost–benefit balance still remains unclear. From this perspective, the approach to reduce the cost for precision manufacturing appears more feasible.

During my attempt to explore the precision manufacturing on the surface of cost-effective polymer (compared to other candidates), there are some technical barriers to be overcame. It must be noted that the ion bombardment on macromolecular system is far more complicated than the silicon one. It would be very interesting to look into the ion sputtering on a conductive polymer (composites) surface with conductivity and thermal induced PDEs, and more substrate related factors as the molecular chain movements, polymer degradation, etc., in future work. As the soft materials typically have low thermal conductivities compared to metals or semiconductors (0.5 W/mK - 1 W/mK for polymers and 100 W/mK for Si) and

making them more susceptible to beam-induced heating and even melting. Therefore, beam-induced heating is expected to play a critical role in the potential alteration of functional chemistry, which should be put in the future work. Soft materials are typically amorphous and also undergo beam damage during evaluation in the TEM, so the surface damage is harder to assess. I also need seek a way to capture the knock-on damage for the surface. Radiolysis damage in soft materials may result in a change in appearance and the preferential destruction or creation of organic functional groups. Such preferential destruction or creation of surface chemical bond will lead to a thin layer of damaged material on the surface which might also cause the concern for surface polish.

Many research opportunities emerge in the field of material science towards the AM assisted advanced manufacturing of bio-inspired structure. Among the rich set of technologies, materials, and digital design for the AM process, cross-disciplinary research will always be wanted to advance the development in these domains. New materials technologies with suitable mechanical and biochemical properties are particularly needed on a time scale with a special emphasis on those that can be integrated into AM technologies by providing suitable bio-integration. In my development of gel based morphing structure, the experimental mechanics work has lots of potentials to be re-developed, the primary one is to change the design to spherical shell, as this would change the stress state by introducing another curvature. The detailed equilibrium wavelength/initial film thickness ratio increases as the film thickness needs be further justified. Hysteresis of instabilities should be

investigated with dependence on the initial gel volume fraction. The mechanics study would be very promising to deliver something interesting for the formation of wrinkles or creases in a curved bilayer. A diagram of the formation of wrinkles, creases in a curved bilayer, should incubate new types of bifurcation behaviour when the moduli and the thicknesses of the film and substrate are designed. Also, the robotic gripper can be re-designed with different structure, may be incorporate the origami design. And simulation of gripper needs be developed to characterize its behaviours and functions. It will be interesting to see the change of formulation of gel, by adding more stimuli responsive components. Dedicated control is highly desired to enable the ideal grasping speed of the gripper or maintain a release or grasping state.

The bioinspired materials/structures community is rapidly developing a more robust understanding of how to design materials with desired structure-property relationship. The IOL work could be continued to study the effect of how a swelling response due to an external stimulus alters light when emitted through a gel lens. The repeatability could be investigated to see if the light behaves in the same manner when the gel is swelled for a second time due to a repeated stimulus such as change in temperature or an applied electric field. Additionally, the transmittance of light could be measured to ascertain if the degree of swelling affects light transmittance. Alternate sizes of cylinders could be fabricated to establish the correlation between gel size, swelling ratio and time to equilibrate for a particular gel composition. The hydrogel could be characterised further by looking at the effects of the cross-linker and content of the initiators. The bio-safety assessment could be expanded by carrying

experiments in animals and to see the long-term effect. Throughout, close interactions with medical practitioners will be helpful to understand the clinical demands and where the current limitations are. Finally, in the biological experiments, coresearchers reported that IOLs are fragile, so how to optimize the formulation and improve the strength of hydrogel is also a good topic to be further studied. Other physical cues will be considered together enable independent tuning of gel modulus, geometry, strain amplitude, strain states, as well as strain rates, in a high throughput way, providing a versatile platform to design IOL. New experimental techniques are still needed to characterize the optical manipulation under bio-environment. The control of optical focus under confinement, dynamic loading, combined with anisotropic and different supporting structure is still waiting to be explored.

The theoretical studies can be extended to see the wrinkle formation and evolution on surface with more complicate patterns. Additional numerical ways might be needed to study these instabilities, i.e., static force-displacement method and pseudo-dynamic loading-unloading method, both of which allow us to find all the stable equilibrium solutions to the boundary value problem under different given strains, including the flat, wrinkle and ridge states. Some different geometries could be introduced, and the lateral coordination of strain energy could be very interesting. A major opportunity exists in applying advances in machine learning to improve the design of personalized materials and smart behaviour, by using machine learning to assist in the optimization of the structure, materials, and print path for the AM of bio-inspired devices. Machine learning is already implemented in a variety

of applications. There will be a need to envision the databases of images for bio-inspired structure and the corresponding materials that inform the design of future parts. The ability to harness these data sets for the design of instabilities will be critical to its successful implementation.

Manufacturing in bio-inspired soft structures is an emerging field. Addressing the above challenges and opportunities will need cross-disciplinary teams that transform the way we design and implement bio-inspired materials and structures. AM assisted manufacturing bio-inspired materials goes far beyond the view of using AM as prototyping technique, indeed it has the potential to transform the way healthcare design and frontier engineering applications, to improve diagnostics, as well as customized tools and electronics/robotic devices. It is hoped that this thesis provides an approach to combine advanced manufacturing method with active materials and surface of the different types of instability morphologies and contributes to the new applications in the healthcare and bio-medical sectors.

Bibliography

1. Pham, D. and S.S. Dimov, *Rapid manufacturing: the technologies and applications of rapid prototyping and rapid tooling*. 2012: Springer Science & Business Media.
2. Campbell, I., D. Bourell, and I. Gibson, *Additive manufacturing: rapid prototyping comes of age*. Rapid prototyping journal, 2012. **18**(4): p. 255-258.
3. Mishra, M.S., *3D printing technology*. Science Horizon, 2014. **43**.
4. Mota, C., et al., *Additive manufacturing techniques for the production of tissue engineering constructs*. Journal of tissue engineering and regenerative medicine, 2015. **9**(3): p. 174-190.
5. Sivarupan, T., et al., *A review on the progress and challenges of binder jet 3D printing of sand moulds for advanced casting*. Additive Manufacturing, 2021: p. 101889.
6. Steinbacher, D.M., *Three-dimensional analysis and surgical planning in craniomaxillofacial surgery*. Journal of Oral and Maxillofacial Surgery, 2015. **73**(12): p. S40-S56.
7. D'Urso, P.S., et al., *Custom cranioplasty using stereolithography and acrylic*. British Journal of Plastic Surgery, 2000. **53**(3): p. 200-204.
8. Liu, Q., M.C. Leu, and S.M. Schmitt, *Rapid prototyping in dentistry: technology and application*. The international journal of advanced manufacturing technology, 2006. **29**(3-4): p. 317-335.
9. Sannomiya, E., et al., *Clinical and radiographic presentation and preparation of the prototyping model for pre-surgical planning in Apert's syndrome*. Dentomaxillofacial Radiology, 2006. **35**(2): p. 119-124.
10. Rengier, F., et al., *3D printing based on imaging data: review of medical applications*. International journal of computer assisted radiology and surgery, 2010. **5**(4): p. 335-341.
11. Gou, M., et al., *Bio-inspired detoxification using 3D-printed hydrogel nanocomposites*. Nature communications, 2014. **5**.
12. Papadakis, E.P., *Ultrasonic Instruments and Devices*. 2001, Acoustical Society of America.
13. Fritzsch, B., *Electric organs: history and potential*. Science, 2014. **345**(6197): p. 631-632.
14. ZHANG, J., et al., *Biological characteristics of eggshell and its bionic application*. Advances in Natural Science, 2015. **8**(1): p. 41-50.
15. Andreou, C.M., Y. Pahitas, and J. Georgiou, *Bio-inspired micro-fluidic angular-rate sensor for vestibular prostheses*. Sensors, 2014. **14**(7): p. 13173-13185.
16. Liang, D. and X.-Y. Wang, *A bio-inspired optical system with a polymer membrane and integrated structure*. Bioinspiration & biomimetics, 2016. **11**(6): p. 066008.
17. Tadepalli, S., et al., *Bio-optics and bio-inspired optical materials*. Chemical reviews, 2017. **117**(20): p. 12705-12763.
18. Costa, D., et al., *Design of a bio-inspired autonomous underwater robot*. Journal of Intelligent & Robotic Systems, 2018. **91**(2): p. 181-192.
19. Zhao, Y., et al., *pH-and temperature-sensitive hydrogel nanoparticles with dual photoluminescence for bioprobes*. ACS nano, 2016. **10**(6): p. 5856-5863.
20. Han, D., et al., *Micro 3D printing of a temperature-responsive hydrogel using projection micro-stereolithography*. Scientific reports, 2018. **8**(1): p. 1-10.

21. Zhang, J., Q. Huang, and J. Du, *Recent advances in magnetic hydrogels.* Polymer International, 2016. **65**(12): p. 1365-1372.

22. Yuk, H., B. Lu, and X. Zhao, *Hydrogel bioelectronics.* Chemical Society Reviews, 2019. **48**(6): p. 1642-1667.

23. Liu, S., et al., *Scaling law and microstructure of alginate hydrogel.* Carbohydrate polymers, 2016. **135**: p. 101-109.

24. Liu, L., et al., *Bright, Multi‐responsive, Sky‐Blue Platinum (II) Phosphors Based on a Tetradentate Chelating Framework.* Angewandte Chemie International Edition, 2017. **56**(31): p. 9160-9164.

25. Kücken, M. and A.C. Newell, *A model for fingerprint formation.* EPL (Europhysics Letters), 2004. **68**(1): p. 141.

26. Pauchard, L. and Y. Couder, *Invagination during the collapse of an inhomogeneous spheroidal shell.* EPL (Europhysics Letters), 2004. **66**(5): p. 667.

27. Yang, W., et al., *Instability of the two-layered thick-walled esophageal model under the external pressure and circular outer boundary condition.* Journal of biomechanics, 2007. **40**(3): p. 481-490.

28. Dumais, J. and C.R. Steele, *New evidence for the role of mechanical forces in the shoot apical meristem.* Journal of plant growth regulation, 2000. **19**(1): p. 7-18.

29. Dervaux, J. and M.B. Amar, *Buckling condensation in constrained growth.* Journal of the Mechanics and Physics of Solids, 2011. **59**(3): p. 538-560.

30. Wiggs, B.R., et al., *On the mechanism of mucosal folding in normal and asthmatic airways.* Journal of Applied Physiology, 1997. **83**(6): p. 1814-1821.

31. Hrousis, C.A., et al., *Mucosal folding in biologic vessels.* J. Biomech. Eng., 2002. **124**(4): p. 334-341.

32. Gao, L. and T.J. McCarthy, *An attempt to correct the faulty intuition perpetuated by the Wenzel and Cassie "laws".* Langmuir, 2009. **25**(13): p. 7249-7255.

33. Young, T., *III. An essay on the cohesion of fluids.* Philosophical transactions of the royal society of London, 1805(95): p. 65-87.

34. Wenzel, R.N., *Resistance of solid surfaces to wetting by water.* Industrial & Engineering Chemistry, 1936. **28**(8): p. 988-994.

35. Cassie, A. and S. Baxter, *Wettability of porous surfaces.* Transactions of the Faraday society, 1944. **40**: p. 546-551.

36. Feng, L., et al., *A super‐hydrophobic and super‐oleophilic coating mesh film for the separation of oil and water.* Angewandte Chemie, 2004. **116**(15): p. 2046-2048.

37. Geraldi, N.R., et al., *Bioinspired nanoparticle spray-coating for superhydrophobic flexible materials with oil/water separation capabilities.* Bioinspiration & Biomimetics, 2018. **13**(2): p. 024001.

38. Gong, Z., et al., *Fabrication of meshes with inverse wettability based on the TiO2 nanowires for continuous oil/water separation.* Chemical Engineering Journal, 2020. **380**: p. 122524.

39. Zhang, L., et al., *Robust and durable superhydrophobic polyurethane sponge for oil/water separation.* Industrial & Engineering Chemistry Research, 2016. **55**(43): p. 11260-11268.

40. Cho, E.-C., et al., *Robust multifunctional superhydrophobic coatings with enhanced water/oil separation, self-cleaning, anti-corrosion, and anti-biological adhesion.* Chemical Engineering Journal, 2017. **314**: p. 347-357.

41. Zhang, Z., et al., *Mechanically durable, superhydrophobic coatings prepared by dual-layer method for anti-corrosion and self-cleaning.* Colloids and Surfaces A: Physicochemical and Engineering Aspects, 2016. **490**: p. 182-188.

42. He, J., et al., *Interaction of miscible solutions and superhydrophobic surfaces.* Surface Engineering, 2019. **35**(5): p. 387-393.

43. Kerr, R.A., *A lot of oil on the loose, not so much to be found.* 2010, American Association for the Advancement of Science.

44. Wang, H., et al., *A robust 3D superhydrophobic sponge for in situ continuous oil removing.* Journal of Materials Science, 2019. **54**(2): p. 1255-1266.

45. Jiang, B., et al., *Covalent layer-by-layer grafting (LBLG) functionalized superhydrophobic stainless steel mesh for oil/water separation.* Applied Surface Science, 2017. **406**: p. 150-160.

46. Zhai, L., et al., *Patterned superhydrophobic surfaces: toward a synthetic mimic of the Namib Desert beetle.* Nano Letters, 2006. **6**(6): p. 1213-1217.

47. Harrison, C., et al., *Sinusoidal phase grating created by a tunably buckled surface.* Applied Physics Letters, 2004. **85**(18): p. 4016-4018.

48. Chan, E.P. and A.J. Crosby, *Fabricating microlens arrays by surface wrinkling.* Advanced Materials, 2006. **18**(24): p. 3238-3242.

49. Chandra, D., S. Yang, and P.-C. Lin, *Strain responsive concave and convex microlens arrays.* Applied Physics Letters, 2007. **91**(25): p. 251912.

50. Chan, E.P., et al., *Surface wrinkles for smart adhesion.* Advanced Materials, 2008. **20**(4): p. 711-716.

51. Lin, P.-C., et al., *Mechanically tunable dry adhesive from wrinkled elastomers.* Soft Matter, 2008. **4**(9): p. 1830-1835.

52. Khang, D.-Y., et al., *A stretchable form of single-crystal silicon for high-performance electronics on rubber substrates.* Science, 2006. **311**(5758): p. 208-212.

53. Kim, J., J. Yoon, and R.C. Hayward, *Dynamic display of biomolecular patterns through an elastic creasing instability of stimuli-responsive hydrogels.* Nature materials, 2010. **9**(2): p. 159-164.

54. Hyun, D.C., et al., *Repeated transfer of colloidal patterns by using reversible buckling process.* Advanced Functional Materials, 2009. **19**(13): p. 2155-2162.

55. Lee, S.G., et al., *Switchable transparency and wetting of elastomeric smart windows.* Advanced materials, 2010. **22**(44): p. 5013-5017.

56. Masuda, H. and M. Satoh, *Fabrication of gold nanodot array using anodic porous alumina as an evaporation mask.* Japanese Journal of Applied Physics, 1996. **35**(1B): p. L126.

57. Lee, D.Y., et al., *Chemical and geometrical criteria for the release of elastomeric 1D nanoarrays from porous nanotemplates.* Langmuir, 2010. **26**(5): p. 3252-3256.

58. Efimenko, K., et al., *Nested self-similar wrinkling patterns in skins.* Nature materials, 2005. **4**(4): p. 293-297.

59. Su, H., et al. *Pneumatic Soft Robots: Challenges and Benefits.* in *Actuators.* 2022. MDPI.

60. Whitesides, G.M., *Soft robotics.* Angewandte Chemie International Edition, 2018. **57**(16): p. 4258-4273.

61. Hughes, J., et al., *Soft manipulators and grippers: a review.* Frontiers in Robotics and AI, 2016. **3**: p. 69.

62. Ng, J.M., et al., *Components for integrated poly (dimethylsiloxane) microfluidic systems.* Electrophoresis, 2002. **23**(20): p. 3461-3473.

63. Zhao, X.-M., Y. Xia, and G.M. Whitesides, *Soft lithographic methods for nano-fabrication.* Journal of Materials Chemistry, 1997. **7**(7): p. 1069-1074.

64.   Li, S., et al., *Fluid-driven origami-inspired artificial muscles*. Proceedings of the National academy of Sciences, 2017. **114**(50): p. 13132-13137.

65.   Paek, J., I. Cho, and J. Kim, *Microrobotic tentacles with spiral bending capability based on shape-engineered elastomeric microtubes*. Scientific reports, 2015. **5**(1): p. 1-11.

66.   Shepherd, R.F., et al., *Multigait soft robot*. Proceedings of the national academy of sciences, 2011. **108**(51): p. 20400-20403.

67.   Mosadegh, B., et al., *Pneumatic networks for soft robotics that actuate rapidly*. Advanced functional materials, 2014. **24**(15): p. 2163-2170.

68.   Shepherd, R.F., et al., *Using explosions to power a soft robot*. Angewandte Chemie International Edition, 2013. **52**(10): p. 2892-2896.

69.   Tolley, M.T., et al. *An untethered jumping soft robot*. in *2014 IEEE/RSJ International Conference on Intelligent Robots and Systems*. 2014. IEEE.

70.   Bartlett, N.W., et al., *A 3D-printed, functionally graded soft robot powered by combustion*. Science, 2015. **349**(6244): p. 161-165.

71.   Wehner, M., et al., *An integrated design and fabrication strategy for entirely soft, autonomous robots*. Nature, 2016. **536**(7617): p. 451-455.

72.   Wang, Y., et al., *Bipolar electrochemical mechanism for the propulsion of catalytic nanomotors in hydrogen peroxide solutions*. Langmuir, 2006. **22**(25): p. 10451-10456.

73.   Vitale, F., et al. *Low-temperature H 2 O 2-powered actuators for biorobotics: Thermodynamic and kinetic analysis*. in *2010 IEEE International Conference on Robotics and Automation*. 2010. IEEE.

74.   Goldfarb, M., et al., *Design and energetic characterization of a liquid-propellant-powered actuator for self-powered robots*. IEEE/ASME transactions on mechatronics, 2003. **8**(2): p. 254-262.

75.   Wehner, M., et al., *Pneumatic energy sources for autonomous and wearable soft robotics*. Soft robotics, 2014. **1**(4): p. 263-274.

76.   Rong, Z., et al., *Bio‐inspired hierarchical polymer fiber‐carbon nanotube adhesives*. Advanced Materials, 2014. **26**(9): p. 1456-1461.

77.   Pan, L., et al., *An ultra-sensitive resistive pressure sensor based on hollow-sphere microstructure induced elasticity in conducting polymer film*. Nature communications, 2014. **5**(1): p. 1-8.

78.   Mannsfeld, S.C., et al., *Highly sensitive flexible pressure sensors with microstructured rubber dielectric layers*. Nature materials, 2010. **9**(10): p. 859-864.

79.   Takei, K., et al., *Nanowire active-matrix circuitry for low-voltage macroscale artificial skin*. Nature materials, 2010. **9**(10): p. 821-826.

80.   Kim, J., et al., *Stretchable silicon nanoribbon electronics for skin prosthesis*. Nature communications, 2014. **5**(1): p. 1-11.

81.   Turner, A.P. and N. Magan, *Electronic noses and disease diagnostics*. Nature Reviews Microbiology, 2004. **2**(2): p. 161-166.

82.   Peris, M. and L. Escuder-Gilabert, *A 21st century technique for food control: Electronic noses*. Analytica chimica acta, 2009. **638**(1): p. 1-15.

83.   Röck, F., N. Barsan, and U. Weimar, *Electronic nose: current status and future trends*. Chemical reviews, 2008. **108**(2): p. 705-725.

84.   Henning, A., et al., *Tunable diameter electrostatically formed nanowire for high sensitivity gas sensing*. Nano Research, 2015. **8**(7): p. 2206-2215.

85.   Song, Y.M., et al., *Digital cameras with designs inspired by the arthropod eye*. Nature, 2013. **497**(7447): p. 95-99.

86. Dagdeviren, C., et al., *Conformable amplified lead zirconate titanate sensors with enhanced piezoelectric response for cutaneous pressure monitoring.* Nature communications, 2014. **5**(1): p. 1-10.

87. Park, J., et al., *Fingertip skin–inspired microstructured ferroelectric skins discriminate static/dynamic pressure and temperature stimuli.* Science advances, 2015. **1**(9): p. e1500661.

88. Someya, T., et al., *Conformable, flexible, large-area networks of pressure and thermal sensors with organic transistor active matrixes.* Proceedings of the National Academy of Sciences, 2005. **102**(35): p. 12321-12325.

89. Yao, H.B., et al., *A flexible and highly pressure‐sensitive graphene‐polyurethane sponge based on fractured microstructure design.* Advanced Materials, 2013. **25**(46): p. 6692-6698.

90. Hou, C., et al., *Highly conductive, flexible, and compressible all‐graphene passive electronic skin for sensing human touch.* Advanced Materials, 2014. **26**(29): p. 5018-5024.

91. Pang, C., et al., *A flexible and highly sensitive strain-gauge sensor using reversible interlocking of nanofibres.* Nature materials, 2012. **11**(9): p. 795-801.

92. Yi, L., et al., *Ultrasensitive strain gauge with tunable temperature coefficient of resistivity.* Nano Research, 2016. **9**(5): p. 1346-1357.

93. Wang, Y., et al., *Ultra-sensitive graphene strain sensor for sound signal acquisition and recognition.* Nano Research, 2015. **8**(5): p. 1627-1636.

94. Yi, L., et al., *Nanoparticle monolayer-based flexible strain gauge with ultrafast dynamic response for acoustic vibration detection.* Nano Research, 2015. **8**(9): p. 2978-2987.

95. Lipomi, D.J., et al., *Skin-like pressure and strain sensors based on transparent elastic films of carbon nanotubes.* Nature nanotechnology, 2011. **6**(12): p. 788-792.

96. Park, S., et al., *Stretchable energy‐harvesting tactile electronic skin capable of differentiating multiple mechanical stimuli modes.* Advanced Materials, 2014. **26**(43): p. 7324-7332.

97. Zang, Y., et al., *Flexible suspended gate organic thin-film transistors for ultra-sensitive pressure detection.* Nature communications, 2015. **6**(1): p. 1-9.

98. Zhou, J., et al., *Flexible piezotronic strain sensor.* Nano letters, 2008. **8**(9): p. 3035-3040.

99. Fan, F.-R., et al., *Transparent triboelectric nanogenerators and self-powered pressure sensors based on micropatterned plastic films.* Nano letters, 2012. **12**(6): p. 3109-3114.

100. Park, H., et al., *Stretchable array of highly sensitive pressure sensors consisting of polyaniline nanofibers and Au-coated polydimethylsiloxane micropillars.* ACS nano, 2015. **9**(10): p. 9974-9985.

101. Choong, C.L., et al., *Highly stretchable resistive pressure sensors using a conductive elastomeric composite on a micropyramid array.* Advanced materials, 2014. **26**(21): p. 3451-3458.

102. Zhu, B., et al., *Microstructured graphene arrays for highly sensitive flexible tactile sensors.* Small, 2014. **10**(18): p. 3625-3631.

103. Gu, Y., et al., *Flexible electronic eardrum.* Nano Research, 2017. **10**(8): p. 2683-2691.

104. Amjadi, M., et al., *Highly stretchable and sensitive strain sensor based on silver nanowire–elastomer nanocomposite.* ACS nano, 2014. **8**(5): p. 5154-5163.

105. Lee, J., et al., *Transparent, flexible strain sensor based on a solution-processed carbon nanotube network*. ACS applied materials & interfaces, 2017. **9**(31): p. 26279-26285.

106. Choi, T.Y., et al., *Stretchable, transparent, and stretch-unresponsive capacitive touch sensor array with selectively patterned silver nanowires/reduced graphene oxide electrodes*. ACS applied materials & interfaces, 2017. **9**(21): p. 18022-18030.

107. Wang, X., et al., *Highly stretchable and wearable strain sensor based on printable carbon nanotube layers/polydimethylsiloxane composites with adjustable sensitivity*. ACS applied materials & interfaces, 2018. **10**(8): p. 7371-7380.

108. Yuan, Z., et al., *Transparent and flexible triboelectric sensing array for touch security applications*. Acs Nano, 2017. **11**(8): p. 8364-8369.

109. Cho, S., et al., *Large-area cross-aligned silver nanowire electrodes for flexible, transparent, and force-sensitive mechanochromic touch screens*. ACS nano, 2017. **11**(4): p. 4346-4357.

110. Kim, D.-J., et al., *Roll-to-roll slot-die coating of 400 mm wide, flexible, transparent Ag nanowire films for flexible touch screen panels*. Scientific reports, 2016. **6**(1): p. 1-12.

111. Chen, F., et al., *Flexible transparent supercapacitors based on hierarchical nanocomposite films*. ACS applied materials & interfaces, 2017. **9**(21): p. 17865-17871.

112. Huang, S., et al., *Flexible electronics: stretchable electrodes and their future*. Advanced Functional Materials, 2019. **29**(6): p. 1805924.

113. Meng, L., et al., *Aligning Ag nanowires by a facile bioinspired directional liquid transfer: toward anisotropic flexible conductive electrodes*. Advanced Materials, 2018. **30**(25): p. 1706938.

114. Ko, Y., et al., *Flexible supercapacitor electrodes based on real metal-like cellulose papers*. Nature communications, 2017. **8**(1): p. 1-11.

115. Xiong, W., et al., *Highly conductive, air‐stable silver nanowire@ iongel composite films toward flexible transparent electrodes*. Advanced Materials, 2016. **28**(33): p. 7167-7172.

116. Zhang, N., et al., *A wearable all‐solid photovoltaic textile*. Advanced Materials, 2016. **28**(2): p. 263-269.

117. Chen, J., et al., *Micro-cable structured textile for simultaneously harvesting solar and mechanical energy*. Nature Energy, 2016. **1**(10): p. 1-8.

118. Li, P., K. Sun, and J. Ouyang, *Stretchable and conductive polymer films prepared by solution blending*. ACS applied materials & interfaces, 2015. **7**(33): p. 18415-18423.

119. Ye, D., et al., *Large‐Scale Direct‐Writing of Aligned Nanofibers for Flexible Electronics*. Small, 2018. **14**(21): p. 1703521.

120. Rong, Q., W. Lei, and M. Liu, *Conductive hydrogels as smart materials for flexible electronic devices*. Chemistry–A European Journal, 2018. **24**(64): p. 16930-16943.

121. Li, H., et al., *High conductive and mechanical robust carbon nanotubes/waterborne polyurethane composite films for efficient electromagnetic interference shielding*. Composites Part A: Applied Science and Manufacturing, 2019. **121**: p. 411-417.

122. Xu, J., et al., *Highly stretchable polymer semiconductor films through the nanoconfinement effect*. Science, 2017. **355**(6320): p. 59-64.

123.	Song, P., et al., *Self-healing and superstretchable conductors from hierarchical nanowire assemblies*. Nature communications, 2018. **9**(1): p. 1-9.

124.	Wang, Y., et al., *A highly stretchable, transparent, and conductive polymer*. Science advances, 2017. **3**(3): p. e1602076.

125.	Lee, Y., et al., *Versatile, High‐Power, Flexible, Stretchable Carbon Nanotube Sheet Heating Elements Tolerant to Mechanical Damage and Severe Deformation*. Advanced Functional Materials, 2018. **28**(8): p. 1706007.

126.	Lee, Y., et al., *Deformable organic nanowire field‐effect transistors*. Advanced Materials, 2018. **30**(7): p. 1704401.

127.	Zhao, W., et al., *Fullerene‐free polymer solar cells with over 11% efficiency and excellent thermal stability*. Advanced materials, 2016. **28**(23): p. 4734-4739.

128.	Park, S., et al., *Ultrastretchable elastic shape memory fibers with electrical conductivity*. Advanced Science, 2019. **6**(21): p. 1901579.

129.	Gao, H., et al., *The research status and challenges of shape memory polymer-based flexible electronics*. Materials Horizons, 2019. **6**(5): p. 931-944.

130.	Lu, H., et al., *Synergistic effect of siloxane modified aluminum nanopowders and carbon fiber on electrothermal efficiency of polymeric shape memory nanocomposite*. Composites Part B: Engineering, 2015. **80**: p. 1-6.

131.	Lu, H., et al., *Structural design of flexible Au electrode to enable shape memory polymer for electrical actuation*. Smart Materials and Structures, 2015. **24**(4): p. 045015.

132.	Hu, J., et al., *Recent advances in shape–memory polymers: Structure, mechanism, functionality, modeling and applications*. Progress in Polymer Science, 2012. **37**(12): p. 1720-1763.

133.	Zhou, M., W. Huang, and X. Meng, *Temperature memory effect in a magnetic shape memory alloy for monitoring of minor over-cooling*. Scripta Materialia, 2017. **127**: p. 41-44.

134.	Luo, X. and P.T. Mather, *Shape memory assisted self-healing coating*. ACS Macro Letters, 2013. **2**(2): p. 152-156.

135.	Zhao, Q., H.J. Qi, and T. Xie, *Recent progress in shape memory polymer: New behavior, enabling materials, and mechanistic understanding*. Progress in Polymer Science, 2015. **49**: p. 79-120.

136.	Cox, L.M., et al., *Light-stimulated permanent shape reconfiguration in cross-linked polymer microparticles*. ACS applied materials & interfaces, 2017. **9**(16): p. 14422-14428.

137.	Huang, L., et al., *Ultrafast digital printing toward 4D shape changing materials*. Advanced materials, 2017. **29**(7): p. 1605390.

138.	Wei, H., et al., *Direct-write fabrication of 4D active shape-changing structures based on a shape memory polymer and its nanocomposite*. ACS applied materials & interfaces, 2017. **9**(1): p. 876-883.

139.	Lendlein, A. and O.E. Gould, *Reprogrammable recovery and actuation behaviour of shape-memory polymers*. Nature Reviews Materials, 2019. **4**(2): p. 116-133.

140.	Yu, Z., et al., *Highly flexible silver nanowire electrodes for shape‐memory polymer light‐emitting diodes*. Advanced Materials, 2011. **23**(5): p. 664-668.

141.	Gaj, M.P., et al., *Organic light-emitting diodes on shape memory polymer substrates for wearable electronics*. Organic Electronics, 2015. **25**: p. 151-155.

142. Wang, J., et al., *Tunable shape memory polymer mold for multiple microarray replications.* Journal of Materials Chemistry A, 2018. **6**(48): p. 24748-24755.

143. Stiller, A.M., et al., *Chronic intracortical recording and electrochemical stability of thiol-ene/acrylate shape memory polymer electrode arrays.* Micromachines, 2018. **9**(10): p. 500.

144. Gutierrez‐Heredia, G., et al., *Highly Stable Indium‐Gallium‐Zinc‐Oxide Thin‐Film Transistors on Deformable Softening Polymer Substrates.* Advanced Electronic Materials, 2017. **3**(10): p. 1700221.

145. Avendano‐Bolivar, A., et al., *Mechanical cycling stability of organic thin film transistors on shape memory polymers.* Advanced Materials, 2013. **25**(22): p. 3095-3099.

146. Chen, Z., et al., *Photon Upconversion Lithography: Patterning of Biomaterials Using Near‐Infrared Light.* Advanced Materials, 2015. **27**(13): p. 2203-2206.

147. Li, P., et al., *Novel programmable shape memory polystyrene film: A thermally induced beam-power splitter.* Scientific reports, 2017. **7**(1): p. 1-10.

148. Veeramuthu, L., et al., *Smart garment energy generators fabricated using stretchable electrospun nanofibers.* Reactive and Functional Polymers, 2019. **142**: p. 96-103.

149. Xu, B., et al., *Electro-responsive polystyrene shape memory polymer nanocomposites.* Nanoscience and Nanotechnology Letters, 2012. **4**(8): p. 814-820.

150. Tang, P., et al., *Intrinsically stretchable and shape memory conducting nanofiber for programmable flexible electronic films.* ACS applied materials & interfaces, 2019. **11**(51): p. 48202-48211.

151. Kwon, J., et al., *Recent progress in silver nanowire based flexible/wearable optoelectronics.* Journal of Materials Chemistry C, 2018. **6**(28): p. 7445-7461.

152. Kim, A., et al., *A pre-strain strategy for developing a highly stretchable and foldable one-dimensional conductive cord based on a Ag nanowire network.* Nanoscale, 2017. **9**(18): p. 5773-5778.

153. Gibson, I., *Advanced manufacturing technology for medical applications: reverse engineering, software conversion and rapid prototyping.* 2006: John Wiley & Sons.

154. Zhang, Y., H.F. Chan, and K.W. Leong, *Advanced materials and processing for drug delivery: the past and the future.* Advanced drug delivery reviews, 2013. **65**(1): p. 104-120.

155. Mellor, S., L. Hao, and D. Zhang, *Additive manufacturing: A framework for implementation.* International Journal of Production Economics, 2014. **149**: p. 194-201.

156. Li, B.-H., et al., *Cloud manufacturing: a new service-oriented networked manufacturing model.* Computer integrated manufacturing systems, 2010. **16**(1): p. 1-7.

157. Davis, J., et al., *Smart manufacturing, manufacturing intelligence and demand-dynamic performance.* Computers & Chemical Engineering, 2012. **47**: p. 145-156.

158. Liu, K. and L. Jiang, *Bio-inspired design of multiscale structures for function integration.* Nano Today, 2011. **6**(2): p. 155-175.

159. Ulbricht, M., *Advanced functional polymer membranes.* Polymer, 2006. **47**(7): p. 2217-2262.

160. Franssila, S., *Introduction to microfabrication.* 2010: John Wiley & Sons.

161. Davari, B., R.H. Dennard, and G.G. Shahidi, *CMOS scaling for high performance and low power-the next ten years.* Proceedings of the IEEE, 1995. **83**(4): p. 595-606.

162. Wagner, C. and N. Harned, *Lithography gets extreme.* Nature Photonics, 2010. **4**(1): p. 24-26.

163. Willson, C.G., R.R. Dammel, and A. Reiser. *Photoresist materials: a historical perspective.* in *Metrology, Inspection, and Process Control for Microlithography XI.* 1997. International Society for Optics and Photonics.

164. Nie, Z. and E. Kumacheva, *Patterning surfaces with functional polymers.* Nature materials, 2008. **7**(4): p. 277-290.

165. Singh, J.P., et al., *Fabrication of magnetic tunnel junctions*, in *Advanced Applications in Manufacturing Enginering.* 2019, Elsevier. p. 53-77.

166. Zell, T., *Present and future of 193 nm lithography.* Microelectronic Engineering, 2006. **83**(4-9): p. 624-633.

167. Ito, T. and S. Okazaki, *Pushing the limits of lithography.* Nature, 2000. **406**(6799): p. 1027-1031.

168. Chou, S.Y. and P.R. Krauss, *Imprint lithography with sub-10 nm feature size and high throughput.* Microelectronic Engineering, 1997. **35**(1-4): p. 237-240.

169. Lee, N.Y. and Y.S. Kim, *A Simple Imprint Method for Multi‐Tiered Polymer Nanopatterning on Large Flexible Substrates Employing a Flexible Mold and Hemispherical PDMS Elastomer.* Macromolecular rapid communications, 2007. **28**(20): p. 1995-2000.

170. Xia, Y., et al., *Unconventional methods for fabricating and patterning nanostructures.* Chemical reviews, 1999. **99**(7): p. 1823-1848.

171. Qin, D., Y. Xia, and G.M. Whitesides, *Soft lithography for micro-and nanoscale patterning.* Nature protocols, 2010. **5**(3): p. 491.

172. Ayyildiz, O., *Customised spectacles using 3‐D printing technology.* Clinical and Experimental Optometry, 2018. **101**(6): p. 747-751.

173. Tseng, A.A., *Recent developments in micromilling using focused ion beam technology.* Journal of micromechanics and microengineering, 2004. **14**(4): p. R15.

174. Ribeiro, R.S.R., et al., *Fabrication of Fresnel plates on optical fibres by FIB milling for optical trapping, manipulation and detection of single cells.* Scientific reports, 2017. **7**(1): p. 1-14.

175. Wood, G.S., et al., *Mass sensor utilising the mode-localisation effect in an electrostatically-coupled MEMS resonator pair fabricated using an SOI process.* Microelectronic Engineering, 2016. **159**: p. 169-173.

176. Genzer, J. and J. Groenewold, *Soft matter with hard skin: From skin wrinkles to templating and material characterization.* Soft Matter, 2006. **2**(4): p. 310-323.

177. Mändl, S. and B. Rauschenbach, *Improving the biocompatibility of medical implants with plasma immersion ion implantation.* Surface and Coatings Technology, 2002. **156**(1-3): p. 276-283.

178. Lobo, D.E., et al., *Micro‐Supercapacitors: Miniaturized Supercapacitors: Focused Ion Beam Reduced Graphene Oxide Supercapacitors with Enhanced Performance Metrics (Adv. Energy Mater. 19/2015).* Advanced Energy Materials, 2015. **5**(19).

179. Ferris, A., et al., *Atypical properties of FIB-patterned RuO x nanosupercapacitors.* ACS Energy Letters, 2017. **2**(8): p. 1734-1739.

180. Klaumünzer, S. and G. Schumacher, *Dramatic growth of glassy Pd 80 Si 20 during heavy-ion irradiation.* Physical review letters, 1983. **51**(21): p. 1987.

181. Snoeks, E., et al., *MeV ion irradiation - induced creation and relaxation of mechanical stress in silica*. Journal of applied physics, 1995. **78**(7): p. 4723-4732.

182. Otani, K., et al., *Three-dimensional morphology evolution of Si O 2 patterned films under MeV ion irradiation*. Journal of applied physics, 2006. **100**(2): p. 023535.

183. Sigmund, P., *Theory of sputtering. I. Sputtering yield of amorphous and polycrystalline targets*. Physical review, 1969. **184**(2): p. 383.

184. Kim, Y.-R., et al., *Focused ion beam induced deflections of freestanding thin films*. Journal of applied physics, 2006. **100**(10): p. 104322.

185. Erlebacher, J., et al., *Spontaneous pattern formation on ion bombarded Si (001)*. Physical review letters, 1999. **82**(11): p. 2330.

186. Facsko, S., et al., *Formation of ordered nanoscale semiconductor dots by ion sputtering*. Science, 1999. **285**(5433): p. 1551-1553.

187. Sigmund, P., *A mechanism of surface micro-roughening by ion bombardment*. Journal of Materials Science, 1973. **8**(11): p. 1545-1553.

188. Choi, Y.J., M.S. Kim, and I. Noh, *Surface modification of a polytetrafluoroethylene film with cyclotron ion beams and its evaluation*. Surface and Coatings Technology, 2007. **201**(9-11): p. 5724-5728.

189. Tibbits, S. *The emergence of "4D printing"*. in *TED conference*. 2013.

190. Gladman, A.S., et al., *Biomimetic 4D printing*. Nature materials, 2016. **15**(4): p. 413-418.

191. Zarek, M., et al., *3D printing of shape memory polymers for flexible electronic devices*. Advanced Materials, 2016. **28**(22): p. 4449-4454.

192. Lee, K.-Y., et al., *Accuracy of three-dimensional printing for manufacturing replica teeth*. The Korean Journal of Orthodontics, 2015. **45**(5): p. 217-225.

193. Li, B., et al., *Application and Development of Modern 3D Printing Technology in the Field of Orthopedics*. BioMed Research International, 2022. **2022**.

194. Jonscher, A., *New interpretation of dielectric loss peaks*. Nature, 1975. **256**(5518): p. 566-568.

195. Tanaka, T., et al., *Mechanical instability of gels at the phase transition*. Nature, 1987. **325**(6107): p. 796-798.

196. Roush, M., et al., *Dynamic simulation of changes in near-surface composition during ion bombardment*. Applications of Surface Science, 1982. **11**: p. 235-242.

197. Kolb, M., R. Botet, and R. Jullien, *Scaling of kinetically growing clusters*. Physical Review Letters, 1983. **51**(13): p. 1123.

198. Ionov, L., *Hydrogel-based actuators: possibilities and limitations*. Materials Today, 2014. **17**(10): p. 494-503.

199. Pecharroman, C., et al., *New percolative BaTiO3–Ni composites with a high and frequency - independent dielectric constant (εr ≈ 80000)*. Advanced Materials, 2001. **13**(20): p. 1541-1544.

200. Makeev, M.A., R. Cuerno, and A.-L. Barabasi, *Morphology of ion-sputtered surfaces*. Nuclear Instruments and Methods in Physics Research Section B: Beam Interactions with Materials and Atoms, 2002. **197**(3-4): p. 185-227.

201. Yang, C. and Z. Suo, *Hydrogel ionotronics*. Nature Reviews Materials, 2018. **3**(6): p. 125-142.

202. Tanaka, T., et al., *Mechanical instability of swelling gels*, in *Studies in Polymer Science*. 1988, Elsevier. p. 203-222.

203. Li, Y. and T. Tanaka, *Kinetics of swelling and shrinking of gels*. The Journal of chemical physics, 1990. **92**(2): p. 1365-1371.

204. Tian, Z., et al., *A review on laser powder bed fusion of inconel 625 nickel-based alloy*. Applied Sciences, 2020. **10**(1): p. 81.

205. Wang, X., et al., *3D printing of polymer matrix composites: A review and prospective*. Composites Part B: Engineering, 2017. **110**: p. 442-458.

206. Tibbits, S., *4D printing: multi‐material shape change*. Architectural Design, 2014. **84**(1): p. 116-121.

207. Hong, S., et al., *3D printing of highly stretchable and tough hydrogels into complex, cellularized structures*. Advanced materials, 2015. **27**(27): p. 4035-4040.

208. Ionov, L., *Soft microorigami: self-folding polymer films*. Soft Matter, 2011. **7**(15): p. 6786-6791.

209. Sridhar, S., et al., *Controlled Cooperative Wetting Enabled Heterogeneous Structured 3D Morphing Transducers*. Advanced Materials Interfaces, 2021. **8**(2): p. 2001211.

210. Wang, C., et al. *Advanced 3D morphing transducers by smart hydrogel patterning*. in *2019 20th International Conference on Solid-State Sensors, Actuators and Microsystems & Eurosensors XXXIII (TRANSDUCERS & EUROSENSORS XXXIII)*. 2019. IEEE.

211. Osada, Y. and A. Matsuda, *Shape memory in hydrogels*. Nature, 1995. **376**(6537): p. 219-219.

212. Behl, M. and A. Lendlein, *Shape-memory polymers*. Materials today, 2007. **10**(4): p. 20-28.

213. Huang, W., et al., *Shape memory materials*. Materials today, 2010. **13**(7-8): p. 54-61.

214. Qi, H.J., et al., *Finite deformation thermo-mechanical behavior of thermally induced shape memory polymers*. Journal of the Mechanics and Physics of Solids, 2008. **56**(5): p. 1730-1751.

215. Yu, K., Q. Ge, and H.J. Qi, *Reduced time as a unified parameter determining fixity and free recovery of shape memory polymers*. Nature communications, 2014. **5**(1): p. 1-9.

216. Xie, T., *Tunable polymer multi-shape memory effect*. Nature, 2010. **464**(7286): p. 267-270.

217. Raviv, D., et al., *& Raskar, R.(2014). Active printed materials for complex self-evolving deformations*. Scientific reports. **4**: p. 7422.

218. Mao, Y., et al., *3D printed reversible shape changing components with stimuli responsive materials*. Scientific reports, 2016. **6**(1): p. 1-13.

219. Ge, Q., H.J. Qi, and M.L. Dunn, *Active materials by four-dimension printing*. Applied Physics Letters, 2013. **103**(13): p. 131901.

220. Wu, J., et al., *Multi-shape active composites by 3D printing of digital shape memory polymers*. Scientific reports, 2016. **6**(1): p. 1-11.

221. Mao, Y., et al., *Sequential self-folding structures by 3D printed digital shape memory polymers*. Scientific reports, 2015. **5**(1): p. 1-12.

222. Ge, Q., et al., *Multimaterial 4D printing with tailorable shape memory polymers*. Scientific reports, 2016. **6**(1): p. 1-11.

223. Werkheiser, M.J., et al. *3D printing in Zero-G ISS technology demonstration*. in *AIAA SPACE 2014 Conference and Exposition*. 2014.

224. Od, H.E. and R.S.F. Chiu, *Spectacle fitting with ear, nose and face deformities or abnormalities*. Clinical and Experimental Optometry, 2002. **85**(6): p. 389-391.

225. Wei, H., et al., *Ultrastretchable, Highly Transparent, Self-Adhesive, and 3D-Printable Ionic Hydrogels for Multimode Tactical Sensing*. Chemistry of Materials, 2021. **33**(17): p. 6731-6742.

226. Liu, J., et al., *Responsive and foldable soft materials.* Trends in Chemistry, 2020. **2**(2): p. 107-122.

227. Kolesky, D.B., et al., *Three-dimensional bioprinting of thick vascularized tissues.* Proceedings of the national academy of sciences, 2016. **113**(12): p. 3179-3184.

228. Villar, G., A.D. Graham, and H. Bayley, *A tissue-like printed material.* Science, 2013. **340**(6128): p. 48-52.

229. Zhang, Y.S., et al., *3D bioprinting for tissue and organ fabrication.* Annals of biomedical engineering, 2017. **45**(1): p. 148-163.

230. Zhang, J., et al., *Sessile Microdroplet‐Based Writing Board for Patterning of Structural Colored Hydrogels.* Advanced Materials Interfaces, 2021. **8**(2): p. 2001201.

231. Breger, J.C., et al., *Self-folding thermo-magnetically responsive soft microgrippers.* ACS applied materials & interfaces, 2015. **7**(5): p. 3398-3405.

232. Tibbits, S., et al., *4D printing and universal transformation.* 2014.

233. Hager, M.D., et al., *Shape memory polymers: Past, present and future developments.* Progress in Polymer Science, 2015. **49**: p. 3-33.

234. Zhou, Y., et al., *From 3D to 4D printing: approaches and typical applications.* Journal of Mechanical Science and Technology, 2015. **29**(10): p. 4281-4288.

235. Momeni, F., et al., *Plant leaf-mimetic smart wind turbine blades by 4D printing.* Renewable Energy, 2019. **130**: p. 329-351.

236. Choong, Y.Y.C., et al., *4D printing of high performance shape memory polymer using stereolithography.* Materials & Design, 2017. **126**: p. 219-225.

237. Bodaghi, M., A. Damanpack, and W. Liao, *Triple shape memory polymers by 4D printing.* Smart Materials and Structures, 2018. **27**(6): p. 065010.

238. Bodaghi, M., A. Damanpack, and W. Liao, *Adaptive metamaterials by functionally graded 4D printing.* Materials & Design, 2017. **135**: p. 26-36.

239. Hu, Y., et al., *A graphene‐based bimorph structure for design of high performance photoactuators.* Advanced Materials, 2015. **27**(47): p. 7867-7873.

240. Liu, Y., et al., *Sequential self-folding of polymer sheets.* Science Advances, 2017. **3**(3): p. e1602417.

241. Kuksenok, O. and A.C. Balazs, *Stimuli-responsive behavior of composites integrating thermo-responsive gels with photo-responsive fibers.* Materials Horizons, 2016. **3**(1): p. 53-62.

242. Wu, J., et al., *Reversible shape change structures by grayscale pattern 4D printing.* Multifunctional Materials, 2018. **1**(1): p. 015002.

243. Miriyev, A., K. Stack, and H. Lipson, *Soft material for soft actuators.* Nature communications, 2017. **8**(1): p. 1-8.

244. Okuzaki, H., et al., *Humidity‐sensitive polypyrrole films for electro‐active polymer actuators.* Advanced Functional Materials, 2013. **23**(36): p. 4400-4407.

245. Xu, B.B., et al., *Reversible Electrochemically Triggered Delamination Blistering of Hydrogel Films on Micropatterned Electrodes.* Advanced Functional Materials, 2016. **26**(19): p. 3218-3225.

246. Johnston, B.G., *Column buckling theory: historic highlights.* Journal of Structural Engineering, 1983. **109**(9): p. 2086-2096.

247. Allen, H.G., *Analysis and design of structural sandwich panels: the commonwealth and international library: structures and solid body mechanics division.* 2013: Elsevier.

248. Bowden, N., et al., *The controlled formation of ordered, sinusoidal structures by plasma oxidation of an elastomeric polymer.* Applied Physics Letters, 1999. **75**(17): p. 2557-2559.

249. Bowden, N., et al., *Spontaneous formation of ordered structures in thin films of metals supported on an elastomeric polymer.* Nature, 1998. **393**(6681): p. 146-149.

250. Cerda, E. and L. Mahadevan, *Geometry and physics of wrinkling.* Physical review letters, 2003. **90**(7): p. 074302.

251. Groenewold, J., *Wrinkling of plates coupled with soft elastic media.* Physica A: Statistical Mechanics and its Applications, 2001. **298**(1-2): p. 32-45.

252. Wang, D., et al., *Spatially configuring wrinkle pattern and multiscale surface evolution with structural confinement.* Advanced Functional Materials, 2018. **28**(1): p. 1704228.

253. Kim, D.-H., et al., *Stretchable and foldable silicon integrated circuits.* Science, 2008. **320**(5875): p. 507-511.

254. Xu, B. and R.C. Hayward, *Low‐voltage switching of crease patterns on hydrogel surfaces.* Advanced Materials, 2013. **25**(39): p. 5555-5559.

255. Khare, K., J. Zhou, and S. Yang, *Tunable open-channel microfluidics on soft poly (dimethylsiloxane)(PDMS) substrates with sinusoidal grooves.* Langmuir, 2009. **25**(21): p. 12794-12799.

256. Ohzono, T. and H. Monobe, *Morphological transformation of a liquid micropattern on dynamically tunable microwrinkles.* Langmuir, 2010. **26**(9): p. 6127-6132.

257. Görrn, P., et al., *Elastically Tunable Self‐Organized Organic Lasers.* Advanced Materials, 2011. **23**(7): p. 869-872.

258. Chung, J.Y., J.P. Youngblood, and C.M. Stafford, *Anisotropic wetting on tunable micro-wrinkled surfaces.* Soft Matter, 2007. **3**(9): p. 1163-1169.

259. Stafford, C.M., et al., *A buckling-based metrology for measuring the elastic moduli of polymeric thin films.* Nature materials, 2004. **3**(8): p. 545-550.

260. Biot, M.A., *Surface instability of rubber in compression.* Applied Scientific Research, Section A, 1963. **12**(2): p. 168-182.

261. Mora, S., et al., *Surface instability of soft solids under strain.* Soft matter, 2011. **7**(22): p. 10612-10619.

262. Best, B., P. Meijers, and A. Savkoor, *The formation of Schallamach waves.* Wear, 1981. **65**(3): p. 385-396.

263. Trujillo, V., J. Kim, and R.C. Hayward, *Creasing instability of surface-attached hydrogels.* Soft Matter, 2008. **4**(3): p. 564-569.

264. Hohlfeld, E. and L. Mahadevan, *Unfolding the sulcus.* Physical review letters, 2011. **106**(10): p. 105702.

265. Cai, S., et al., *Osmotic collapse of a void in an elastomer: breathing, buckling and creasing.* Soft Matter, 2010. **6**(22): p. 5770-5777.

266. Wang, C., et al., *A flexible topo-optical sensing technology with ultra-high contrast.* Nature communications, 2020. **11**(1): p. 1-7.

267. Xiao, R., et al., *Fiber Surface/Interfacial Engineering on Wearable Electronics.* Small, 2021. **17**(52): p. 2102903.

268. Zhu, C., et al., *Ultraelastic Yarns from Curcumin‐Assisted ELD toward Wearable Human−Machine Interface Textiles.* Advanced Science, 2020. **7**(23): p. 2002009.

269. Sharp, J.S. and R.A. Jones, *Micro‐buckling as a Route Towards Surface Patterning.* Advanced Materials, 2002. **14**(11): p. 799-802.

270. Edmondson, S., et al., *Buckling in quasi‐2D polymers*. Advanced materials, 2006. **18**(6): p. 724-728.

271. Velankar, S.S., V. Lai, and R.A. Vaia, *Swelling-induced delamination causes folding of surface-tethered polymer gels*. ACS applied materials & interfaces, 2012. **4**(1): p. 24-29.

272. Vella, D., et al., *The macroscopic delamination of thin films from elastic substrates*. Proceedings of the National Academy of Sciences, 2009. **106**(27): p. 10901-10906.

273. Ebata, Y., A.B. Croll, and A.J. Crosby, *Wrinkling and strain localizations in polymer thin films*. Soft Matter, 2012. **8**(35): p. 9086-9091.

274. Casper, M.D., et al., *Surface wrinkling by chemical modification of poly (dimethylsiloxane)-based networks during sputtering*. Soft Matter, 2013. **9**(32): p. 7797-7803.

275. Yin, J. and M.C. Boyce, *Unique wrinkles as identity tags*. Nature, 2015. **520**(7546): p. 164-165.

276. Chen, D., et al., *Stimuli‐responsive buckling mechanics of polymer films*. Journal of Polymer Science Part B: Polymer Physics, 2014. **52**(22): p. 1441-1461.

277. Nguyen, J. and L. Werner, *Intraocular lenses for cataract surgery*. 2018.

278. Werner, L., *Biocompatibility of intraocular lens materials*. Current opinion in Ophthalmology, 2008. **19**(1): p. 41-49.

279. Maddula, S., et al., *Pathology of 157 human cadaver eyes with round-edged or modern square-edged silicone intraocular lenses: analyses of capsule bag opacification*. Journal of Cataract & Refractive Surgery, 2011. **37**(4): p. 740-748.

280. Xu, Y., H. Liu, and L. Song, *Novel drug delivery systems targeting oxidative stress in chronic obstructive pulmonary disease: a review*. Journal of Nanobiotechnology, 2020. **18**(1): p. 1-25.

281. Wu, J., Y. Li, and Y. Zhang, *Use of intraoral scanning and 3-dimensional printing in the fabrication of a removable partial denture for a patient with limited mouth opening*. The Journal of the American Dental Association, 2017. **148**(5): p. 338-341.

282. Bracci, R., E. Maccaroni, and S. Cascinu, *Bioresorbable airway splint created with a three-dimensional printer*. New England Journal of Medicine, 2013. **368**(21): p. 2043-5.

283. Banks, J., *Adding value in additive manufacturing: researchers in the United Kingdom and Europe look to 3D printing for customization*. IEEE pulse, 2013. **4**(6): p. 22-26.

284. Gross, B.C., et al., *Evaluation of 3D printing and its potential impact on biotechnology and the chemical sciences*. 2014, ACS Publications.

285. Coakley, M.F., et al., *The NIH 3D print exchange: a public resource for bioscientific and biomedical 3D prints*. 3D printing and additive manufacturing, 2014. **1**(3): p. 137-140.

286. Fukushima, T., et al., *Fully plastic actuator through layer‐by‐layer casting with ionic‐liquid‐based bucky gel*. Angewandte Chemie International Edition, 2005. **44**(16): p. 2410-2413.

287. Regehr, K.J., et al., *Biological implications of polydimethylsiloxane-based microfluidic cell culture*. Lab on a Chip, 2009. **9**(15): p. 2132-2139.

288. Tan, A., et al., *Rapid fabrication of microfluidic devices in poly (dimethylsiloxane) by photocopyingPresented at the 14th International Symposium on Microscale Separations and Analysis, Boston, January 13–18, 2001*. Lab on a Chip, 2001. **1**(1): p. 7-9.

289. Fiddes, L.K., et al., *A circular cross-section PDMS microfluidics system for replication of cardiovascular flow conditions*. Biomaterials, 2010. **31**(13): p. 3459-3464.

290. Matsuzaki, R. and A. Todoroki, *Wireless flexible capacitive sensor based on ultra-flexible epoxy resin for strain measurement of automobile tires*. Sensors and Actuators A: Physical, 2007. **140**(1): p. 32-42.

291. Cabezudo, N., et al., *Enhancement of surface wettability via micro-and nanostructures by single point diamond turning*. Nanotechnology and Precision Engineering, 2019. **2**(1): p. 8-14.

292. Scott, S.M. and Z. Ali, *Fabrication methods for microfluidic devices: An overview*. Micromachines, 2021. **12**(3): p. 319.

293. Holmes, D.P., et al., *Control and manipulation of microfluidic flow via elastic deformations*. Soft Matter, 2013. **9**(29): p. 7049-7053.

294. Wang, Y., et al., *A biorobotic adhesive disc for underwater hitchhiking inspired by the remora suckerfish*. Science Robotics, 2017. **2**(10).

295. Morin, S.A., et al., *Camouflage and display for soft machines*. Science, 2012. **337**(6096): p. 828-832.

296. Polygerinos, P., et al., *Soft robotic glove for combined assistance and at-home rehabilitation*. Robotics and Autonomous Systems, 2015. **73**: p. 135-143.

297. Martinez, R.V., et al., *Robotic tentacles with three‐dimensional mobility based on flexible elastomers*. Advanced materials, 2013. **25**(2): p. 205-212.

298. Ilievski, F., et al., *Soft robotics for chemists*. Angewandte Chemie, 2011. **123**(8): p. 1930-1935.

299. Larson, C., et al., *Highly stretchable electroluminescent skin for optical signaling and tactile sensing*. Science, 2016. **351**(6277): p. 1071-1074.

300. Martinez, R.V., et al., *Elastomeric origami: programmable paper‐elastomer composites as pneumatic actuators*. Advanced functional materials, 2012. **22**(7): p. 1376-1384.

301. Kwok, S.W., et al., *Magnetic assembly of soft robots with hard components*. Advanced Functional Materials, 2014. **24**(15): p. 2180-2187.

302. Trivedi, D., et al., *Soft robotics: Biological inspiration, state of the art, and future research*. Applied bionics and biomechanics, 2008. **5**(3): p. 99-117.

303. DOĞRUER, C.U., A.B. KOKU, and M. DÖLEN, *Springer Tracts in Advanced Robotics*. 2008.

304. Kofod, G., et al., *Energy minimization for self-organized structure formation and actuation*. Applied Physics Letters, 2007. **90**(8): p. 081916.

305. Pelrine, R., et al., *High-speed electrically actuated elastomers with strain greater than 100%*. Science, 2000. **287**(5454): p. 836-839.

306. Smela, E., O. Inganäs, and I. Lundström, *Controlled folding of micrometer-size structures*. Science, 1995. **268**(5218): p. 1735-1738.

307. Xu, H., et al., *Ferroelectric and electromechanical properties of poly (vinylidene-fluoride–trifluoroethylene–chlorotrifluoroethylene) terpolymer*. Applied Physics Letters, 2001. **78**(16): p. 2360-2362.

308. Zhang, Q., et al., *An all-organic composite actuator material with a high dielectric constant*. Nature, 2002. **419**(6904): p. 284-287.

309. Hines, L., et al., *Soft actuators for small‐scale robotics*. Advanced materials, 2017. **29**(13): p. 1603483.

310. Han, M.W. and S.H. Ahn, *Blooming knit flowers: Loop‐linked soft morphing structures for soft robotics*. Advanced materials, 2017. **29**(13): p. 1606580.

311. Tajbakhsh, A. and E. Terentjev, *Spontaneous thermal expansion of nematic elastomers*. The European Physical Journal E, 2001. **6**(2): p. 181-188.

312. Hamlen, R., C. Kent, and S. Shafer, *Electrolytically activated contractile polymer.* Nature, 1965. **206**(4989): p. 1149-1150.

313. Shiga, T. and T. Kurauchi, *Deformation of polyelectrolyte gels under the influence of electric field.* Journal of Applied Polymer Science, 1990. **39**(11‐12): p. 2305-2320.

314. Osada, Y., H. Okuzaki, and H. Hori, *A polymer gel with electrically driven motility.* Nature, 1992. **355**(6357): p. 242-244.

315. Zhang, J., *Design, Modelling, and Control of Soft-Bodied Magnetic Miniature Robots.* 2018, University of Toronto (Canada).

316. Kim, Y., et al., *Printing ferromagnetic domains for untethered fast-transforming soft materials.* Nature, 2018. **558**(7709): p. 274-279.

317. Ebron, V.H., et al., *Fuel-powered artificial muscles.* Science, 2006. **311**(5767): p. 1580-1583.

318. Park, S.-J., et al., *Phototactic guidance of a tissue-engineered soft-robotic ray.* Science, 2016. **353**(6295): p. 158-162.

319. Nawroth, J.C., et al., *A tissue-engineered jellyfish with biomimetic propulsion.* Nature biotechnology, 2012. **30**(8): p. 792-797.

320. Li, Z., et al., *A stimuli-responsive gel impregnated surface with switchable lipophilic/oleophobic properties.* Soft matter, 2020. **16**(6): p. 1636-1641.

321. Ahuja, K. and S. Bayas. *Global Additive Manufacturing With Metal Powders Market Size by Manufacturing Technique (Powder Bed {Direct Metal Laser Sintering, Selective Laser Melting, Electron Beam Melting}, Blown Powder {Direct Metal Deposition, Laser Engineering Net Shapes}), By Material (Alloy {Titanium [Ti6Al4V, Ti6Al4V (ELI)], Cobalt [CoCr, CoCr WC, CoCr Mo], Copper [C18150, CuCr1Zr, CuNi2SiCr], Nickel[Inconel 625, Inconel 718, Hastelloy X], Aluminum [ALSi12, ALSi7Mg, ALSi10Mg], Aluminum Nitride, Aluminum Oxide, Magnesium, Molybdenum, Zirconium, Zirconium Dioxide, Silicon Carbide, Tungsten, Tungsten Carbide, Stainless Steel {Austenitic Steel, Martensitic Steel, Duplex Steel, Ferritic Steel}, Other Steel {High Speed Steel, Tool Steel, Low Alloy Steel}, Precious Metal {Platinum}, By Application (Aerospace, Automotive, Medical, Oil & Gas, Energy [Nuclear, Renewable]), Industry Analysis Report, Regional Outlook, Application Potential, Competitive Market 2022- 2030.* 2022 [cited 2022; Available from: https://www.gminsights.com/industry-analysis/additive-manufacturing-with-metal-powders-market?gclid=Cj0KCQjw3eeXBhD7ARIsAHjssr_qhN8WjUeyuv5lRdAj9pBsitU2u4az9ZXk0qW9hqO0NaIcT_nOfHcaAmaxEALw_wcB.

322. Hood, P.J. and D.E. Havens, *Structural and optical applications for shape memory polymers (SMP).* 2006, Google Patents.

323. Hood, P.J., et al., *Method of making and using shape memory polymer composite patches.* 2010, Google Patents.

324. Lei, M., et al., *Micro-mechanics of nanostructured carbon/shape memory polymer hybrid thin film.* Soft Matter, 2016. **12**(1): p. 106-114.

325. Xu, B., et al., *Thermo-mechanical properties of polystyrene-based shape memory nanocomposites.* Journal of Materials Chemistry, 2010. **20**(17): p. 3442-3448.

326. Taherian, R., *Experimental and analytical model for the electrical conductivity of polymer-based nanocomposites.* Composites Science and Technology, 2016. **123**: p. 17-31.

327. Barna, Á., et al., *Producing metastable nanophase with sharp interface by means of focused ion beam irradiation.* Journal of Applied Physics, 2009. **105**(4): p. 044305.

328. Möller, W., W. Eckstein, and J. Biersack, *Tridyn-binary collision simulation of atomic collisions and dynamic composition changes in solids.* Computer Physics Communications, 1988. **51**(3): p. 355-368.

329. Sun, J., et al., *An investigation of redeposition effect for deterministic fabrication of nanodots by focused ion beam.* Precision engineering, 2012. **36**(1): p. 31-36.

330. Ibrahim, D., et al., *Dimensional error of selective laser sintering, three-dimensional printing and PolyJet™ models in the reproduction of mandibular anatomy.* Journal of Cranio-Maxillofacial Surgery, 2009. **37**(3): p. 167-173.

331. Winder, A., M. Ruben, and G. Sheraidah, *Tear calcium levels and contact lens wear.* British Journal of Ophthalmology, 1977. **61**(8): p. 539-543.

332. Simpson, J.T., S.R. Hunter, and T. Aytug, *Superhydrophobic materials and coatings: a review.* Reports on Progress in Physics, 2015. **78**(8): p. 086501.

333. Yilgör, E., C.K. Söz, and I. Yilgör, *Wetting behavior of superhydrophobic poly (methyl methacrylate).* Progress in Organic Coatings, 2018. **125**: p. 530-536.

334. Bhushan, B. and Y.C. Jung, *Natural and biomimetic artificial surfaces for superhydrophobicity, self-cleaning, low adhesion, and drag reduction.* Progress in Materials Science, 2011. **56**(1): p. 1-108.

335. Wang, S., et al., *Bioinspired surfaces with superwettability: new insight on theory, design, and applications.* Chemical reviews, 2015. **115**(16): p. 8230-8293.

336. Kochkodan, V. and N. Hilal, *A comprehensive review on surface modified polymer membranes for biofouling mitigation.* Desalination, 2015. **356**: p. 187-207.

337. Kreder, M.J., et al., *Design of anti-icing surfaces: smooth, textured or slippery?* Nature Reviews Materials, 2016. **1**(1): p. 1-15.

338. Zhang, C., D.A. Mcadams, and J.C. Grunlan, *Nano/Micro‐Manufacturing of Bioinspired Materials: a Review of Methods to Mimic Natural Structures.* Advanced Materials, 2016. **28**(30): p. 6292-6321.

339. Zhang, P., et al., *Designing Bioinspired Anti‐Biofouling Surfaces based on a Superwettability Strategy.* Small, 2017. **13**(4): p. 1503334.

340. Huang, X., Y. Sun, and S. Soh, *Stimuli‐responsive surfaces for tunable and reversible control of wettability.* Advanced Materials, 2015. **27**(27): p. 4062-4068.

341. Rhee, D., W.K. Lee, and T.W. Odom, *Crack‐Free, soft wrinkles enable switchable anisotropic wetting.* Angewandte Chemie, 2017. **129**(23): p. 6623-6627.

342. Lu, H., et al., *Spontaneous biaxial pattern generation and autonomous wetting switching on the surface of gold/shape memory polystyrene bilayer.* Composites Part B: Engineering, 2017. **122**: p. 9-15.

343. Liu, Y., J. Genzer, and M.D. Dickey, *"2D or not 2D": Shape-programming polymer sheets.* Progress in Polymer Science, 2016. **52**: p. 79-106.

344. Xu, B., et al., *Mechanical properties of attapulgite clay reinforced polyurethane shape-memory nanocomposites.* European Polymer Journal, 2009. **45**(7): p. 1904-1911.

345. Moon, M., et al., *A. Vaziri A, and JW Hutchinson.* P. Natl. Acad. Sci. USA, 2007. **104**: p. 1130.

346. Xu, B., et al., *Thermal-mechanical properties of polyurethane-clay shape memory polymer nanocomposites.* Polymers, 2010. **2**(2): p. 31-39.

347.	Giannuzzi, L.A. and M. Utlaut, *A review of Ga+ FIB/SIMS*. Surface and interface analysis, 2011. **43**(1‑2): p. 475-478.

348.	Roediger, P., et al., *Focused-ion-beam-inflicted surface amorphization and gallium implantation—New insights and removal by focused-electron-beam-induced etching*. Nanotechnology, 2011. **22**(23): p. 235302.

349.	Völlner, J., et al., *Topography evolution mechanism on fused silica during low-energy ion beam sputtering*. Journal of Applied Physics, 2011. **109**(4): p. 043501-043501-6.

350.	Oehrlein, G.S., R.J. Phaneuf, and D.B. Graves, *Plasma-polymer interactions: A review of progress in understanding polymer resist mask durability during plasma etching for nanoscale fabrication*. Journal of Vacuum Science & Technology B, Nanotechnology and Microelectronics: Materials, Processing, Measurement, and Phenomena, 2011. **29**(1): p. 010801.

351.	Cahill, D.G., *Morphological instabilities in thin-film growth and etching*. Journal of Vacuum Science & Technology A: Vacuum, Surfaces, and Films, 2003. **21**(5): p. S110-S116.

352.	Brostow, W., B.P. Gorman, and O. Olea-Mejia, *Focused ion beam milling and scanning electron microscopy characterization of polymer+ metal hybrids*. Materials Letters, 2007. **61**(6): p. 1333-1336.

353.	Brunner, S., et al., *Investigation of multilayered aluminium-coated polymer laminates by focused ion beam (FIB) etching*. Surface and Coatings Technology, 2006. **200**(20-21): p. 5908-5914.

354.	Pialat, E., et al., *Milling of polymeric photonic crystals by focused ion beam*. Materials Science and Engineering: C, 2005. **25**(5-8): p. 618-624.

355.	Mulders, J., D. De Winter, and W. Duinkerken, *Measurements and calculations of FIB milling yield of bulk metals*. Microelectronic engineering, 2007. **84**(5-8): p. 1540-1543.

356.	Muñoz-García, J., et al., *Observation and modeling of interrupted pattern coarsening: Surface nanostructuring by ion erosion*. Physical review letters, 2010. **104**(2): p. 026101.

357.	Muñoz-García, J., M. Castro, and R. Cuerno, *Nonlinear ripple dynamics on amorphous surfaces patterned by ion beam sputtering*. Physical review letters, 2006. **96**(8): p. 086101.

358.	Bradley, R.M. and J.M. Harper, *Theory of ripple topography induced by ion bombardment*. Journal of Vacuum Science & Technology A: Vacuum, Surfaces, and Films, 1988. **6**(4): p. 2390-2395.

359.	Eklund, E.A., et al., *Submicron-scale surface roughening induced by ion bombardment*. Physical review letters, 1991. **67**(13): p. 1759.

360.	Mitsui, T., et al., *Nanoscale volcanoes: accretion of matter at ion-sculpted nanopores*. Physical review letters, 2006. **96**(3): p. 036102.

361.	Rodríguez-Laguna, J., S.N. Santalla, and R. Cuerno, *Intrinsic geometry approach to surface kinetic roughening*. Journal of Statistical Mechanics: Theory and Experiment, 2011. **2011**(05): p. P05032.

362.	Kardar, M., G. Parisi, and Y.-C. Zhang, *Dynamic scaling of growing interfaces*. Physical Review Letters, 1986. **56**(9): p. 889.

363.	Makeev, M.A. and A.-L. Barabási, *Effect of surface roughness on the secondary ion yield in ion sputtering*. Applied physics letters, 1998. **73**(15): p. 2209-2211.

364.	Cuerno, R. and A.-L. Barabási, *Dynamic scaling of ion-sputtered surfaces*. Physical review letters, 1995. **74**(23): p. 4746.

365.	Castro, M., et al., *Self-organized ordering of nanostructures produced by ion-beam sputtering*. Physical review letters, 2005. **94**(1): p. 016102.

366. Muñoz-García, J., R. Cuerno, and M. Castro, *Coupling of morphology to surface transport in ion-beam-irradiated surfaces: normal incidence and rotating targets.* Journal of Physics: Condensed Matter, 2009. **21**(22): p. 224020.

367. Walmann, T., et al., *Scaling relations for the lengths and widths of fractures.* Physical review letters, 1996. **77**(27): p. 5393.

368. Mullins, W.W., *Theory of thermal grooving.* Journal of Applied Physics, 1957. **28**(3): p. 333-339.

369. Herring, C., *Effect of change of scale on sintering phenomena.* Journal of Applied Physics, 1950. **21**(4): p. 301-303.

370. Mullins, J. and M. Lettieri, *Chemosurgery of facial wrinkles.* Texas state journal of medicine, 1963. **59**: p. 488-495.

371. Jain, H. and J. Mundy, *Analysis of ac conductivity of glasses by a power law relationship.* Journal of Non Crystalline Solids, 1987. **91**(3): p. 315-323.

372. Voss, S., A. Imre, and H. Mehrer, *Mixed-alkali effect in Na–Rb borate glasses: A tracer diffusion and electrical conductivity study.* Physical chemistry chemical physics, 2004. **6**(13): p. 3669-3675.

373. Makeev, M.A. and A.-L. Barabasi, *Secondary ion yield changes on rippled interfaces.* Applied physics letters, 1998. **72**(8): p. 906-908.

374. Muñoz-García, J., R. Cuerno, and M. Castro, *Short-range stationary patterns and long-range disorder in an evolution equation for one-dimensional interfaces.* Physical Review E, 2006. **74**(5): p. 050103.

375. Kim, J., et al., *One-dimensional pattern of Au nanodots by ion-beam sputtering: formation and mechanism.* Nanotechnology, 2011. **22**(28): p. 285301.

376. Dai, X., et al., *Recoverable and self-healing electromagnetic wave absorbing nanocomposites.* Composites Science and Technology, 2019. **174**: p. 27-32.

377. King, J.A., et al., *Electrical conductivity of carbon‐filled polypropylene‐based resins.* Journal of applied polymer science, 2009. **112**(1): p. 425-433.

378. Motaghi, A., A. Hrymak, and G.H. Motlagh, *Electrical conductivity and percolation threshold of hybrid carbon/polymer composites.* Journal of applied polymer Science, 2015. **132**(13).

379. Li, J. and J.-K. Kim, *Percolation threshold of conducting polymer composites containing 3D randomly distributed graphite nanoplatelets.* Composites science and technology, 2007. **67**(10): p. 2114-2120.

380. Dang, Z.M., Y.H. Lin, and C.W. Nan, *Novel ferroelectric polymer composites with high dielectric constants.* Advanced Materials, 2003. **15**(19): p. 1625-1629.

381. Petra, P., M. Sergej, and A. Ingo, *Dielectric spectroscopy on melt processed polycarbonate-multiwalled carbon nanotube composites.* Polymer, 2003. **44**: p. 5023-5030.

382. Regev, O., et al., *Preparation of conductive nanotube–polymer composites using latex technology.* Advanced Materials, 2004. **16**(3): p. 248-251.

383. Dang, Z.M., et al., *Giant dielectric permittivities in functionalized carbon‐nanotube/electroactive‐polymer nanocomposites.* Advanced Materials, 2007. **19**(6): p. 852-857.

384. Karasek, L., et al., *Percolation concept: polymer-filler gel formation, electrical conductivity and dynamic electrical properties of carbon-black-filled rubbers.* Polymer journal, 1996. **28**(2): p. 121-126.

385. Mehrer, H., *Diffusion in solids: fundamentals, methods, materials, diffusion-controlled processes.* Vol. 155. 2007: Springer Science & Business Media.

386. Nicoli, M., R. Cuerno, and M. Castro, *Unstable nonlocal interface dynamics.* Physical review letters, 2009. **102**(25): p. 256102.

387. Ishitani, T., et al., *Focused‐ion‐beam '"cutter"' and '"attacher"' for micromachining and device transplantation.* Journal of Vacuum Science & Technology B: Microelectronics and Nanometer Structures Processing, Measurement, and Phenomena, 1991. **9**(5): p. 2633-2637.

388. Roy, X., P. Sarazin, and B.D. Favis, *Ultraporous nanosheath materials by layer‐by‐layer deposition onto co‐continuous polymer‐blend templates.* Advanced Materials, 2006. **18**(8): p. 1015-1019.

389. Cuerno, R., et al., *Surface nanopatterns induced by ion-beam sputtering.* Journal of Physics: Condensed Matter, 2009. **21**(22): p. 220301.

390. Woodward, M.A. and M. Sitti, *Morphological intelligence counters foot slipping in the desert locust and dynamic robots.* Proceedings of the National Academy of Sciences of the United States of America, 2018. **115**(36): p. E8358-E8367.

391. Elphick, M.R. and R. Melarange, *Neural control of muscle relaxation in echinoderms.* Journal of Experimental Biology, 2001. **204**(5): p. 875-885.

392. Lin, H.T., G.G. Leisk, and B. Trimmer, *GoQBot: a caterpillar-inspired soft-bodied rolling robot.* Bioinspiration & Biomimetics, 2011. **6**(2): p. 026007.

393. Ren, Z., et al., *Multi-functional soft-bodied jellyfish-like swimming.* Nture Communations, 2019. **10**(1): p. 2703.

394. Liu, J., et al., *Shaping and Locomotion of Soft Robots Using Filament Actuators Made from Liquid Crystal Elastomer–Carbon Nanotube Composites.* Advanced Intelligent Systems, 2020. **2**(6): p. 1900163.

395. Pena-Francesch, A., et al., *Biosynthetic self-healing materials for soft machines.* Nature Materials, 2020. **19**(11): p. 1230-1235.

396. Dong, X., et al., *Bioinspired cilia arrays with programmable nonreciprocal motion and metachronal coordination.* Science advances, 2020. **6**(45): p. eabc9323.

397. Liu, L., D.J. Broer, and P.R. Onck, *Travelling waves on photo-switchable patterned liquid crystal polymer films directed by rotating polarized light.* Soft Matter, 2019. **15**(40): p. 8040-8050.

398. Matsuda, T., et al., *Mechanoresponsive self-growing hydrogels inspired by muscle training.* Science, 2019. **363**(6426): p. 504-508.

399. Ni, C.J., et al., *Autonomous Shapeshifting Hydrogels via Temporal Programming of Photoswitchable Dynamic Network.* Chemistry of Materials, 2021. **33**(6): p. 2046-2053.

400. Yang, D., et al., *Buckling of Elastomeric Beams Enables Actuation of Soft Machines.* Advanced Materials, 2015. **27**(41): p. 6323-6327.

401. Wani, O.M., et al., *An Artificial Nocturnal Flower via Humidity-Gated Photoactuation in Liquid Crystal Networks.* Advanced Materials, 2019. **31**(2): p. 1805985.

402. Martinez, R.V., et al., *Elastomeric Origami: Programmable Paper-Elastomer Composites as Pneumatic Actuators.* Advanced Functional Materials, 2012. **22**(7): p. 1376-1384.

403. Guvendiren, M., J.A. Burdick, and S. Yang, *Solvent induced transition from wrinkles to creases in thin film gels with depth-wise crosslinking gradients.* Soft Matter, 2010. **6**(22): p. 5795-5801.

404. Xu, B. and R.C. Hayward, *Low-voltage switching of crease patterns on hydrogel surfaces.* Advanced Materials, 2013. **25**(39): p. 5555-5559.

405. Liu, K., et al., *Programmable Reversible Shape Transformation of Hydrogels Based on Transient Structural Anisotropy.* Advanced Materials, 2020. **32**(28): p. 2001693.
406. Yuk, H., et al., *Hydraulic hydrogel actuators and robots optically and sonically camouflaged in water.* Nat Commun, 2017. **8**: p. 14230.
407. Li, M., et al., *In-air fast response and high speed jumping and rolling of a light-driven hydrogel actuator.* Nat Commun, 2020. **11**(1): p. 3988.
408. Kim, C.-C., et al., *Highly stretchable, transparent ionic touch panel.* Science, 2016. **353**(6300): p. 682-687.
409. Liu, X., et al., *Hydrogel machines.* Materials Today, 2020. **36**: p. 102-124.
410. Palleau, E., et al., *Reversible patterning and actuation of hydrogels by electrically assisted ionoprinting.* Nat Commun, 2013. **4**: p. 2257.
411. Xu, B., et al., *A Remotely Controlled Transformable Soft Robot Based on Engineered Cardiac Tissue Construct.* Small, 2019. **15**(18): p. 1900006.
412. Li, F., et al., *Near-infrared light-responsive dynamic wrinkle patterns.* Science Advances, 2018. **4**(4): p. eaar5762.
413. Wang, T., et al., *Wrinkling and smoothing of a soft shell.* Journal of the Mechanics and Physics of Solids, 2020. **134**: p. 103738.
414. Ma, T., et al., *Dynamic wrinkling pattern exhibiting tunable fluorescence for anticounterfeiting applications.* Nat Commun, 2020. **11**(1): p. 1811.
415. Yang, S., K. Khare, and P.-C. Lin, *Harnessing Surface Wrinkle Patterns in Soft Matter.* Advanced Functional Materials, 2010. **20**(16): p. 2550-2564.
416. Stoop, N., et al., *Curvature-induced symmetry breaking determines elastic surface patterns.* Nat Mater, 2015. **14**(3): p. 337-342.
417. Li, T., et al., *Hierarchical 3D Patterns with Dynamic Wrinkles Produced by a Photocontrolled Diels-Alder Reaction on the Surface.* Advanced Materials, 2020. **32**(7): p. 1906712.
418. Liu, L. and P.R. Onck, *Topographical changes in photo-responsive liquid crystal films: a computational analysis.* Soft Matter, 2018. **14**(12): p. 2411-2428.
419. Liu, Q., et al., *Elastocapillary Crease.* Physical Review Letters, 2019. **122**(9): p. 098003.
420. Jin, L., S. Cai, and Z. Suo, *Creases in soft tissues generated by growth.* Europhysics Letters, 2011. **95**(6): p. 64002.
421. Kim, J., J. Yoon, and R.C. Hayward, *Dynamic display of biomolecular patterns through an elastic creasing instability of stimuli-responsive hydrogels.* Nat Mater, 2010. **9**(2): p. 159-164.
422. Kim, P., M. Abkarian, and H.A. Stone, *Hierarchical folding of elastic membranes under biaxial compressive stress.* Nture Communations, 2011. **10**(12): p. 952-957.
423. Al-Rashed, R., et al., *Buckling patterns in biaxially pre-stretched bilayer shells: wrinkles, creases, folds and fracture-like ridges.* Soft Matter, 2017. **13**(43): p. 7969-7978.
424. Yang, Y., et al., *Pattern Transitions in a Soft Cylindrical Shell.* Physical Review Letters, 2018. **120**(21): p. 215503.
425. Ouchi, T., et al., *Effects of Stiff Film Pattern Geometry on Surface Buckling Instabilities of Elastic Bilayers.* Acs Applied Materials & Interfaces, 2018. **10**(27): p. 23406-23413.
426. Jin, L., *Mechanical Instabilities of Soft Materials: Creases, Wrinkles, Folds, and Ridges.* 2014, Harvard University.
427. Edmondson, S., et al., *Buckling in Quasi-2D Polymers.* Advanced Materials, 2006. **18**(6): p. 724-728.

428.	Nojoomi, A., et al., *Bioinspired 3D structures with programmable morphologies and motions*. Nat Commun, 2018. **9**(1): p. 3705.

429.	Zhao, Q., et al., *A bioinspired reversible snapping hydrogel assembly*. Materials Horizons, 2016. **3**(5): p. 422-428.

430.	Holmes, D.P., et al., *Bending and twisting of soft materials by non-homogenous swelling*. Soft Matter, 2011. **7**(11): p. 5188-5193.

431.	Na, J.H., et al., *Programming reversibly self-folding origami with micropatterned photo-crosslinkable polymer trilayers*. Adv Mater, 2015. **27**(1): p. 79-85.

432.	Angelo, C., et al., *DNA sequence–directed shape change of photopatterned hydrogels via high-degree swelling*. Science, 2017. **357**: p. 1126-1130.

433.	Wang, Z.J., et al., *Site-Specific Pre-Swelling-Directed Morphing Structures of Patterned Hydrogels*. Angewandte Chemie-International Edition, 2017. **56**(50): p. 15974-15978.

434.	Fan, W., et al., *Dual-gradient enabled ultrafast biomimetic snapping hydrogel materials of hydrogel materials*. Science Advances, 2019. **5**: p. eaav7174.

435.	Zhou, Y., et al., *Biasing Buckling Direction in Shape‐Programmable Hydrogel Sheets with Through‐Thickness Gradients*. Advanced Functional Materials, 2019. **29**(48): p. 1905273.

436.	Lee, H., et al., *Prescribed pattern transformation in swelling gel tubes by elastic instability*. Physical Review Letters, 2012. **108**(21): p. 214304.

437.	Arifuzzaman, M., et al., *Geometric and Edge Effects on Swelling-Induced Ordered Structure Formation in Polyelectrolyte Hydrogels*. Macromolecules, 2013. **46**(22): p. 9083-9090.

438.	Takahashi, R., et al., *Coupled instabilities of surface crease and bulk bending during fast free swelling of hydrogels*. Soft Matter, 2016. **12**(23): p. 5081-5088.

439.	Pezzulla, M., et al., *Curvature-Induced Instabilities of Shells*. Physical Review Letters, 2018. **120**(4): p. 048002.

440.	Pezzulla, M., et al., *Curvature-driven morphing of non-Euclidean shells*. Proceedings of the Royal Society a-Mathematical Physical and Engineering Sciences, 2017. **473**(2201): p. 20170087.

441.	Stein-Montalvo, L., et al., *Buckling of geometrically confined shells*. Soft Matter, 2019. **15**(6): p. 1215-1222.

442.	Tanaka, T., et al., *Mechanical instability of gels at the phase transition*. Nature, 1987. **325**(26): p. 796-798.

443.	Tanaka, T., et al., *Mechanical Instability of Swelling Gels*. Studies in Polymer Science ed. 1988, Amsterdam: Elsevier Science Publishers B.V.

444.	Takahashi, K., T. Takigawa, and T. Masuda, *Swelling and deswelling kinetics of poly(N-isopropylacrylamide) gels*. The Journal of Chemical Physics, 2004. **120**(6): p. 2972-2979.

445.	Seo, J., et al., *Multiscale reverse engineering of the human ocular surface*. Nature medicine, 2019. **25**(8): p. 1310-1318.

446.	Liu, C., et al., *Mucin‐Like Glycoproteins Modulate Interfacial Properties of a Mimetic Ocular Epithelial Surface*. Advanced Science, 2021. **8**(16): p. 2100841.

447.	Hu, Y., et al., *Pump‐color selective control of ultrafast all‐optical switching dynamics in metaphotonic devices*. Advanced Science, 2020. **7**(14): p. 2000799.

448. Chu, C., et al., *Multimodal Photoacoustic Imaging‐Guided Regression of Corneal Neovascularization: A Non‐Invasive and Safe Strategy*. Advanced Science, 2020. **7**(14): p. 2000346.

449. Hashemi, H., et al., *Global and regional prevalence of age-related cataract: a comprehensive systematic review and meta-analysis*. Eye, 2020. **34**(8): p. 1357-1370.

450. Flaxman, S.R., et al., *Global causes of blindness and distance vision impairment 1990–2020: a systematic review and meta-analysis*. The Lancet Global Health, 2017. **5**(12): p. e1221-e1234.

451. Pascolini, D. and S.P. Mariotti, *Global estimates of visual impairment: 2010*. British Journal of Ophthalmology, 2012. **96**(5): p. 614-618.

452. Ridley, H., *Further observations on intraocular acrylic lenses in cataract surgery*. Transactions - American Academy of Ophthalmology and Otolaryngology. American Academy of Ophthalmology and Otolaryngology, 1953. **57**(1): p. 98-106.

453. Ridley, H., *Intra-Ocular Acrylic Lenses*. A Recent Development in the Surgery of Cataract, 1952. **36**(3): p. 113-122.

454. Shen, Z., et al., *Clinical comparison of patient outcomes following implantation of trifocal or bifocal intraocular lenses: a systematic review and meta-analysis*. Scientific Reports, 2017. **7**(1): p. 45337.

455. Awasthi, N., S. Guo, and B.J. Wagner, *Posterior Capsular Opacification: A Problem Reduced but Not Yet Eradicated*. Archives of Ophthalmology, 2009. **127**(4): p. 555-562.

456. Salerno, L., et al., *Multifocal intraocular lenses: Types, outcomes, complications and how to solve them*. Taiwan Journal of Ophthalmology, 2017. **7**(4): p. 179-184.

457. Findl, O., et al., *Interventions for preventing posterior capsule opacification*. Cochrane Database of Systematic Reviews, 2010(2).

458. Lambert, S.R., et al., *Long-term Effect of Intraocular Lens vs Contact Lens Correction on Visual Acuity After Cataract Surgery During Infancy: A Randomized Clinical Trial*. JAMA Ophthalmology, 2020. **138**(4): p. 365-372.

459. Sanders, D. and J.A. Vukich, *Comparison of implantable collamer lens (ICL) and laser-assisted in situ keratomileusis (LASIK) for low myopia*. Cornea, 2006. **25**(10): p. 1139-1146.

460. Khandelwal, S.S., et al., *Effectiveness of multifocal and monofocal intraocular lenses for cataract surgery and lens replacement: a systematic review and meta-analysis*. Graefe's Archive for Clinical and Experimental Ophthalmology, 2019. **257**(5): p. 863-875.

461. Hoffer, K.J. and G. Savini, *Update on Intraocular Lens Power Calculation Study Protocols: The Better Way to Design and Report Clinical Trials*. Ophthalmology, 2020. **In press**.

462. Wang, L. and D.D. Koch, *Intraocular Lens Power Calculations in Eyes with Previous Corneal Refractive Surgery: Review and Expert Opinion*. Ophthalmology, 2020.

463. Kane, J.X. and D.F. Chang, *Intraocular Lens Power Formulas, Biometry, and Intraoperative Aberrometry: A Review*. Ophthalmology, 2020. **In press**(In press): p. In press.

464. Wirtitsch, M.G., et al., *Effect of haptic design on change in axial lens position after cataract surgery*. Journal of Cataract & Refractive Surgery, 2004. **30**(1): p. 45-51.

465.	Oshika, T., et al., *Mid-term and long-term clinical assessments of a new 1-piece hydrophobic acrylic IOL with hydroxyethyl methacrylate.* Journal of Cataract & Refractive Surgery, 2020. **46**(5): p. 682-687.

466.	Li, Y., et al., *Responsive Hydrogels Based Lens Structure with Configurable Focal Length for Intraocular Lens (IOLs) Application.* Macromolecular Symposia, 2017. **372**(1): p. 127-131.

467.	Isaacson, A., S. Swioklo, and C.J. Connon, *3D bioprinting of a corneal stroma equivalent.* Experimental Eye Research, 2018. **173**: p. 188-193.

468.	Ko, J., et al., *Semi-automated fabrication of customized ocular prosthesis with three–dimensional printing and sublimation transfer printing technology.* Scientific Reports, 2019. **9**(1): p. 2968.

469.	Famery, N., et al., *Artificial chamber and 3D printed iris: a new wet lab model for teaching Descemet's membrane endothelial keratoplasty.* Acta Ophthalmologica, 2019. **97**(2): p. e179-e183.

470.	Kim, J., et al., *Wearable smart sensor systems integrated on soft contact lenses for wireless ocular diagnostics.* Nature Communications, 2017. **8**(1): p. 14997.

471.	Famery, N., et al., *Artificial chamber and 3D printed iris: a new wet lab model for teaching Descemet's membrane endothelial keratoplasty.* Acta Ophthalmologica, 2019. **97**(2): p. e179-e183.

472.	Dong, L., et al., *Adaptive liquid microlenses activated by stimuli-responsive hydrogels.* Nature, 2006. **442**(7102): p. 551-554.

473.	Kang, S., M. Duocastella, and C.B. Arnold, *Variable optical elements for fast focus control.* Nature Photonics, 2020. **14**(9): p. 533-542.

474.	Berto, P., et al., *Tunable and free-form planar optics.* Nature Photonics, 2019. **13**(9): p. 649-656.

475.	Ma, Z.-C., et al., *Smart Compound Eyes Enable Tunable Imaging.* Advanced Functional Materials, 2019. **29**(38): p. 1903340.

476.	Ward, E.J., et al., *2D Titanium Carbide (Ti3C2Tx) in Accommodating Intraocular Lens Design.* Advanced Functional Materials, 2020. **30**(47): p. 2000841.

477.	Chen, L., et al., *Thermal-responsive hydrogel surface: tunable wettability and adhesion to oil at the water/solid interface.* Soft Matter, 2010. **6**(12): p. 2708-2712.

478.	Kolberg, A., et al., *Opposing Temperature Dependence of the Stretching Response of Single PEG and PNiPAM Polymers.* Journal of the American Chemical Society, 2019. **141**(29): p. 11603-11613.

479.	Lima, L.H., Y. Morales, and T. Cabral, *Ocular Biocompatibility of Poly-N-Isopropylacrylamide (pNIPAM).* Journal of Ophthalmology, 2016. **2016**: p. 5356371.

480.	Xue, H., et al., *Antibacterial coatings based on microgels containing quaternary ammonium ions: Modification with polymeric sugars for improved cytocompatibility.* Colloid and Interface Science Communications, 2020. **37**: p. 100268.

481.	Yoshida, R., et al., *Comb-type grafted hydrogels with rapid deswelling response to temperature changes.* Nature, 1995. **374**(6519): p. 240-242.

482.	Kaneko, Y., et al., *Influence of Freely Mobile Grafted Chain Length on Dynamic Properties of Comb-Type Grafted Poly(N-isopropylacrylamide) Hydrogels.* Macromolecules, 1995. **28**(23): p. 7717-7723.

483.	Apsite, I., et al., *Microfabrication Using Shape-Transforming Soft Materials.* Advanced Functional Materials, 2020. **30**(26): p. 1908028.

484. Tzounis, L., et al., *Temperature-Controlled Catalysis by Core–Shell–Satellite AuAg@pNIPAM@Ag Hybrid Microgels: A Highly Efficient Catalytic Thermoresponsive Nanoreactor.* ACS Applied Materials & Interfaces, 2019. **11**(32): p. 29360-29372.

485. Erol, O., et al., *Transformer Hydrogels: A Review.* Advanced Materials Technologies, 2019. **4**(4): p. 1900043.

486. Wang, Y., et al., *Smart, Photothermally Activated, Antibacterial Surfaces with Thermally Triggered Bacteria-Releasing Properties.* ACS Applied Materials & Interfaces, 2020. **12**(19): p. 21283-21291.

487. Bayat, N., et al., *A reversible thermoresponsive sealant for temporary closure of ocular trauma.* Science Translational Medicine, 2017. **9**(419): p. eaan3879.

488. Doberenz, F., et al., *Thermoresponsive polymers and their biomedical application in tissue engineering – a review.* Journal of Materials Chemistry B, 2020. **8**(4): p. 607-628.

489. Haq, M.A., Y. Su, and D. Wang, *Mechanical properties of PNIPAM based hydrogels: A review.* Materials Science and Engineering: C, 2017. **70**: p. 842-855.

490. Fyodorov, S.N., M.A. Galin, and A. Linksz, *Calculation of the optical power of intraocular lenses.* Investigative Ophthalmology & Visual Science, 1975. **14**(8): p. 625-628.

491. Fernández, J., et al., *New method to assess the accuracy of intraocular lens power calculation formulas according to ocular biometric parameters.* Journal of Cataract & Refractive Surgery, 2020. **46**(6): p. 849-856.

492. Alba-Bueno, F., F. Vega, and M.S. Millán, *Design of a Test Bench for Intraocular Lens Optical Characterization.* Journal of Physics: Conference Series, 2011. **274**.

493. González-Méijome, J.M., et al., *Refractive index and equilibrium water content of conventional and silicone hydrogel contact lenses.* 2006. **26**(1): p. 57-64.

494. Lee, S.J., et al., *Surface calcification of hydrophilic acrylic intraocular lens related to inflammatory membrane formation after combined vitrectomy and cataract surgery.* Journal of Cataract & Refractive Surgery, 2010. **36**(4): p. 676-681.

495. Walker, N.J., et al., *Calcification of hydrophilic acrylic intraocular lenses in combined phacovitrectomy surgery.* Journal of Cataract & Refractive Surgery, 2010. **36**(8): p. 1427-1431.

496. Fellman, M.A., et al., *Calcification of a hydrophilic acrylic intraocular lens after Descemet-stripping endothelial keratoplasty: Case report and laboratory analyses.* Journal of Cataract & Refractive Surgery, 2013. **39**(5): p. 799-803.

497. Yokoi, T., et al., *Crystallization of calcium phosphate in polyacrylamide hydrogels containing phosphate ions.* Journal of Crystal Growth, 2010. **312**(16): p. 2376-2382.

498. Winder, A.F., M. Ruben, and G.A. Sheraidah, *Tear calcium levels and contact lens wear.* British Journal of Ophthalmology, 1977. **61**(8): p. 539-543.

499. Uotila, M.H., R.E. Soble, and J. Savory, *Measurement of tear calcium levels.* Invest Ophthalmol, 1972. **11**(4): p. 258-259.

500. Chen, X., et al., *Hydrogel Bioadhesives with Extreme Acid‐Tolerance for Gastric Perforation Repairing.* Advanced Functional Materials, 2022: p. 2202285.

501. Li, J.-W., et al., *Biosafety of a 3D-printed intraocular lens made of a poly (acrylamide-co-sodium acrylate) hydrogel in vitro and in vivo.* International Journal of Ophthalmology, 2020. **13**(10): p. 1521.

502. Liu, Y.-C., T.T. Wong, and J.S. Mehta, *Intraocular lens as a drug delivery reservoir.* Current opinion in ophthalmology, 2013. **24**(1): p. 53-59.

503. Ford, J., L. Werner, and N. Mamalis, *Adjustable intraocular lens power technology.* Journal of Cataract & Refractive Surgery, 2014. **40**(7): p. 1205-1223.

504. Boyer, D., et al., *Long-term (60-month) results for the implantable miniature telescope: efficacy and safety outcomes stratified by age in patients with end-stage age-related macular degeneration.* Clinical Ophthalmology (Auckland, NZ), 2015. **9**: p. 1099.

505. Johnston, I., et al., *Mechanical characterization of bulk Sylgard 184 for microfluidics and microengineering.* Journal of Micromechanics and Microengineering, 2014. **24**(3): p. 035017.

506. Kim, B., et al., *A comparison among Neo-Hookean model, Mooney-Rivlin model, and Ogden model for chloroprene rubber.* International Journal of Precision Engineering and Manufacturing, 2012. **13**(5): p. 759-764.

507. Nania, M., et al., *Sub-100 nm wrinkling of polydimethylsiloxane by double frontal oxidation.* Nanoscale, 2017. **9**(5): p. 2030-2037.

Appendix

Publications are presented in this section. Please see following pages for detail.

ADVANCED 3D MORPHING TRANSDUCERS BY SMART HYDROGEL PATTERNING

Cong Wang[1], Sreepathy Sridhar[1], Jonathan G. Terry[2], Ansu Sun[1], Zhenghong Li[3], Haibao Lv[3], Ben B. Xu[1] and Yifan Li[1]

[1]Mechanical and Construction Engineering, Faculty of Engineering and Environment, Northumbria University, Newcastle upon Tyne, NE1 8ST, UK

[2]SMC, Institute for Integrated Micro and Nano Systems, School of Engineering, University of Edinburgh, Edinburgh, EH9 3JF, UK

[3]Science and Technology on Advanced Composites in Special Environments Laboratory, Harbin Institute of Technology, Harbin, 150080, P.R. CHINA

ABSTRACT

This paper demonstrates a unique way of creating heterogeneous layered structures of soft functional materials for advanced transducer applications. Hydrogel droplets with different composites were patterned by a "two-parallel plate" configuration used in microfluidics applications. Resulted heterogeneous layered structures of hydrogel were created, generating reconfigurable 3D (3-dimensional) deformation responding to discrete levels of stimulation inputs.

KEYWORDS

Heterogeneous hydrogel, droplet microfluidics, responsive swelling, flexible sensors, surface wettability

INTRODUCTION

Morphing soft materials responding to external stimulation (e.g. electrical, mechanical and chemical) have promising applications in various fields, such as flexible electronics, biomedical transducers and soft robotics. One of the desirable developments is to make the self-shaping process controllable and programmable, at least for specific configurations.

Wang et al. [1] has demonstrated 3D shape control through planar (flat) patterned, homogeneous swell-able hydrogels. "Pre-designed" complex deformations were demonstrated by the periodically patterned hydrogel blocks made from multi-step lithographically. The shape morphing was then generated due to elastic mismatch between non-swelling substrate and swelling gel blocks [1, 2]. Holed "swelling masks" were employed to control the swelling directions, in order to re-configure the deformation patterns [1].

Whilst patterned homogenous layered structures can provide "pre-designed" 3D shapes, the post-swelling configurations are fixed in [1, 2]. For reconfigurable morphing structures which dynamically change shapes responding to stimulation, heterogenous structures are desired.

Uniform heterogenous bio-content deposition was achieved previously by droplet microfluidics utilizing surface wettability (hydrophobic/philic patterns) [3]. More recently, using droplet microfluidics to control the formation of encoded multifunctional, and heterogeneous hydrogel building blocks have been exploited to form complex hydrogel architectures, inspired by natural bio-structures [4, 5].

In such cases [1, 4], two parallel plates with millimeter to sub-millimeter gap in-between (similar to a Hele-Shaw Cell) were introduced to help achieve a uniformly thin deposited layer.

Combining the latest development in smart hydrogel patterning, and the hydrogel-based 3D morphing technology brings the great potential of next generation re-configurable, stimuli-responsive, morphing soft transducers.

METHODOLOGY

The state of the art of this work are demonstrated from the following two aspects:

• Heterogeneous hydrogel blocks patterned and layered by controlled surface wetting at hydrophobic and hydrophilic boundaries (figure 1). The layer thickness and uniformity are ensured and controlled by droplet volume and the gap between the two parallel plates shown in figure 1.

• Reconfigurable 3D morphing response to the stimulation inputs such as changing ionic concentration and temperature of the solution this hydrogel structure is immersed in.
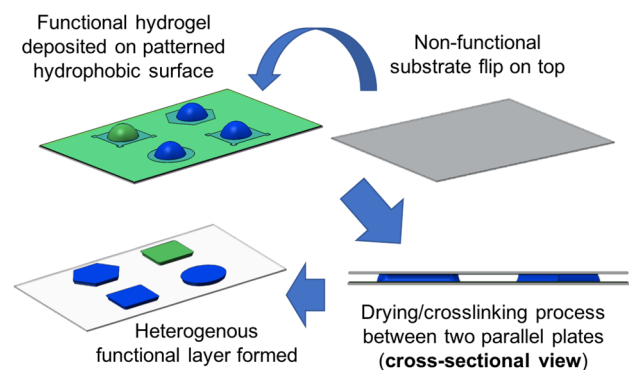
Figure 1: Schematic view of the heterogenous hydrogel structure patterned by hydrophobic/philic surface.

The hydrogel used are Poly(Acrylamide-Sodium Acrylate), created from poly-acrylamide (PAAm) network with Sodium Acrylate (SA) which contains free positive sodium ions. N,N'-Methylenebisacrylamide (BisAA or MBAA) was used as a cross linker, with N,N,N′,N′-Tetramethylethylenediamine (TEMED) and Ammonium Persulfate (APS) used as initiators for the polymerization process.

Article

Spatially Engraving Morphological Structure on a Polymeric Surface by Ion Beam Milling

Ansu Sun [1], Ding Wang [1] , Honghao Zhou [1], Yifan Li [1], Chris Connor [1], Jie Kong [2],*, Jining Sun [3],* and Ben Bin Xu [1],*

[1] Mechanical and Construction Engineering, Faculty of Engineering and Environment, Northumbria University, Newcastle upon Tyne NE1 8ST, UK

[2] MOE Key Laboratory of Materials Physics and Chemistry in Extraordinary Conditions, Shaanxi Key Laboratory of Macromolecular Science and Technology, School of Science, Northwestern Polytechnic University, Xi'an 710072, China

[3] School of Engineering and Physical Sciences, Heriot-Watt University, Edinburgh EH14 4AS, UK

* Correspondence: kongjie@nwpu.edu.cn (J.K.); jining.sun@hw.ac.uk (J.S.); ben.xu@northumbria.ac.uk (B.B.X.)

check for updates

Abstract: Polymer surface patterning and modification at the micro/nano scale has been discovered with great impact in applications such as microfluidics and biomedical technologies. We propose a highly efficient fabricating strategy, to achieve a functional polymer surface, which has control over the surface roughness. The key development in this fabrication method is the polymer positive diffusion effect (PDE) for an ion-bombarded polymeric hybrid surface through focused ion beam (FIB) technology. The PDE is theoretically explored by introducing a positive diffusion term into the classic theory. The conductivity-induced PDE constant is discussed as functions of substrates conductivity, ion energy and flux. The theoretical results agree well with the experiential results on the conductivity-induced PDE, and thus yield good control over roughness and patterning milling depth on the fabricated surface. Moreover, we demonstrate a controllable surface wettability in hydrophobic and superhydrophobic surfaces (contact angles (CA) range from 108.3° to 150.8°) with different CA hysteresis values ranging from 31.4° to 8.3°.

Keywords: ion beam milling; topographic surface; wetting; contact angle hysteresis

1. Introduction

Surface patterning and modification at micro-/nano-scales have been of great importance in creating functional surfaces for a wide range of applications, such as water repelling and self-cleaning [1–4], antifouling [5], anti-icing [6], adhesion control, and drag reduction technologies [7,8]. To create surfaces with desired roughness and topography, some techniques have been commonly used, such as lithography-based plasma etching and deposition, coating on top of patterned substrates, and/or soft-lithography pattern transferring, and, more recently, creating stimuli-responsive surface cracking, wrinkling [9–13] and other deformations on smart material surfaces [14–16].

The focused ion beam (FIB) technique has proven its efficiency in manufacturing semiconductors, metals and metal oxides, with its unique capability for rapid prototyping and high precision [17,18]. The fundamental mechanism of FIB is that highly energetic ions driven by an electrical field knock atoms off the material surface by electro-collision and the recoil action between the ion and target material surface (Figure 1). For ion-milled surfaces, the morphological evolution can cause kinetic roughness, which has attracted increasing research interest in recent decades [19–21]. However, limited attempts have been reported on the topic of FIB processing on polymeric substrates, since the charging effect from the insulated polymer matrix significantly reduces manufacturing precision,

Interfacial Interaction Enhanced Rheological Behavior in PAM/CTAC/Salt Aqueous Solution—A Coarse-Grained Molecular Dynamics Study

Dongjie Liu [1,2], Yong Li [3], Fei Liu [2], Wenjing Zhou [1], Ansu Sun [4], Xiaoteng Liu [4], Fei Chen [1,*], Ben Bin Xu [4,*] and Jinjia Wei [1,2,*]

[1] School of Chemical Engineering and Technology, Xi'an Jiaotong University, Xi'an 710049, China; jun080511@stu.xjtu.edu.cn (D.L.); wj.zhou@mail.xjtu.edu.cn (W.Z.)

[2] State Key Laboratory of Multiphase Flow in Power Engineering, Xi'an Jiaotong University, Xi'an 710049, China; bestceo@xjtu.edu.cn

[3] Drilling and Production Engineering Research Institute, Chuanqing Drilling and Exploration Engineering Company Ltd, CNPC, Xi'an 710018, China; liyong_gcy@cnpc.com.cn

[4] Mechanical and Construction Engineering, Faculty of Engineering and Environment, Northumbria University, Newcastle upon Tyne, NE1 8ST, UK; ansu.sun@northumbria.ac.uk (A.S.); terence.liu@northumbria.ac.uk (T.L.)

* Correspondence: Correspondence: feichen@xjtu.edu.cn (F.C.); ben.xu@northumbria.ac.uk (B.B.X.); jjwei@xjtu.edu.cn (J.W.) Tel.: +86-029-82664375 (J.W.)

Abstract: Interfacial interactions within a multi-phase polymer solution play critical roles in processing control and mass transportation in chemical engineering. However, the understandings of these roles remain unexplored due to the complexity of the system. In this study, we used an efficient analytical method—a nonequilibrium molecular dynamics (NEMD) simulation—to unveil the molecular interactions and rheology of a multiphase solution containing cetyltrimethyl ammonium chloride (CTAC), polyacrylamide (PAM), and sodium salicylate (NaSal). The associated macroscopic rheological characteristics and shear viscosity of the polymer/surfactant solution were investigated, where the computational results agreed well with the experimental data. The relation between the characteristic time and shear rate was consistent with the power law. By simulating the shear viscosity of the polymer/surfactant solution, we found that the phase transition of micelles within the mixture led to a non-monotonic increase in the viscosity of the mixed solution with the increase in concentration of CTAC or PAM. We expect this optimized molecular dynamic approach to advance the current understanding on chemical–physical interactions within polymer/surfactant mixtures at the molecular level and enable emerging engineering solutions.

Keywords: rheology; shear viscosity; shear rates; molecular dynamic

1. Introduction

Polymers and surfactants are essential additives that have been frequently used in petroleum engineering [1–4], process intensification [5], mass transportation [6], sewage systems [7], drag delivery [8,9], etc. Within a polymer/surfactant mixture, macromolecule chains and surfactant micelles can chemically/physically interact to generate unique structures/phases such as swollen cages, bottlebrushes, etc. [10]. Those structures can bring programmable viscosity and the reduction of surface tension, which can significantly influence the downstream applications in detergents, pharmaceuticals, and cosmetics [11]. Some studies have been performed to understand the mechanism for those chemically/physically interactions in mixtures without salt [12–16], however,

ARTICLE

Stimuli-responsive gel impregnated surface with switchable lipophilic/oleophobic properties

Zhenghong Li [a], Yingzhi Liu [a], Ming Lei [a], Ansu Sun [b], Sreepathy Sridhar [b], Yifan Li [b], Xuqing Liu [c], Haibao Lu *[a], Yong Qing Fu [b] and Ben Bin Xu *[b]

In this paper, we developed a novel morphing surface technique consisting of 3D printed miniature groove structure and injected stimuli-responsive hydrogel pattern, which is capable of switching between lipophilicity and oleophobicity under certain stimuli. Under swelling, the geometrical change of hydrogel will buckle the surface due to the structural confinement and create a continuous transition of surface topology. Thus, it will yield a change on surface wetting property from oleophilic to super-oleophobic with a contact angle of oil of 85° to 165°. We quantitatively investigate this structure-property relationship using finite element analysis and analytical modeling, and the simulation results and the modeling are in good agreement with the experimental ones. This morphing surface also holds its potentials to be developed into autonomous system for future sub-sea/off-shore engineering applications to separate oil and water.

1 Introduction

Developing novel and controllable wettability approaches using functional surfaces has attracted significant research interests, with underwater super-oleophobic surfaces being one of the hottest areas with promising applications in micro-fluidics, oil/water separation, marine antifouling coating, and self-cleaning technology.[1-7] For example, Jiang's group previously found an interesting phenomenon from fish, where its self-cleaning skin has a multi-length-scale hierarchical structure to enable an outstanding under water oleophobic property and on-demand surface wettability control, thus allowing fish to move freely in the oil-contaminated water.[8]

Aizenberg et.al developed a rough structure to lock the liquid to prepare a smooth liquid-infused porous surface (SLIPS), inspired by the structure of the pitcher plant.[9] This surface is good at reducing the viscous force of the liquid on the surface and can repel all liquids. Lu et al. prepared TiO_2 particles of two different sizes and ethanolic suspension with a certain proportion of fluorosilicone, using spray or dip coating methods to adhere them to the surface with double-sided tape. The surface was then immersed in hexadecane to obtain a tough, ultra-smooth and superhydrophobic material.[10] Rykaczewski et al. made micro-pattern arrays on silicon using the photolithography method, then the arrays were post-processed with octadecyltrichlorosilane hydrophobic layer, before infused the surface with ultra-light lubricating oil after

adding perfluoro oil. This effectively prompts the droplet condensation of liquid with low surface tension.[11]

Bio-compatible and stimuli-responsive hydrogel materials can sense the environmental changes with adjustable responses controlled by their compositions and physical properties. Suo et al. demonstrated a hydrogel interferometer with adaptive colouration, providing a facilely tuneable way for broader functionalities.[12] Moreover, hydrogels are consisted of unique hydrophilic groups, whose internal three-dimensional (3D) crosslinked polymer network can absorb and retain large amounts of water molecules, which opens up opportunities for interface/surface structure designs to be applied in aqueous environment. For example, Liu's group used hydrogels to simulate fish scales' surfaces, which can be used in underwater super-oleophobic surface.[13,14] The conventional approach for oil/water separation is heavily relied on the hydrophilic nature of materials, *e.g.* using the hydrogel structures for oil/water separation.[15-17] However, the surfaces of such structures can be easily contaminated by oil residues, while the fabrication cost is normally high.

Recently, additive manufacturing, *e.g.* 3D printing, have re-invented the rapid prototyping technologies with a great efficiency.[18] Whilst there are great application potentials, some technical challenges remain, such as facilitation of complicated geometries and printing precisions. Currently, researchers have applied soft functional materials together with structural designs for enhanced actuating/sensing.[19,20] For example, Lewis et al fabricated strain sensors within highly conformal and extensible elastomeric matrices.[21] Kang et al printed integrated structures of a hydrogel and an elastomer in an arbitrary sequence, which enables new soft robotics concepts for medicine engineering.[22] Lei et al used 3D printing to achieve an auxetic metamaterial, which can continuously

a. *State Key Laboratory of Science and Technology on Advanced Composites in Special Environments, Harbin Institute of Technology, Harbin 150080, P.R. China.*
b. *Smart Materials and Surfaces Laboratory, Faculty of Engineering and Environment, Northumbria University, Newcastle upon Tyne NE1 8ST, UK.*
c. *School of Materials, University of Manchester, Oxford Road, Manchester, United Kingdom, M13 9PL.*
† E-mail: luhb@hit.edu.cn and ben.xu@northumbria.ac.uk

Soft Matter Accepted Manuscript

Controlled Cooperative Wetting Enabled Heterogeneous Structured 3D Morphing Transducers

Sreepathy Sridhar, Cong Wang, Jonathan G. Terry, Xue Chen, Ansu Sun, Zhenghong Li, Haibao Lv, Ben Bin Xu, and Yifan Li*

A unique microfluidics approach for functional hydrogel patterning with multilayered heterogeneous structures is presented. Prepolymer solution droplets with differentiated sodium acrylate concentrations are dispensed/printed in a wetting-controlled "two-parallel plate" (TPP, like a Hele-Shaw Cell) system. The gelation within the system enables hydrogel bilayer structures with reconfigurable 3D deformations driven by in-plane and through-thickness heterogeneity under stimuli-responsive mask-less swelling/deswelling. The cooperation between swelling mismatch of functional groups results in a higher complexity of 3D reconfiguration in responding to discrete levels of stimulation inputs. This facile patterning technology with an in-built ionic hierarchy can be scaled up/down with advanced transducing functionalities in various fields.

1. Introduction

Inspired by nature,[1–3] morphing soft materials responding to external stimulation (e.g., electrical, mechanical, and chemical) has proven to exhibit applicability in various fields,[4–9] but not restricted to flexible electronics,[10,11] 4D printing,[12,13] biomedical transducers,[14] and soft robotics.[15,16] One of the desirable developments is to make the morphing process programmable[17–22] and reversible[23,24] through structured soft functional materials, which enable effective shape configuration design according to the applications. As one of the popular candidates, hydrogels have

drawn more significant attentions due to their open network structures, and ability to generate large changes[25,26] (therefore high deformation) in volume responding to various external stimulation. For example, by creating through-thickness,[20] in-plane gradient,[27] or combining the two[28] in structuring dissimilar hydrogel functional layers and blocks, controllable deformation such as bending and folding can be achieved.

The through-thickness gradient approach typically employs a hydrogel bilayer structure where the swelling behavior remains dissimilar across the thickness.[8] The differential swelling leads to internal stress mismatch and influence out-of-plane 3D morphing configurations, resulting a single configuration at certain external conditions (e.g., temperature, ion concentration).[16] When external conditions are altered, a wider range of deformation magnitude and/or a reversed shape (e.g., bending towards opposite direction, "C" becomes "Ɔ") can be achieved, and more complicated configurations can be accomplished via advanced 2D shape patterning.[8,21,29] On the other hand, the in-plane gradient approach typically employs 2D heterogeneity via a single layer of patterned functional hydrogel on the same plane, resulting in a bistable status where the buckling could happen in either directions.[16] Combining the ideas from both through-thickness and in-plane gradient modes, through a controlled "preswelling" process that determines swelling direction, programmable complex deformations were demonstrated by the "site-specific" patterned hydrogel blocks.[17,27] The resultant shape-morphing structure generated due to in-plane elastic mismatch between nonswelling substrate and controlled swellable gel blocks was more or less fixed.[17,27] Moreover, such an approach always requires pairs of silhouetted/holed "preswelling masks" to assist and orchestrate the swelling command, in order to reconfigure the deformation patterns.[16,17] Also, once deformed, it will be difficult/impossible to apply the silhouetted/holed mask again to reconfigure the shape. For the required bilayer system, thickness uniformity is important due to its role in initiating the inherent stress distribution. For homogeneous hydrogel single-layer structures, patterned or not, this can be achieved by spin coating, or molding the prepolymer hydrogel (pre-gel) in a "two-parallel plate" (TPP, like a Hele-Shaw cell) configuration, followed by gelation processes.[8,30] Inspired by natural biostructures, a single layer of encoded heterogeneous hydrogel building blocks has been exploited to form hierarchical complex hydrogel architectures, using droplet microfluidics (DMF) surface wetting control to guide the gel formation.[31]

S. Sridhar, Dr. C. Wang, Dr. X. Chen, A. Sun, Prof. B. B. Xu, Dr. Y. Li
Mechanical and Construction Engineering
Faculty of Engineering and Environment
Northumbria University
Newcastle upon Tyne NE1 8ST, UK
E-mail: yifan.li@northumbria.ac.uk
Dr. J. G. Terry
School of Engineering
Institute for Integrated Micro and Nano Systems
University of Edinburgh
Edinburgh EH9 3JF, UK
Z. Li, Prof. H. Lv
Science and Technology on Advanced Composites in Special
Environments Laboratory
Harbin Institute of Technology
Harbin 150080, P. R. China

The ORCID identification number(s) for the author(s) of this article can be found under https://doi.org/10.1002/admi.202001211.

Understanding complex dynamics of interfacial reconstruction in polyampholyte hydrogels undergoing mechano-chemo-electrotaxis coupling

Ziyu Xing[1]**, Haibao Lu**[1] ⓘ**, Ansu Sun**[2]**, Yong Qing Fu**[2]**, Muhammad Wakil Shahzad**[2] **and Ben Bin Xu**[2]

[1] National Key Laboratory of Science and Technology on Advanced Composites in Special Environments, Harbin Institute of Technology, Harbin 150080, People's Republic of China
[2] Faculty of Engineering and Environment, Northumbria University, Newcastle upon Tyne NE1 8ST, United Kingdom

E-mail: luhb@hit.edu.cn and ben.xu@northumbria.ac.uk

CrossMark

Abstract
Polyampholyte (PA) hydrogels have attracted significant attention for their superior mechanical strength and toughness compared with other conventional hydrogels. In this study, we present a novel thermodynamic approach to understanding the mechano-chemo-electrotaxis coupling and interfacial dynamics in PA hydrogels. Flory–Huggins theory, carried out through an interfacial free-energy model, is the foundation for the quantitative study of the mechanically constitutive relationship of the PA gels. The proposed free-energy model is further extended to describe the mechano-chemo-electrotaxis switching and interfacial dynamics by co-relating the Williams–Landel–Ferry equation and scaling laws. It was concluded that the interfacial bonding strength is the key factor influencing the mechanical strength and reconstruction reversibility of the PA macromolecular gel system. The resulting analytical outcomes showed good agreement with the reported experimental data. We opine that the proposed model will guide the future application of PA hydrogels.

Keywords: polyampholyte hydrogel, interfacial dynamics, coupling model

(Some figures may appear in colour only in the online journal)

1. Introduction

Hydrogel represents a group of important soft matter with versatile features, such as bespoke biocompatibility [1], superior biodegradability [2] and high stretchability [3]. The intrinsic nature of low macromolecular concentration in hydrogels usually results in a relatively low Young's modulus and a reasonable elasticity [4, 5], enabling their potential for application in biological/biomedical engineering [1, 2, 6]. On the other hand, such low macromolecular concentration also limits the wide range of engineering applications of these materials due to the environmental impact on the mechanical properties, such as brittleness, unscalability and non-adaptivity [7–12].

However, polyampholyte (PA) hydrogel has been recently discovered to have the potential to overcome its limitations and improve properties such as the mechanical strength, elongation and tensile strength to 1–10 MPa, 1000% and 100–1000 J m^{-2}, respectively [13]. The molecular structure of PA hydrogels normally consists of strong bonds working as permanent cross-linking points and weak bonds working as reversible sacrificial bonds [12, 14]. Under mechanical loading, the weak bonds break first to dissipate the mechanical energy through a reversible mechanochemical transition [15–20], while the strong bonds serve as permanent cross-linking points to dissipate the mechanical energy through deformation. Therefore, the mechanical properties of

1

A TUNABLE MORPHING POLYELECTROLYTE SYSTEM FOR SMART OCULAR APPLICATIONS

Ansu Sun, Sreepathy Sridhar, Xue Chen, Yifan Li*, and Ben B. Xu*

¹Department of Mechanical and Construction Engineering, Northumbria University, Newcastle upon Tyne, United Kingdom

Yifan.li@northumbria.ac.uk
Ben.xu@northumbria.ac.uk

ABSTRACT

For the first time, a focal-length tunable intra-ocular lens (IOL) device has been realized by a standard-shaped, homogeneous "one material" system. Different to existing technologies, this poly(N-isopropylacrylamide) gel (PNIPAM) based polyelectrolyte system doesn't require any additional materials (e.g. metal electrodes, movable mechanical structures) to achieve a controllable lens shape transformation for the focal-length shifting actuation. The designed morphological deformation mechanism employs ionic-strength responsive mechanical buckling via controlled swelling of PNIPAM in phosphate buffered saline (PBS) with similar concentration to human eye liquid. This unique approach will unlock great potential in a wide range of smart ocular applications.

KEYWORDS

PNIPAM, PNIPAAm, responsive polymer, intra-ocular lens, focal length, swelling;

INTRODUCTION

The crystalline lens (CL) is the main functional part for the focusing control mechanism of human eyes, directing the light coming through the cornea towards the retina. Cataract is a common eye disease that affects the human eye via CL opacification. It comprises around half of the world blindness, while the number of patients will continue to increase with the aging population [1-3]. Since the invention of modern cataract surgery with artificial Intra Ocular Lenses (IOLs), it has been developed significantly into an effective way to cure this problem [4, 5]. One desirable property is the switchable focal length, where adaptive vision correction is needed when eye conditions change [6, 7]. While existing multifocal IOL designs provide a benefit for near and intermediate vision for some cases, they do not allow dynamic focus length shifting in a continuous fashion. Technical innovations towards new generation of eye implants are therefore desired in terms of improving patient experiences as well as driving efficiencies in public healthcare expenditure.

Meanwhile, latest manufacturing technologies have enabled advanced materials for smart ocular system applications, such as 3D printed artificial cornea [8], customized ocular prosthesis [9], 3D printed iris [10], smart contact lenses with ocular pressure sensing [11,12]. Looking beyond human ocular applications, tunable bio-optical configurations in other advanced devices have been achieved in recent developments, which no longer require complicated mechanical units [13 – 15]. Some of the recently developed smart polymer achieve tunable optical focal length, responding to and controlled by external

stimulation such as pH-responsive [16], electric field [17], and ion concentration [18] with mechanical confinement structures or electrical interconnects. However, limited efforts have been found on developing easy-to-implant artificial ocular device with responsive focal shifting, since the above devices may require non-compatible materials (e.g. metal electrodes), liquid/solid interactions and stimuli for actuation are hard to fulfil in in-vivo, as in the human eyes.

With these regards, we proposed and demonstrated a new polyelectrolyte system based on PNIPAM (also named PIPAAM or PNIPAAm), to advance the robust optical implant technology with focal shifting. For the first time, tunable morphological deformation has been realized by a homogeneous "one-material" polyelectrolyte system with either freestanding (this abstract's focus), or edge-confined configurations.
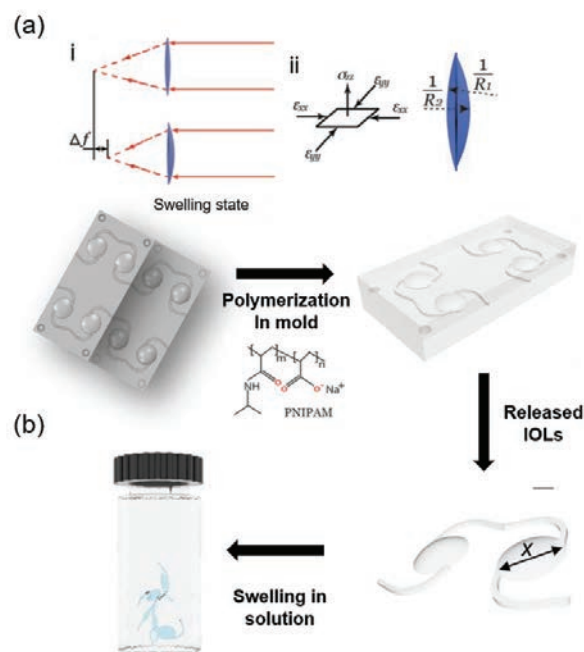

Figure 1: (a) Proposed focal length shifting mechanism: mechanical buckling of the dual-curved IOL shape change; (b) Low cost and facile fabrication process of the PNIPAM tunable IOLs

The designed morphological deformation mechanism is to be achieved by responsive mechanical buckling, which is a common phenomenon in thin, soft structures that may yield rapid out-of-plane deformation (**Fig. 1a**). Such out-of-plane deformation results in dynamic changes in designed IOL morphology parameters therefore achieving

Research Article

Spatially and Reversibly Actuating Soft Gel Structure by Harnessing Multimode Elastic Instabilities

Yingzhi Liu,[⊥] Ansu Sun,[⊥] Sreepathy Sridhar, Zhenghong Li, Zhuofan Qin, Ji Liu, Xue Chen, Haibao Lu,* Ben Zhong Tang,* and Ben Bin Xu*

Cite This: *ACS Appl. Mater. Interfaces* 2021, 13, 36361−36369

Read Online

ACCESS | Metrics & More | Article Recommendations | Supporting Information

ABSTRACT: Autonomous shape transformation is key in developing high-performance soft robotics technology; the search for pronounced actuation mechanisms is an ongoing mission. Here, we present the programmable shape morphing of a three-dimensional (3D) curved gel structure by harnessing multimode mechanical instabilities during free swelling. First of all, the coupling of buckling and creasing occurs at the dedicated region of the gel structure, which is attributed to the edge and surface instabilities resulted from structure-defined spatial nonuniformity of swelling. The subsequent developments of post-buckling morphologies and crease patterns collaboratively drive the structural transformation of the gel part from the "open" state to the "closed" state, thus realizing the function of gripping. By utilizing the multi-stimuli-responsive nature of the hydrogel, we recover the swollen gel structure to its initial state, enabling reproducible and cyclic shape evolution. The described soft gel structure capable of shape transformation brings a variety of advantages, such as easy to fabricate, large strain transformation, efficient actuation, and high strength-to-weight ratio, and is anticipated to provide guidance for future applications in soft robotics, flexible electronics, offshore engineering, and healthcare products.

KEYWORDS: hydrogel, swelling, creasing, buckling, shape transformation
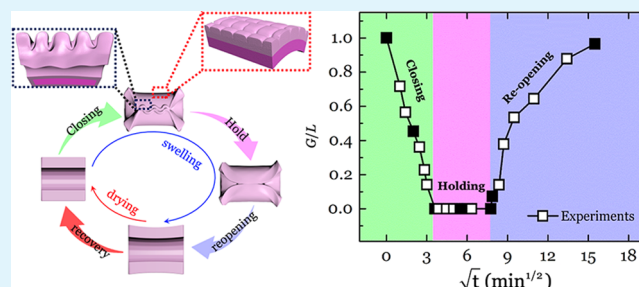
1. INTRODUCTION

Soft matter-based biosystems widely exist in nature to support lives such as octopus, starfish, caterpillars, etc., by fulfilling adaptive shape changes and responsive motions to allow them to survive in complex environments.[1−5] Inspired by these features, a number of soft actuator concepts[6−11] have been developed to mimic dedicated actuations/motions, e.g., soft grippers actuated by inflation of a pneumatic network to manipulate fragile and irregular objects,[12] a humidity- and light-driven liquid crystal network actuator[13] to mimic self-shape morphing of flowers, and bellow-like actuators[14] with origami structures enabled various motions. The discovery of superior bio-inspired robotic structure/mechanisms with desired working capacity, efficient actuation, high strength-to-weight ratio, on-demand shape programmability, and low cost is highly desired for frontier engineering applications.

Responsive hydrogel-based configurable structures can undergo shape transformation and perform complicated pattern generation spontaneously and reversibly in the presence of external stimuli, such as temperature, ionic strength, pH, light, solvent, and electric field.[15−19] Together with its soft, biodegradable, and biocompatible properties, a hydrogel has been seen as an ideal candidate to build soft robotics,[20] soft actuators,[21,22] and soft electronics.[23,24] Notably,

Palleau et al.[25] created soft hydrogel tweezers through electrically assisted ionoprinting and demonstrated the gripping/releasing of small objects. Using a 3D printing technique, Xu and co-workers[26] fabricated an airplane-like swimming gel robot that could remotely control different motions under near-infrared light. Yuk et al.[20] exploited the hydraulic actuation of hydrogels to develop soft robotics, which is capable of optical and sonic camouflage in water. While the above attempts provide advancements in exploring the novel actuating mechanism, the overall fabrication, assembly, and actuation of these devices heavily rely on the support from instruments and infrastructure, which will considerably limit the application/commercialization of hydrogel actuators at the scale-up level.

Mechanical instabilities including wrinkling,[27−33] creasing,[34−37] folding,[38−40] ridging,[41−44] buckling,[45,46] and bending[47] have brought a unique approach to realize programmable